The University Of Sheffield.

An Experimental Investigation on the Roles of Pore Fluid and Polydispersity in Granular-flow Mechanisms

By:

Yuting Zhao

Supervised by:

Dr Elisabeth Bowman

A thesis submitted in partial fulfilment of the requirements for the degree of Doctor of Philosophy

The University of Sheffield

Department of Civil and Structural Engineering

October 2022

Declaration

I declare that this thesis is an original report of my research that has been composed solely by myself and has not been submitted for any previous degree or professional qualification. Except where the source of information is clearly stated by reference and where the contribution of others is acknowledged, I confirm that the work contained in this thesis is entirely my own.

Signed,

October 2022

Acknowledgements

This work would not have been possible without the help of many people. First of all, my deepest gratitude goes to my main supervisor, Dr Elisabeth Bowman, for her knowledge, guidance, patience, encouragement and fullest support that have helped me enormously throughout the entirety of my PhD journey. Secondly, I must greatly appreciate Mark Foster and Paul Blackbourn, the departmental senior technicians, for their indispensable technical support to my long-running laboratory work.

I would love to give special thanks to the members of the collaborative research project, The Rosetta Stone Network: Prof Andy Take and his postgraduate student Alexander Taylor-Noonan (Queen's University, Canada), Prof Roland Kaitna (BOKU, Vienna, Austria), Dr Brian McArdell (WSL, Switzerland), and Prof Jim McElwaine (Durham University); they had been giving me countless valuable suggestions and inspirations with their expertise. And thanks to The Leverhulme Trust for funding this research project.

I would like to sincerely thank my second supervisors Dr James Shucksmith and Dr Paul Shepley for their advice and feedback at the key moments of my research, and would also like to extend this appreciation to all the staff in the Geotechnical Engineering Group and in the Technical Support Team of the Department of Civil and Structural Engineering.

Finally, thanks to my friends, my family and, particularly, my girlfriend, for supporting me through these four years.

Yuting Zhao

October 2022

Abstract

Geophysical granular flows like debris flows attract the broad attention of engineers and researchers as a natural hazard that threatens life and properties. The material composition of natural debris flows, i.e. well-graded angular sediments saturated with water, greatly complexifies the debris-flow mechanism, hindering the establishment of a universal physical framework. The prevailing granular-flow research commonly keeps the material relatively consistent, composed of either highly idealised particles (i.e. dry, monodisperse and spherical) if the fundamental physics and constitutive laws are preferred, or rather realistic soils (i.e. saturated, polydisperse and angular) if hazard assessment and the macroscopic similarities with geophysical flows are of interest. However, few studies have paid attention to intermediate states where flow materials extend from idealised to realistic and hence, the processes by which the flow mechanisms gradually become more complex. This study attempts to fill this gap by investigating the fundamental roles of pore fluid and polydispersity (i.e. the property of solid flow material containing multiple grain sizes) on the granular-flow mechanism via small-scale flume experiments and to improve the understanding of the formation of complex debris-flow behaviours.

The experimental work in this study adopted a small-scale inclined flume to conduct granular flows with three separate conditions, i.e. dry uniform, wet uniform and wet well-graded. Bulk flow mobility was analysed from the flow deposits, normal stresses and pore fluid pressures were acquired by sensors mounted at the flume bed and the side-view velocity information was derived by Particle Image Velocimetry (PIV) from a series of images captured by a stationary high-speed camera. A smooth continuous evolution of pore fluid pressure from negative values to positive values with water content was exhibited in wet uniform granular flows, where the developed pore pressures were found to be highly correlated with bulk flow mobility: the runout is overall retarded when negative suction dominates the flow surge but is enhanced when positive pore pressure prevails. When no suction (negative pore pressure) was evident, the bulk

mobility of wet granular flows, whether uniform or well-graded, formed an approximately fixed-slope linear relationship with water content. Excess pore pressure did not appear in wet uniform flows and hence buoyancy seems adequate to contribute to the achievable high bulk mobility and increased flow velocity, which is related to the lessening of local shear between solids due to the increase in pore fluid involved in uniform flows. For well-graded flows, excess pore pressure can be produced at high water content but did not notably increase the flow velocity; instead, higher water content and larger pore pressure seem to result in significantly smaller shear strength of the flow material and thus larger shear deformation during the deposition process. Therefore, for the tested granular flows, the fundamental influence of pore fluid is to adjust the solid contact stress with either suction or buoyancy, thereby affecting the velocity profile and shear mechanism of the wet granular flow; the fundamental influence of polydispersity, on the other hand, is to change the deformation mechanism of the flow material.

The obtained experimental results offer new insight into the pore fluid effect, as the smooth transition of pore pressure from negative to positive, which is highly associated with the variation of the correlated bulk flow mobility, does not appear to have been reported previously. Pore pressure measurements for granular flows in laboratory-scale flume experiments are generally rare and this study can provide valuable data that are referenceable for future work. Velocity profiles of uniform and well-graded flows may assist the selection of appropriate parameters to account for solid interaction in granular-flow modelling. The high bulk mobility and deposit morphology achieved in the tested wet granular flows, similar to those of debris flows, enhance confidence in the application of small-scale experiments.

Contents

Notation

A	Basal area of the flow material [m^2]
C_c	Curvature coefficient
C_u	Uniformity coefficient
c’	Effective cohesion of the dry soil [Pa]
D	Grain size [m]
E	Stiffness [Pa]
$\overline{E_k}$	Kinetic energy of the “main surge” [J]
e	Void ratio
g	Gravitational acceleration [m/s^2]
H′	Elevation drop of the centre of gravity [m]
h	Local flow thickness [m]
k	Hydraulic permeability [m^2]
L	Flow length (not used) [m]
L	Deposit length or travel distance calculated from the inclined flume outlet [m]
L′	Horizontal moving distance of the centre of gravity [m]
L*	Travel distance normalised by the deposit length
m	Flow mass [kg]
N_{Sav}	Savage number
N_{Bag}	Bagnold number
N_{fric}	Friction number

p_a	Pore air pressure [Pa]
p_w	Pore water pressure [Pa]
p_{basal}	Basal pore fluid pressure [Pa]
p_{st}	Basal fluid pressure due to the fluid weight [Pa]
r_p	Radius of the pore space or the curved meniscus in a capillary tube [m]
S	Saturation degree
S_r	Residual saturation degree
T_s	Surface tension of water [N/m]
t	Time [s]
t*	Time normalised by the "main surge" duration
t_{diff}	Timescale for pore pressure dissipation [s]
u	Flow velocity [m/s]
u_{ave}	Depth-averaged velocity [m/s]
u_{slip}	Slip velocity [m/s]
u_{surf}	Surface velocity [m/s]
V_{bulk}	Bulk solid volume [L]
$\overline{W_F}$	Work done by Coulomb friction during the "main surge" [J]
w	Gravimetric water content
w_{sat}	Saturation water content
X	Slope distance from the point under the hopper centre to the downslope load cell [m]
x	Unit flow length per PIV time interval [m]
x*	Relative flow length normalised by the "main surge" length
α_T	Travel angle [°]
Γ	Bulk shear rate [1/s]
$\dot{\gamma}$	Local shear rate [1/s]
δ	Averaged grain size [m]

η	Kinematic viscosity of fluid [m^2/s]
η_{air}	Kinematic viscosity of air [m^2/s]
η_w	Kinematic viscosity of water [m^2/s]
θ	Slope angle [°]
θ_c	Contact angle of the grain-water interface [°]
θ_f	Filling angle [°]
λ	Coefficient associated with the arrangement of spherical particles
μ	Dynamic viscosity of fluid [Pa.s]
ρ	Bulk density [kg/m^3]
ρ_s	Solid density [kg/m^3]
ρ_f	Fluid density [kg/m^3]
σ	Normal stress [Pa]
σ_{basal}	Basal normal stress [Pa]
σ'_{basal}	Basal effective normal stress [Pa]
σ_{st}	Basal normal stress due to the weight of flow material [Pa]
τ	Shear stress or shear strength [Pa]
υ_s	Volumetric solid fraction
$\upsilon*$	Maximum (close-packed) volumetric solid fraction
ϕ’	Internal friction angle [°]
χ	Parameter dependent on the saturation degree
ψ	Matric suction [Pa]

List of Figures

List of Tables

1. Introduction

1.1. Background

Debris flows develop when mixtures of water and solid mass with a large range of particle sizes rapidly move downslope due to gravitational forces. Considered a destructive and deadly natural disaster, debris flows often demonstrate great velocity and impact, along with high incidence in rainy, mountainous regions. Understanding the debris-flow mechanisms is needed to accurately estimate their hazard and to protect lives and properties.

However, current knowledge about debris flows is insufficient. The establishment of a straightforward, universal and globally valid theoretical framework is hindered by the complex nature of debris-flow material, and the consequent strong, varied solid-fluid interactions distinguish debris flows from other geological phenomena (Iverson, 1997). Instead, the available frameworks of debris-flow analysis are often based on semi-empirical approaches with simplifications of local-scale interactions. For example, the widely accepted hydraulic model employing depth-averaged equations, which is preferred for allowing the realistic unsteady flow motion, replaces heterogeneous mixture with an equivalent fluid continuum and simplifies fluid effects into a rudimentary friction reduction (Hungr, 1995; Gray et al., 1999; Denlinger and Iverson, 2001; Hungr et al., 2005). This type of approach is convenient to use in practice, yet leaves the fundamental debris-flow mechanisms poorly described, hence showing a few deficiencies: empirical parameters that highly depend on specific flow conditions need to be calibrated from real events, and scale consistency is required to guarantee morphological relevance. As Iverson (2015) says, similarities in geomorphology do not imply similar flow processes, and identical bulk flow behaviours can result from totally different mechanisms. Faithful descriptions of fundamental mechanisms are necessary for better debris-flow estimation.

On the other hand, flow mechanisms can be precisely captured when the material is highly idealised (e.g. dry, monodisperse, composed of identical spheres), in which case the flowing medium is generally referred to as "granular flow". Simple material allows decomposing bulk flow behaviours into a combination of basic processes, which are achievable through constitutive laws. Confidence has been provided in presenting rheologies of individual typical granular flow configurations (GDR MiDi, 2004), particularly the flow on a channelised inclined plane discussed by Jop et al. (2006). Yet, such analysing approach cannot be directly applied to debris-flow prediction due to the obvious mismatching of flow conditions. A gap remains between the current understanding of flow mechanisms and their application to real-life situations.

Knowledge regarding the evolution of fundamental mechanisms is absent when the flow material shifts from idealised to realistic. From dry to saturated and uniform to well-graded, the participation of pore fluid and polydispersity seems to greatly complicate the dynamics of granular media, to a point where the estimation of macroscopic flow behaviours (e.g. flow depth and bulk mobility) cannot be derived from an accurate description of microscopic physical process. To gradually deepen the understanding of more complex granular flows, attempts have been made to consider debris-flow properties such as polydispersity (Gray et al., 2015) and unsteady motion (Parez et al., 2016) when exploring fundamental mechanisms; however, few studies have tried to make the flow material as realistic as possible. In this sense, establishing a smooth transition of the material composition from idealised to realistic is valuable as it can help to give an insight into the internal physical process where flow mechanisms become increasingly complex.

1.2. Aims of Research

This research aims to investigate by small-scale experiments the evolution of fundamental debris-flow mechanisms during the transition of material composition from idealised to realistic; specifically, to clarify the roles that pore fluid and polydispersity play in the behaviours of small-scale experimental flume flows, in which the material is initially composed of dry uniform spheres, then mixed with water to oversaturation, and eventually added with well-graded real soil to replace spherical grains. With regard to the direct contribution, this research provides experimental data with clear conditions showing both bulk flow behaviours and internal dynamics, which can be utilised to calibrate, verify and improve numerical models.

Two types of flow behaviours are particularly focused on: (i) local-scale dynamics of the granular medium, including basal stresses, velocities, shear mechanisms, and momentum transfer; and (ii) bulk mobility, one of the crucial debris-flow characteristics and one of the biggest engineering concerns regarding debris-flow hazard assessment. These two aspects respectively represent the analyses from microscopic to macroscopic perspectives and the interests of granular physicists and engineers; therefore, the connection between the two aspects can bridge engineering and granular physics, facilitating the communication between the two separate principles.

1.3. Outline of the Thesis

The content in this thesis is organised as follows. Chapter 2 briefly reviews physical frameworks of idealised and realistic granular flows and the current knowledge of the influence of pore fluid and polydispersity. Chapter 3 introduces the methodology of this experimental study, containing the small-scale flume experiments (including the experimental setup, source material, test conditions and test procedure) and data analysis methods (including PIV analysis, the quantification of bulk flow mobility and dimensional analysis). Chapter 4, Chapter 5 and Chapter 6 respectively present the results of dry uniform flows, fluid-mixed uniform flows and fluid-mixed well-graded flows; each chapter covers the analyses of granular-flow deposits, flow profiles along the longitudinal direction, flow heights, sensor signals, PIV-derived velocities and flow regimes. Chapter 7 compares and contrasts the obtained results of separate test groups to deduce the influence of the existence of pore fluid and the participation of well-graded solids on the fundamental granular-flow mechanisms. Chapter 8 draws the final conclusions of this thesis, along with the limitations of this work and some expectations to the future work.

2. Literature Review

Preface

Terminology must be stated to avoid the ambiguity potentially brought by the interchangeable wording. “Debris flow” is a geological term referring to a gravity-driven moving mass different from “rock avalanche” (which lacks the influence of viscous fluid phase) or “mudflow” (which lacks the participation of coarse solids); “granular flow” is a more general and broader concept distinguished from “fluid flow” highlighting that interparticle contacts are non-negligible. The material composition of debris flow is naturally complex, thus if debris-flow behaviours are desired to be reproduced in experimental works, samples are better to be as realistic as possible. “Realistic flow” in this study refers to saturated flows involving well-graded irregular-shaped solids, which lead to the flow condition closest to that of debris flows; while “idealised flow” refers to the dry monodisperse flows of rigid spherical particles, which are usually used when analysing local-scale granular flow mechanics. Note that requiring the flow to be at a steady state (i.e. not accelerating) is not included in the definition of “idealised flow” as it normally would be, since material composition is the main focus of this study. Natural debris flows can exhibit the properties of both “granular flow” and “fluid flow” depending on the material composition; however, for small-scale flows like those in the experimental work of this study, the effect of fluid viscosity that develops pore pressure and reduces the effective stress, which weakens the friction among particles is reduced (Iverson, 2015) and thus solid grains are easier to maintain in close contact and are less likely to be fluidised. Therefore, in the context of this thesis, “debris flow” is roughly regarded as a specific type of “granular flow” with “realistic flow” conditions.

A debris flow event consists of mobilisation, motion and deposition. Mobilisation is a big part of debris/granular flow research, including considerations like failure mechanism, yield criteria, liquefaction, the emergence of dispersive pressure and the regime change of granular media from

jammed “solid” to flowing “liquid”; these topics are not involved in this study. Additionally, mass exchange (i.e. erosion and mass loss) that commonly occurs in natural geophysical flows is also not investigated here. The granular flow behaviours of focus in this study include the local dynamics during the downslope process and the macroscopic runout features in the depositional area.

The literature review of this thesis is structured as follows. Sec. 2.1 gives basic information about granular flows and debris flows, including their definitions, classifications, and essential complexities. Sec. 2.2 briefly reviews several typical modelling approaches for granular flows, discussing their strengths and shortcomings. Sec. 2.3 introduces several dimensionless numbers that are often used to differentiate between flow regimes which are dominated by different momentum transfer mechanisms. These three sections explain the difficulties and current theories of describing the fundamental flow mechanisms when the flow composition transforms from idealised into realistic. Sec. 2.4 briefly reviews the established knowledge about pore fluid and pore pressure; while Sec. 2.5 takes an interest in different grain sizes and their impact on debris-flow behaviours. These two sections show the gap in the current understanding of the roles of pore fluid and polydispersity in granular flow mechanisms. Finally, Sec. 2.6 gives critiques of the referenced literature and locates this study within the body of granular flow and debris flow research.

2.1. Granular Flow and Debris Flow

2.1.1. Definition of Granular Flow

Granular flows are flow motions of particulate solids where mechanics are dominated by interparticle contacts (Brennen, 2005). The criteria of granular flows are straightforward. First, particles constituting granular flows must belong to granular media, which requires that: (i) grains are effectively rigid, and (ii) grain sizes are typically larger than 100 μm (such particles are categorised as “granular media”) to ignore Brownian movement, van der Waals force, air drag and thermal agitation. Second, whether dry or wet, solid concentration must be sufficiently high to an extent that solid interparticle momentum transfer can determine the bulk flow properties (Brennen, 2005). Particularly, dry particles exposed in the air are usually referred to as “powder” or “granular material” while particles suspended in liquid as “suspension” (Andreotti

et al., 2013); according to the definition, granular flows must be composed of "granular material" or "granular media".

Granular flows can occur in a variety of geometries as no criterion of moving pattern is introduced in the definition. GDR MiDi (2004) details six main configurations often investigated in granular flow studies (Figure 2-1): (i) simple plane shear, (ii) annular shear, (iii) vertical silo, (iv) inclined plane, (v) heap flow, and (vi) rotating drum. Constitutive behaviours derived from each geometry have been well-described individually but cannot be applied to another configuration (GDR MiDi, 2004); common laws across different configurations are still a challenge. To directly compare with debris flows, "granular flow" in later sections only refers to those on a channelised inclined plane (i.e. chute flows) unless otherwise specified; correspondingly, the term "granular media" is used when describing more general characteristics.

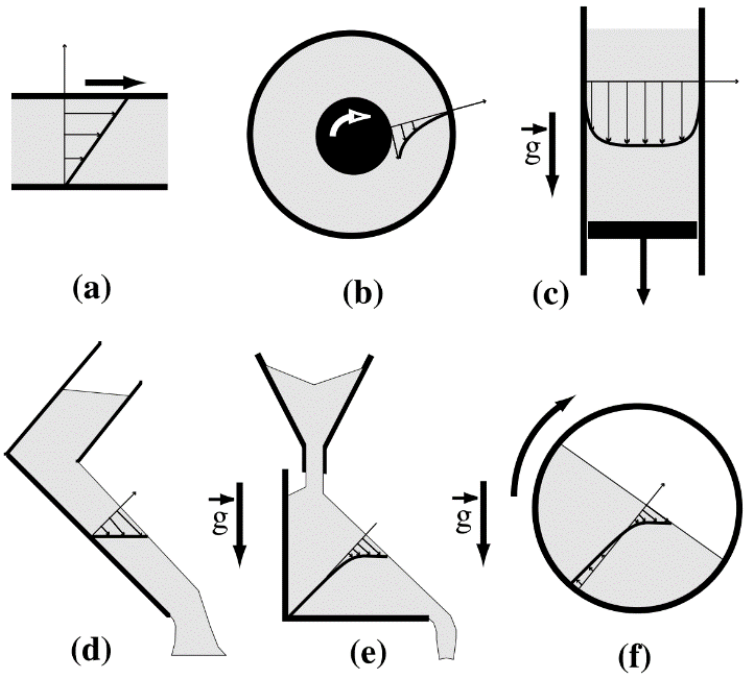

Figure 2-1: Main granular flow configurations (GDR MiDi, 2004): (a) plane shear, (b) annular shear, (c) vertical silo, (d) inclined plane, (e) heap flow, (f) rotating drum.

2.1.2. Definition of Debris Flow

From a fairly early stage of the research, "debris flow" has been broadly adopted to describe a slurry-like mass movement containing a considerable amount of both fine and coarse sediments (Carter, 1975). Classification schemes discriminating debris flows from other mass movements are generally divided into two categories: one defines debris flows depending on geophysical features like moving mechanisms and material properties, i.e. from a macroscopic or geological

perspective (Varnes, 1978; Hutchinson, 1988; Hungr et al., 2001); while the other is based mainly on flow regimes which can be represented by the dominant physical process occurring inside the flow, i.e. from a microscopic or rheological perspective (Davies, 1988; Coussot and Meunier, 1996; Iverson, 1997; Takahashi, 2001).

According to the landslide material classification system established by Hungr et al. (2001) designed for engineering geology, a "debris flow" must: (i) consist of non-cohesive, unsorted (i.e. well-graded or polydisperse) debris material whose plasticity index is usually lower than 5%, (ii) contain less than 30% fines content, i.e. silt and clay (< 0.074 mm), (iii) be fully saturated with water, (iv) move very rapidly with a velocity at least greater than 3 m/min, and (v) move in a regular confined channel covering a large portion of the flow path and ending with an alluvial fan. This definition gives user-friendly parameters related to debris-flow material composition and kinematics and points out the necessity of the channelised flow path.

Focusing on the evolving physical mechanism results from increasing solid content in a fluid flow, a rheological classification proposed by Coussot and Meunier (1996) and later on modified by Schatzmann (2005) distinguish mass movements by two parameters: solid volume fraction (or volumetric sediment concentration), and percentage of fine material (< 0.04 mm in this case). Within this framework, the concept "debris flow" is defined by a solid volume fraction intermediate between those of hyper-concentrated flow and block-type landslide, as shown in Figure 2-2, and is possible to be subdivided into more types: (A) granular debris flow, where coarser grains are in the majority of the solid phase and their interactions dominate the flow mechanics; (B) viscous-granular flow, where the dominant mechanism transits from solid contacts to viscous shear; (C) viscous debris flow where fines content takes more than 10% of the solids and the entire flow acts rather like a homogeneous viscous fluid; and (D) mudflow, which is usually not considered as a debris-flow type in engineering and possesses more fine particles than coarse grains. Additionally, natural debris flows typically contain solid grains with a volume fraction of 50-80% as proposed by Iverson (1997), or 30-65% in the flow front and gradually decreasing towards the tail as reported by Hutter et al. (1994).

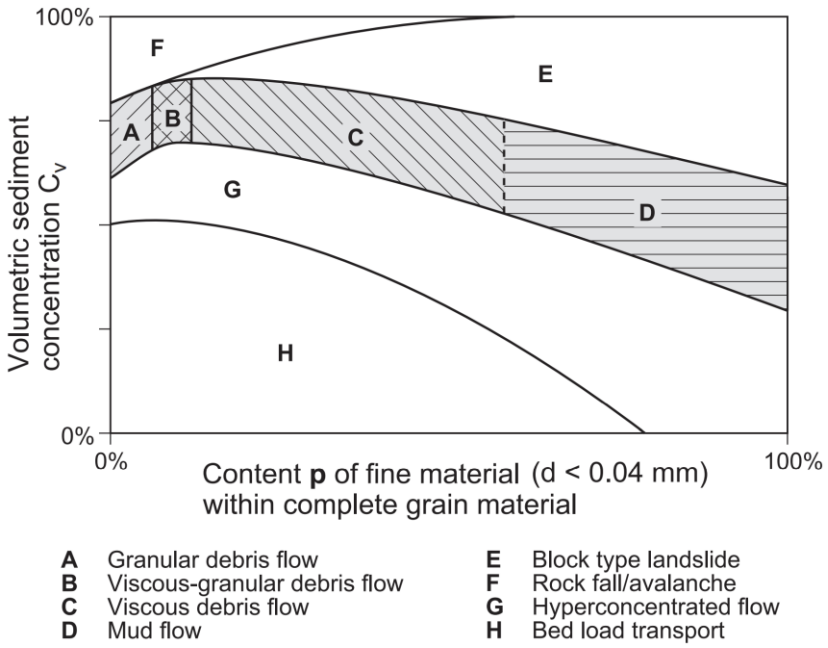

Figure 2-2: Mass movements classification proposed by Coussot and Meunier (1996) and modified by Schatzmann (2005), in which "debris flows" are marked as A-D.

2.1.3. Complexities of Granular Flows

A valid theoretical framework of granular media is challenged by many difficulties. A large number of particles can be involved and multiple non-linear intergranular interactions (e.g. Coulomb friction, inelastic collision, and, if immersed in viscous fluids, hydrodynamic contacts) can coexist in a granular medium. As explained by Andreotti et al. (2013), the complex grain-level interactions and the huge number of grains greatly increase the cost of tracking the dynamics of individual grains, resulting in a preference for continuum modelling with averaged quantities of grains. However, regarding aggregation of particles as a continuum also seems doubtful. Since big particles do not experience Brownian movement, granular media cannot rapidly achieve local thermal equilibrium as liquid and gas do; in other words, in a system of particulate solids, local mechanics cannot be determined by averaging the macroscopic state. The separation between the microscopic scale and macroscopic scale of granular media is unclear, i.e. the scale where mechanics of individual grains start to not affect bulk behaviours of the entire medium thickness is unavailable. These issues can be alleviated if the mechanics of every individual grain is identical and sustained. As a result, the rheology of granular flows at present is not well-described without the simplest condition, i.e. steady motion of the idealised flow material.

However, more complicated debris-flow material that has to be faced in reality is far from idealised conditions. Solid grains of various sizes and viscous fluid create strong interactions that distinguish debris flow from other geophysical phenomena, leading to high mobility as well as huge impact force (Iverson, 1997). The first unique debris-flow characteristic is the heterogeneous surge. Within a debris-flow surge, solid particles experience dynamical sorting both normal to and along the flow direction depending on their sizes: vertically, larger grains tend to move closer to the flow surface and smaller grains to the bottom, becoming a matrix carrying the upper flow body; longitudinally, largest boulders accumulate at the unsaturated flow front, relatively coarse grains suspend in the saturated flow body, and fine silt or clay gather at the hyper-concentrated liquefied flow tail (Pierson, 1986; McArdell et al., 2007; Leonardi et al., 2015). This sorting process called "grain size segregation" allows the flow to alter rheological features in time and space (Figure 2-3Figure 2-3).

Corresponding to different zones in a segregated debris-flow surge (Figure 2-3), distinct flow dynamics is exhibited due to different dominant interactions. During debris-flow motion, five types of interactions can simultaneously exist: (i) intergranular contacts (colliding, sliding and self-locking), (ii) interactions with the underlying bed, (iii) interactions between grains and interstitial fluid, (iv) viscous shear of the pore fluid, and (v) interactions with ambient fluid (Delannay et al., 2017); whereupon complex stresses are generated inside debris flow, mainly including (i) solid inertial (collisional) stress, (ii) fluid inertial stress, (iii) solid quasi-static (Coulomb frictional) stress, (iv) fluid quasi-static (viscous shear) stress, and (iv) solid-fluid interaction stress due to pore fluid resisting the grain rearrangement motion (Iverson, 1997). Multiple interactions with different dominance tend to generate distinguishing stress states depending on grain size: the momentum transfer from larger particles is governed more by gravity, while smaller particles are more easily influenced by fluid effects. At the flow head, granular collisional stresses over large clasts dominate; in the following flow body, granular shear stresses play a bigger role with smaller grain size and denser packing; meanwhile, viscous pore fluid effects step in, gradually buffering granular contacts as grains become finer and finer approaching to the rear, until small grains are no longer in contact with each other and viscous fluid shear dominates the momentum exchange; in the dilute tail part, the fully suspended fine particles are too scattered to drag the fluid, resulting in a stress state mainly determined by fluid inertia, which seems to surpass viscous shear in the turbulent flow tail for natural debris flows according to Iverson and Denlinger (2001). The coexisting different stress states make local-scale debris-flow rheologies very difficult to present.

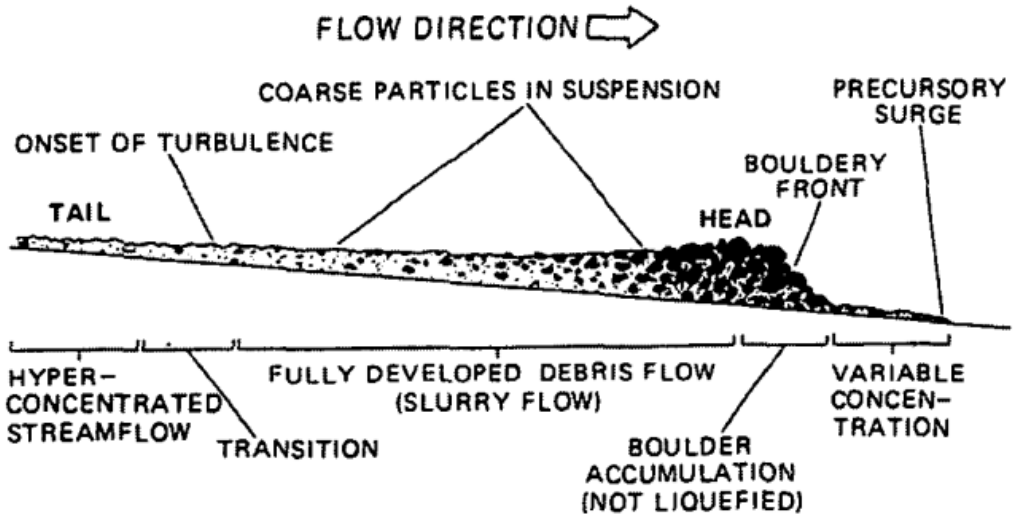

Figure 2-3: Grain size segregation in a heterogeneous debris flow surge (Pierson, 1986).

Another important debris-flow characteristic is high and persistent pore pressure brought by large compressibility and moderate permeability of the flow material, which are properties that result from well-graded sediments and cannot be produced by monodisperse grains (Iverson, 1997). This nonequilibrium pore pressure is believed to contribute to the high debris-flow mobility, but its mechanism remains uncertain, leaving several different explanations and no default consensus. More details about pore fluid pressure are presented in Sec. 2.4.

2.2. Physical Frameworks of Granular Flow

2.2.1. Conventional Debris-flow Models

Two types of theoretical model were commonly applied in the early debris-flow research: one approximates debris-flow material as a single-phase viscoplastic continuum, whereas the other assumes solid grains are fully and uniformly dispersed in the fluid phase. Both types of models have laid significant groundwork for the physical understanding of debris flows, but also possess essential shortcomings.

The viscoplastic model, also referred to as the Bingham model, originates from a recognition that debris-flow material can physically behave like both plastic solids and viscous fluid (Johnson, 1965; Yano and Daido, 1965); debris flow was then modelled as a viscoplastic material that remains rigid until subjected to shear stresses over its plastic yield strength, after which exhibits properties of Newtonian viscous fluid (Johnson, 1965; Johnson, 1970; Johnson, 1984). Coulomb

friction can also be involved in the viscoplastic model by introducing a normal-stress-depended frictional strength into the yield strength (Johnson, 1965; Johnson, 1970; Johnson, 1984); in this case, the yielding of debris-flow material follows the Coulomb failure criterion and is solely controlled by cohesion. The defect of the viscoplastic model is the limited application to only muddy debris flows rich in fine sediments, in which the matrix deformation governs the flow motion (Whipple, 1997). In a Bingham fluid, the yield strength or shear strength should increase with the bulk viscosity as more fines content is added; however, the increase of fines content helps to improve the bulk mobility and to decrease the apparent strength of debris flows (Major, 1996). This indicates that debris-flow characteristics cannot be properly represented by viscoplastic rheology, which ignores the crucial contribution of coarse grains interacting with pore fluid.

The other type is the inertial flow model established by Takahashi (1978) and Takahashi (1981) based on the work of Bagnold (1954) which gives constitutive relations of solid-fluid mixtures, where monodisperse large spheres are dispersed in fluid, in both inertial and viscous flow regimes. The inertial flow model adopts Bagnold's constitutive relation between shear stress and shear strain for the inertial flow regime to account for behaviours of the granular debris flow where collisions of large clasts dominate the momentum exchange and effects of viscous or turbulent fluid can be ignored. This model gives insight into the role of large particles in debris-flow mechanics, but with a few issues. Firstly, the original experiments in Bagnold (1954) were carried out in an annular shear cell in which the densities of particles and fluid were balanced, i.e. the gravity effect was eliminated, so that intergranular normal stresses (or the radial "dispersive pressures" as used by the author) tend to drive particles away from each other when sheared; in realistic debris flows, on the contrary, gravity greatly impacts the stress development and shear motion by facilitating enduring granular contact. Secondly, the lack of enduring granular contact leads to the absence of frictional self-locking that must happen during the mobilisation and deposition of debris-flow material (Major, 1996). Thirdly, as grains are assumed uniformly dispersed and separated in the fluid, the pore fluid is not able to be over-pressurised, i.e. no excess pore pressure is allowed; this again contradicts with field observations.

2.2.2. Depth-averaging Approach

Depth-averaged equations of mass and momentum balance proposed by Savage and Hutter (1989) have been widely applied to geophysical mass movements for simplicity and independence from microscopic parameters. The depth-averaging approach was originally

employed to describe the release of a finite granular mass from rest on a rough inclined plane and its application requires several assumptions: (i) the flow is shallow, i.e. flow thickness is much smaller than flow length, (ii) the flow material is regarded as a continuum, which means the flow size exceeds individual grain size, (iii) the change in void ratio and thus in bulk density of the flow material is ignored, (iv) the basal friction is subject to Coulomb friction law, and (v) the basal friction angle is a constant independent of shear strain and solid volume fraction. Later in the modified depth-averaged models proposed by Hungr (1995), basal friction calculation has been generalised to account for flow resistance responding to different regimes: plastic flow (which adopts constant shear strength), friction flow (where flow resistance sorely depends on effective basal normal stress), Newtonian laminar flow (where velocity is linear with dynamic viscosity), turbulent flow (where flow resistance is a function of squared flow velocity – noting that this is a different concept of "turbulence" than is typically used in fluid mechanics), Bingham flow (which considers the flow material as a Bingham viscoplastic medium), Coulomb viscous flow (where the Bingham yield strength depends on effective stress, as described in Sec. 2.2.1), Voellmy flow (Voellmy, 1955) (which combines the effects of friction and turbulence i.e. the influence of velocity-squared). Under these assumptions, the bed layer of flow material is where the sliding occurs and the stress distribution across the flow depth is then simplified into the stress state of the bed layer, in which the normal and shear stress varies only with flow depth.

Developments have been made in the modelling of debris flows along with other geophysical mass movements based on the depth-averaged governing equations. A depth-integrated model provided by Pudasaini and Hutter (2003) generalises the application of Savage and Hutter (1989) into granular avalanches on curved and twisted channels. The dynamic analysis (DAN) numerical model developed by Hungr (1995) as well as its three-dimensional version (DAN3D) by McDougall and Hungr (2004) have been designed for runout analysis and risk assessment on landslides, avalanches and debris flows; these models divide the entire granular mass into a series of "slices" along the longitudinal direction and simplify the internal interactions into the actions between every two slices. The Coulomb mixture model provided by Iverson and Denlinger (2001) uses not local rheology of the material to predict the motion, but the interaction between solid grains and viscous pore fluid, in which the role of pore pressure is to reduce Coulomb friction; depending on the magnitude and diffusion rate of pore pressure, this model can describe a variety of geophysical mass movements from granular avalanches to debris flows to viscous flood.

Models using the depth-averaging approach contribute substantially to debris-flow research and hazard assessment; they are usually practical and user-friendly, requiring few input parameters that are convenient to measure. These models hold the advantage that they can easily include the interaction between solid and fluid phases, though in a rudimentary manner, as only the fluid effect on the basal boundary is necessary. However, these models are mostly phenomenological and semi-empirical, highly relying on back-analysis and calibration data from real flow events, which are not easy to collect. Also, the internal physics of debris flows (and other granular mass movements), such as velocity and stress distribution across the flow depth, acceleration normal to the bed, and complex solid-fluid interactions, are often oversimplified. One of the direct consequences of not accurately reflecting the flow mechanism is that, as the internal debris-flow physics varies with scale (Iverson and Denlinger, 2001; Iverson, 2015), estimations of depth-averaged models work best only at scales close to the field scale; this raises questions about model scaling and limits the understanding of fundamental debris-flow mechanisms.

2.2.3. The μ(I) Rheology

The μ(I) rheology systematically developed by Jop et al. (2006) is a nonlinear constitutive law for dense steady idealised granular flows on an inclined rough bed and is empirically determined from experimental results. The basic assumption is that the local friction everywhere at the flow-bed boundary is decided by the plane shear constitutive friction law. In a simple plane shear configuration, as shown in Figure 2-4, where perfectly rigid spherical particles are confined and steadily sheared by two parallel planes, the relationship between shear stress and shear rate is solely controlled by the inertial number (da Cruz et al., 2005; Lois et al., 2005). The inertial number, I, expresses the relative importance of inertia (i.e. the shear stress, τ) and confining pressure (i.e. the normal stress, σ), and is defined as:

$$I = \frac{\dot{\gamma}\delta}{\sqrt{\sigma/\rho_s}} \tag{2-1}$$

in which ρ_s is the grain density; $\dot{\gamma}$ is the characteristic shear rate; δ is the characteristic grain diameter. Physically, the inertial number can be interpreted as the ratio of the timescale of normal confinement, i.e. the time needed for grains to be squeezed from the upper layer to a lower position, to the timescale of shearing deformation (GDR MiDi, 2004).

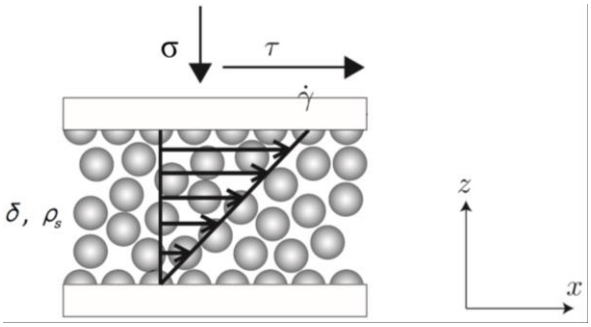

Figure 2-4: Schematic illustration of plane shear configuration (Andreotti et al., 2013).

As the dynamic friction coefficient (μ) under plane shear depends only on the inertial number (I), which essentially includes the shear rate, the constitutive shear stress-shear rate relationship is given by:

$$\left|\frac{\tau}{\sigma}\right| = \mu(I), \qquad \tau = \mu(I) \cdot \sigma \tag{2-2}$$

The relationship between the friction coefficient μ and the inertial number I was then reported by Jop et al. (2005), by combining the I-depended depth-averaged velocity profile proposed by GDR MiDi (2004) and the basal μ expression presented by Pouliquen and Forterre (2002) as a function of depth-averaged velocity and flow thickness; the original form of μ was fitted from experiments done by Pouliquen (1999) where idealised flows of glass spheres were steadily released on a wide rough plane. The μ(I) constitutive relationship at the flow-bed boundary is given as:

$$\mu(I) = \mu_1 + \frac{\mu_2 - \mu_1}{I_0/I + 1} \tag{2-3}$$

in which I_0, μ_1 and μ_2 are all empirical constants obtained from experimental measurements. The I_0 value depends on solid material, slope inclination and volume fraction, but is of a minor variation; and the values of μ_1 and μ_2 depend on solid material and grain size (Jop et al., 2005). The μ(I) profile with an evolving inertial number I is shown in Figure 2-5.

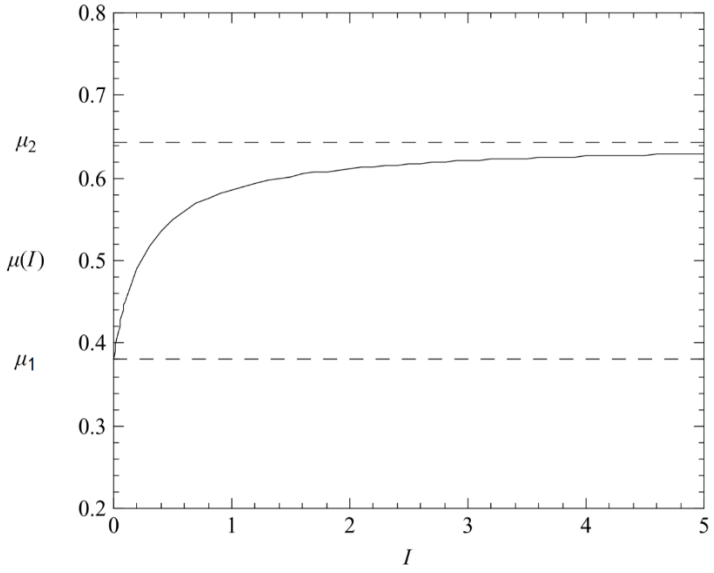

Figure 2-5: Basal friction coefficient μ as a function of the inertial number I (Jop et al., 2005).

The μ(I) rheology has shown a good agreement with steady fully-developed idealised granular flows and has been proved valid when the inertial number is within a large intermediate range (Barker et al., 2015). The biggest limitation of this local rheology may be the adoption of a simple shear-rate-depended friction law, which loses validity close to the flow threshold (i.e. when the steady uniform flow regime is just achieved or, from another perspective, when the flow is thinner than a critical flow thickness depended on the slope angle (Pouliquen, 1999)) and the flow boundaries (i.e. the free surface and the bottom layer, where the experimentally measured shear rates do not agree with the estimation (GDR MiDi, 2004)). Holyoake and McElwaine (2012) also reported that the μ(I) rheology fails to give accurate estimations for highly inertial (I > 0.5) steady polydisperse dry granular flows on a steep slope (θ = 30°-50°). In summary, the local μ(I) rheology derived from idealised conditions has quite a few limitations.

2.2.4. Kinetic Theory

Another framework of idealised granular flows is born from the physical analogy between the random motion of solid particles in a highly collisional regime and the thermal motion of gas molecules: high-speed solid particles tend to move separately, independently and freely, rather than moving together as an entirety (Campbell, 1990). Similar to gas molecules, which are often assumed small, rigid and elastic spheres that interact via collisions, solid grains can also be regarded as frictionless, monodisperse spherical particles often colliding with each other, although the collisional contact between a pair of solid spheres is usually short and inelastic; unlike the elastic collision of ideal gases which creates no loss in average momentum but in heat,

the inelasticity of solid grains allows energy to dissipate on the collisional contact through heat, plastic deformation, attrition and breakage (Gollin, 2017). The description of rapid and dilute granular flow using the kinetic theory of gases starts from the work of Ogawa (1978), which proposes an important concept of "granular temperature" analogised from "thermodynamic temperature". Granular temperature is defined by the mean-square value of the random velocity (i.e. the difference from the mean velocity vector of the bulk granular body) and represents twice the fluctuation kinetic energy of a unit mass of particles; this concept has soon become a key of analysing collisional granular movements. Higher granular temperature indicates a more agitated and saltating granular movement, higher grain vibrational energy is converted from flow translational energy, a more dilute flow material and hence higher potential to flow but also higher energy dissipation from collisions.

The kinetic theory has been a useful tool to improve the analyses of idealised granular flows, especially those from numerical simulation. For example, a model for idealised granular flows down a rough plane with spherical bumps was established by Louge (2003); the constitutive relation for granular flows of rough inelastic particles was theoretically deduced by Kumaran (2006) based on the simulation results of Silbert et al. (2001) and Mitarai and Nakanishi (2005); Chialvo and Sundaresan (2013) modified the model developed by Garzó and Dufty (1999) to allow the rheological description of densely-packed frictional particles; Gollin et al. (2017a) compared the estimations of steady, fully developed granular flows from extended kinetic theory with that from discrete element method (DEM) simulations. However, the kinetic theory is appropriate for gas-solid systems, not for geophysical flows with more complex material compositions. The similarities between solid particles and gases require neglectable quasi-static intergranular contacts and solid-fluid interactions; the pore fluid effect in the kinetic-theory modelling is usually represented as viscous drag on particles, which is adequate only when solid collision controls the momentum exchange; such a case cannot be found in debris flows saturated with viscous fluid. The particular emphasis on granular collisions and the absence of pore fluid effect make the application of classical kinetic theory to realistic flow material seem hopeless.

2.3. Dimensional Analysis

Dimensional analysis of debris flows was first proposed by Iverson (1997) as a method of classifying debris flow and identifying flow behaviour styles. By pairwise comparisons, a few dimensionless numbers can express the individual importance of five fundamental stresses (Sec. 2.1.3) in debris flows. These dimensionless numbers have been utilised to describe and discriminate the flow regimes, and also to reproduce flow events at a laboratory scale with reasonably physical similarities (Iverson, 1997; Iverson and Denlinger, 2001). Due to the typical scale effects highlighted by Iverson (2015), similar quantities of dimensionless numbers are the key to ensuring the physical relevance between laboratory model granular flows and realistic geophysical debris flows. Although a steady shear flow of uniform spheres immersed in viscous fluids is assumed in the original stress calculations, the dimensional analysis still provides a reliable reflection of the local-scale granular-flow dynamics. Thus, even though replicating field-scale flow behaviours is not a necessity for this study, dimensional analysis is needed to show the small-scale flow dynamics and to be compared with results from large-scale flows.

2.3.1. Savage Number

The original form of the Savage number was presented by Savage (1984) describing dry granular flow regimes and was then modified by Iverson (1997) adding friction angle and hydrostatic buoyancy into the function. The modified Savage number (N_{Sav}) is defined by the ratio of solid inertial stress to quasi-static solid stress as:

$$N_{Sav} = \frac{\rho_s \dot{\gamma}^2 \delta^2}{(\rho_s - \rho_f)gh\cos\theta\tan\phi'} \quad (2\text{-}4)$$

in which: ρ_s and ρ_f are the solid and fluid density, respectively; $\dot{\gamma}$ is the characteristic shear rate; δ is the characteristic grain diameter; g is the gravitational acceleration; h is the debris flow thickness normal to the bed; θ is the slope angle; ϕ' is the effective solid friction angle.

Considering the flowing grains in contact with the bed where the stresses are easier to measure, the equation can be transformed as (Iverson et al., 2010):

$$N_{Sav} = \frac{\rho_s \dot{\gamma}^2 \delta^2}{\sigma_{basal} - p_{basal}} \quad (2\text{-}5)$$

where σ_{basal} is the total basal normal stress, p_{basal} is the basal fluid pressure, hence $\sigma_{basal} - p_{basal}$ represents effective basal normal stress. Compared with Eq.(2-1), the Savage number is equivalent to the square of the inertial number, indicating that these two dimensionless numbers are essentially the same but mechanically comprehended in different ways.

As suggested by Savage and Hutter (1989), collisional stresses dominate over frictional stresses borne by sliding and sustained contacts if N_{Sav} in Eq. (2-5) exceeds about 0.1; otherwise, friction dominates the flow behaviour. The enhancement of a collisional tendency, i.e. a reduction in total basal normal stress (σ_{bed}), results in a decrease in N_{Sav} value (Zhou and Ng, 2010).

2.3.2. Bagnold Number

The Bagnold number is defined as the ratio of solid inertial stress to viscous fluid shear stress (Bagnold, 1954; Iverson and Denlinger, 2001):

$$N'_{Bag} = \left[\frac{\upsilon_s^{1/3}}{\upsilon_*^{1/3} - \upsilon_s^{1/3}}\right]^{1/2} \frac{\rho_s \dot{\gamma} \delta^2}{\eta} \qquad (2\text{-}6)$$

where υ_s is the volumetric solid fraction (concentration); $\upsilon*$ is the maximum (close-packed) volumetric solid fraction; η is the Newtonian viscosity of the interstitial fluid.

For highly sheared, steady, uniform flows of sphere-liquid mixtures, $N'_{Bag} > 450$ indicates that collisions dominate the flow regime, in which normal and shear stresses are proportional to the squared shear rate ($\dot{\gamma}^2$); while $N'_{Bag} < 40$ represents a "macro-viscous" regime where normal and shear stresses are found proportional to shear rate ($\dot{\gamma}$) (Bagnold, 1954; Savage and Sayed, 1984). Iverson (1997) provided another form of Bagnold number, N_{Bag}, by replacing the term in square brackets with the ratio of the solid fraction to the fluid fraction as:

$$N_{Bag} = \frac{\upsilon_s}{1 - \upsilon_s} \frac{\rho_s \dot{\gamma} \delta^2}{\eta} \qquad (2\text{-}7)$$

A collision-dominated flow regime is inferred when $N_{Bag} > 200$.

2.3.3. Friction Number

The friction number, which physically expresses the ratio of shear stress produced by enduring contacts to viscous shear stress, is identified by simply forming a ratio of Bagnold number to Savage number (Iverson and LaHusen, 1993):

$$N_{fric} = \frac{N_{Bag}}{N_{Sav}} = \frac{\upsilon_s}{1-\upsilon_s}\frac{\sigma_{basal} - p_{basal}}{\dot{\gamma}\eta} \quad (2\text{-}8)$$

Note that although the solid shear component is written as the effective normal stress (σ_{basal} - p_{basal}) for the convenience of calculation, its original form as shown in Eq.(2-4) is a function of the granular layer thickness, h.

Solid shear stresses exceed pore fluid viscous shear stresses when N_{fric} is larger than 2000 based on the threshold values of N_{Bag} = 200 and N_{Sav} = 0.1 (Iverson, 1997); this threshold was claimed to be overestimated as the critical Bagnold number and Savage number were derived from idealised experiments (Parsons et al., 2001). The experimental work done by Parsons et al. (2001) gives a much lower threshold, which is approximately 100. A small value of N_{fric} can result from a low solid fraction or high viscosity, possibly indicating a continuous flow. An increase in N_{fric} has been reported to amplify bed normal stresses (Zhou and Ng, 2010).

2.3.4. Darcy Number

Similar to the original Darcy number in fluid dynamics which suggests the permeability of the porous medium according to Darcy's law, the Darcy number of granular flows represents the ability of pore fluid pressure to buffer the solid inertia producing relative movements (Iverson, 1997); thus the granular flow version of Darcy number is defined by the ratio of solid-fluid interaction stress to solid inertial stress as:

$$N_{Dar} = \frac{\eta}{\upsilon_s \rho_s \dot{\gamma} k} \quad (2\text{-}9)$$

in which k is the hydraulic permeability of the granular medium with a unit of m^2. k is dependent on the grain size and porosity of the solid phase; a higher permeability is usually found in coarse-grained solids such as rocks. The value of the Darcy number in large-scale geophysical flows has been reported by (Iverson, 1997) to be at least a few hundred (in sand-gravel experimental flows) and can be greater than 10^7 (in mudflows), indicating that solid inertial movements are highly impeded by the pore fluid pressure in natural debris flows. One shortcoming of Darcy number of debris flows is that a threshold value seems to not have been proposed, thus no criterion is available for reference as to whether the pore fluid can effectively resist the grain inertial movement.

2.3.5. Reynolds Number

The Reynolds number in classic fluid mechanics identifies laminar from turbulent flows. Using the ratio of fluid inertial stress at a grain scale to viscous shear stress (Iverson, 1997), the grain Reynolds number can be calculated by:

$$N_{Rey} = \frac{\rho_f \dot{\gamma} \delta^2}{\eta} \tag{2-10}$$

Specially, if the depth-averaging approach is applied, a quasi-Reynolds number provided by Iverson and Denlinger (2001) is given by:

$$N'_{Rey} = \frac{\rho h \sqrt{gL}}{\eta v_f} \tag{2-11}$$

where ρ is the total density of the flow and L is the flow length. Generally, $N'_{Rey} \gg 1$ suggests a turbulent flow dominated by fluid inertia while $N'_{Rey} \ll 1$ represents a laminar flow dominated by viscous shear. Iverson and Denlinger (2001) also reported that in large-scale debris flows, the value of the quasi-Reynolds number is commonly greater than 3×10^5, suggesting that the fluid is highly turbulent when flowing at the debris-flow bulk velocity. However, the physical definition of "flow length" is not well-established and thus the choice of lengthscale L is relatively arbitrary, raising questions on the validity of the estimation of quasi-Reynolds number; the grain Reynolds number, on the other hand, physically makes more sense by using grain diameter as the lengthscale, although identical velocity between solid and fluid phases seems to be assumed. Additionally, small-scale flows tend to exhibit lower level of pore-pressure development than large-scale flows do (Iverson, 2015), thus solid contacts in general are less likely to be overcome by fluid forces in small-scale experiments; this scale effect is crucial when modelling geophysical flows but is less relevant when analysing the fundamental effects of pore fluid on small-scale granular-flow mechanisms as the dominant momentum transport is affected little by the relative importance between fluid inertia and viscous shear.

2.4. Pore Fluid in Granular Flows

The fluid phase in a grain-fluid mixture is usually termed "pore fluid" (i.e. the fluid filling the voids within a porous medium such as soil or rock) or "interstitial fluid" (i.e. the fluid occupying

the spaces between particles). “Pore fluid” is from soil mechanics whereas “interstitial fluid” is originally a biological concept; thus in this study the term “pore fluid” is employed and mainly refers to liquid instead of gas.

Pore fluid can interact with solid grains in various forms: a granular medium is more stable when a small amount of liquid is added in (e.g. moist sandcastles), but becomes easier to move farther when filled up with fluid (e.g. debris flows); grains can also be completely separated by and suspended in fluid, in which case they move along with the fluid (e.g. slurry floods). Although debris flows are overall fully saturated with viscous fluid, the flow front is known to be unsaturated or almost dry. Thus pore fluid effects on both unsaturated and saturated granular media are worth looking into.

2.4.1. Unsaturated Granular Media

In an unsaturated granular medium, moisture adheres on the surface of discrete solid particles as thin films due to surface tension and capillarity; when a pair of film-covered grains are about to get in contact, a liquid bridge is formed between the grains, bonding grains together. Liquid bridges can be formed in different patterns among the solid grains according to the amount of liquid and different configurations have been classified by Urso et al. (1999), as shown in Figure 2-6. A “pendular state”, where each pair of grains is linked by an individual liquid bridge, is obtained when the grains are only slightly wetted; the next “funicular state” is the configuration where some of the pores are filled but separate binary liquid bridges still exist; with an increased amount of pore fluid, the “capillary state” is achieved, all the pores within a cluster of grains are filled up and concave menisci are developed on the outer surface of the cluster; finally, the saturated cluster becomes a “droplet” with convex menisci on the surface. For the pendular state illustrated in Figure 2-6 (a), the force acting on the most basic liquid bridges between two monosized spheres has been analytically calculated by Fisher (1926); Rumpf (1962), and has been experimentally supported by Haines (1925); the effects of pore fluid on slightly wetted monodisperse granular media have been widely investigated using numerical simulations, e.g. Scholtès et al. (2009); Than et al. (2017); Zhang et al. (2022).

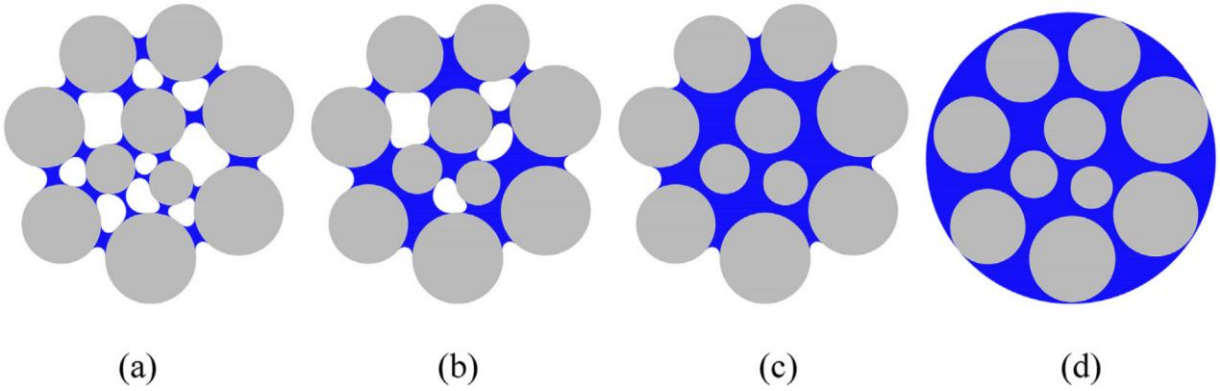

Figure 2-6: Four patterns of liquid bridge formation: (a) pendular; (b) funicular; (c) capillary; (d) droplet (Zhang et al., 2022).

Microscopically, the developed liquid bridges provide additional static stability (Hornbaker et al., 1997), shear strength (Fredlund et al., 1978) and tensile strength (Pierrat and Caram, 1997) to the unsaturated granular medium since the air pressure applied to the menisci tends to prevent the liquid bridges from rupture by relative motion between grains; this leads to an "apparent cohesion" in the granular medium. This cohesion (or attractive force, adhesive force, capillary force) due to liquid bridges between solid grains is connected, from the macroscopic perspective, with the "matric suction", which is conventionally defined by the difference between air pressure and pore water pressure, $p_{air} - p_w$, in the elastoplastic modelling of unsaturated soil (Alonso et al., 1990; Wheeler and Sivakumar, 1995); as "cohesion" and "suction" in the granular medium are essentially the same, they both depend on the pore fluid distribution in the interstitial spaces and thereby on the amount of pore fluid or saturation degree. The nonlinear relationship between the saturation degree and the matric suction in unsaturated soil is usually presented by the soil-water characteristic curve (SWCC) as shown in Figure 2-7 (a). Vanapalli et al. (1996) divided the SWCC for the entire desaturation process into three zones: (i) the initial "boundary effect zone" where pores are mostly occupied by fluid and small air bubbles are only discretely distributed within the fluid, causing an increase in suction with very little change in saturation degree; (ii) the "transition zone" where the air starts to become continuous in response to the decreased amount of pore fluid, and to produce menisci in the pores; (iii) the "residual zone" where the remaining pore fluid has become discontinuous in the pores, thus the increased suction no longer significantly reduces the saturation degree.

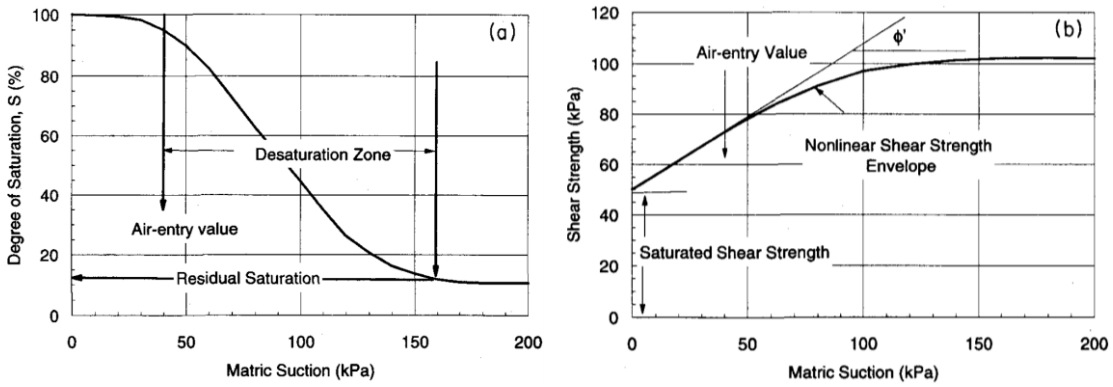

Figure 2-7: (a) Typical soil-water characteristic curve (SWCC) and (b) the corresponding relationship between shear strength of and matric suction in the unsaturated soil Vanapalli et al. (1996).

Moreover, a prediction approach to the shear strength of unsaturated soil using SWCC parameters has also been proposed by Vanapalli et al. (1996). The original shear strength calculation of unsaturated soil was provided by Bishop (1959) and was modified from the Mohr-Coulomb failure criterion; the shear strength is given by:

$$\tau = c' + [(\sigma - p_{air}) + \chi(p_{air} - p_w)] \tan \phi' \qquad (2\text{-}12)$$

where c' is the effective cohesion of the dry soil, Φ' is the internal friction angle, and χ is a parameter dependent on the saturation degree. Later Fredlund et al. (1978) extended this equation to allow the parameter χ to be linked with the increment of the internal friction angle due to matric suction; this leads to the Vanapalli et al. (1996) version calculating the shear strength of unsaturated soil by:

$$\tau = c' + (\sigma - p_{air}) \tan \phi' + (p_{air} - p_w) \tan \phi' \cdot \frac{S - S_r}{100 - S_r} \qquad (2\text{-}13)$$

in which S is the saturation degree of the soil and S_r is the residual saturation degree equivalent to the minimum saturation degree in the SWCC. The resultant shear strength plot against the saturation degree is demonstrated in Figure 2-7 (b). Suction due to desaturation generates a nonlinear increase in the shear strength of the granular medium; the strengthening rate gradually decreases with the suction, eventually reaching a plateau when the residual saturation degree is met.

2.4.2. Saturated Granular Media

Starting from the simplest situation where one spherical grain moves with a constant velocity in a still fluid, the solid-fluid interaction only contains drag force from fluid and the dynamics of

the particle is governed by the grain Reynolds number as shown in Eq. (2-10). The fluid drag in a low Reynolds number regime mostly results from viscous diffusion, while in a high Reynolds number flow it results from convective transport (Andreotti et al., 2013); a detailed drag force calculation can be found in Guyon et al. (2015). In unsteady fluid flows, however, the dynamics of a moving grain becomes complicated: analytical solutions for hydrodynamic forces in laminar flows are only valid within a limited range of Reynolds number and dimensional analysis seems the only reliable method beyond that range; forces applied to the grain in highly-inertial flows are even more complex, as they can be caused by both grain perturbance and fluid turbulence, and are poorly understood at present (Andreotti et al., 2013).

At the mesoscopic level, the effects of fluid on a sheared saturated granular medium can be cursorily explained using the plane shear configuration previously mentioned in Sec. 2.2.3. Referring back to the shear cell in Figure 2-4, the inertial number governing the granular flow rheology physically represents the comparison between the timescales for grain falling and shearing. When the rigid spheres are fully immersed in a viscous fluid and are confined by permeable plates at both boundaries (Figure 2-8), fluid can be regarded as sheared together with the solids, thus pore fluid mainly affects the timescale for the vertical movement of grains, i.e. grain rearrangement, whether by exerting viscous drag or turbulent drag; in the viscous case, this fluid drag corresponds with the solid-fluid interaction stress mentioned in Iverson (1993) and Iverson (1997). The inertial number increases with the grain rearrangement timescale, hence the shearing timescale is relatively shorter and the shear deformation of grains is facilitated.

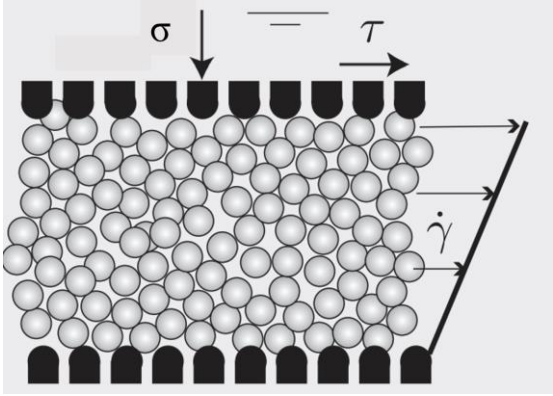

Figure 2-8: Plane shear configuration of saturated granular medium (Andreotti et al., 2013).

Sustained high pore fluid pressure generated in saturated gravity-driven granular flows is a feature of interest for engineers as it has been commonly observed in debris-flow fieldwork (e.g. McArdell et al. (2007); McCoy et al. (2010)) and laboratory experiments (e.g. Iverson et al.

(2010); Kaitna et al. (2016)); these high pore pressures are normally greater than the hydrostatic values and are therefore considered to be "excess" pore pressure. Excess pore pressure can occur in geophysical flows when solid material is consolidated during deposition and/or is contracted during the unsteady non-uniform motion (Iverson, 1997) but its mechanism is not fully revealed yet. Many theories have been proposed to explain the excess pore pressure development, e.g. centripetal acceleration resulting from a concave flow channel (Te Chow, 1959), the weight transfer from solid particles to pore fluid (Hampton, 1979), the temporary blockage of pore necks (i.e. narrow gaps between grains interlinking larger pore spaces) in response to large normal stresses over grains (Pierson, 1981) and Reynolds stresses due to turbulence (Hotta and Ohta, 2000). Goren et al. (2010) found that pore fluid can be pressurised by rapid fluid flow through a highly permeable granular medium, or by the contraction of pore space volume with poor drainage, in which case the fluid compressibility and the amount of overall compaction may be the controlling parameters. Kaitna et al. (2016) reports that the excess pore pressure seems not necessarily relevant to centripetal acceleration, grain collision, the change in bulk volume and Reynolds stress, and attributes the pore volume variation to the material overriding in the debris-flow front.

It is seen that pore fluid pressure does not develop very much before reaching the peak height of the debris-flow surge, showing asynchronous variation with normal stress (Takahashi, 1991; Iverson, 1997). This is because the pore fluid cannot instantly respond to the pressure gradient resulting from the change in pore space (Kaitna et al., 2016); the reaction delay time may depend on the fluid viscosity and the permeability of the granular medium (see Sec. 2.3.4). However, the increased nonequilibrium pore fluid pressure can persist for a considerably long time, even longer than the debris-flow duration (Pierson, 1981). The timescale for pore pressure dissipation can be defined by (Iverson, 1997):

$$t_{diff} = \frac{\eta h^2}{kE} \tag{2-14}$$

where E is the stiffness of the flow material; kE/η is the pore pressure diffusivity; the flow thickness h represents the length of the drainage path. High pore pressure is applied to the debris flow throughout the moving process if this timescale equals or exceeds the flow duration.

Pore fluid pressure is crucial to the granular flow analysis as it affects the stress states of the solid grains. For a granular medium saturated with, immersed in or suspended in fluid, effective normal stresses over the grain skeleton calculated from Terzaghi's principle (Terzaghi and Peck,

1948) are reduced by pore fluid pressure; the effective normal stress can be expressed as in Eq. (2-5) given an isotropic stress state on grains, i.e. the normal stresses at a point are identical in every direction. The Coulomb friction between grains is mitigated by the decreased effective normal stress and the shear resistance of the granular medium is therefore weakened. The pore pressure dynamically fluctuating during the rapid shearing deformation of the flow material can even support all the stresses over grains within a short time, leaving solid grains in no contact stress temporarily (Iverson and LaHusen, 1989); if this zero-stress condition persists, the grains are "liquefied" or "fluidised" as commonly found in the hyper-concentrated debris-flow tail (see Sec. 2.1.3). Observation by Pierson (1981) shows that the existence of excess pore pressure can significantly reduce the shear strength of the debris-flow material by over 90% compared with that in unsaturated conditions. This leads to the association between the development of excess pore pressure and the enhanced bulk mobility of saturated granular flows.

2.4.3. Impact of Pore Fluid on Flow Mobility

Large bulk mobility is one of the most typical debris-flow characteristics and is thought by many to be associated firmly with high and sustained pore fluid pressure (e.g. Pierson (1981); Iverson (1997); McArdell et al. (2007)). The increase in bulk mobility can be deemed equivalent to a lower "apparent friction" at the flow-bed boundary throughout the entire flow path, whether quantified by the coefficient of friction H/L (in which H is the drop in elevation of the centre of mass and L is the horizontal moving distance of the centre of mass) (Straub, 1996) or travel angle α_T (i.e. the angle of the energy line going from the centre of mass of the source volume to that of the deposit). Microscopically, Breard et al. (2020) confirmed that the raised pore pressure reduces the local basal friction of granular flows by mitigating the effective basal normal stress instead of affecting the interface friction coefficient; this agrees with the fundamental role of pore fluid in porous media as mentioned earlier.

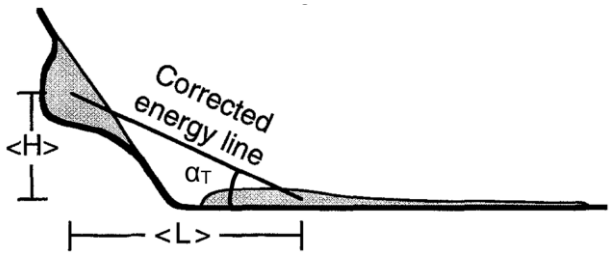

Figure 2-9: Sketch of the debris-flow sliding model showing the energy line corrected from Heim (1932) (after Straub (1996)).

Since the high pore pressure can persist until the flow stoppage, the basal shear resistance to the flowing granular medium may be assumed to be reduced throughout the entire flow event, where the mobility is sustained. However, Iverson (1997) also pointed out that excess pore pressure does not have to occur in a debris-flow surge and a long debris-flow runout is not necessarily caused by a sustained nonequilibrium pore fluid pressure – a high level of granular temperature can achieve the targeted large mobility as well; furthermore, the influence of pore fluid pressure decreases with the reduction of flow scale (Iverson, 2015), hence the mobility of small-scale granular flows may be influenced little by excess pore pressure. Although excess pore pressure is common in natural debris flows and is indeed helpful to maintain the flow motion, it may not be the only contribution of pore fluid to the bulk mobility of saturated granular flows.

Leaving the pore pressure aside, the increase in water content of the granular medium does enhance the bulk mobility of saturated granular flows. Unfortunately, few studies focus on the variation of granular flow behaviours induced by evolving water content. Hürlimann et al. (2015) reported an exponential growth of runout distance with water content using real debris-flow material and a laboratory-scale inclined shallow flume. Zhou et al. (2016) found that, in a low range of water content (0 – 30%), minimum mobility is achieved during the nonlinear development with water content when the granular flow is partly moist rather than fully dry; this minimum mobility and the relevant "critical water content" was explained by the additional shear strength due to matric suction (see Sec. 2.4.1). Yin et al. (2019), on the other hand, obtained a monotonically increasing relationship between water content and bulk mobility from centrifuge experiments with submarine debris flows, in which high water content ranges from 0.93 to 1.49. Nevertheless, the fundamental role of pore fluid in granular flows is not fully-understood and is worth further investigation.

2.5. The Effects of Polydispersity

The term "polydispersity" describes the feature that particles of multiple different sizes are involved in the system; in this study, the polydisperse system contains a large variety of grain sizes that can form a well-graded (also referred to as poorly-sorted) size distribution. The degree of polydispersity, i.e. the gradation, of a granular medium can be determined by the grain size distribution curve which gives the relative amount by weight of particles in different sizes (Holtz

and Kovacs, 1981). Gradation can be quantified by two parameters: the uniformity coefficient, C_u, and the curvature coefficient, C_c; the definitions of these two coefficients are given by:

$$C_u = \frac{D_{60}}{D_{10}}, \qquad C_c = \frac{(D_{30})^2}{D_{10} \cdot D_{60}} \tag{2-15}$$

where D_{10}, D_{30} and D_{60} denote the grain size at which 10%, 30% and 60% of the grains by weight are finer in the medium. D_{10} is also known as the "effective grain size" based on the hydraulic conductivity estimation of uniform sands (Hazen, 1892), but other grain sizes have been claimed to control the permeability of porous media, such as the mean grain size suggested by Slichter (1902) and referential grain size corresponding with the Kozeny-Carman's equation (Kozeny, 1927; Carman, 1937; Carman, 1939) which allows the permeability of a polydisperse medium to be determined by more complex calculation process; this referential grain size was reported by Urumović et al. (2016) to be close to D_{40} (i.e. the size where 40% particles in the sample are smaller) in non-cohesive granular media. Although it is questionable if D_{10} can be the "effective grain size" controlling the permeability of well-graded material, D_{10} is still used here in the calculations of C_u and C_c, as these two parameters are independent of hydraulic properties and only reflects the distribution pattern of grain size.

C_u close to 1 means a relatively uniform grain size distribution whereas larger C_u indicates a more well-graded medium. C_c presents the smoothness of the grain size distribution curve: $1 < C_c < 3$ means that grains of all different sizes are contained in the medium and are of relatively close weight; C_c outside this range suggests that grains of certain sizes are excessive, insufficient or missing in the medium, in which case the material is "gap-graded". A well-graded granular medium requires a C_c between 1 and 3, and a C_u greater than 4 for gravels or 6 for sand; should any of these criteria provided by the Unified Soil Classification System be not met, the medium is to be classified as "poorly graded" (Holtz and Kovacs, 1981).

Natural granular flows are commonly polydisperse, containing a wide range of grain sizes; this property allows granular flows to exhibit bulk behaviours different from those of monodisperse flows (Phillips et al., 2006; Goujon et al., 2007; Moro et al., 2010). However, most experimental and numerical investigations of the internal mechanics of granular flows adopt uniform systems (e.g. Jop et al. (2006); Manzella and Labiouse (2013); Gollin (2017)); while in well-controlled experiments of realistic debris flows (e.g. Iverson et al. (2010); Hürlimann et al. (2015); Zhou et al. (2018)), the consideration of polydispersity is usually limited to the effect of fines content, which has been noticed as early as the work of Major (1996). Macroscopically, the impact of

granular flow material changing from monodisperse to polydisperse on the bulk flow behaviours is straightforward, yet the internal physics controlling the differences between uniform and well-graded flows remains not clear and quantitative descriptions of those differences are not currently available.

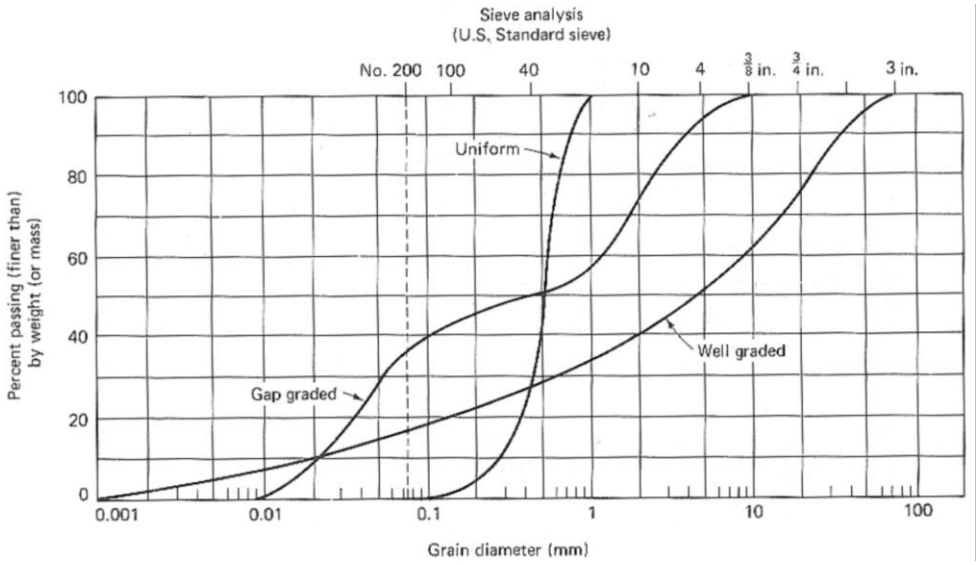

Figure 2-10: Grain size distribution curves of uniform, well-graded and gap-graded material (Sanvitale, 2010).

2.5.1. Size Segregation

Grain size segregation (Sec. 2.1.3) happens when a polydisperse granular flow is sheared in the gravitational field (Savage and Lun, 1988). Grains can segregate according to other properties such as shape, density and resilience, but particle size is believed the key to driving the segregation phenomenon (Williams, 1976). The mechanism for grain size segregation has been widely studied, mainly using bidisperse particles (e.g. Hill et al. (1997); Alexander et al. (2004); Conway et al. (2006); Goujon et al. (2007)). Although segregation can be affected by more than ten different mechanisms (McCarthy, 2009), the combination of kinetic sieving (i.e. granular flows in the gravity-driven motion is similar to a "random fluctuated sieve" and fine grains are statistically more probable than coarse grains to fall into the voids within the lower granular layer) (Middleton, 1970) and squeeze expulsion (i.e. individual grains can be squeezed upwards and out from the original layer by the imbalanced interaction forces) (Savage and Lun, 1988) is recognised as the dominant mechanism for the size segregation of sheared dense granular flows; this combined effect termed "gravity-driven segregation" allows fine particles to move towards the bottom and coarse sediments towards the free surface of the granular flow. Another segregation pattern, which transports boulders towards the front and fines towards the rear, is

induced by the strong shear of the granular mass (Gray, 2018): since the free surface velocity of granular flows is higher than the velocity of the lower portion, larger grains lifted to the surface are preferentially carried towards the flow front, and after being overrun by the following flow body they may rise to the surface again and then move to the front again; hence, coarse grains are continuously transported to and are concentrated at the flow front, eventually forming a typical debris-flow surge as shown in Figure 2-3. More details about mechanisms for grain size segregation can be found in Gray et al. (2015) and Gray (2018).

Grain size segregation in polydisperse granular flows is noteworthy to debris-flow studies for resulting in unique dynamics that cannot be found in uniform flows. For instance: the spatial distribution of hydraulic diffusivity of the flow material, and thereby that of pore pressure, are highly affected by size segregation (Iverson et al., 2010); the dry granular surge front with larger grains and high permeability experiences higher local resistance and may serve as a "moving dam" to impede the longitudinal propagation of the upstream slurry part, facilitating the excess pore pressure development (Pierson, 1986); fine grains spread at the bottom layer of polydisperse flows can adjust basal interactions with both channel bed and the overlying coarser particles (Goujon et al., 2007). However, the effects of size segregation on well-graded granular flows are rarely focused on. Segregation in polydisperse granular flows needs further investigation to accurately analyse and estimate the dynamics of realistic granular flows.

2.5.2. Pore Pressure

The development and dissipation of pore fluid pressure are influenced by the presence of various grain sizes in the granular flow. First of all, fine solids pose vital impacts on debris-flow behaviours. Fines content controls the hydraulic permeability of a porous medium (Hazen, 1892; Hazen, 1911); permeability is remarkably reduced by just adding a few fines to larger particles (Pires-Sturm and DeJong, 2022). The lower permeability of granular media, which can be caused by the decreased particle size and/or void ratio (Huang et al., 2019), allows the pore pressure more easily to increase and sustain (Pires-Sturm and DeJong, 2022). Kaitna et al. (2016) considered another mechanism for high pore pressure sustainability: the pore fluid viscosity is increased by mixing with fine particles and provides higher resistance to the settlement of larger sediments, thus solids separated by excess pore pressure find it to be more difficult to reestablish enduring contacts. This mechanism is indirectly supported by the work of Yang et al. (2020), which found that platy coarser clasts can be suspended longer in pore fluids as they have larger specific surface areas, and hence the flow material is easier to liquefy; however, platy clasts reduce the volume of pore spaces at the same time, resulting in lower peak values of pore pressure. Nevertheless, the increase of fines content has been widely agreed to significantly

enhance the peak value and sustainability of high pore pressure (Pierson, 1981; Major, 1996; Iverson et al., 2010; Kaitna et al., 2014).

Well-graded granular media possess other important factors to pore pressure generation. A good gradation primarily improves the packing efficiency (i.e. the proportion of total space occupied by particles) of the granular medium; as a result, the dilation tendency is enhanced when the medium is sheared while shear deformation is weakened, i.e. the effective shear stiffness of the granular medium is increased (Pires-Sturm and DeJong, 2022). However, well-graded material can meanwhile increase the magnitude of the developed pore pressure when fully saturated (Belkhatir et al., 2014; Kaitna et al., 2014) and thus is more likely to liquefy and lose the enduring solid interactions; with grain size segregation, the internal of well-graded flow material tends to keep the developed excess pore pressure and pushes the flow margin, where unsaturated or dry coarser grains experience higher friction (Sanvitale, 2010). The pore pressure magnitude also increases with the enhanced material compressibility (Iverson, 2015) and the decrease in D_{10} (i.e. effective grain size) and D_{50} (i.e. the grain size where half the sample is coarser, also known as mean grain size) (Belkhatir et al., 2014).

2.5.3. Bulk Flow Mobility

Whether dry or saturated, granular flows with a wide range of grain sizes can exhibit great bulk mobility, which can be attributed to interactions among fine and coarse grains. In the dry case, bulk mobility, quantified by the moving distance of the centre of mass from the start of flow to arrest, increases with smaller grain sizes (Cagnoli and Romano, 2012); this can be explained by the decreased specific energy loss per unit flow mass (Cagnoli and Romano, 2010a; Cagnoli and Romano, 2010b). The highest bulk mobility occurs when fines content in dry granular flows reaches a certain critical value before which the mobility increases with the concentration of fine particles (Phillips et al., 2006; Moro et al., 2010). An explanation for this phenomenon offered by Yang et al. (2015) is that a small number of fines spread beneath coarser grains can function as “wheels”, producing low rolling friction at the flow-bed boundary and effectively lubricating the basal interactions; this wheel structure, however, may fail when fines content rises beyond the critical value as the additional fine grains gathering together can be jammed and forced to slide.

For polydisperse granular flows saturated with fluids, i.e. debris flows, bulk mobility is also enhanced by the increased fines content (Iverson, 1997; Hürlimann et al., 2015). A critical value

of fines content corresponding with the maximum mobility seems not to have been discovered; this is not surprising since the percentage of silt and clay is generally very small. According to Iverson (1997), the longer runout and extensive spreading of debris flows are mainly due to the decreased frictional resistance by fine grains; additionally, experiments done by Sanvitale (2010) showed that the highly inhomogeneous distribution of excess pore pressure in segregated debris flows allows the minor part of flow margin to be pushed forward and sideward by the major part of the internal flow body, resulting in larger travel distances; for less segregated flows, in contrast, the pore pressure distribution is more uniform and thus the boost of mobility driven by persistent excess pore pressure is weaker. Sanvitale (2010) also systematically analysed the impact of grain size distribution on debris-flow runout behaviours: with the same mean grain size, longer runout and higher segregation level are given by more well-graded material; if the gradation is identical, travel distance is then reduced with the increase in mean grain size, and this tendency can be strengthened by the larger uniformity coefficient, C_u, of the source material.

2.6. Critiques

This chapter reviews some of the predecessors' research for granular flows to propose the following arguments:

(i) Granular flows are complex phenomena that usually need the idealisation of flow material (i.e. assuming the material to be dry and monodisperse) to determine the constitutive relations and to predict the bulk flow behaviours.

(ii) Physical frameworks of debris flow, where realistic material composition (i.e. saturated and well-graded) must be considered, often simplify the internal mechanics to estimate the final deposition.

(iii) Dimensional analysis is currently the most reliable tool to reflect the local-scale physics of realistic debris flows and can be utilised when analysing debris-flow dynamics. The Savage number (and its alternative form used in granular physics, the Inertial number) and Bagnold number have been well-defined and widely accepted, while the Darcy number and Reynolds number have some issues that limit their applicability and are less relevant to the small-scale granular-flow behaviours focused on in this study.

(iv) Realistic debris flows show different bulk behaviours from idealised granular flows (e.g. higher bulk mobility, heterogeneous nonuniform surge, presence of pore fluid pressure); this is the result of the source material containing pore fluid and polydisperse solid grains.

(v) The influence of pore fluid on granular flow behaviours has been widely studied, but the mechanism for pore fluid enhancing the bulk mobility of granular flows, which is one of the primary engineering concerns, is not fully determined.

(vi) Research about polydispersity is not very rich, as analyses of internal granular flow dynamics mainly employ idealised material whereas those using well-graded flows often focus on the change in fines content; direct dynamical contrasts between uniform and well-graded flows are rare.

(vii) A gap regarding the roles of pore fluid and polydispersity in the mechanism for the evolution of bulk flow behaviours remains in the granular flow research.

Therefore, to understand the change in the physical process of granular flows experienced during the evolution of material composition from idealised to realistic, the roles of pore fluid and polydispersity in granular flow dynamics are needed to investigate and are the issues of interest in this study.

3. Methodology

Preface

Small-scale laboratory experimentation is the method used in this study to investigate the influence of pore fluid and polydispersity on granular flows. The experimental setup is a small-scale inclined flume system (Sec. 3.1.1). Two types of granular media, monodisperse ceramic beads and polydisperse real soil (Sec. 0), are utilised to perform dry uniform, wet uniform and wet non-uniform granular flows (Sec. 3.1.3). A set of sensors, including two loadcells (LC), two pore-pressure transducers (PPT) and an ultrasonic sensor, are installed on the downstream part of the tilting flume to collect data on basal normal stresses, basal pore fluid pressure and flow thickness, respectively (Sec. 3.1.1 and Appendix A). A high-speed camera fixed near the flume end and pointing at the sensor-installed zone captures a series of high-speed images to record the flow motion, which later can be translated into velocity information via Particle Image Velocimetry (PIV) analysis (Sec. 3.2). Final deposits of tested flows are measured and analysed to derive their bulk flow mobility (Sec. 3.3). After combining the mechanical and kinematic data, dimensional analysis (Sec. 3.5) is carried out for each tested flow to determine the dominant stress-transfer mechanism and flow regime.

It should be stated that, as this study is part of the Rosetta Stone Network, the experimental apparatus and material adopted in this study are in coordination with other investigations in the project. This project partly aims to provide high-quality experimental data with well-defined boundary conditions to improve the calibration and validation of the existing debris-flow numerical models; hence, although some experimental conditions such as scale, bed roughness, material size and density are not similar to the realistic debris-flow characteristics, those factors can easily be utilised and changed as the input of numerical models (Bowman et al., 2021). Both the uniform beads and well-graded soils are shared among all the members of the Rosetta Stone Network to achieve direct comparisons of flowing granular media produced by different

configurations. The small-scale inclined flume used in this study parallels the large-scale flume in Queen's University, Canada; with the same source material and similar experimental setup, contrasts between granular flows from these two flume systems should reflect the scale effect.

3.1. Small-scale Experiments

3.1.1. Experimental Setup

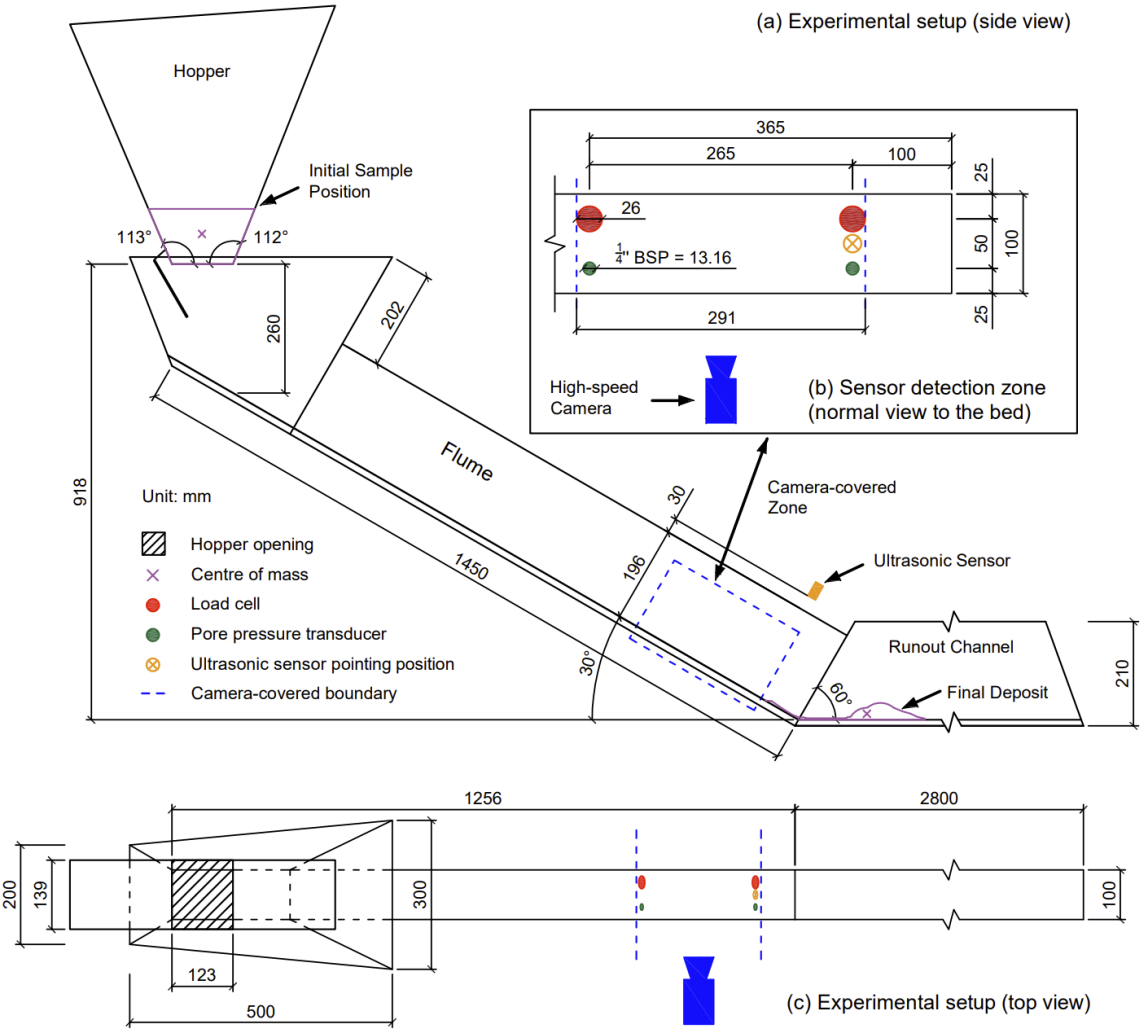

Figure 3-1: Experimental setup. (a) Side view; (b) zoomed-in sensor detection zone; (c) top view.

The experimental apparatus consists of a metal hopper, a tilting flume, and a horizontal runout channel, as shown in Figure 3-1 and Figure 3-2 (a). Similar flume systems, where the experimental configurations are not completely identical, have been used in previous studies such as Gollin (2017) and Sanvitale (2010). The flume made of clear acrylic and inclined at 30° is 1450 mm long and 100 mm wide. About 80% of the flume is confined by 196 mm high

sidewalls, and the remaining 20% at the upstream end has higher sidewalls to receive the released material; high sidewalls and narrow flume width help to produce thicker flow depths, allowing observations of side-view flow profiles. The flume bottom is covered with a layer of machine-roughened aluminium which is relatively smooth and allows the variation in slip velocity of granular flows to be produced and observed more easily. Data acquisition sensors are installed near the downstream end of the flume; Figure 3-1 (b) and Figure 3-2 (b) demonstrate the mounting position of all the sensors, including two loadcells (LC) and two pore-pressure transducers (PPT) on the flume bed, plus one ultrasonic sensor above the flume. LCs give total stress signals normal to the bed; PPTs give basal pore fluid pressure responses, which are only available in wet tests; the ultrasonic sensor detects the distance to the flow surface and outputs flow height values. PPTs require saturation to measure the fluid pressure; to prevent solid grains from pressurising the PPT-saturating water and interfering with the measurement, metal meshes with 0.5 mm aperture size are plugged into transducer holes as filters to block the grains out. More details of sensors and their calibration processes can be found in Appendix A. A high-speed camera is placed near the flume outlet where the granular flow is fully developed and is about to run into the horizontal channel, recording the flow motion in a 2-D planar side view.

The hopper at the top of the flume system is over 40 litres in volume, with a roughly 120 x 140 mm rectangular opening in the bottom, serving as a container for storing and releasing the experimental material. A pneumatically-operated trapdoor is attached to the hopper, as shown in Figure 3-2 (c). Before releasing the material, the trapdoor is closed and is pushed upwards by a pneumatic actuator driven by air pressure, thereby the hopper opening is fully sealed without leakage. Once releasing the applied air pressure, the actuator drives outward to release the trapdoor, which is dragged away by a spring so that the trapdoor opens rapidly; the trapdoor activation also triggers the microswitch linking to the high-speed camera and data acquisition box, synchronising the material release and data recording.

The confined acrylic runout channel is located at the exit of the flume to collect the outflows and allow deposition development. The confined runout channel (Figure 3-1 and Figure 3-2 (a)) is 1400 mm long, 100 mm wide and 210 mm high, with a bevelled sidewall at 60 degrees towards the flume outlet. The same width as the flume, matching sidewall angles, and the height-adjustable base frame, on which the runout channel is placed, guarantee a tight joint between the runout channel and the inclined flume. When necessary, another identical runout channel can be placed at the distal end of the one jointed with the inclined flume, achieving a maximum horizontal channel length of 2800 mm as shown in Figure 3-1. The assembly approximately

forms a 2-D domain, as the breadth throughout the system is considerably narrow and flow behaviours do not significantly vary in the lateral direction. The 2-D flow path prevents the deposit from spreading to the flanks and forming an alluvial fan that typically occurs in realistic geophysical mass movements; however, it also allows bulk mobility to be straightforwardly represented by travel distance along the horizontal direction.

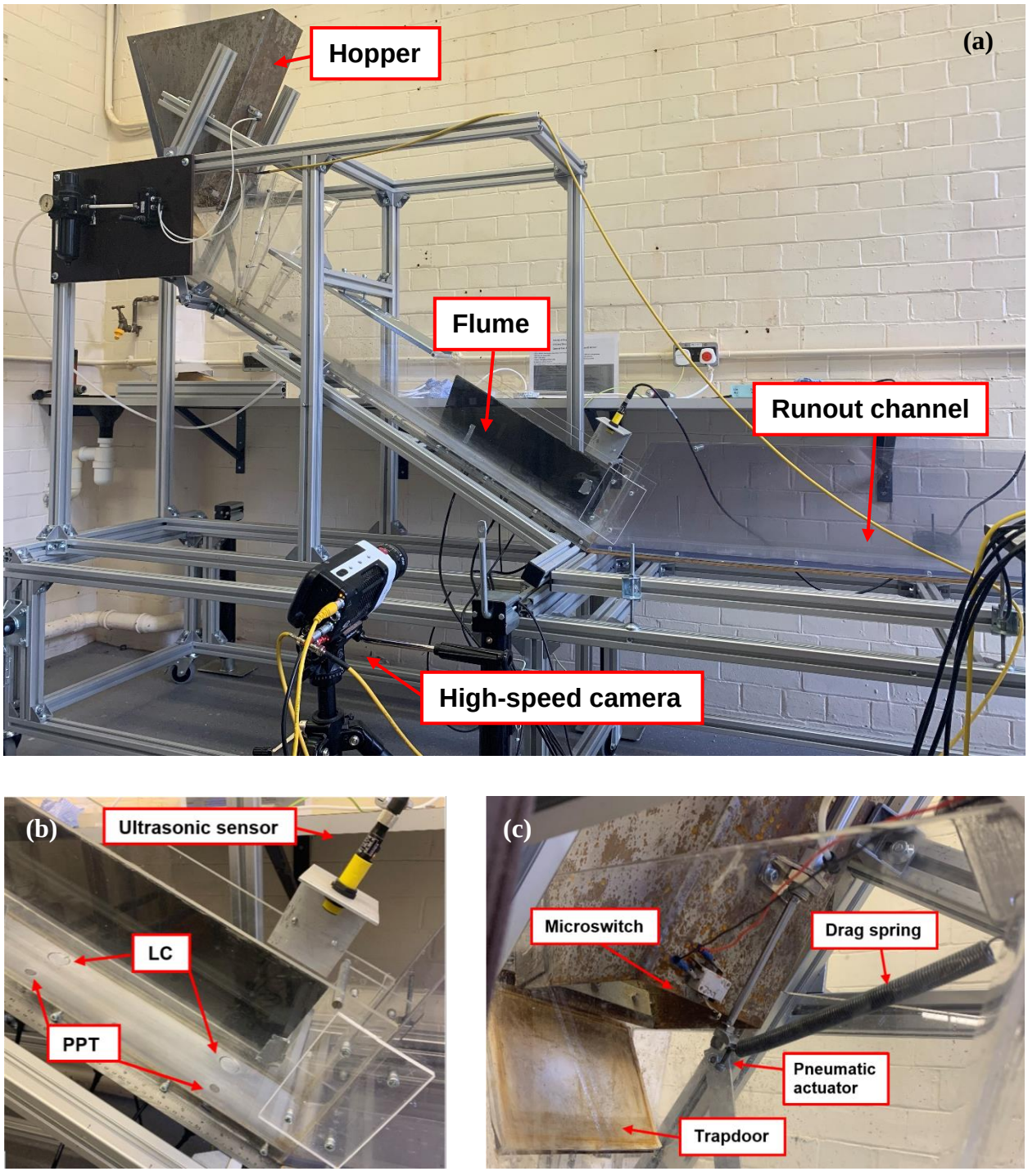

Figure 3-2: Real photos of the experimental setup. (a) small-scale flume system; (b) sensor-installed zone; (c) hopper-operating system.

The small-scale flume system has many clear practical advantages of low cost, easy manufacture and convenient assembly and modification; from the experimental perspective, most importantly, this laboratory-scale setup allows fast preparation and conduction of experiments, precise control of test variables, repetitive calibration of sensors (especially PPTs), and careful data measurements. However, the small scale also brings limitations. The tested granular flows undergo strong sidewall frictions which limit the development of the flow velocity profile and may reduce the representativity of PIV measurements as flow motion visible on the sidewall differs from that measured internally (Sanvitale and Bowman, 2017). The small size of the tested flows leads to decreased development of positive pore pressure but increased shear resistance caused by pore-fluid viscous and cohesive stress (Iverson, 2015); this typical scale effect does not interfere with the study on the fundamental pore-fluid effects but reduces the relevance of experiments to field-scale flow behaviours. Similarly, the narrow runout channel and smooth basal boundary are not necessarily consistent with the realistic geophysical flow conditions but also result in favourable aspects: the confined runout matches the 2D flow path assumption in the analysis of bulk flow mobility, and the smooth bed facilitates the observation of small variation in slip velocities in the shallow tested flows.

3.1.2. Source Material

Two types of granular media are required to show the evolution of flow material from idealised to realistic in the flume experiments: one needs to be rigid, uniformly graded and near-spherical, and the other should be well-graded and irregularly shaped. Saint-Gobain Norpro's Denstone® 2000 Support Media, a product of pseudo-spherical ceramic beads about 3 mm in nominal size, was selected as the idealised granular medium due to its hardness (to ensure relatively consistent particle characteristics throughout multiple test runs), roughness (to obtain notable frictional grain contacts), sphericity and uniformity. The physical properties of Denstone 2000 are given in Table 3-1 and a photograph of the ceramic beads is presented in Figure 3-3 (a).

The well-graded solid material referred to as "Maple Mud" consists of multiple soil products with different ranges of grain size. The constituent soil products, as shown in Figure 3-3 (b) and (c), are designed to be mixed according to the recipe provided in Table 3-2 to reach a grain size distribution as depicted in Figure 3-4; the intended grain size distribution corresponds to "PSD9" distribution used in Sanvitale (2010), which is adequately well-graded (C_u = 21 and C_c = 1.1) and has been proved to produce consistent bulk flow mobility, evident grain size segregation and is comparable to some finer flow mixtures from the Illgraben site in Switzerland (McArdell, pers.

comm.). The mixed sample gives D_{10} = 0.164 mm, D_{50} = 1.909 mm, and D_{90} = 5.561 mm. As plotted in Figure 3-4, the D_{90} value in this study seems lower than that of previous works; this may result from the breakage of coarser angular particles during sieving or transportation. The coarsest part of grains being smaller in size may lead to slightly reduced impact force (which is not measured in this study) and degree of size segregation in the deposit (Sanvitale, 2010), but the effects should be subtle overall as more than 70% of the size distribution follows the recipe, including the size range controlling the permeability and hence the pore pressure development. Owing to the well-graded material, Maple Mud is considerably denser than Denstone 2000 ceramic beads, possessing a bulk density of 1850 kg/m^3 and a void ratio of 0.39; note that the bulk density of Maple Mud was measured when the sample was most closely packed, where the bulk volume does not vary observably. In addition, Maple Mud, composed of well-graded soil, was considered to be more likely to generate non-equilibrium (i.e. excess) pore fluid pressure (as in real debris flows or in other laboratory polydisperse flows such as in Kaitna et al. (2014); Okada (2014)), than the uniform and relatively large Denstone 2000 ceramic beads were (similar to the pore pressure measured in Hotta and Sciences (2012); Stancanelli et al. (2015)).

Figure 3-3: Photographs of experimental solid materials. (a) Denstone 2000 ceramic beads; (b) and (c) Maple Mud constituent soils, where material labels are consistent with those in Table 3-2.

Property	Denstone 2000 Beads	Data Source
Grain Density (kg/m^3)	2.241×10^3	a
Nominal Size (mm)	3	c
Diameter (mm)	2.8 – 4.3	c
Average Diameter (mm)	3.85	a
Average Void Ratio	0.575	d
Average Bulk Density (kg/m^3)	1.417×10^3	d
Sphericity (%)	92.2	a
Restitution Coefficient	0.611	a
Internal Friction Angle (°)	33.7	b
Friction Angle on the Aluminium Bed (°)	21	d

Table 3-1: Physical parameters of Denstone 2000 ceramic beads. Data are from (a) Coombs (2018), (b) Raymond (2002), (c) Denstone 2000 datasheet,(d) measurement and calculation.

Product Label	Main Size Range (mm)	Mix Proportion
Target Products Ltd. Filter Silica Sands and Gravels (1/8" to 1/4" size)	3.36 – 9.5	35.5%
Target Products Ltd. Filter Silica Sands and Gravels (4 to 10 mesh size)	1.7 – 3.	12.5%
Target Products Ltd. Filter Silica Sands and Gravels (10 to 20 mesh size)	0.6 – 1.7	10.0%
Target Products Ltd. Filter Silica Sands and Gravels (16 to 30 mesh size)	0.3 – 1.18	10.0%
Target Products Ltd. Filter Silica Sands and Gravels (30 to 50 mesh size)	0.212 – 0.6	10.0%
Target Products Ltd. Industrial 70 Sand	0.075 – 0.42	12.0%
Lane Mountain Silica Sand (125)	0.063 – 0.212	10.0%

Table 3-2: Recipe for Maple Mud.

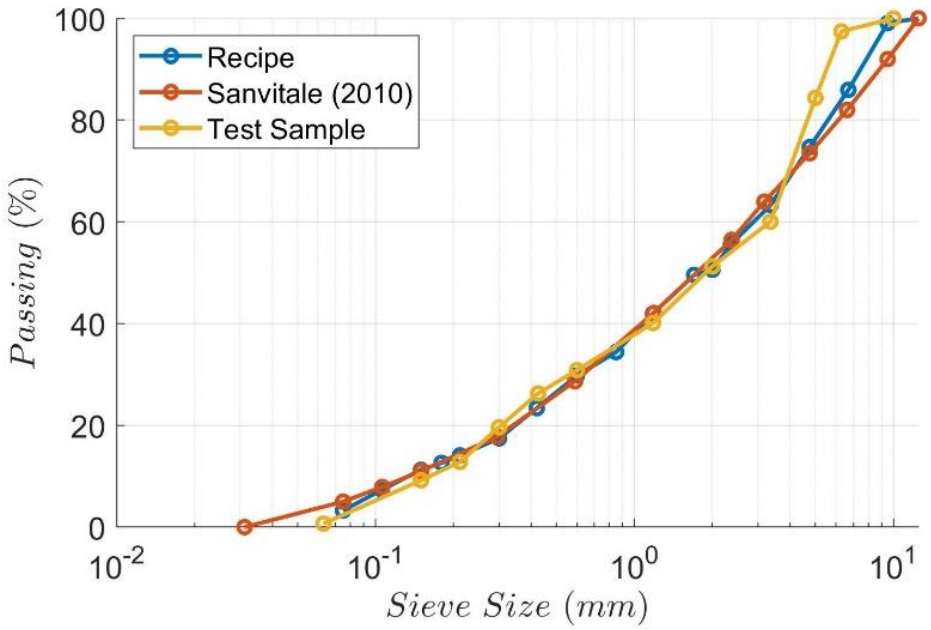

Figure 3-4: Particle size distribution curves of Maple Mud, where blue denotes the distribution following the recipe, red the one utilised in Sanvitale (2010), and yellow the one measured in this study.

3.1.3. Test Conditions

Experiments in this study are categorised into a few different test groups based on source volume and water content as shown in Table 3-3. For convenience, each test group is labelled according to its material and sample conditions: "C" stands for "ceramic beads", "M" for Maple Mud, "D" for "dry", "S" for "saturated", "W" for "wet" including both saturated or unsaturated conditions, "U" for "uniform" and "G" for well-graded. The controlled variable of "dry" and "saturated" tests is the bulk dry volume of solids, while that of "wet" tests is water content. The special group "2CWU" is supplementary to "CWU", but is separated as an individual group because experiments were undertaken before the flume was fully fixed and fastened, leading to apparatus conditions unidentical to "CWU" tests. More details about sample information, such as the measured weight, void ratio and bulk density can be checked in the result chapters.

Different test groups are designed to show the effects of pore fluid and polydispersity on granular flow behaviours through comparison and contrast from the most simple, idealised flows to the most complex. "CDU" tests use dry ceramic beads to set up a benchmark and validate the experimental configuration since sufficient data of dry chute flows can be found to compare with in the literature. "CSU" tests add water to the ceramic beads until the sample is oversaturated (to ensure most beads can be transported to the horizontal runout channel even for the sample in the lowest volume), showing the effect of saturating pore fluid by contrasting with "CDU" dry flows.

"CWU" and "2CWU" tests gradually change the amount of water mixed in the sample to produce granular flows from slightly wetted to saturated, and hence exhibit the difference in granular flow behaviours led by evolving water content. "MSG" flows adopt well-graded Maple Mud in the same bulk volumes as in "CSU" tests and highlight the impact of the presence of polydispersity in saturated granular flows. "MWG" tests, similar to "CWU" tests, focus on the flow behaviours evolving with different water content, but also show the response of well-graded material to changing water content by contrasting with "CWU" flows.

Test Group	Bulk dry volume (L)	Gravimetric water content
CDU	0.75 – 4.00	0.00
CSU	0.75 – 4.00	0.45
CWU	2.00	0.01 – 0.40
2CWU	2.00	0.35 – 0.45
MSG	0.75 – 3.00	0.22
MWG	2.00	0.20 – 0.30

Table 3-3: Experiment groups and the respective controlling variables.

3.1.4. Test Procedure

A test starts from sample preparation and the preparing processes for ceramic beads and Maple Mud are slightly different. Ceramic beads in a designed volume are measured and weighed in a measuring jar and then poured into the closed hopper. For "saturated" and "wet" tests, water is also measured and weighed to obtain the intended water content. A portion of water is firstly added to the dry grains in the hopper to the point where the water level is just observable on the top surface, given a sufficient water volume; whereafter the remaining water is weighed to calculate the consumed mass of water, and is then poured into the hopper. This procedure enables the saturating water content and void ratio (as mentioned in Sec. 0) of the sample at rest to be calculated, yielding the average saturating water content for uniform ceramic beads being 0.256 while that for well-graded Maple Mud being 0.21. For Maple Mud, on the other hand, the weighed solids must be put into the hopper after water, as the process of pouring water takes sufficient time for the well-graded solids to consolidate into a dense agglomerat that is very difficult to stir and to fluidise.

For tests that involve water, two more steps are necessary. (i) PPTs must be properly saturated; specifically, the transducer hole needs to be filled with de-aired water without air bubbles

entrained inside; this is done by injecting de-aired water from a needled syringe into the transducer hole; this process should be done before the sample is mixed in the hopper. (ii) The mixture in the hopper must be manually stirred continuously until opening the hopper gate, especially when using Maple Mud which can be fluidised by the agitation and contains fine sands and silt that can be suspended in the fluid phase; ceramic beads are too large to suspend and tend to settle down very quickly even when the sample is highly agitated.

The source material is dropped into the flume system when the hopper-sealing trapdoor is opened; simultaneously, the stationary high-speed camera and the data acquisition system are both activated by the microswitch. The flow is formed and developed during the downslope motion along the inclined flume, passing by the sensor-mounted and camera-filmed area, and then flushing into the horizontal runout channel. The outflow decelerates and eventually stops in the channel. At the end of the test, the deposit is measured and filmed to capture the side-view shape before cleaning the apparatus.

3.2. Particle Image Velocimetry (PIV)

Particle Image Velocimetry (PIV) is a well-established optical method of kinematic measurement. This non-intrusive measurement technique has been broadly utilised in laboratory experiments to obtain the velocity distribution of flowing substances, whether composed of solid, liquid or gas. For the uniform spherical solid material, another optical measurement technique known as Particle Tracking Velocimetry (PTV) is also suitable to give satisfactory velocity measurement and even works better on tracking the variation in volume fraction; however, PTV which measures displacement by tracing the movement of individual particles does not work with polydisperse flow material at present. The decisive advantage of PIV application for this study is that PIV gives a velocity field over a planar flow domain, hence permitting the detection of particles of various sizes and practically allowing the analysis on well-graded granular flows; this enables a consistency of the measurement approach used on different flow materials. Comprehensive reviews of the PIV technique have been provided in the literature, e.g. Adrian et al. (2011). This section only introduces the basic information of PIV analysis based on the PIV software adopted in this study, GeoPIV, which is established by White et al. (2003) and has been previously utilised by many, e.g. Sanvitale and Bowman (2012); Gollin et al. (2017b); Coombs (2018).

3.2.1. Fundamental Procedure

PIV derives velocity information from a series of images captured by the continuous shooting of a high-speed camera recording the flow motion. For each high-speed image, a domain of interest is divided into a grid of smaller subdomains, commonly known as the “interrogation windows” or “patches”; in GeoPIV each rectangular patch is defined by five nodes, namely four vertices and one centroid. The entire domain of interest containing multiple rows and columns of patches is then referred to as a “mesh”. Given a stationary position of mesh, locations of flowing particles within all the patches evolve with the image sequence, in which images are separated by a certain time interval, Δt. After all the subimages within patches are determined for the first chosen image, the closest matches for those subimages are then searched in the image at the next time step. To save processing time, each patch is searched individually in the next image and only within a user-defined range of the neighbouring zone. The most probable displacement of a patch within Δt can be extracted by comparing the patch location in the corresponding image pair; for a digital system, this comparison is processed by maximizing the cross-correlation function of the image intensity field between the image pair via Fourier transform. A displacement field of the interested domain during the time interval between two frames can then be obtained by repeatedly applying the cross-correlation to the whole mesh. Furthermore, Eulerian velocity vectors of all patches can be generated by dividing the displacement by the time interval. The analysis is applied to all the images consecutively to produce the velocity distribution of the entire flow body. A depiction of the analysis principle is shown below in Figure 3-5.

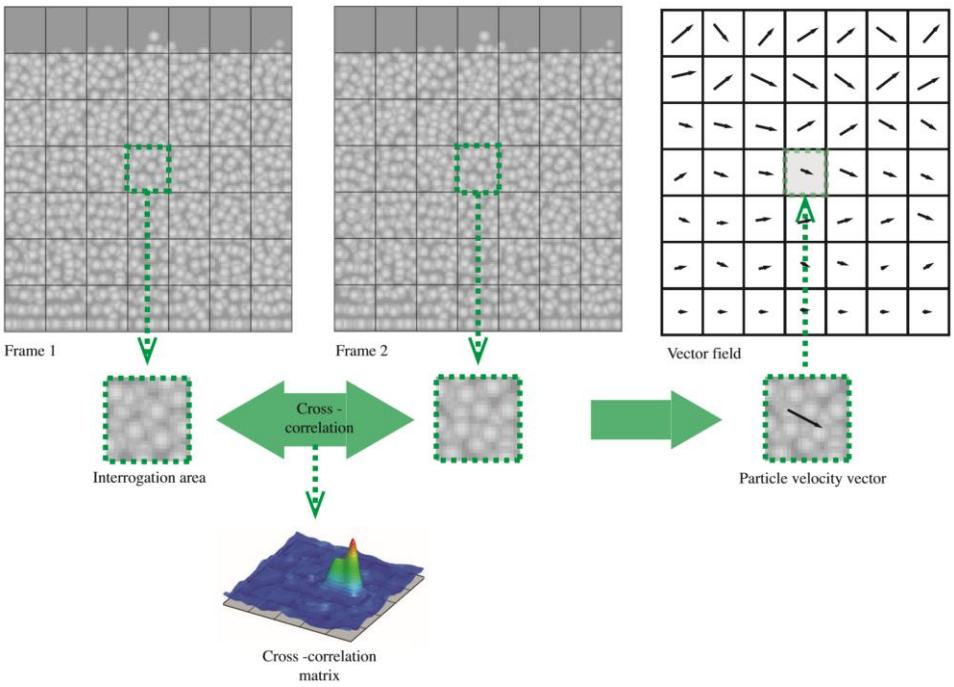

Figure 3-5: Schematic illustration of PIV analysis principle (Gollin, 2017).

PIV analysis requires visible particles to show their moving track in the flow field. For flows consisting of non-transparent materials, such as solid grains involved in this study, the opaque particles can produce image texture with light and shade contrasts to identify the flow motion; a consequent drawback of this, however, is that measurements and observations are only allowed at the external boundaries of the flow. In the case of transparent flowing substance, which is not used in this study, seeding of tracers and fluorescence-based visualisation may be involved in high-speed photography; an example of applying PIV analysis to flows of transparent glass particles can be found in Sanvitale and Bowman (2017).

3.2.2. Parameter Setting

High-speed images were captured in 1280 x 800 pixels resolution at different framerates for different test materials: 1200 frames per second (fps) for ceramic bead flows and 3000 fps for Maple Mud flows; the lower framerate ensured the capture of the entire uniform flow event as the high-speed camera has an upper limit for frame numbers per run, while the higher framerate gave better PIV estimation on well-graded flows as less difference between each image pair facilitates the cross-correlation. The camera view was just enough to cover both the upslope and downslope sensors (Figure 3-1), yielding an image scale of 0.2266 mm per pixel; hereafter, when giving a pixel length, the corresponding approximate real length is also provided.

A version of GeoPIV, dubbed "static mesh GeoPIV" was used (Sanvitale and Bowman, 2012). The stationary mesh in the PIV analysis created at the downslope sensor position, as shown in Figure 3-6 (a), was made up of four columns of 24 x 24 pixels (≈ 5.44 mm) replicating every 12 pixels (≈ 2.72 mm) along the x-direction and 2 pixels (≈ 0.45 mm) along the z-direction; the small z-spacing enabled precise vertical velocity distributions. For Maple Mud, patch size equals about 2.85 D_{50}, hence the image density is 8.12 D_{50} per patch, complying with the recommended 5 – 10 particles per patch by Adrian et al. (2011). For ceramic beads, each patch contains 2 full grains on average (patch size ≈ 1.4δ); the patch size is relatively small but is still larger than twice the maximum local displacement (a requirement of accurate cross-correlation proposed by Raffel et al. (2018)) of about 11 pixels (≈ 2.49 mm), and can avoid an over-averaging of local velocities of multiple grains. To accurately identify boundary velocities, the mesh was ranged from more than one patch below the bed to at least half a patch above the eye-observed peak flow thickness, ensuring both basal boundary and flow surface could be found in the centre of a patch.

3.2.3. Postprocessing Velocity Profiles

Velocity profiles derived from PIV analysis need postprocessing to delete undesired data. Figure 3-6 (b) shows an example of a velocity curve before and after postprocessing. The first step is to remove velocity values above the flow surface, which is identified by the maximum velocity; these data may be generated by patches not filled with grains, indicating that the side-view flow surface is below the centre of the patch. Similar circumstances occur at the basal boundary. The "basal patch centre" dash line in Figure 3-6 (b) corresponds with the vertical position of the blue patch in Figure 3-6 (a), below which a portion of the image inside a patch is the stationary textured flume bed. The inclusion of this bed would lower the calculated velocity. Those lower data close to the flume bed need to be replaced by estimations from uniformised velocity gradients (i.e. making the velocity gradient near the bed identical to that between the two points above the basal patch centre), but not until the velocity curves are fitted by power functions and smoother profiles are produced. This is to guarantee a convex shape of the fitted velocity curve: as shown in Figure 3-6 (b), a portion of the velocity curve above the basal patch centre is concave even when the flow is thin, in which case the whole velocity profile may be fitted into a concave curve if velocity values near the bed have been amended closer to those in the concave portion. By checking the frames corresponding to the velocity profile in Figure 3-6 (b), the hand-calculated slip velocity is 1.35 m/s, consistent with the estimated slip velocity; this shows that the amendment of velocity values below the basal patch centre can give satisfactory outcomes.

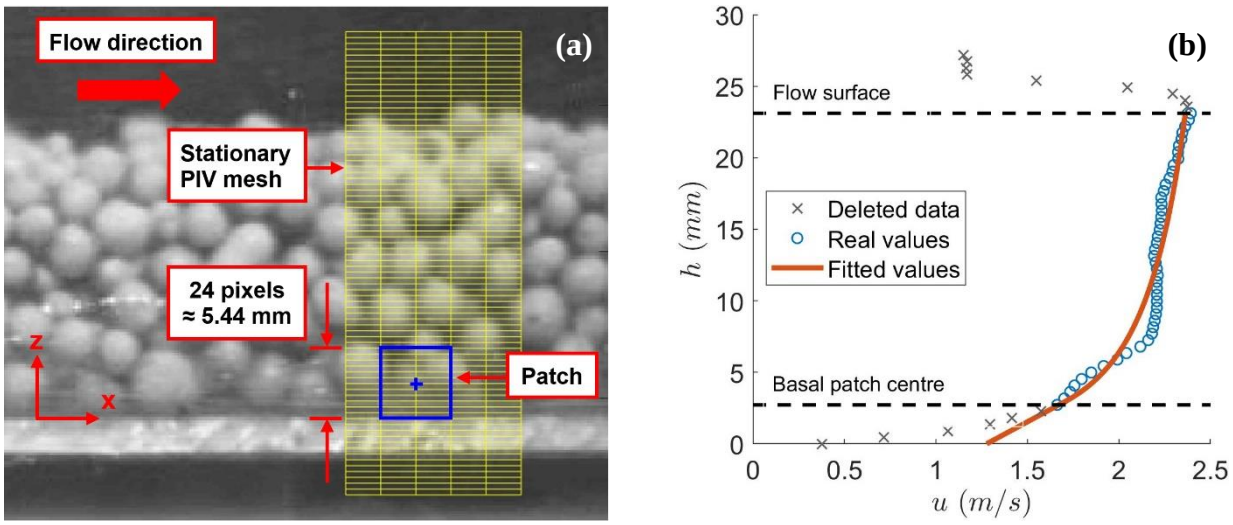

Figure 3-6: (a) Schematic diagram of PIV analysis, where a typical patch denoted with a blue square and the stationary PIV mesh in yellow are highlighted. (b) Example of velocity profile showing the original data from PIV analysis and processed data fitted by a power function.

3.3. Identification of "Main Surge"

In this study, the granular flow surge, excluding precursory grains and flow tail, is referred to as "main surge"; the identification of the "main surge" is to remove the parts containing less valuable information from the analysis. As depicted in Figure 2-3, debris flow can be divided into a series of sections including precursory grains, flow head, flow body and flow tail. The flow tail of a wet granular flow in a small-scale flume is generally very thin and moves very slowly, lengthening the flow duration over which PIV is difficult to apply; analysing the flow tail seems unnecessary since this part of the flow only contains a small portion of solid grains and contributes little to the final runout. Similarly, a few saltating and dispersed precursory grains hardly affects runout behaviours and cannot produce regular velocities and stresses, hence data from this part may be less reliable and comparable.

The "main surge" part of a granular flow is identified based on several criteria. The start point of a main surge is defined by the moment when the flow height begins to continuously rise. The end point of a main surge, however, is determined when either flow height or basal normal stress achieves a minimum within a user-defined range in which the boundary between flow body and flow tail can be observed; finding the minima of two parameters reduces the risk of not involving all the flow head and flow body, as the PIV-analysed zone (giving the flow height estimation) and sensor-mounted zone (giving the basal normal stress response) may not perfectly in line and

thus the data plotting of either one of the factors may look incomplete; the final selection of the end point is one of these two minimum points with a larger time index. Figure 3-7 takes CSU 2.0 test (i.e. the saturated flow with 2L source volume and 0.45 water content) as an example to highlight the difference between the main surge, which is denoted using asterisks, from other parts, which use dashed lines, in a test. As is shown in the plot, the "flow tail" part depicted in dashed lines, which is too shallow (basically a one-grain layer) to expect accurate PIV results and takes too long as grains just slowly slide down on the flume bed, seems less important than the main surge; quotation marks indicate that the "flow tail" mentioned here may not be identical to its physical definition but is more of an expression showing its distinction from the main surge. Also, note that precursory grains are more notable in dry granular flows than in wet flows as referenced in Figure 3-7.

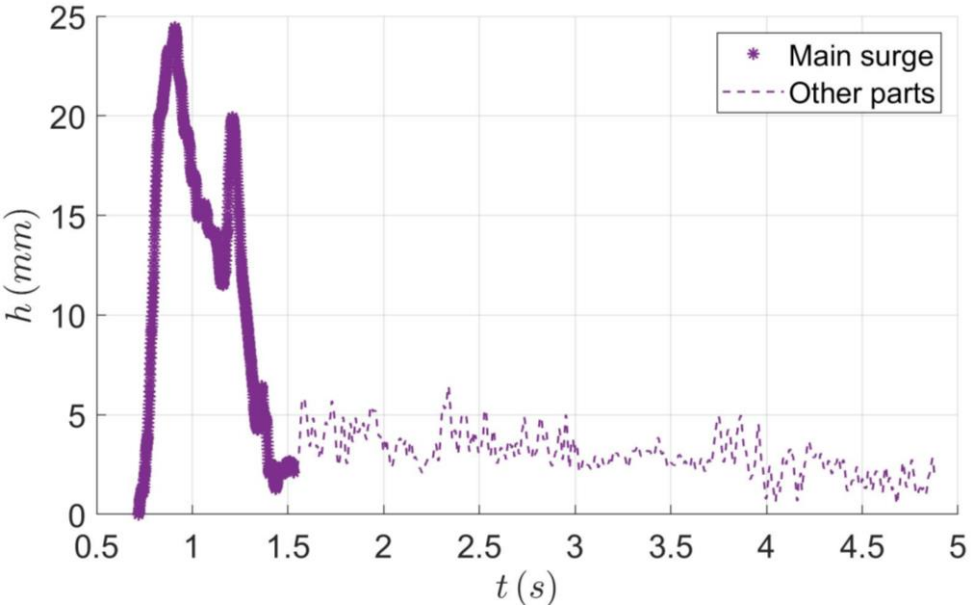

Figure 3-7: Identification of "main surge" of a granular flow (example from CSU 2.0 test), in which asterisks represent the "main surge" part whereas dash lines denote other parts.

3.4. Bulk Flow Mobility

Two parameters were selected to quantify bulk flow mobility: travel angle (α_T) and travel distance (L). Travel angle, as described in Figure 2-9 represents the apparent friction calculated from the initial and final positions of Centre of Gravity (COG) and is the main parameter for

characterising bulk mobility since the moving distance of COG is affected by both external and internal energy loss. The travel angle is a measure of the efficiency of a flow from a fundamental physical perspective. Travel distance from the inclined flume outlet to the distal end of the deposit considers the spreading of grains, allowing quick comparisons among flows with similar runout mechanisms. Travel distance is also what is typically considered by civil infrastructure engineers carrying out risk analysis on the potential for debris flow hazard, as this determines the extent to which infrastructure may be spatially affected by a debris flow. The reliability of these two parameters is ensured by the 2-D flow path where flow material cannot move to the flanks and higher flow mobility can certainly push the deposit forward.

The travel angle and travel distance of a tested granular flow are derived from the final deposit in the horizontal runout channel. As explained in Sec. 3.1.4, the side-view geometry of the deposit was video-recorded by a smartphone after every test. Later the deposit outline was drawn in the drafting software AutoCAD based on a series of pictures saved from the video, as depicted in Figure 3-8 (a); 2×2 mm grids were put on these pictures, which were scaled to actual sizes, to draw the deposit outline as regular polylines. Only the domain in the centre of the camera view was kept for each picture to minimise the distortion in deposit geometry due to the fisheye effect.

Travel distance is hand-measured after the completion of deposition; the length of the sketched deposit outline must meet the measured value. Travel distance of a wet flow deposit is easy to identify, as a heap containing a large number of grains is oriented towards the distal end, producing a clear and well-bounded deposit margin; for dry flows, however, the heap tends to rest towards the slope and the distal margin of the deposit is blurred by a few scattered grains. Figure 3-8 (a) presents an exampled dry flow deposit of ceramic beads as well as the determination of the anterior boundary of a dry deposit, which is defined by a transversal line where half the channel width can be occupied by approximately 15 grains.

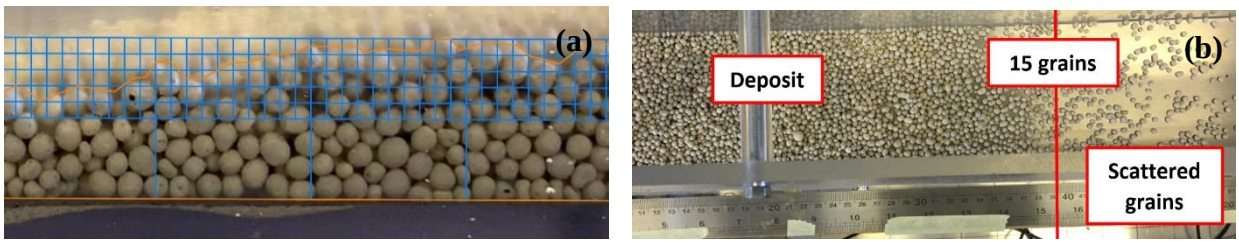

Figure 3-8: Schematic illustrations of (a) determining the range of dry flow deposits, where the red line divides the deposit body from scattered individual grains and (b) drawing deposit outlines from video frames.

Travel angle is generally determined after drawing the deposit geometry with the calculation of COG positions within the initial source material and the final deposit. The hopper lifts the source material to a position above the flume bed, giving a minor increase in the gravitational initial potential energy. However, unlike liquid flow discharged from an hourglass where the flow rate depends on the pressure applied to the aperture and hence on the height of fluid, solid grains in a vertical container can achieve a bottom pressure independent of their piling height, as the weight of grains can be transferred to the sidewall of the container by granular arching and can then be supported by sidewall friction (Janssen, 1895). Hence the COG within a frictional granular mass placed in a hopper has no bearing on the outflow behaviour or flowrate and the additional height contributes very little to the available energy for flow. To understand better the influence of the release height on the consequent travel angle, trials of 2L dry uniform flows were initiated from both the hopper and a lifting-gate system; results show that, in contrast with the flow initially resting on the flume bed, the hopper-released flow gives higher bulk mobility (longer travel distance and farther COG) but also generates a larger travel angle (Figure 3-9 (a)) due to consideration of the additional drop height. Therefore, travel angle estimation needs to be amended.

Considering the analogy between a hopper and a silo, one idea for correcting the travel angle estimation is to fix the initial position of COG at the centre of the hopper base (the green cross and green dash line in Figure 3-9 (b)), assuming that granular flows "begin" when falling out from the hopper gate. Experiments done by Aguirre et al. (2010) demonstrate that the mass flow rate of solid grains through an orifice is essentially determined not by pressure but by the driving mechanism and the orifice geometry and can be quantified as a function of local grain velocity at the outlet in a gravity-driven system. In this scenario, the bulk flow mobility should be mainly dependent on the falling height, i.e. the drop in elevation from the hopper base to the flume bed below, since the local velocity of grains through the hopper gate may not vary significantly with either source volume or water content. However, granular flows can lose a portion of velocity when hitting the flume bed as shown in Figure 3-9 (b). According to Dunatunga and Kamrin (2015), free-falling grains in a cluster undergo no interactive stress as they are discrete and disconnected, but they densify and solidify as soon as touching a fixed plane to enable intergranular stress transfer. When this phenomenon takes place in a small-scale narrow flume, the downslope flow motion may not occur before a short solidification of dropping material, indicating that granular flows practically "begin" at a relatively dense regime at the flume bed, wherever the grains initially come from. With this interpretation, the higher mobility of a

hopper-released flow (Figure 3-9 (a)) may be because only a small portion of grains falling simultaneously out from the hopper need to accelerate from a nonstatic state immediately after solidifying on the flume bed, hence the flow is not mobilised from a highly frictional state where particles are firmly in enduring contact; while in the lifting-gate case, the entire mass that sits statically on the flume bed at the beginning has to be gradually mobilised and to overcome higher friction. Therefore, the assumption that granular flows "begin" at the flume bed seems reasonable and it allows the estimated travel angles to be compared with results derived from the widely-used lifting-gate configuration. A hypothetical initial state of the source material as well as the corresponding energy line are depicted in blue colour in Figure 3-9 (b), where the cross-section (i.e. top-view) geometry of the blue block imitates that of the flow dropping out from the hopper; this initial condition is an approximation of the state of granular media before flowing downslope, but it gives a more satisfactory energy line (and hence a more appropriate travel angle estimation) in comparison with the red and green lines starting within and at the base of the hopper, respectively.

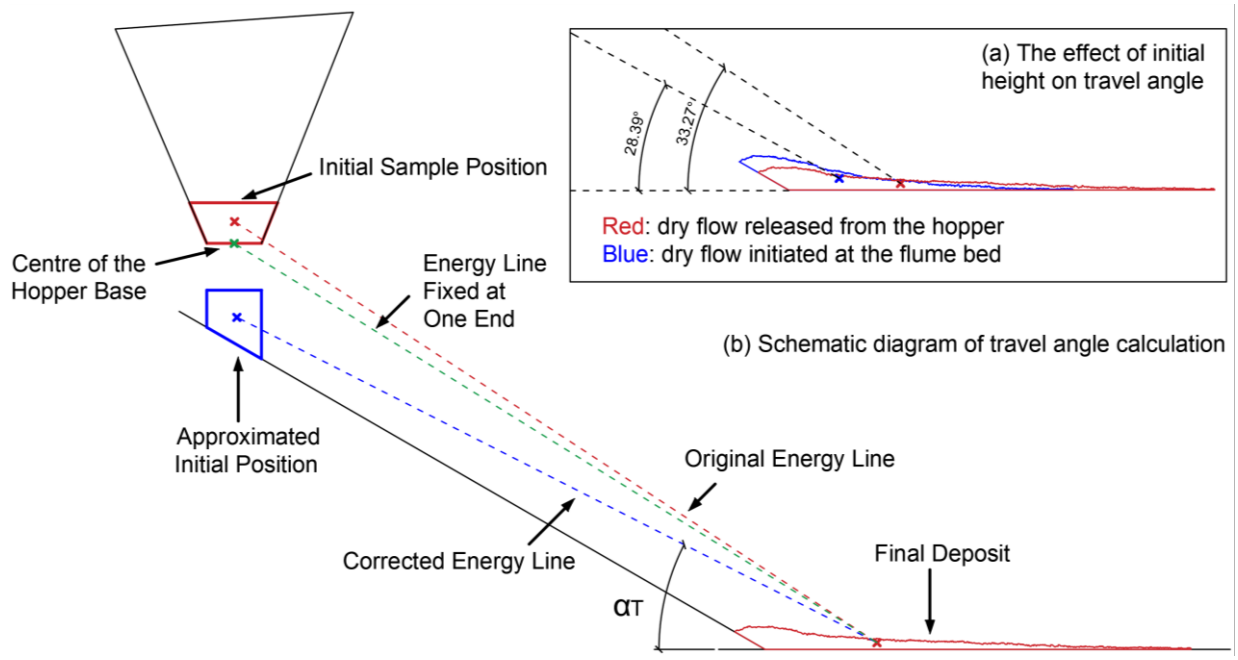

Figure 3-9: (a) The effect of initial height on travel angle, where deposits are produced by 2L dry ceramic beads; (b) schematic diagram of travel angle calculation, in which the original energy line related to real sample position is in red colour, the attempted line to a fixed starting point at the hopper base in green, and the corrected line to an approximated initial position at flume bed in blue.

3.5. Dimensional Analysis

To identify the flow regime and the dominant stress-transfer mechanism, dimensional analysis in this study utilises dimensionless numbers introduced in Sec. 2.3, including the Savage number, Bagnold number, and friction number; Darcy number and Reynolds number are excluded due to their shortcomings explained in previous sections. As velocity profiles can be provided by PIV, local values of dimensionless numbers distributed across the flow depth are also calculated. The local Savage number at a height z below the flow thickness h is defined by the following equation and is rewritten from Eq.(2-5) to make use of measured basal effective stress data rather than theoretically estimated values:

$$N_{Sav}(\mathrm{z}) = \frac{\rho_s \dot{\gamma}^2(z)\delta^2}{(\sigma_{basal} - p_{basal})\left(1 - \frac{z}{h}\right)} \tag{3-1}$$

in which $\dot{\gamma}(z)$ is the local shear rate; the denominator $(\sigma_{basal} - p_{basal})\cdot(1 - z/h)$ gives the local effective stress that is assumed to grow linearly with the flow depth from a stress-free state at the flow surface (i.e. a triangular stress distribution along the flow depth). Grain size δ = 3.85 mm is clear for uniform ceramic beads; whereas for well-graded Maple Mud, the appropriate choice of δ is more ambiguous. Sanvitale and Bowman (2017) has provided flume experiment data of polydisperse granular flows showing that the dependence of momentum exchange on grain size exists even when the grain sizes are relatively uniform and only cover one order of magnitude; grains in a larger size (D_{90}, i.e. the size where 90% of grains in the sample are finer) tend to be dominated by collisions and those in a smaller size (D_{10}) by friction. Considering grain size segregation, δ for Maple Mud is represented by the local mean grain size D_{50} that varies with the longitudinal position in the flow body. The relationship of the local D_{50} value with the position in the flow body is assumed to be equivalent to that in the final deposit (see Sec. 6.2 and 6.3 for the detailed calculation based on Maple Mud deposits).

The local Bagnold number at the height z amended from Eq.(2-7) is given by:

$$N_{Bag}(\mathrm{z}) = \frac{\upsilon_s}{1 - \upsilon_s} \cdot \frac{\rho_s \dot{\gamma}(\mathrm{z})\delta^2}{\eta} \tag{3-2}$$

in which assumptions are made that the solid fraction υ_s is constant in the flow body, and the dynamic viscosity of the pore fluid η linearly varies with the water content from the value of air, η_{air}, to that of water, η_w; the value of η can be approximated by:

$$\eta = \begin{cases} \dfrac{w\eta_w + (w_{sat} - w)\eta_{air}}{w_{sat}} & (w < w_{sat}) \\ \eta_w & (w \geq w_{sat}) \end{cases} \tag{3-3}$$

where w_{sat} is the saturating water content of the granular medium; for uniform ceramic beads w_{sat} = 0.256, while for well-graded Maple Mud w_{sat} = 0.21.

The local friction number at the height z, by its definition, can be calculated by the ratio of $N_{Sav}(z)$ to $N_{Bag}(z)$:

$$N_{fric}(z) = \frac{N_{Bag}(z)}{N_{Sav}(z)} = \frac{\upsilon_s}{1 - \upsilon_s} \cdot \frac{(\sigma_{basal} - p_{basal})\left(1 - \frac{z}{h}\right)}{\eta\dot{\gamma}(z)} \tag{3-4}$$

Additionally, threshold values of $N_{Sav}(z)$, $N_{Bag}(z)$ and $N_{fric}(z)$ demarcating different flow regimes comply with the values given in the literature (see Sec. 2.3) and are 0.1, 200 and 100, respectively.

4. Dry Uniform Flows: Results

Preface

The CDU (Ceramic beads, Dry, Uniform) test group involves the idealised granular flows composed of dry uniform pseudo-spheres. Details about the experimental setup, source material and test procedure of CDU small-scale flume tests can be found in Chapter 3. This chapter presents CDU test results and is structured as follows: Sec. 4.1 gives measured data from CDU tests; Sec. 4.2 records the macroscopic morphology of flow deposits and the analysis of bulk flow mobility; Sec. 4.3 demonstrates the longitudinal flow profiles and the comparison of flow heights; Sec. 4.4 contrasts load-cell responses of all CDU flows; Sec. 4.5 gives velocity information of dry granular flows, including velocity profiles and time history of depth-averaged velocities; finally, Sec. 4.6 shows the estimation of the Savage number, Bagnold number and friction number, including their local values and mean values across the flow height, to analyse the evolution of momentum exchange within dry granular flows.

4.1. Test Information

Source volume (more accurately the bulk volume of dry grains) is set as the experimental variable for all the CDU tests and the value utilised in each test is included in the test label; e.g. the label “CDU 0.75” signifies that the bulk dry volume of the sample is 0.75 litres. Measured data for CDU tests, collected from the sample before releasing from the hopper, the final deposit in the horizontal runout channel and the AutoCAD morphological analysis (see Sec. 3.3), are given in Table 4-1, in which: (i) “bulk dry volume” is the volume of grains closely packed in the measuring jar; (ii) void ratio and porosity are assumed identical to those from CSU (Ceramic

beads, Saturated, Uniform) tests (see Chapter 4 Preface for values and Sec. 3.1.4 for measuring process); (iii) "volume in the hopper" corresponds to a slightly more naturally packed state of grains calculated from porosity; (iv) "bulk density" is derived from the measured sample mass and the calculated sample volume in the hopper; (v) "runout" is the length of deposit calculating from the start of and along the horizontal channel (see Sec. 3.3 for identifying the front edge of deposit); (vi) "inclined length" is the length of deposit calculating from the flume end and towards the upslope direction; (vii) "travel angle" is the only parameter that is not directly measured but is determined by the energy line drawn from the source material to the final deposit (see Sec. 3.3).

Test		CDU 0.75	CDU 1.0	CDU 1.5	CDU 2.0	CDU 4.0
Source measurements	Bulk dry volume (L)	0.75	1	1.5	2	4
	Solid mass (g)	1120.5	1488.45	2223.15	2920.39	5806.35
	Void ratio	0.598	0.579	0.585	0.566	0.582
	Porosity	0.374	0.367	0.369	0.361	0.368
	Volume in the hopper (cm^3)	799.1	1049	1573	2040	4098
	Bulk density (g/cm^3)	1.402	1.419	1.414	1.431	1.417
Deposit measurements	Runout (mm)	600	690	800	940	970
	Inclined length (mm)	30	30	96	115	280
Morphological analysis	Travel angle (°)	27.6	27.2	28.1	27.9	30.1

Table 4-1: Test information of CDU tests.

4.2. Deposit Analysis

The typical deposition process of CDU flows given in Figure 4-1 is taken from the CDU 2.0 test (i.e. the dry uniform flow with 2L source volume) and shows that a dry granular deposit tends to lean against the slope, forming a backward heap, i.e. the majority of grains do not flow to the distal edge of the deposit but rest near the inclined flume outlet. Figure 4-1 also exhibits how the majority of grains are left behind close to the slope: as dry grains flowing into the runout channel decelerate and come to rest from the flow front to the rear (Figure 4-1 (a)), a granular jump (similar to a hydraulic jump) occurs and the stationary granular heap consequently thickens (Figure 4-1 (b)); the settled grains at the front keep jamming the following flow body until nearly the upstream end of the heap (Figure 4-1 (c)). The flow movement is blocked by the deposited

leading edge because flowing grains cannot overcome the intergranular frictional resistance to the shear or inertial movement after running into the horizontal channel.

Figure 4-1: Deposition process of dry granular flows. (a) Dry flow enters the runout channel, (b) flow front stops and the body settles accordingly, and (c) deposition continuously develops backwards.

The deposit morphologies of all the CDU flows are summarised in Figure 4-2, in which the horizontal scale is five times compared with the vertical scale and each deposit's Centre of Gravity (COG) is highlighted by a solid circle sharing the same colour as the deposit outline. All the dry deposits show similar shapes as in Figure 4-1 (c), indicating a consistent deposition mechanism shared across CDU flows. With an increased source volume, a larger portion of the material is left on the slope to build a thicker heap and the COG of the deposit locates slightly more towards the upstream position (Figure 4-2). The side-view morphologies, as well as the COG distribution of CDU deposits in Figure 4-2, are similar to those of other dry granular flows or landslides, e.g. Smith et al. (2006); Bryant et al. (2014); Coombs (2018); Cheng et al. (2019); Li et al. (2021).

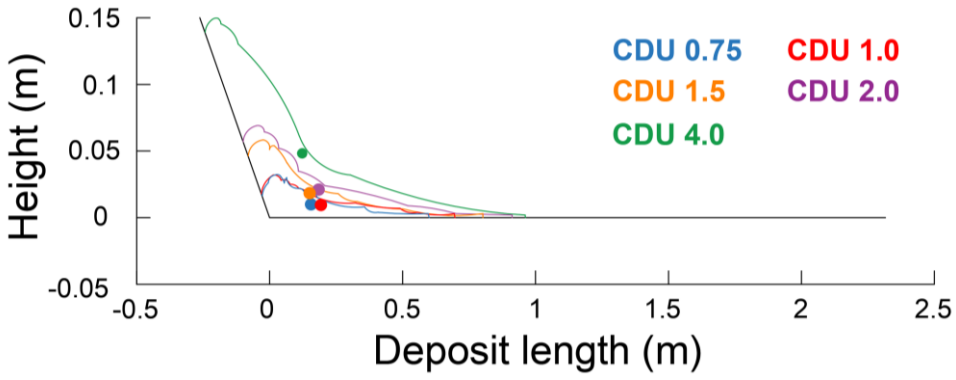

Figure 4-2: Deposit side-view outlines of CDU flows. The horizontal scale is 5 times the vertical scale. Filled dots represent the locations of the centre of gravity.

The profiles of travel distance and travel angle against source volume of CDU flows (Figure 4-3) are translated from deposits presented in Figure 4-2. Travel distance (Figure 4-3 (a)) roughly steadily grows with source volume between 0.75L – 4L, but shows little difference when source volume varies from 2L to 4L; this means that the spreading potential of dry granular flows increases with source volume until the volume becomes relatively large (4L). Although the boundary between scattered grains and the main deposit body is not absolute (Sec. 3.3) and the spread range of dry grains, which is the main factor of travel distance, cannot be identical from test to test, the overall evolving tendency of travel distance with source volume illustrated in Figure 4-3 (a) is still clear: a larger volume (and hence a larger number) of grains can spread farther when the source volume is relatively small, whereas it is more difficult for grains in a large source volume (4L for the small-scale flume) to flow into the runout channel, tending to rest on the slope, limiting the number of grains available for the spreading. The high impedance to the grains occurring in the 4L dry flow may be due to the blockage of the channel due to the rising deposit: once stopped, the thicker and denser flow can more easily block a larger number of grains in the following flow body. Travel angle (Figure 4-3 (b)), on the other hand, shows a gently rising trend with source volume, indicating a slightly decreasing bulk flow mobility; this agrees with the COG positions observed in Figure 4-2. Despite the overall rising trend, dry granular flows with evolving source volume seem to result in similar travel angles (about only 3° difference at most); hence the source volume for dry granular flows seems to have little impact on bulk flow mobility.

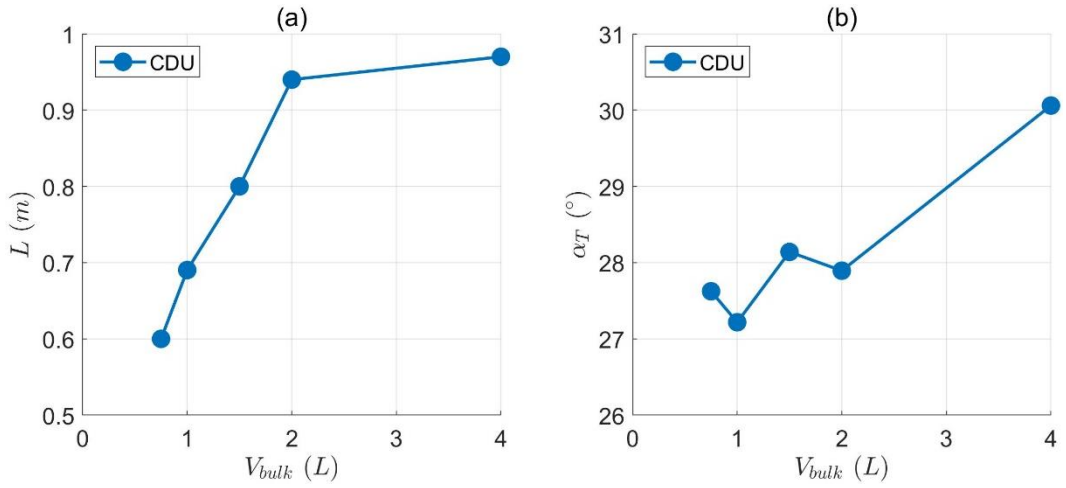

Figure 4-3: Evolution of (a) travel distance L and (b) travel angle α_T of CDU flows with source volume, V_{bulk}.

4.3. Flow Profile

Figure 4-4 shows flow profiles of CDU tests recorded by the high-speed camera at the downslope position; each row represents a tested flow with a different source volume, while the three columns give, respectively, the leading edge, the main flow body and the flow tail from the right-hand side to the left-hand side (as the flow is moving from left to right in the camera view). For each tested dry flow, the image of leading edge is determined when a loose collection of grains (i.e. not individual scattered particles) reaches the edge of the camera view; the image of main body is defined by the frame where the eye-observed maximum flow height is at the right-hand edge; the image of flow tail is represented by the frame in which the last grain starts to leave the left-hand edge of the camera view, hence photographs shown in subplot (j) and (m) involve a static pile of grains on the slope formed before the trailing end of flow enters the camera view. With an increased source volume: (i) the leading edge tends to be less dispersed and more gathered, (ii) the main body becomes thicker and denser, producing a smoother top surface and fewer saltating grains, and (iii) the flow tail part remains similar except that the granular heap resting on the slope occupies a larger space in the camera view (starting from the CDU 1.5 test in which the heap is only visible at the right-hand side edge of the image).

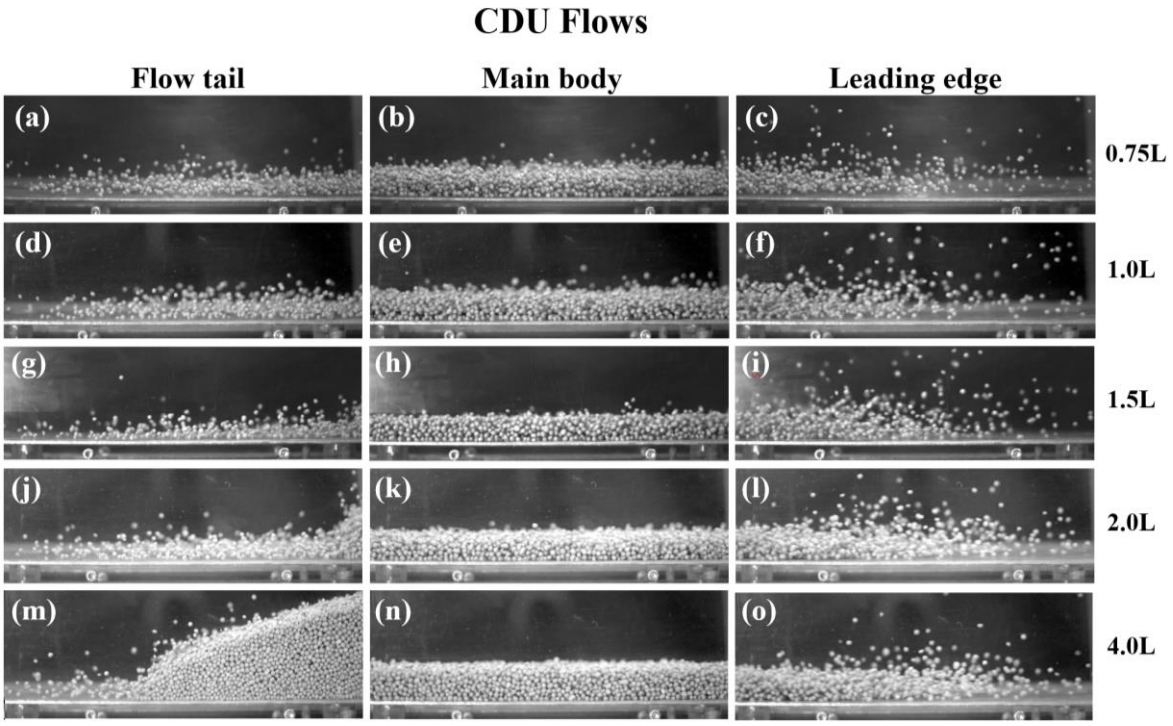

Figure 4-4: Recorded profiles of CDU dry flows where the camera view is tilted at 30° to make its bottom side parallel with the inclined flume bed. Three columns are the flow tail, main body and leading edge of each tested flow, while five rows are five tested flows with evolving source volumes that are exhibited in the test labels at the right-hand side margin.

Saltating grains can interfere with ultrasonic sensor detection, resulting in ineffective flow height measurement (see Appendix A-4). Contrasts between flow height measurements by the ultrasonic sensor and by PIV analysis for each CDU flow are provided in Figure 4-5, where data from the ultrasonic sensor (in blue asterisks) are calibrated raw data but those from PIV (in red curves) are processed data. Ultrasonic sensor responses highly disagree with PIV detection, not only in terms of flow height values but also at the beginning and the end of the flow. Taking the most inconsistent CDU 0.75 flow as an example, the flow height measured by the ultrasonic sensor reduces to zero about 0.5s before the end of PIV analysis, which corresponds with the image where the granular flow leaves the camera view. The difference between these two measurements seems to reduce for larger source volume, however ultrasonic sensor responses for dry granular flows are still questionable. Therefore, the flow height estimation for CDU flows relies on PIV results, but some potential errors should be considered: (i) flow height may be slightly overestimated as grains at the top surface of the flow can be observed in the image captured at the sidewall; this issue can potentially pose more influence if grains saltate near the surface; (ii) the PIV-detected zone (the mesh in Figure 3-6 (a)) is probably not perfectly in line with the mounted position of the ultrasonic sensor, as suggested by the CDU 4.0 subplot of Figure 4-5; the highest plateau where sensor data and PIV data overlap means that the two measurements can both give the correct height response to a static granular pile, hence the rising part after about t = 2s shows that PIV very likely detects the grain accumulation slightly later than the ultrasonic sensor.

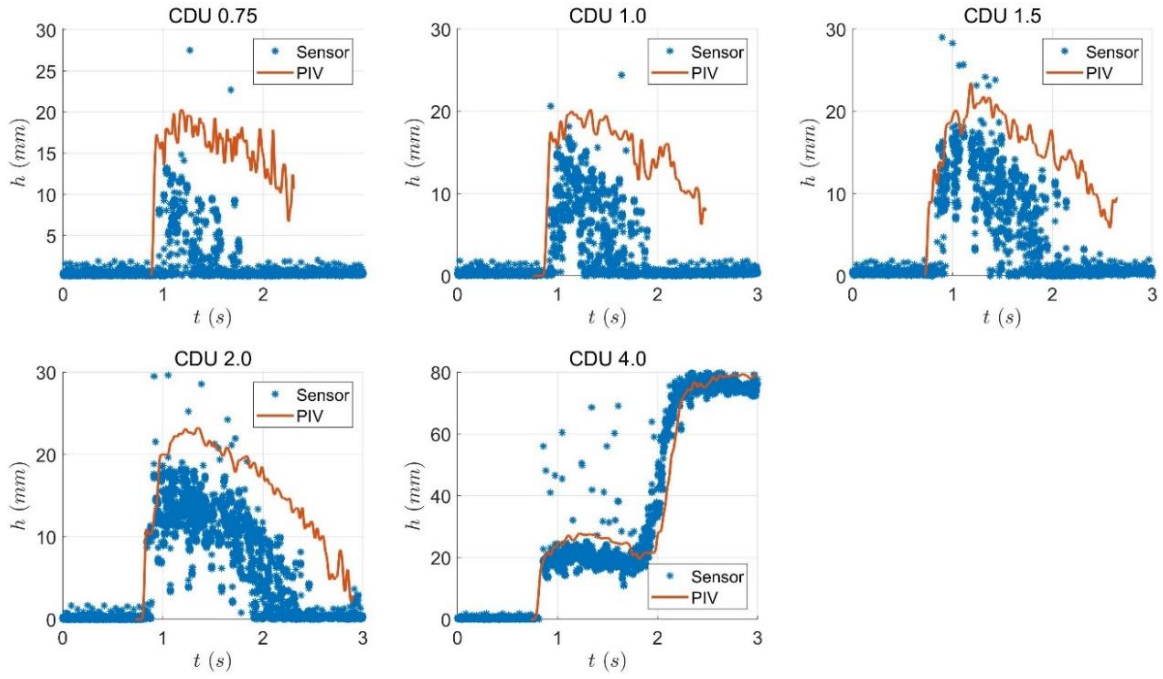

Figure 4-5: Contrasts between flow height measured by the ultrasonic sensor and PIV analysis.

Flow heights based on PIV analysis are compared in Figure 4-6. Figure 4-6 (a) and (b) demonstrate the evolution of absolute and normalised flow height with time (t), in which the "main surge" part of each flow (see Sec. 3.3) is given using a solid line whereas others are in dashed line. Overall, the flow grows thicker and enters the PIV-detected zone earlier with a larger source volume, but the dry flows of 0.75L and 1L bulk volume give similar flow height profiles. This is because CDU 0.75 and CDU 1.0 flows are highly dilute and saltating, barely sliding along the downslope direction, thus flow heights of these flows appear larger due to the involvement of more interparticle voids; in contrast, the flow height increase becomes more apparent with an increasing source volume over 1.5L, where the produced flow is denser and mostly translational.

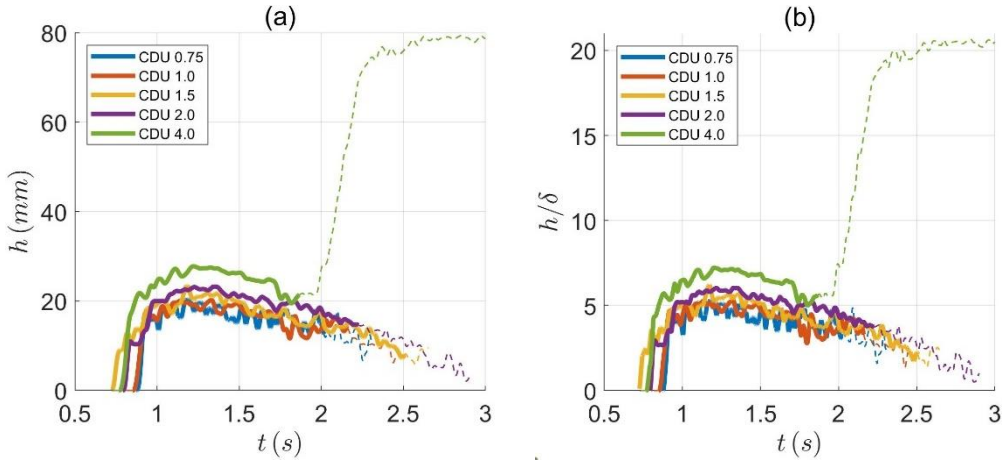

Figure 4-6: Time histories of (a) absolute CDU flow height and (b) normalised CDU flow height by averaged grain size, in which the "main surge" of the flow is highlighted by the solid line and other parts (precursory grains and flow tail) are in dash lines.

4.4. Basal Normal Stress

Basal normal stress (σ_{basal}) data were directly measured by load cells in all the CDU tests and were then adjusted to match the flow height measurement. Theoretically, basal normal stress should equal the stress responding to the weight of a granular flow with a known density and flow height on the load cell, which can be expressed as:

$$\sigma_{st} = \rho g h \cos\theta \tag{4-1}$$

where ρ is the bulk density of the flow material, g is the gravitational acceleration, h is the flow height and θ is the slope angle. Note that the calculation of theoretical basal normal stress (σ_{st})

uses the flow height measured along the bed-normal direction as universally done in practice, despite that the load-cell signals actually result from the bed-normal pressure acted by a vertical column of flow material on the load cell. The schematic illustration given in Figure 4-7 shows that the normal stress measured by load cells should be due to ρgh, but that calculated from flow height (h) should equal ρgh·cosθ. Since normal stress due to the bed-normal flow height is more relevant to both realistic measurement and numerical simulation, in this study σ_{basal} is determined by the measured basal normal stress multiplied by cosθ. In addition, the σ_{st} calculation presumes a uniform distribution of density (and thus volume fraction), which is untrue, and ignorable bed-normal pressure contribution caused by internal solid interactions, which is a usual consideration as the velocity difference between flow units is often assumed only occurring along the flow direction (i.e. bed-parallel direction).

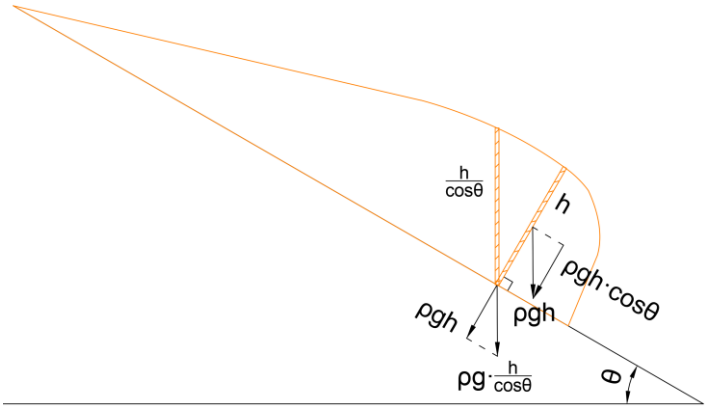

Figure 4-7: Schematic diagram of the bed-normal pressure detected by load cell (ρgh) and that theoretically calculated from flow height (ρgh·cosθ).

Figure 4-8 contrasts normal stress values from load-cell measurements with those from theoretical calculations for each CDU flow to assess the reliability of load-cell signals. In test CDU 4.0, the close match between sensor data and estimated results near the final plateau part shows that load-cell signals can provide accurate normal stress output, with acceptable differences that are probably due to the imperfect estimation of bulk density throughout the flow; for the "main surge" part where grains are in motion, a larger difference appears, relative to the case of the static granular pile and theoretical values seem to be overestimated as flow height can be overestimated. Overall, flow heights and accordingly, the theoretical solutions of basal normal stress, produce larger errors with lower source volume (similar to Figure 4-5), as the inertial motion of grains greatly dilutes the flow and reduces the volume fraction. Note that after the surges pass in tests CDU 2.0 and CDU 4.0, load-cell signal curves present a rise-and-fall which should be related to the phenomenon of grains piling up in the flume but does not appear in the

flow height curve; this might reflect the shock when flowing grains hit against the granular heap that is just piling up in the inclined flume and covering the downslope load cell, whereas PIV analysis cannot capture this shock.

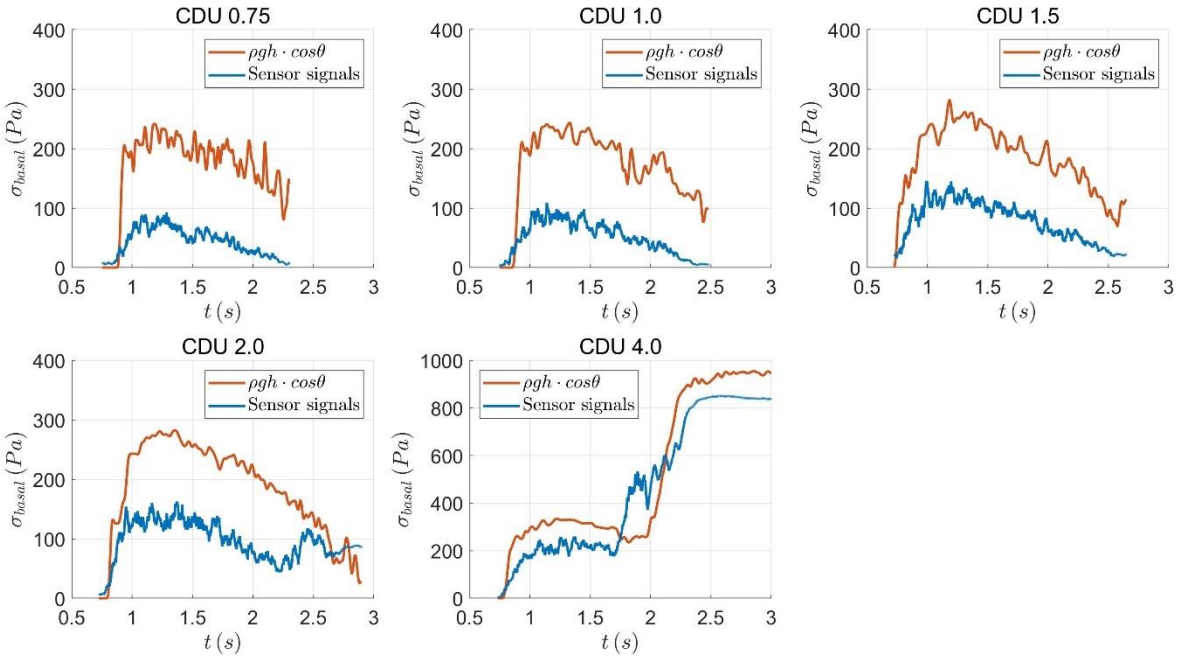

Figure 4-8: Contrasts between basal normal stresses measured from load-cell responses and those estimated from flow height for all CDU flows at the downslope position.

A comparison of normal stress histories of CDU flows is given in Figure 4-9, in which subplots (a) and (b) respectively illustrate the σ_{basal} measured by the upslope and downslope load cell. The stresses from dry flows with source volumes from 1.5L – 4L do not drop to zero after the surges pass the downslope load cell due to the heap formation (Figure 4-4); the CDU 4.0 data beyond 400 Pa (at which the y-axis breaks) at the downslope position, which corresponds with the heap formation on the slope, are not shown in Figure 4-9 (b), since normal stresses of granular flows in motion are more of interest. At both positions, the dry flows with larger source volume produce larger σ_{basal} and enter the sensor detection zones earlier. It is notable that σ_{basal} values at the upslope position also appear to be slightly larger than those at the downslope position, potentially implying a dilating tendency throughout the downward motion of these dry granular flows.

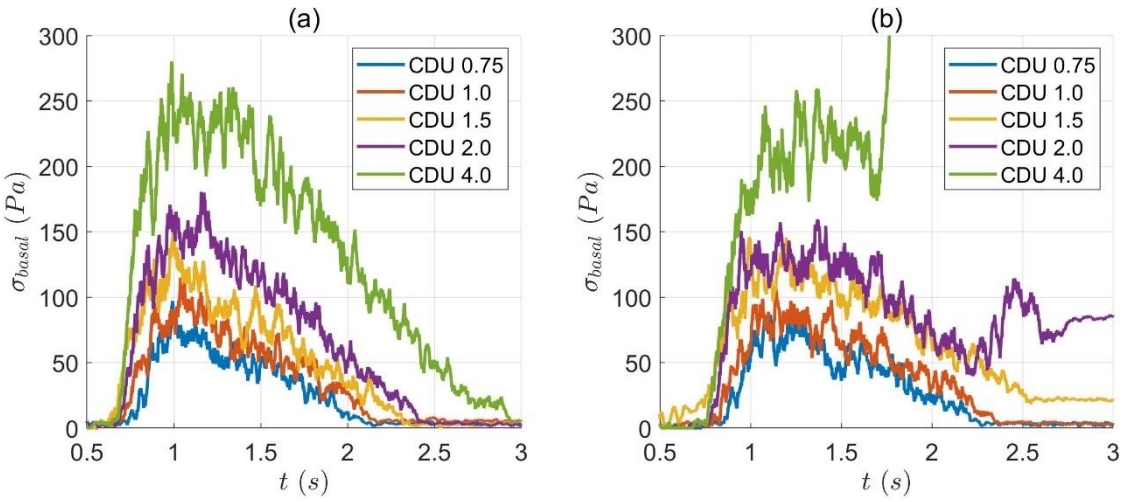

Figure 4-9: Basal normal stresses of CDU flows against time at (a) upslope position and (b) downslope position.

4.5. Flow Velocity

Velocity profiles of CDU flows are provided in Figure 4-10, where actual velocity values and power-fitted values (see Sec. 3.2.3) are given separately. For each flow, the plotted velocity curves are spaced at a regular time interval of t* = 5%, i.e. 5% of the "main surge" duration starting from the flow front; the colour transition scheme shows the spatial distribution of velocity curves, where yellow denotes the flow front and blue the flow rear (not necessarily the flow tail, as the flow motion of CDU 4.0 terminates earlier than flow tail enters the camera view); the red dashed line in every subplot represents the position of the basal patch centre as shown in Figure 3-6, below which the PIV measurements may not be fully accurate. Generally, the fitted velocity curves manage to keep the shapes of the original ones, thus analyses of flow behaviours can be derived from fitted velocities for the convenience of observation and contrast; a small error remains that a few velocity profiles are fitted to concave curves (e.g. as shown in CDU 1.0 subplot in Figure 4-10 (b)); such curves, which are in the minority, can be ignored when analysing the velocity profiles and grain moving patterns and can be kept when producing the depth-averaged velocity. Part of the precursory surge may be included at the beginning of the defined "main surge", e.g. two short yellow curves not touching the x-axis in the original profiles of CDU 1.5 (Figure 4-10 (a)); those curves are less noticeable after power-fitting (Figure 4-10 (b)) as they no longer look like velocities of dispersed grains.

Velocity profiles of all CDU flow in Figure 4-10 exhibit clear consistency. The velocity magnitude gradually decreases from the flow front (yellow curves) to the flow rear (blue curves)

but does not show a significant difference among all the subplots. The velocity curves' shapes look similar within the same flow and among different volumes, suggesting a relatively consistent moving pattern of dry grains. Hence the flow velocity seems not to noticeably vary with source volume. Additionally, all the velocity curves present low curvature and shape, resulting in nearly straight lines, giving a similar velocity gradient across the flow depth. To show more detail in contrasting the velocity shapes, the velocity curve near the time-point where the flow height reaches the maximum value is chosen from each CDU flow and plotted in Figure 4-11, in which subplot (a) shows a coordinate system of flow height (h) and flow velocity (u), while subplot (b) shows a coordinate system of normalised height (z/h) and the normalised velocity by depth-averaged velocity (u/u_{ave}); here the velocity information taken at the position of the peak flow height is used to represent that of the flow front where the flow velocity is usually measured in fieldwork (e.g. Arattano et al. (2000); Marchi et al. (2002); Hürlimann et al. (2003); McArdell et al. (2007); Arattano and Marchi (2008)). Another Figure 4-12, using velocity profiles averaged over 0.01 second (which is approximately 1% of the main surge duration) both before and after the peak height (i.e. 0.02s in total) in the identical coordinate systems as in Figure 4-11, is given to reduce the random error of individual instantaneous velocity curves; the averaged normalised velocity profiles in Figure 4-12 (b) give similar distribution compared with the instantaneous profiles in Figure 4-11 (b), although less difference is created between the averaged velocities; this similarity shows that the evolution tendency of velocity profiles illustrated in Figure 4-11 is correctly captured.

In Figure 4-11 (a), velocity profiles at the peak flow heights of different CDU flows are seen to be similar in shape; aside from the 0.75L flow, the velocity at peak flow height tends to reduce across the depth as source volume increases, indicating that the peak flow height appears further from the leading edge. Figure 4-11 (b) shows a lower normalised slip velocity (at z/h = 0), a higher normalised surface velocity (at z/h = 1) and a more curved velocity shape with increasing source volume. With an increased source volume, although the velocity curves at the peak flow height are very similar in shape, being close to straight lines, the local velocity gradient produces a slightly larger difference from the flow surface to the flume bed; this means that dry granular flows with larger source volume are subjected to relatively stronger shear.

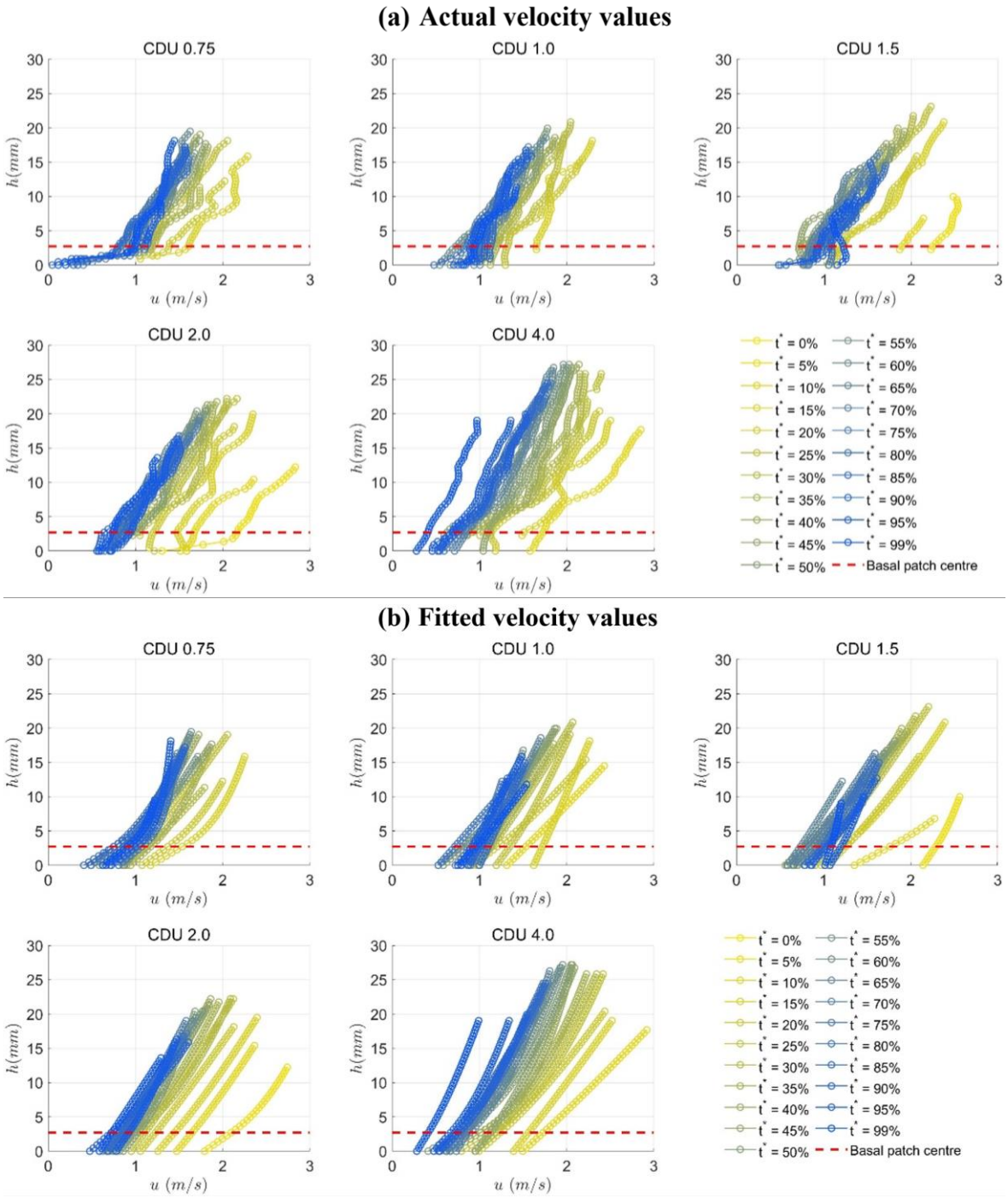

Figure 4-10: Velocity profiles of CDU flow distributed in subplots with (a) actual velocity data and (b) power-fitted velocity data. Velocity curves are plotted every 5% time for the duration of the "main surge". Yellow curves are closer to the flow front and blue to the flow rear; red dash lines denote the position of the basal patch centre.

Depth-averaged velocities of CDU flows (Figure 4-13) also show similar evolution with time. All the depth-averaged velocities within the "main surge" can approximately collapse onto a curve that starts with the maximum value at the leading edge, then gradually drops with time until plateauing when approaching the flow tail (the inconsistent trailing end of test CDU 4.0 is due to the grains piling up on the slope). The highly superposed depth-averaged velocity profiles

against time imply that the increase of source volume fails to effectively improve the flow velocity; this agrees with the similarity among velocity profiles of all CDU tests observed in Figure 4-10.

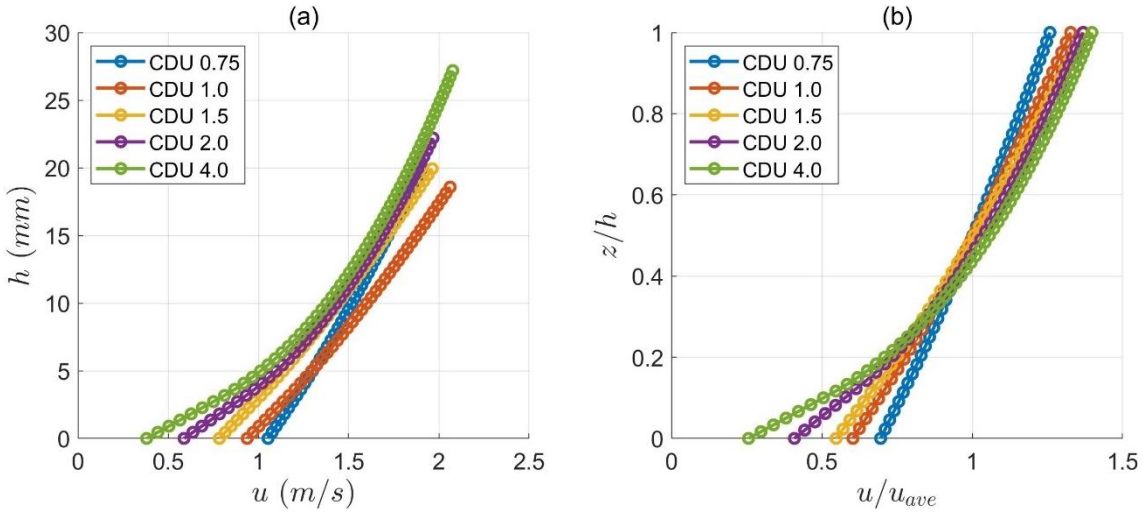

Figure 4-11: Velocity profiles at the peak flow height for all CDU flows. (a) Velocity against flow height, and (b) Normalised velocity (by depth-averaged velocity) against normalised flow height.

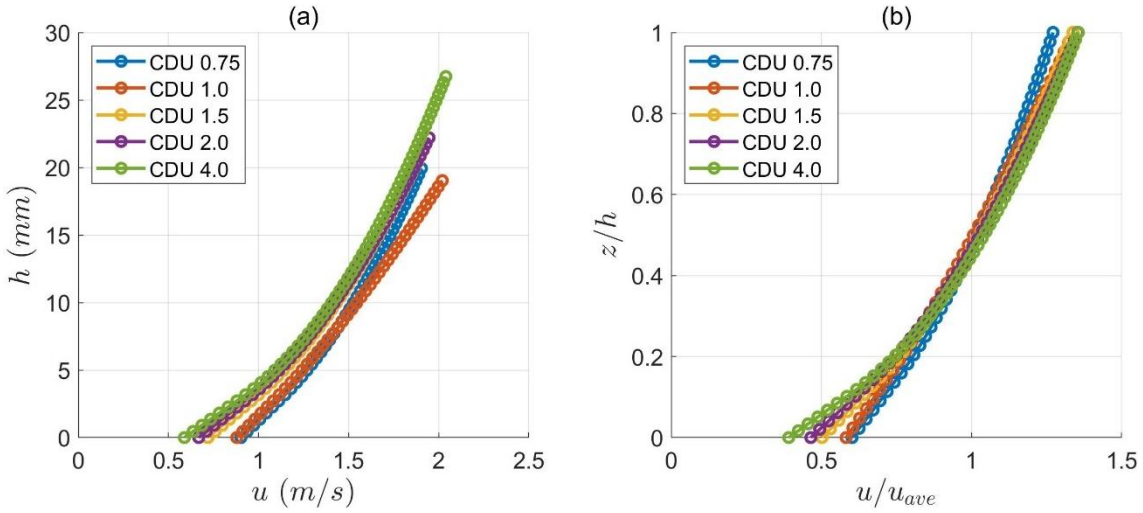

Figure 4-12: Velocity profiles averaged over 0.02s around the peak flow height for all CDU flows. (a) Velocity against flow height, and (b) Normalised velocity (by depth-averaged velocity) against normalised flow height.

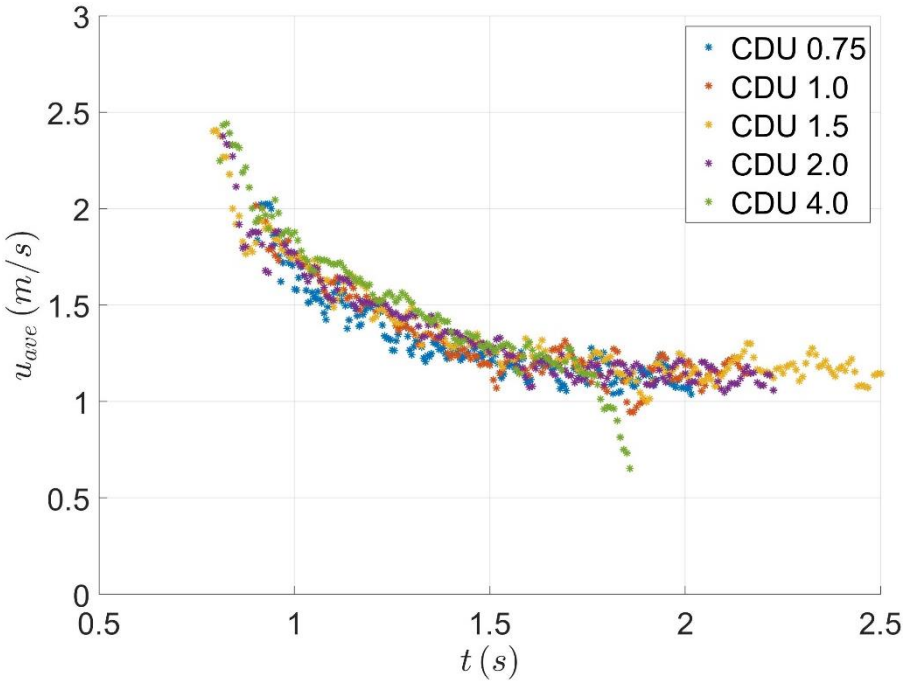

Figure 4-13: Time histories of depth-averaged velocities of CDU flows.

4.6. Dimensional Analysis

The determination of dimensionless numbers to describe flow regimes is discussed in Sec. 3.5. Local results of dimensional analyses showing the dominant momentum transfer mechanism based on the fitted velocity fields are given in Figure 4-14, where the structures of Savage number (N_{Sav}), Bagnold number (N_{Bag}) and friction number (N_{fric}) along the normalised flow height are depicted in subplots (a), (b) and (c), respectively. For each CDU flow, the data curve at the peak flow height is chosen to represent the dynamics of the flow front. As described in Sec. 2.3, the threshold value yields 0.1 N_{Sav}, 200 for N_{Bag} and 100 for N_{fric}; local values of N_{Bag} and N_{fric} are much beyond their thresholds, hence threshold values for all three numbers are not presented in Figure 4-14. Air, as the fluid in dry flow conditions, cannot produce strong viscous shear on the big and heavy ceramic beads utilised in CDU tests, hence N_{Bag} and N_{fric} are both of enormous magnitudes, reflecting that the effects of both solid inertia and solid friction highly surpass that of viscous fluid shear. Local values of N_{Sav} are also larger than the threshold, suggesting that solid inertial stress dominates the momentum exchange in all the CDU flows over the solid frictional stress. Additionally, the dry flow with the smallest volume (i.e. CDU 0.75) has a lower N_{Sav} and N_{Bag} than expected; this may be due to the imperfect choice of position as the flow is so dilute that a fully-accurate match of peak flow height is difficult to find.

Among the three numbers, the distribution of N_{Sav} along the flow height shows the most dramatic variation with source volume. When the source volume increases from 0.75L – 4L, N_{Sav} is greatly reduced, except in a small portion close to the bed, reshaping the profile from being larger in the upper portion and nearly consistent in the lower portion to larger at upper and lower boundaries and significantly smaller in the middle; this means that dry granular flows of small volumes experience stronger grain collisions near the flow surface and weaker near the bed, but with a larger volume the flow tends to be more frictional, especially the internal flow body (i.e. excluding the boundary layers at both flow surface and flume bed). N_{Bag} presents tilted curves smaller above the basal layer and larger at the basal layer; as source volume increases, the curves become more tilted and have larger differences between the value at the surface and that at the bed, indicating that a larger source volume stimulates the inertial movement of grains near the bed while the grains at the flow surface experience more viscous shear. N_{fric} shows that resistance to CDU flows is mostly provided by Coulomb solid friction rather than viscous fluid shear, which applies mainly to the flow surface and lowers the N_{fric} of the affected grains, and the solid friction becomes even stronger with an increased source volume.

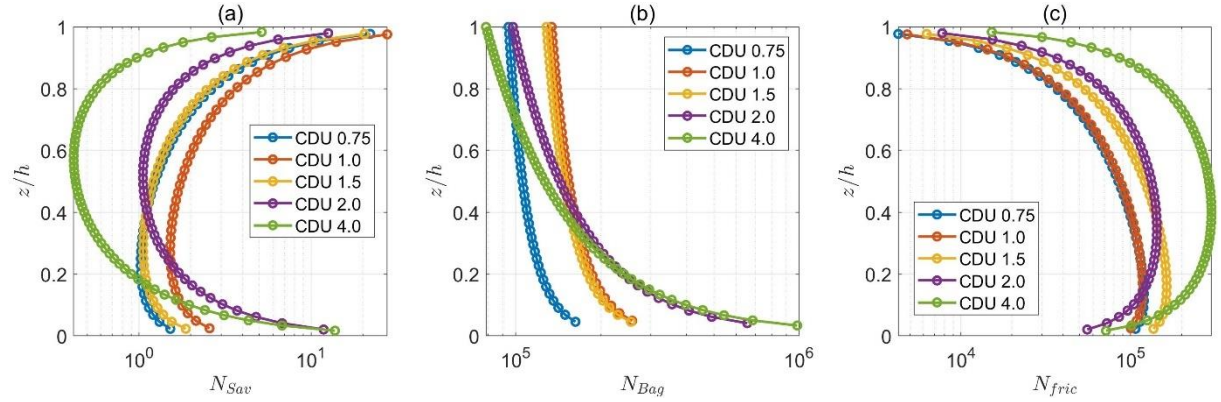

Figure 4-14: Local values of (a) Savage number, (b) Bagnold number and (c) friction number across the normalised height at the peak flow height for all CDU flows.

Straightforward correlations between the flow height normalised by grain size (h/δ) and the mean values of three dimensionless-number profiles ($\overline{N}_{Sav}$, $\overline{N}_{Bag}$ and $\overline{N}_{fric}$) are given in Figure 4-15, where hollow circles mark the data before the peak flow height and asterisks the data after. For each dimensionless number, data points of the mean value over the depth against the normalised flow height are regularly distributed within a limited and fixed range, demonstrating a direct dependency of momentum exchange in dry granular flows on the flow thickness. Note that some individual outliers come from the parts that are not strictly within the "main surge", e.g. green stars near h/δ = 6 in Figure 4-15 (a) and (c) correspond with the transitional part where

grains are about to pile up as a heap in CDU 4.0, and stars within h/δ = 2 - 4 in Figure 4-15 (b) are related to the dilute flow tail where dispersed grains bear higher air resistance. When the dry flow becomes thicker (due to the increase of source volume in the case of CDU tests), $\overline{N}_{Sav}$ decreases almost linearly, $\overline{N}_{Bag}$ remains roughly unchanged, and $\overline{N}_{fric}$ takes a close-to-linear growth; this means that solid friction is notably enhanced within the "main surge" of a thicker dry granular flow, while the relative relationship between solid inertia and viscous shear stays approximately the same.

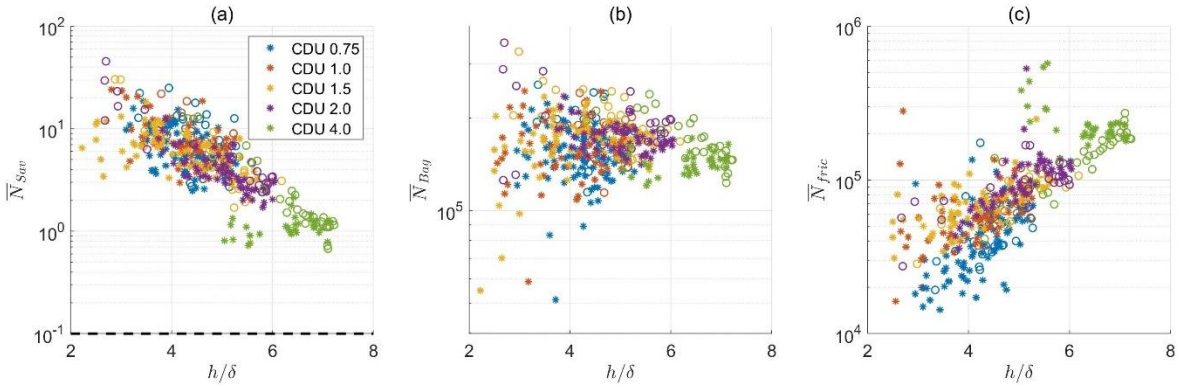

Figure 4-15: Mean values across the depth of (a) Savage number, (b) Bagnold number and (c) friction number against the normalised flow height by averaged grain size for all CDU flows, in which hollow circles denote the flow part before the maximum flow height while asterisks the part after.

5. Fluid-mixed Uniform Flows: Results

Preface

Fluid-mixed uniform flows include two types of test groups: the CSU (Ceramic beads, Saturated, Uniform) group with varying source volume and the CWU (Ceramic beads, Wet, Uniform) group with evolving water content; both groups use granular mixtures that are composed of uniform pseudo-spheres as the solid phase and water as the fluid phase. Details about the experimental setup, source material and test procedure of CSU and CWU small-scale flume tests can be found in Chapter 3.

This chapter presents the results of CSU and CWU tests and is structured as follows: Sec. 5.1 introduces the test conditions and measurements of different test groups; Sec. 5.2 records the macroscopic morphology of flow deposits and the analysis of bulk flow mobility; Sec. 5.3 demonstrates the longitudinal flow profiles and the comparisons of flow heights; Sec. 5.4 provides basal normal stress and basal pore pressure data (which is the highlight of these fluid-mixed tests) collected from all the tests; Sec. 5.5 gives velocity information of fluid-mixed granular flows, including velocity profiles and time history of depth-averaged velocities; finally, Sec. 5.6 shows the Savage number, Bagnold number and friction number estimation, including their local values and mean values across the flow height, to analyse the evolution of momentum exchange within both unsaturated and saturated granular flows.

5.1. Test Information

The test variable for the CSU group is source volume (or bulk volume of solid grains, excluding the fluid phase) whereas for the CWU group, it is gravimetric water content; correspondingly, the water content in CSU flows (0.45) and source volume in CWU tests (2 litres) are constant. Values of the variable are shown in the test labels, e.g. "CSU 2.0" means the tested flow is the saturated flow with 2L source volume and "CWU 0.10" represents a wet flow with 0.1 water content; noting that "Wet" in the CWU label flow indicates that the flow can be unsaturated or saturated. The designed water content of 0.45 for the CSU group can assuredly drive most flow material to the horizontal runout channel, even for the flow with the smallest source volume; this aims to meet the expectation that saturated granular flows should give relatively high bulk flow mobility. Additionally, another test group named "2CWU" can be regarded as a supplement to or a special member of the CWU group: 2CWU tests use varying water content as CWU flows do, but were carried out with a slightly more vibrated flume (i.e. the frame of grooved bars are not tightly fixed to the ground and nor to the inclined channel, hence the flume can vibrate when impacted by the dropped solids), which is a condition closer to that in CSU tests than in CWU tests (i.e. the entire setup was firmly fixed in CWU tests); the CWU group is the focus here when analysing the role of water content as it covers a wider range of moisture than the 2CWU group does, while 2CWU group is mainly utilised as a control group to support CWU results and to show the effect of the flume vibration.

Table 4-1, Table 5-2 and Table 5-3 provide test information for the CSU, CWU and 2CWU groups respectively; data sources are listed in all three tables. As the CWU group involves water content (w) ranging from 0.01 to 0.45 while the solid material is saturated at only about w = 0.256 (see Sec. 3.1.4), the unsaturated CWU tests with w = 0.01 – 0.25 are allocated to Table 5-2 (a) while the saturated tests with w = 0.30 – 0.45 are allocated to Table 5-2 (b). Most parameters in these tables are also presented in Table 4-1 (i.e. the test information of dry uniform flow tests) and their details can be found in Sec. 4.1; parameters exclusively for fluid-mixed flows are explained as follows: (i) water content is measured by weight; (ii) bulk density here is the density of the granular medium full of pore fluid inside, i.e. for oversaturated samples with water superfluous to fill out the pores, the water layer over the top surface of grains is not included in the bulk density calculation; (iii) the "inclined length" value 1460 mm in Table 5-2 (a) means that grains on the slope can extend from the flume outlet to the upstream end.

Test		CSU 0.75	CSU 1.0	CSU 1.5	CSU 2.0	CSU 4.0
Source measurements	Bulk dry volume (L)	0.75	1	1.5	2	4
	Solid mass (g)	1120.51	1564.92	2242.1	2904.82	5781.83
	Fluid mass (g)	504.31	704.44	1009.01	1307.43	2601.98
	Water content	0.45				
	Void ratio	0.598	0.579	0.585	0.566	0.582
	Porosity	0.374	0.367	0.369	0.361	0.368
	Volume in the hopper (cm^3)	799.11	1082.88	1581.11	2033.37	4087.28
	Bulk density (g/cm^3)	1.775	1.799	1.784	1.79	1.782
Deposit measurements	Runout (mm)	530	690	1105	1360	2309
	Inclined length (mm)	110	80	160	125	100
Morphological analysis	Travel angle (°)	26.9	24.9	22	20.9	18.2

Table 5-1: Test information of CSU tests with varying source volumes.

(a)

Test		CWU 0.01	CWU 0.10	CWU 0.15	CWU 0.25
Source measurements	Bulk dry volume (L)	2			
	Solid mass (g)	2909.54	2875.7	2854.97	2920.69
	Fluid mass (g)	29.6	287.62	428.62	730.18
	Water content	0.01	0.1	0.15	0.25
	Void ratio	0.564	0.571	0.575	0.562
	Porosity	0.361	0.363	0.365	0.36
	Volume in the hopper (cm^3)	2030.7	2015.6	2006.35	2035.67
	Bulk density (g/cm^3)	1.447	1.569	1.637	1.793
Deposit measurements	Runout (mm)	610	390	410	500
	Inclined length (mm)	95	1460	1460	1080
Morphological analysis	Travel angle (°)	28.4	31.3	31.4	29.9

(b)

Test		CWU 0.30	CWU 0.35	CWU 0.40	CWU 0.45
Source measurements	Bulk dry volume (L)	2			
	Solid mass (g)	2910.52	2910.94	2914.22	2920.17
	Fluid mass (g)	873.35	1019.05	1165.88	1314.81
	Water content	0.3	0.35	0.4	0.45
	Void ratio	0.564	0.576	0.563	0.5
	Porosity	0.361	0.366	0.36	0.363
	Volume in the hopper (cm^3)	2031.14	2047.43	2032.79	2046.28
	Bulk density (g/cm^3)	1.792	1.786	1.793	1.789
Deposit	Runout (mm)	505	880	1265	1804

measurements	**Inclined length (mm)**	610	196	140	110
Morphological analysis	**Travel angle (°)**	29	24.1	20.7	17.6

Table 5-2: Test information of (a) unsaturated and (b) saturated CWU tests with varying water content.

Test		**2CWU 0.35**	**2CWU 0.37**	**2CWU 0.39**	**2CWU 0.41**	**2CWU 0.43**
Source measurements	**Bulk dry volume (L)**			2		
	Solid mass (g)	2906.48	2889.57	2905.91	2901.45	2897.24
	Fluid mass (g)	1017.34	1069.33	1133.34	1189.55	1246.1
	Water content	0.35	0.37	0.39	0.41	0.43
	Void ratio	0.577	0.576	0.577	0.569	0.575
	Porosity	0.366	0.365	0.366	0.363	0.365
	Volume in the hopper (cm^3)	2045.44	2031.6	2044.34	2031.57	2036.04
	Bulk density (g/cm^3)	1.786	1.787	1.786	1.79	1.787
Deposit measurements	**Runout (mm)**	665	810	945	1060	1145
	Inclined length (mm)	260	210	200	130	135
Morphological analysis	**Travel angle (°)**	26.3	24.8	23.6	22.7	22

Table 5-3: Test information of 2CWU tests with varying water content.

5.2. Deposit Analysis

Depending on the water content, three different deposition forms were observed in the fluid-mixed flow tests as shown in Figure 5-1. In the case where w = 0.01 and grains are only slightly wetted (Figure 5-1 (a)), the deposit exhibits a shape similar to that of dry granular flows (as in Figure 4-1), with a few grains left on the flume bed; when moisture increases (to w = 0.1 for instance, as in Figure 5-1 (b)) but the sample is still unsaturated, a large portion of grains are stuck on the flume bed and are unable to run into the horizontal channel, leaving a deposit covering a very short distance in the runout channel but stretching far away towards the upslope direction; when the moisture gradually saturates the flow material, most grains start to be able to flow out from the inclined flume, forming a granular heap in the runout channel (Figure 5-1 (c)); if the water content is sufficiently high (e.g. w = 0.35 as in Figure 5-1 (d)), a forward heap where the majority of grains tend to accumulate near the distal end of the deposit can be formed and can be pushed away from the flume.

The deposition process of the wet flow in Figure 5-1 (d) is exhibited in Figure 5-2. The flow head decelerates when running into the horizontal runout channel (Figure 5-2 (a)) and then stops while the following flow body is still moving at a relatively high speed (Figure 5-2 (b)); these following grains do not stop but climb up the deposit when hitting the static granular front, as they cannot push the settled grains to the flanks in the confined runout channel. After the climbing grains consolidate on the granular heap, water initially entrained within the grains in the flow body flows out from the pores and flows back from the deposit (Figure 5-2 (c)), levelling out behind the stationary granular heap (Figure 5-2 (d)) before slowly permeating forward through the heap eventually. This indicates that, at a relatively high water content (e.g. w = 0.35), pore fluid can provide an "extra push" to the grains in the main flow body so that those solid particles can overcome the intergranular friction within the static granular heap. On the other hand, the deposit shapes in Figure 5-1 (b) and (c) suggest that this "extra push" does not occur in flows with lower water content, meaning that the reduction of frictional resistance requires a certain amount of water and cannot be achieved in highly unsaturated conditions. Thus, the morphology and deposition mechanism of wet granular flows are directly dependent on water content or saturation degree.

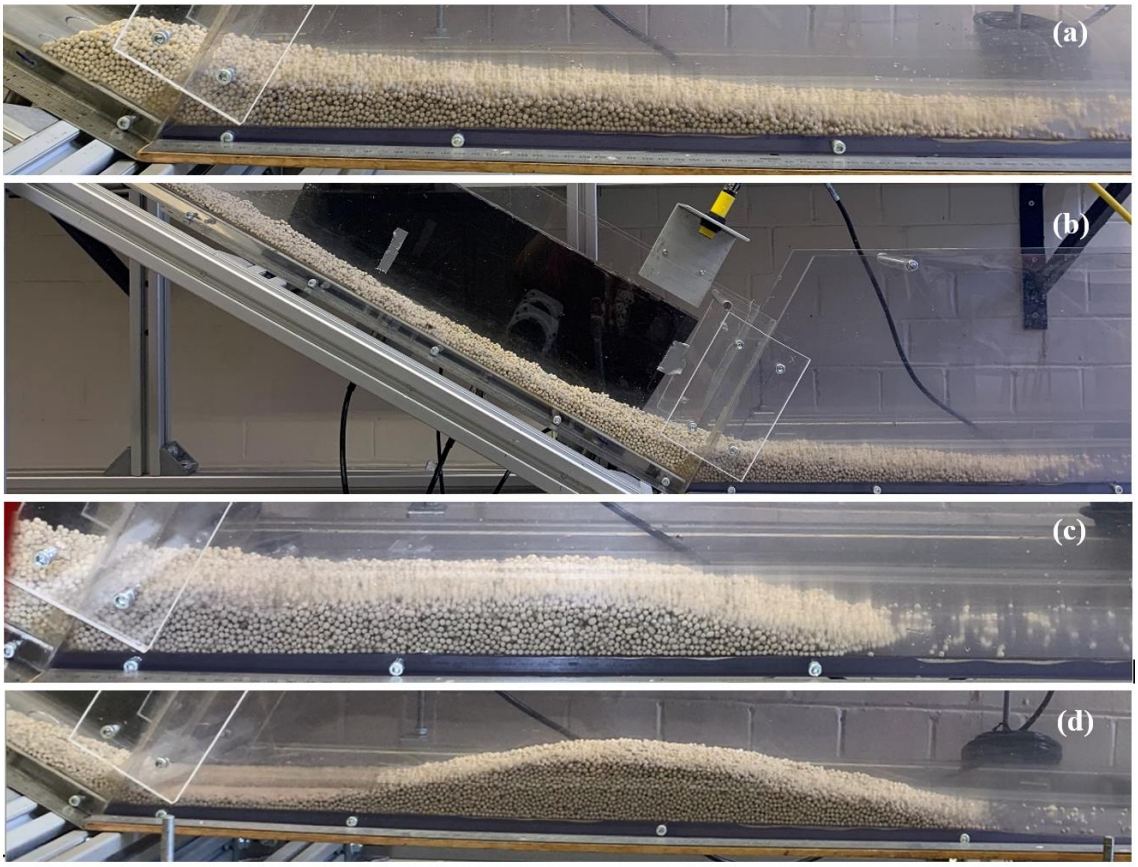

Figure 5-1: Deposits of wet granular flows with different water content where (a) w = 0.01, (b) w = 0.1, (c) w = 0.3 and (d) w = 0.35.

Figure 5-2: Deposition process of the w = 0.35 wet flow. (a) The flow head enters the runout channel; (b) the flow head stops while the following flow body climbs up the static front; (c) grains in the flow body come to rest on the heap and water flows back from the heap; (d) water levels out behind the heap.

Deposit morphologies of CSU, CWU and 2CWU flows are summarised in Figure 5-3, Figure 5-4, and Figure 5-5, respectively; the horizontal scale in each figure is five times compared with the vertical scale. Each deposit's Centre of Gravity (COG) is denoted by a filled circle sharing the same colour as that of the deposit outline, which is drawn in solid lines except for "CWU 0.00" in Figure 5-4 (a) and "2CWU 0.45" in Figure 5-5; deposit side-view shapes of these two specific flows are depicted using dotted lines to show that they are borrowed from other test groups: "CWU 0.00" is a 2L dry granular flow test (as can be deduced by its label) and "2CWU 0.45" is identical to "CSU 2.0" but labelled differently.

All the tests within their own group present highly credible evolution in both runout distance and the position of COG. With an increased source volume (Figure 5-3), the forward granular heap accumulates thicker and moves farther in the runout channel. For unsaturated CWU tests with low water content, Figure 5-4 (a) provides a detailed description of the morphological evolution. At first, "CWU 0.01" containing only 1% moisture by weight gives a deposit shape as well as COG position that are remarkably similar to those of "CWU 0.00" dry flow, although the deposit of "CWU 0.01" looks smaller due to the loss of a small portion of grains resting on the flume

bed; the COG of "CWU 0.10" deposit locates fairly high on the slope, indicating that for a water content somewhere between 1% and 10%, the pore fluid with starts to stick the majority of grains on the slope rather than drive them into the runout channel; then when the water content increases from 0.1 to 0.25, the deposit length does not vary much but the COG position consistently shifts closer to the flume end, implying that more material tends to reach the runout channel instead of remaining on the slope. On the other hand, wet granular flows in the saturated condition (i.e. CWU tests in Figure 5-4 (b) and 2CWU tests in Figure 5-5) give a clear trend that the deposit length and COG distance both grow with water content.

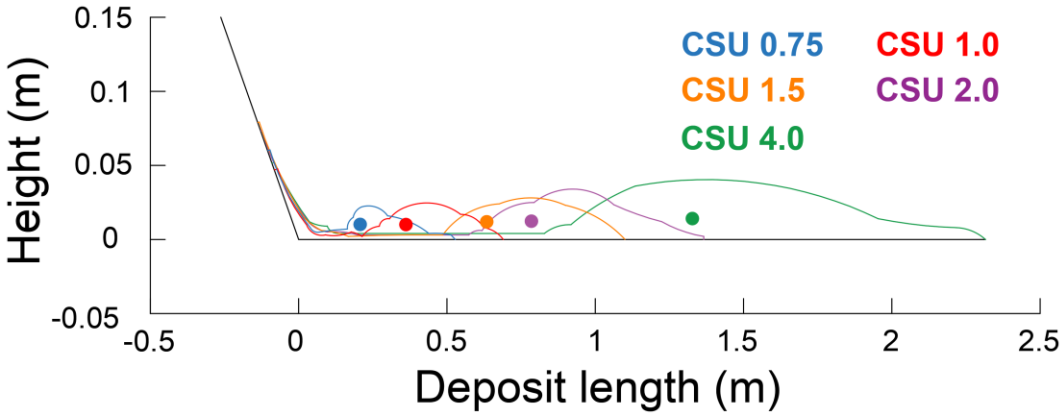

Figure 5-3: Deposit side-view outlines of CSU flows. The horizontal scale is 5 times the vertical scale. Filled dots represent the locations of the centre of gravity (COG).

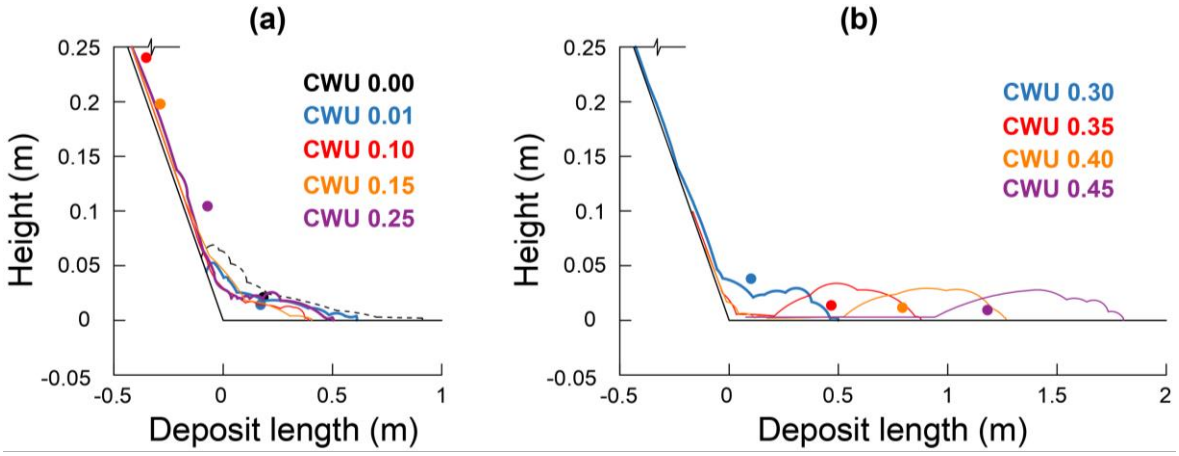

Figure 5-4: Deposit side-view outlines of (a) unsaturated and (b) saturated CWU flows. The horizontal scale is 5 times the vertical scale. Filled dots represent the locations of COG.

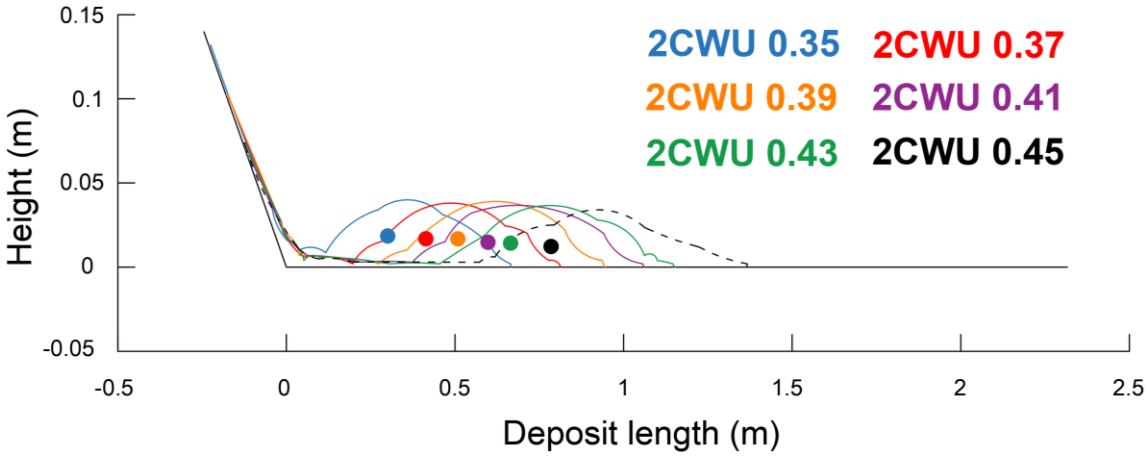

Figure 5-5: Deposit side-view outlines of 2CWU flows. The horizontal scale is 5 times the vertical scale. Filled dots represent the locations of COG.

Analyses of travel distance (L) and travel angle (α_T) give evident bulk flow mobility results of different tests. Travel distance consistently increases and travel angle decreases with the source volume of CSU flows (Figure 5-6), suggesting that saturated granular flows in larger volumes possess higher bulk flow mobility, although the rate of bulk mobility increase seems to slightly reduce with source volume. Echoing the observation in Figure 5-4 and Figure 5-5, the CWU flows produce bulk flow mobility lower than that of dry flows (w = 0) in a low range of moisture but higher when the water content is relatively high: the travel distance of wet granular flows exceeds that of a dry flow between w = 0.35 – 0.40 (approximately 0.37 as shown in (Figure 5-7 (a)) while travel angle is lower than that of a dry flow until the water content increases to about 0.32 (Figure 5-7 (b)). For convenience, here a parameter termed "boundary water content", w_b, is defined as the water content at which the wet flow gives the same bulk mobility as the dry flow in an identical source volume. As the runout behaviour includes both the transport of flow material as a whole (which is represented mainly by travel angle) and the spreading of particles (which is reflected by travel distance), this boundary water content describing the macroscopic depositional results can be different when the bulk flow mobility is quantified by different factors, hence the boundary water content for travel distance is denoted by $w_{b,L}$ and for travel angle is by $w_{b,\alpha}$. With an increasing water content below the w_b value, both L and α_T drop initially until meeting their respective minimum, and then gradually grow at a relatively low rate before water content reaches another threshold value (for the 2L CWU flows this value is roughly w = 0.3) after which those two factors increase almost linearly at a higher rate with the water content; this close-to-linear growth continues even after w exceeds w_b for both factors. $w_{b,L}$ is larger than $w_{b,\alpha}$, but the values for both of them are greater than the saturating water content for ceramic beads which is w = 0.256. Travel distance and travel angle profiles of 2CWU tests

against water content in Figure 5-7 show similar approximate linearities to CWU test data; however, due to the stronger flume vibration, 2CWU flows demonstrate slightly lower bulk mobility (i.e. smaller L and larger α_T) than CWU flows do within the same range of water content.

The influence of water content on bulk flow mobility is also found to be affected by source volume. Travel distance results of wet granular flows with various source volumes and water content are summarised in Figure 5-8, in which the y-axis is a new parameter "travel distance ratio" (r_L) defined by the ratio of the travel distance (L) of a wet flow to that of a dry flow in the identical volume (i.e. the block dashed line in Figure 5-8 at $r_L = 1$ means that the wet flow and dry flow can propagate the same distance in the runout channel). Note that this travel distance ratio describes observational results on bulk flow mobility which is a combination of many effects, hence its relationship with water content and source volume does not necessarily point to a specific physical process. Data plotted in Figure 5-8 are collected from the 2CWU test group and preliminary tests, where the flume condition is close to that in 2CWU tests and where the travel angles are unavailable. As the water content used in those experiments are relatively high, the travel distances due to the same source volume are assumed to form a close-to-linear relationship with water content (as observed in Figure 5-7 (a)) and are approximated by a straight line; thus, r_L produced by wet flows in four different source volumes (1, 1.5, 2 and 4 litres) are presented as four straight lines in Figure 5-8. These four lines possess very similar gradients while their intercepts and similarly their boundary water content $w_{b,L}$ (which in Figure 5-8 is the w value where the inclined data line intersects with the horizontal dashed line) increase with the source volume. Within the range of high water content where the linear approximation is valid, the travel distance ratio of wet granular flows can be regarded as growing linearly with the water content, and the increasing rate does not notably vary with source volume, but the boundary water content significantly decreases with source volume. This means that, with a larger source volume, the bulk flow mobility of wet flows can exceed that of dry flows at a lower water content, i.e. wet flows in larger volumes produce higher bulk flow mobility; another inference is that, since the boundary water content cannot be negative, the bulk flow mobility of wet granular flows may no longer become lower than that of dry flows when the source volume is sufficiently large, i.e. the reduction effect of low water content on bulk flow mobility is weakened and can eventually be eliminated by an increased source volume.

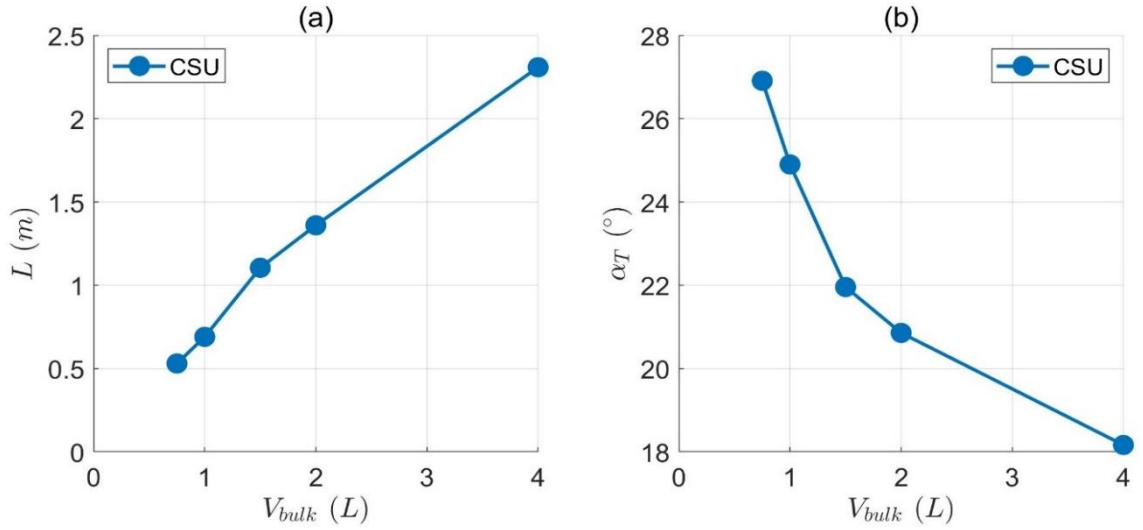

Figure 5-6: Evolution of (a) travel distance (L) and (b) travel angle (α_T) of CSU flows with source volume (V_{bulk}).

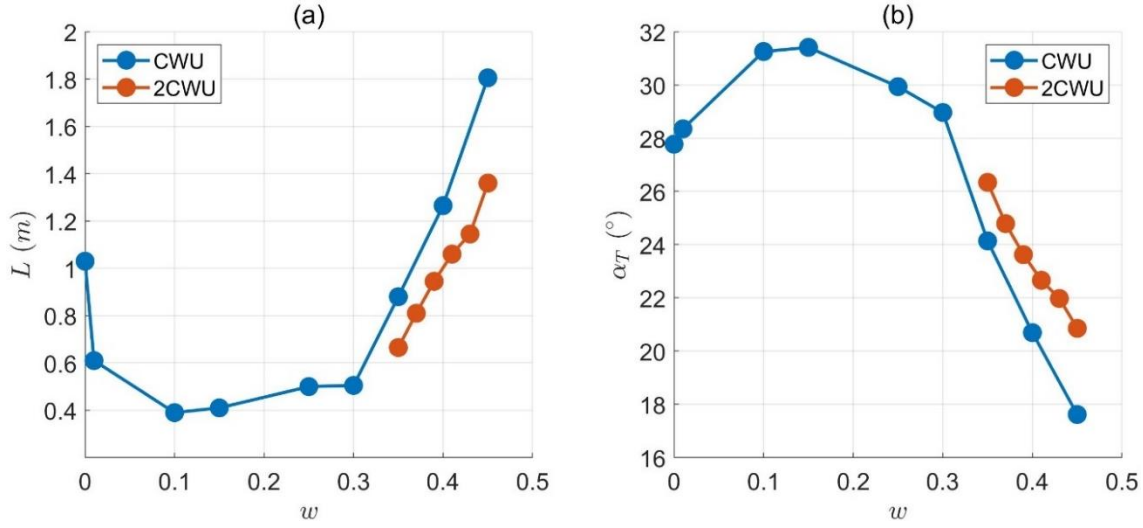

Figure 5-7: Evolution of (a) travel distance (L) and (b) travel angle (α_T) of CWU and 2CWU flows with water content (w).

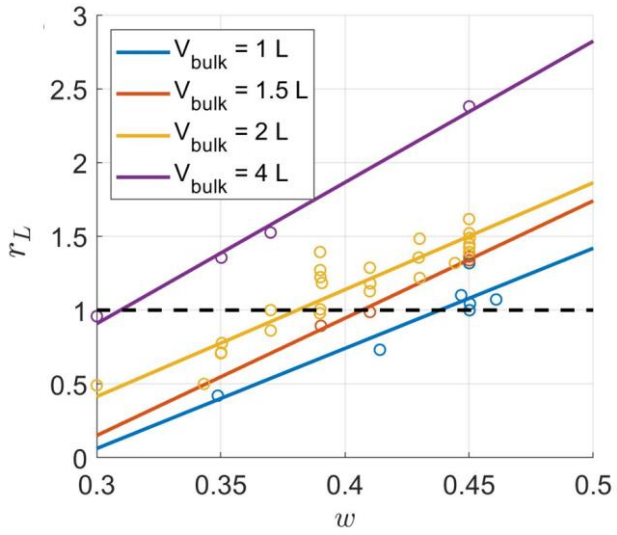

Figure 5-8: Evolution of travel distance ratio (r_L) with water content (w) for wet granular flows in different volumes.

5.3. Flow Profile

Camera-recorded flow profiles of CSU, CWU and 2CWU tests at the downslope sensor-installed zone are shown in Figure 5-9, Figure 5-10 and Figure 5-11, respectively; each row represents a tested flow with a different test variable (i.e. source volume for CSU tests and water content for CWU and 2CWU tests) while the three columns give the leading edge, the main flow body and the flow tail from the right-hand side to the left-hand side (as the flow is moving from left to right in the camera view). The selection of photographs for the leading edge and main body of the fluid-mixed flows follows the same criteria as described in Sec. 4.3 but that for the flow tail is different. As the flow tail part in fluid-mixed flows commonly becomes increasingly thin and slow when approaching the very end of the flow, the position of the flow tail chosen for the comparison should be considered to ensure meaningful differences can be observed; the part immediately after the main surge (see Sec. 3.3) is selected for the images in the first column of the figures below when the flow material can move out from the camera view, whereas when grains eventually pile up in the image, the final static heap is captured to contrast the grain accumulation results. Note that the CWU group comprises eight tests as listed in Table 5-2 but only shows six flows in Figure 5-10; this is because the high-speed images for "CWU 0.15" and "CWU 0.45" tests were excluded due to non-ideal video recording.

For saturated granular flows with increased source volumes as shown in Figure 5-9: (i) the leading edge tends to be less dispersed and more agminate, (ii) the main body becomes thicker and denser, producing a smoother top surface and fewer saltating grains, and (iii) the flow tail part remains similar. For wet flows with evolving water content, on the other hand, CWU tests in Figure 5-10 illustrate that: (i) the leading edge becomes less saltating but the variation extent is barely noticeable; (ii) only the flows with 0.01 and 0.1 water content exhibit notably thinner main flow bodies with saltating grains above the top surfaces, while other flows stay relatively similar; (iii) flow material does not pile up in the camera view when the flow is slightly wetted ($w = 0.01$) and when w is expected greater than the boundary water content $w_{b,\alpha}$ ($w = 0.35$ and 0.4), whereas when the water content ranges from 0.1 to 0.3, the granular heap in the flow tail part becomes steeper as more grains are pushed towards the flume outlet. Finally, 2CWU flows in Figure 5-11 are all relatively close; this may be because all the water content values adopted in this test group are above the corresponding $w_{b,\alpha}$ value which can be estimated from Figure 5-7 (b). Overall, the side-view flow profiles demonstrate that the leading edge and the main body parts of the flow are mainly affected by source volume while the flow tail is unaffected; the

influence of water content on the flow profile is very evident when the flow is unsaturated but seems much less so when saturated.

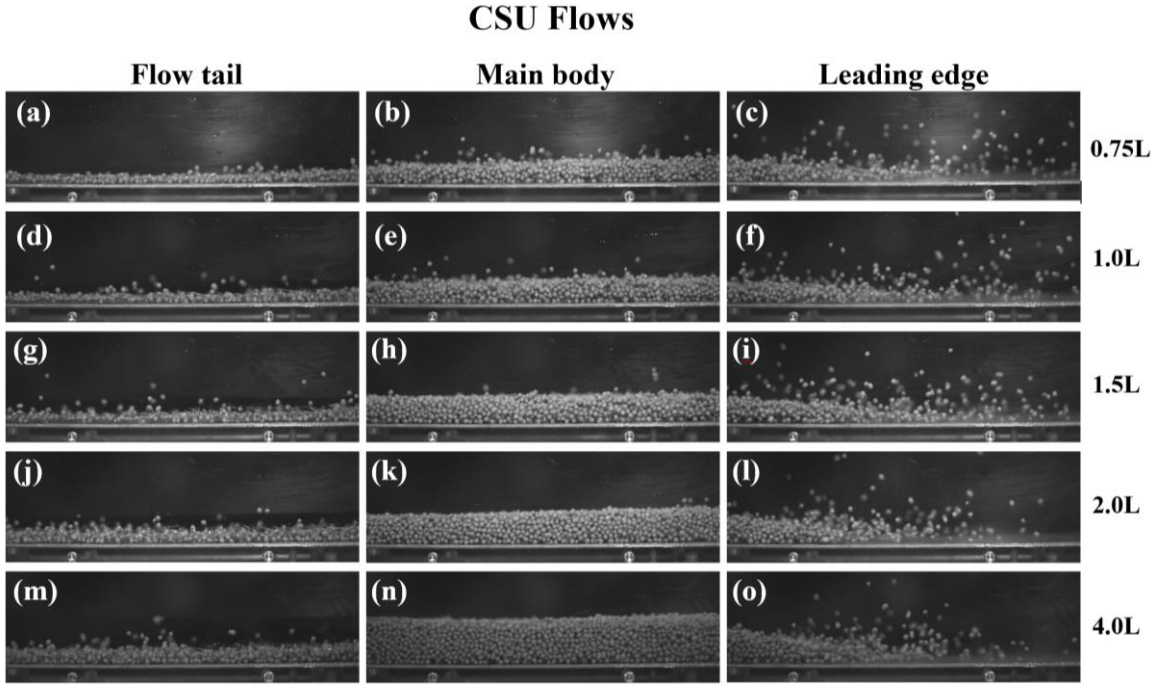

Figure 5-9: Recorded profiles of CSU flows where the camera view is tilted at 30° to make its bottom side parallel with the inclined flume bed. Three columns are the flow tail, main body and leading edge of each tested flow, while five rows are five tested flows with evolving source volumes that are exhibited in the test labels at the right-hand side margin.

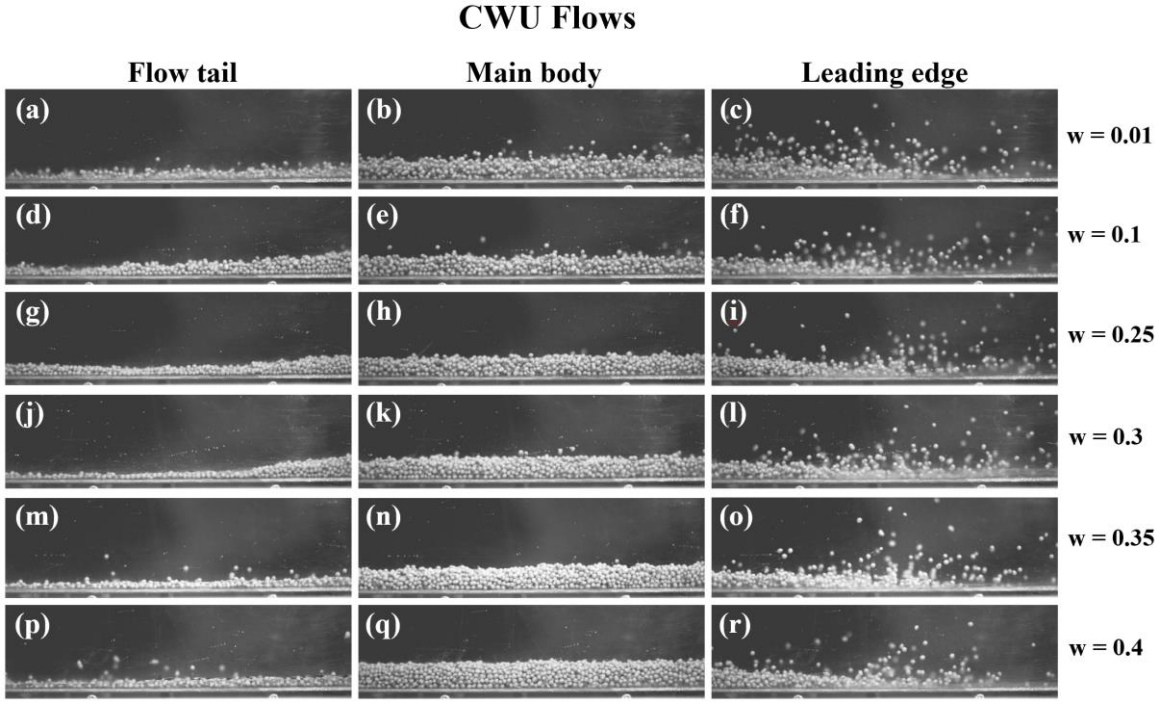

Figure 5-10: Recorded profiles of CWU flows where the camera view is tilted at 30° to make its bottom side parallel with the inclined flume bed. Three columns are the flow tail, main body and leading edge of each tested flow, while five rows are five tested flows with an evolving water content that are exhibited in the test labels at the right-hand side margin.

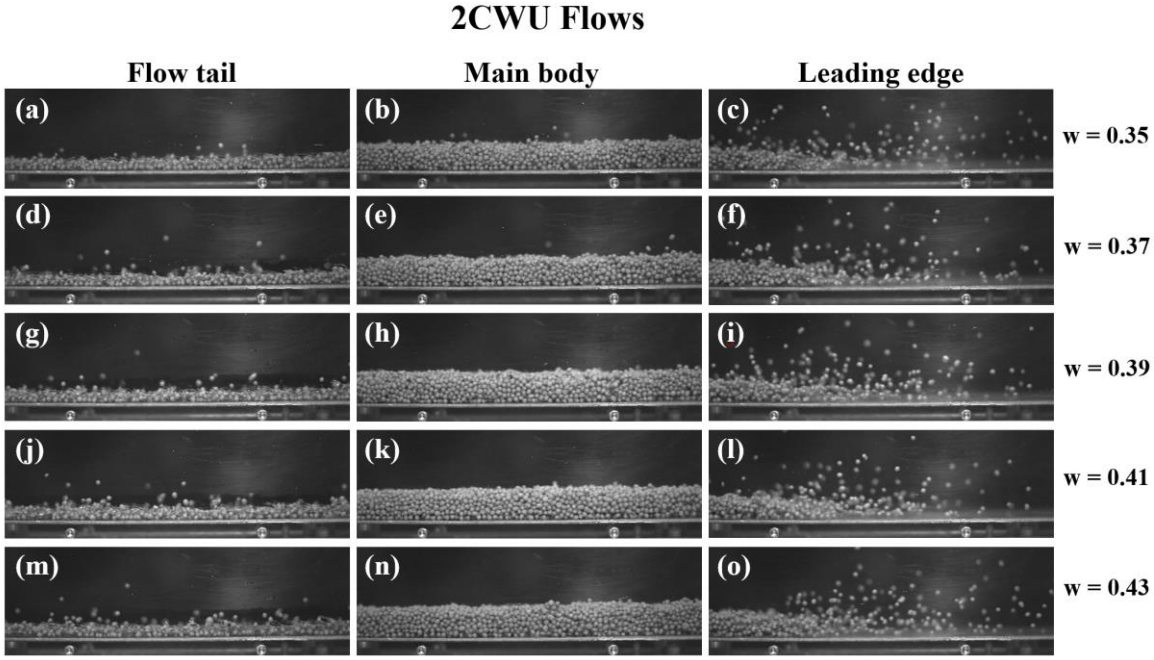

Figure 5-11: Recorded profiles of 2CWU flows where the camera view is tilted at 30° to make its bottom side parallel with the inclined flume bed. Three columns are the flow tail, main body and leading edge of each tested flow, while five rows are five tested flows with an evolving water content that are exhibited in the test labels at the right-hand side margin.

Considering that the transparent fluid cannot be observed in the high-speed images, two trials using dyed water with red food colouring and 2L ceramic beads were carried out to visualise the behaviours of the fluid phase in wet granular flows. Photos of the main flow bodies of coloured wet flows with 0.35 and 0.45 water content are given in Figure 5-12 (a) and (b); both water content values are larger than the saturation water content of a static sample (0.256). For the w = 0.35 wet flow, dyed water is barely visible at the sidewall boundary and can only be dimly observed at the gaps between particles; while for the w = 0.45 flow, the dyed water can clearly be seen from the flume sidewall and the solids are immersed in liquid. This indicates that pore fluid is held within the granular body of the w = 0.35 wet flow, but can spill from the pores when the water content increases to 0.45.

Flow height measurements using the ultrasonic sensor and PIV analysis show good agreement for fluid-mixed granular flows. The contrast between these two flow height measurements for CSU and CWU test groups is given in Figure 5-13 (a) and (b), where data from the ultrasonic sensor are denoted by blue asterisks and from the PIV by red curves. As shown in the plots, the accuracy of flow height measurement can decrease when the flow is unsaturated. In “CWU 0.01”, the ultrasonic sensor is affected by the collisional movement of grains around t = 2s and cannot

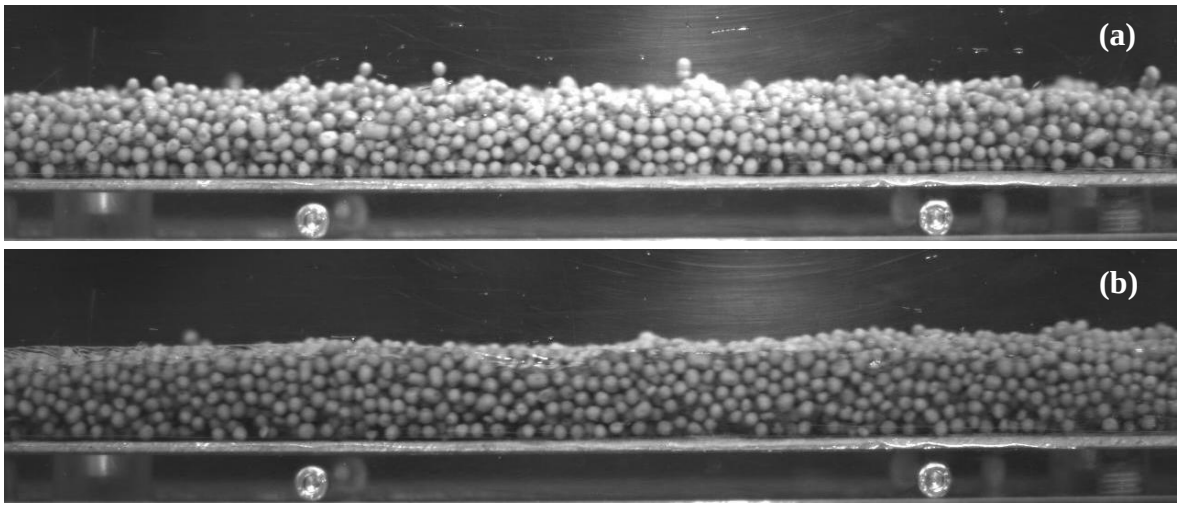

Figure 5-12: The main flow bodies of wet granular flows with (a) 0.35 water content and (b) 0.45 water content. Flow materials are composed of 2L ceramic beads and dyed water.

detect the flow thickness which can be seen in high-speed photos; this is similar to the case of dry flows (see Sec. 4.3 and Figure 4-5) but with smaller discrepancies between sensor response and PIV estimation; conversely, the PIV detection of flow surface may produce errors when grains start to pile up, as red curves tend to drop down at the end for CWU flows with 0.1, 0.25 and 0.3 water content; fortunately, those parts where grains accumulate on the slope are not important in the flow analyses. Nevertheless, employing PIV-detected flow height is reliable with both evolving source volume and water content.

PIV-based flow heights of CSU, CWU and 2CWU flows are respectively presented in Figure 5-14, Figure 5-15 and Figure 5-16, where the "main surge" part of each flow (see Sec. 3.3) is highlighted by solid lines and other parts are denoted by dashed lines; all the subplots (a) in the following three figures demonstrate the absolute flow heights (h) whereas subplots (b) present the flow heights normalised by the averaged grain size (h/δ). All the saturated flows in CSU tests and wet flows with high water content (w > 0.3) in CWU and 2CWU tests generate two separate peaks or waves in the "main surge" part; this differs from the surge shape of unsaturated wet flows (w < 0.3) and of dry flows (see Figure 5-16). The flow height of saturated flows significantly increases with source volume (Figure 5-14). With an increasing water content from unsaturated to saturated (Figure 5-15), the flow height of wet flows slightly increases, but more noticeably, the flow height profile changes from being more uniformly distributed along the time axis to gathering as a higher surge within a shorter time close to the start of the flow duration, suggesting that a higher water content allows the flow material to concentrate towards the

leading edge. For wet flows with higher water content (Figure 5-16), this tendency of concentration is less apparent but still observable.

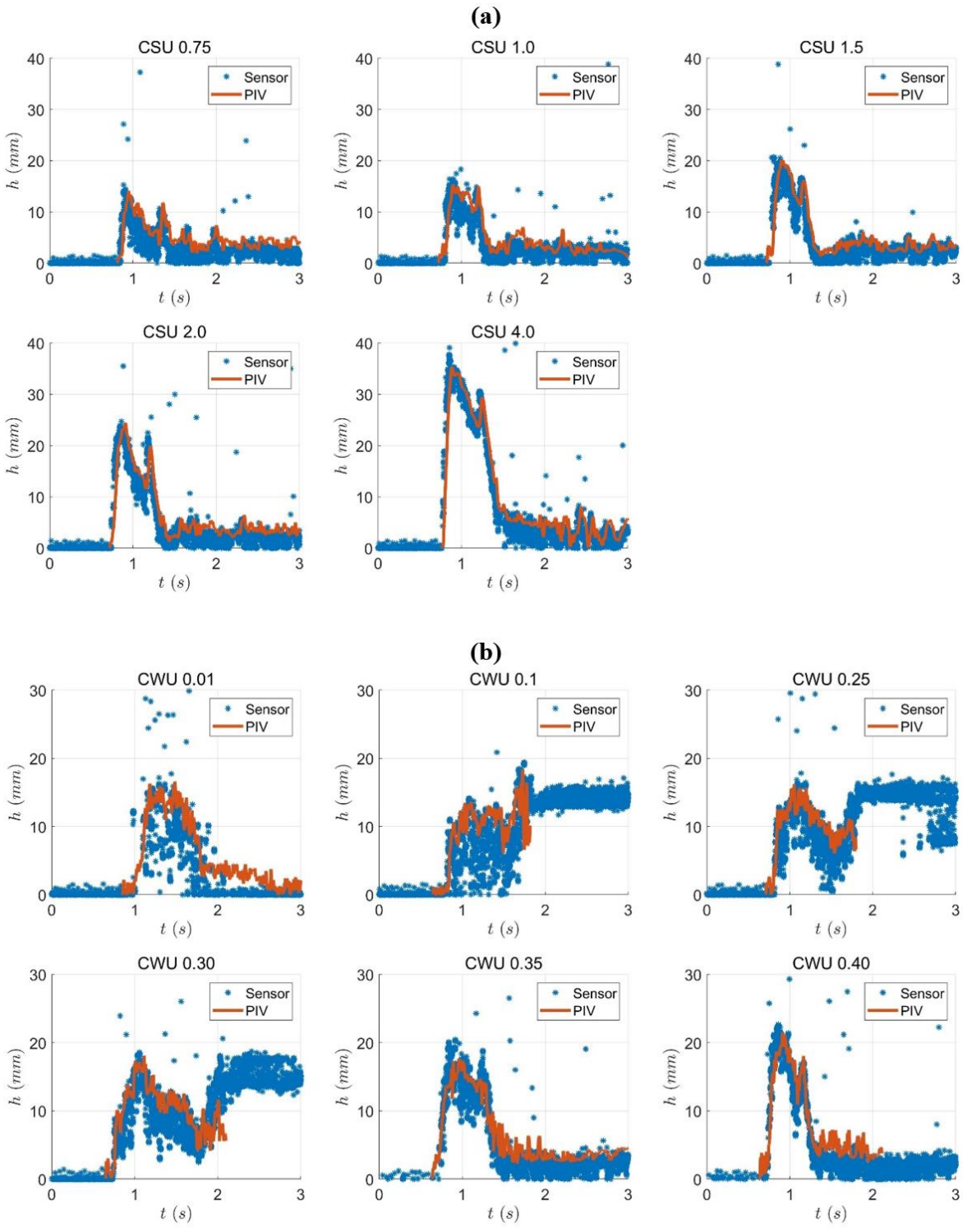

Figure 5-13: Contrasts between flow height of (a) CSU flows and (b) CWU flows measured by the ultrasonic sensor (in blue asterisks) and PIV analysis (in red lines).

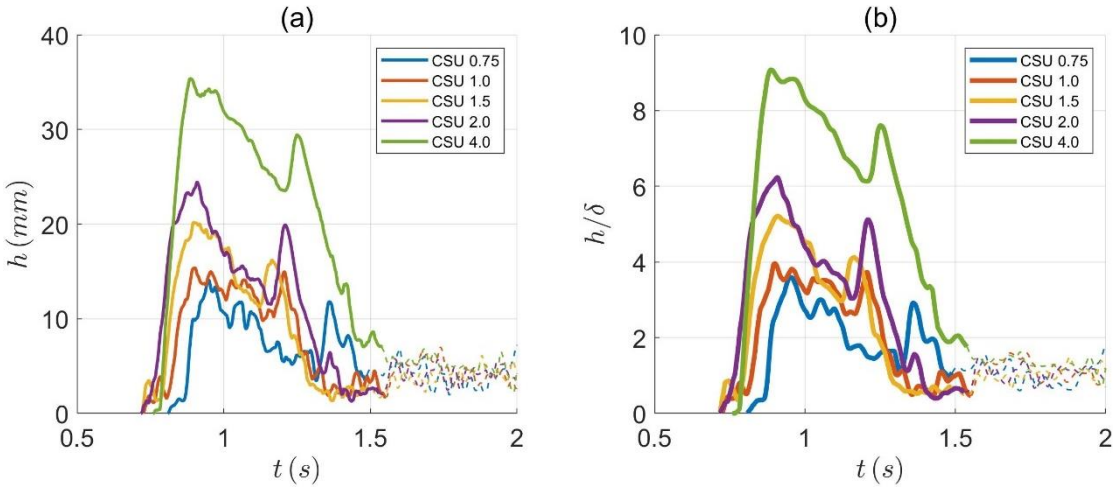

Figure 5-14: Time histories of (a) absolute CSU flow height and (b) normalised CSU flow height by averaged grain size, in which the "main surge" of the flow is highlighted by the solid line and other parts are in dashed lines.

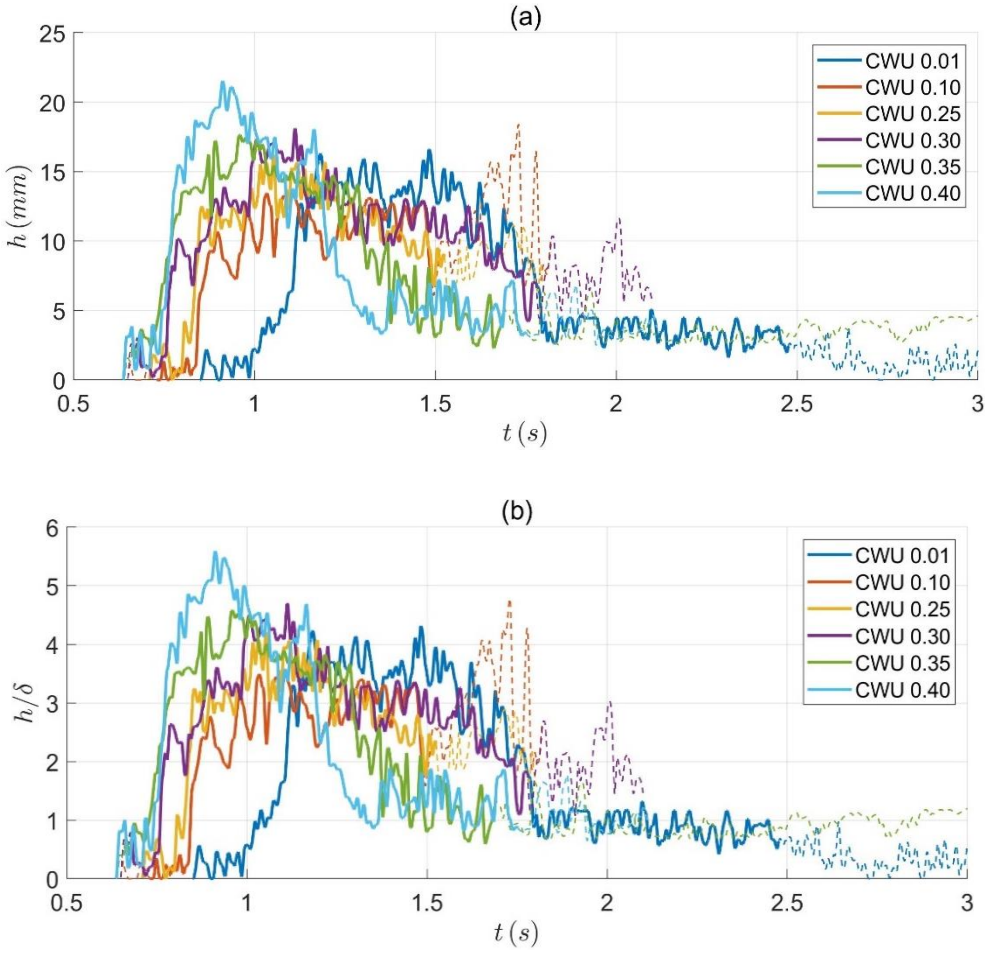

Figure 5-15: Time histories of (a) absolute CWU flow height and (b) normalised CWU flow height by averaged grain size, where the "main surge" of the flow is in solid lines and other parts in dashed lines.

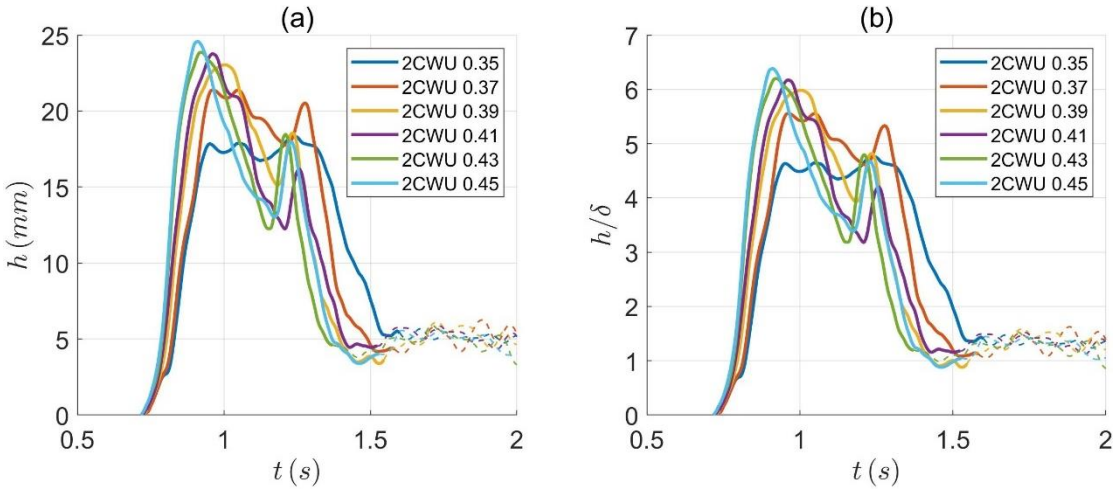

Figure 5-16: Time histories of (a) absolute 2CWU flow height and (b) normalised 2CWU flow height by averaged grain size, in which the "main surge" of the flow is in solid lines and other parts in dashed lines.

5.4. Basal Normal Stress and Pore Pressure

Basal normal stress (σ_{basal}) and basal pore pressure (p_{basal}) were collected from all the fluid-mixed flow experiments. In Figure 5-17Figure 4-8, the σ_{basal} and p_{basal} measured at the downslope sensor-installed position are contrasted with the estimated normal stress and pore pressure due to the weight of steady flow material and that of its fluid phase; the equation for steady-flow basal normal stress, σ_{st}, is given in Eq. (4-1), while the steady-flow basal pore pressure, p_{st}, is defined by:

$$p_{st} = \rho_w g h \cos\theta \qquad (5\text{-}1)$$

where ρ_w is the density of water taking the value of 997 kg/m^3 at 25℃, g is the gravitational acceleration, h is the flow height and θ is the slope angle of 30°; this calculation assumes a fully saturated flow surge, i.e. the depth of fluid equals the flow height (h). Similar to Figure 5-16, solid lines in Figure 5-17 represent the "main surge" part (on which the flow analysis focuses) of the flow whereas dashed lines represent the others; as σ_{st} and p_{st} are dependent on flow height (h) which is derived from PIV analysis, data curves before the start of PIV analysis for each test are not exhibited.

Several interesting results can be observed in Figure 5-17. First, p_{basal} gives both positive and negative values in fluid-mixed flows; more specifically, the length where negative p_{basal} values are distributed along the time axis decreases with both source volume and water content. Due to

the grain size segregation (see Sec. 2.1.3), the granular flow snout is known to be dry or unsaturated and hence a small portion of negative basal pore pressure is expected, as shown in the "CSU 4.0" subplot in Figure 5-17 (a); however, in small-volume tests like CSU 0.75 and unsaturated tests such as CSU flows from w = 0.01 to 0.25, the main surges of granular flows are mostly, if not entirely, controlled by negative p_{basal} rather than positive. Second, the negative p_{basal} becomes stronger from w = 0.01 to 0.1, and then when the water content further increases, the negative p_{basal} weakens and the positive p_{basal} grows larger in value and takes dominance in the distribution along the time axis (Figure 5-17 (b)); this is associated with the evolution of bulk flow mobility with water content (Figure 5-7), implying a direct connection between bulk mobility and pore pressure. Thirdly, p_{basal} rarely (except an instant of peak value in the "CSU 4.0" flow and a short part of the "CWU 0.40" flow rear close to its flow tail) surpasses p_{st}, indicating that excess pore pressure does not manifest in the fluid-mixed granular flows and does not contribute to their enhanced bulk flow mobility compared with dry flows. Lastly, although σ_{basal}, σ_{st} and p_{st} consistently increase with both source volume and water content, σ_{st} is quite close to σ_{basal} when the granular flow is unsaturated (w < 0.25) and then becomes lower than σ_{basal} when the water content exceeds 0.25; this means that low water content values give basal normal stress that is relatively similar to that of steady flows, while higher water content tends to increase the normal stress over and above that of the theoretical weight of flow material.

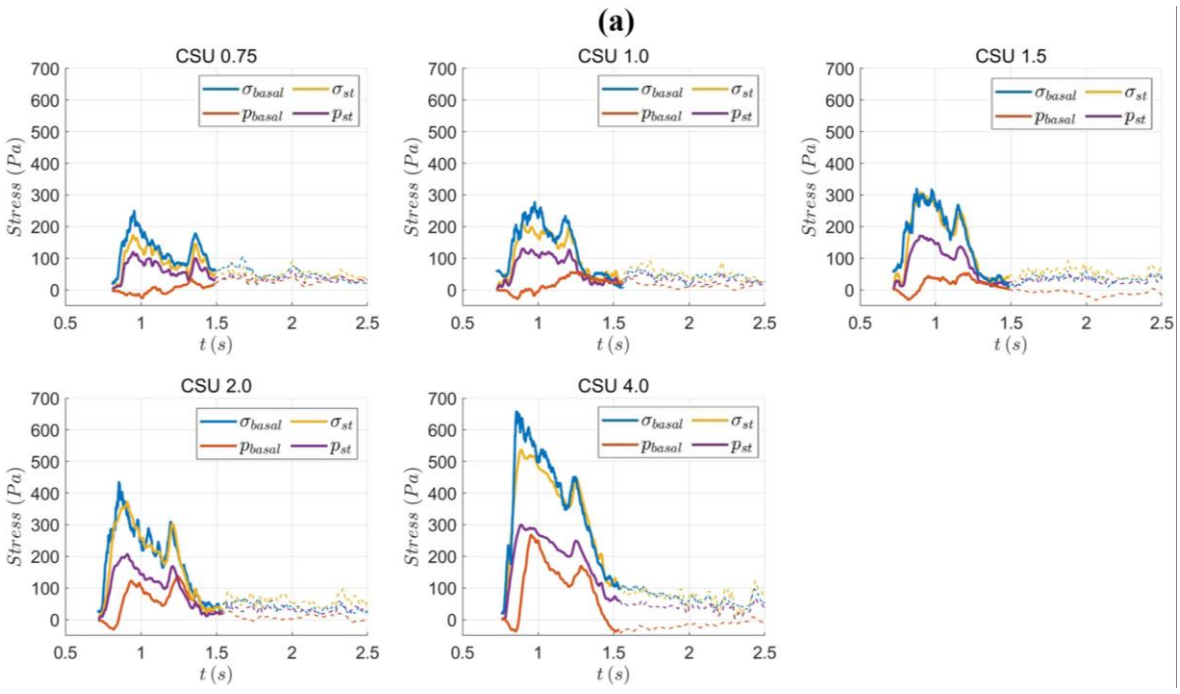

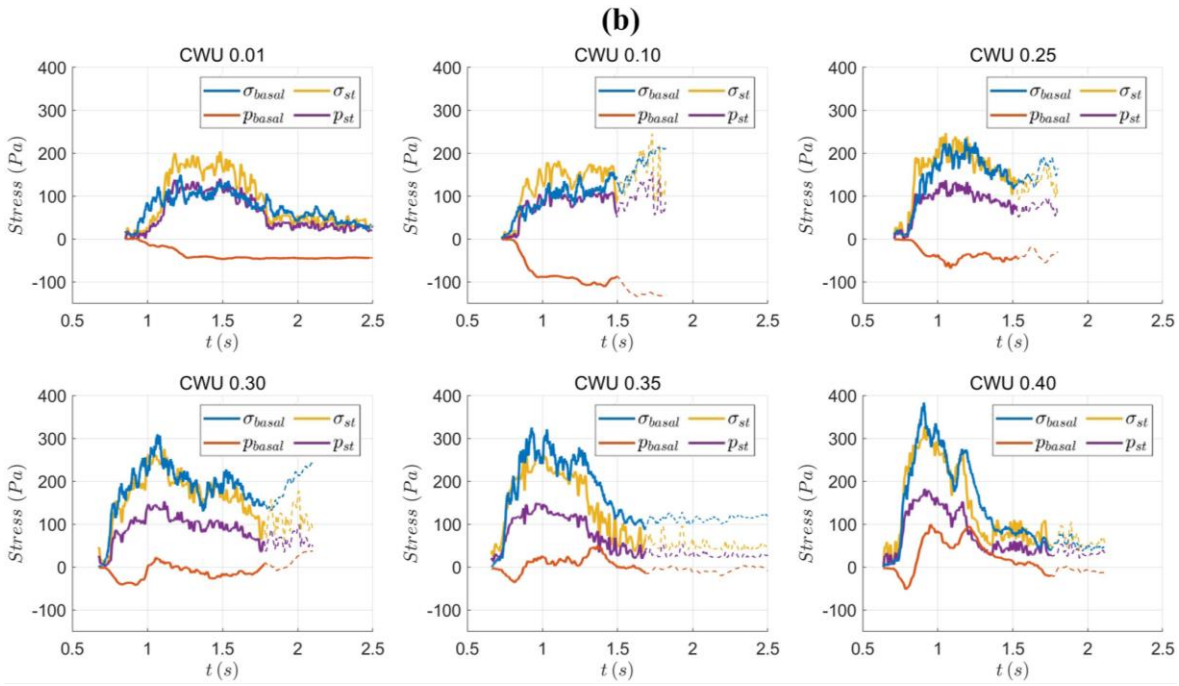

Figure 5-17: Contrasts between basal normal stress (σ_{basal}), basal pore pressure (p_{basal}), theoretical steady-flow basal normal stress (σ_{st}) and theoretical steady-flow basal pore pressure (p_{st}) at the downslope position. Data from (a) CSU flows and (b) CWU flows are shown.

The comparison of normal stress histories of CSU, CWU and 2CWU flows are given in Figure 5-18, Figure 5-19 and Figure 5-20, where subplots (a) and (b) respectively illustrate the σ_{basal} measured by the upslope and downslope load cell. Overall, the load-cell signals echo the flow height results in Sec. 4.3: σ_{basal} increases with both source volume and water content while its distribution along the time axis tends to show a trend of concentrating towards the front when water content rises. An interesting finding is that the upslope σ_{basal} seems larger than the downslope value when the water content is low (e.g. w = 0.01 and 0.1 in Figure 5-19), but with higher water content ($w \geq 0.3$ from CWU tests), the downslope σ_{basal} values in all three figures (w = 0.45 for CSU flows) are higher or at least are comparable to the upslope ones. As suggested by Figure 5-17 (b), this may be related to the phenomenon that high water content results in an apparently greater flow material density than its theoretical density (i.e. resulting in a higher measured total normal stress than is estimated from constant-density statics).

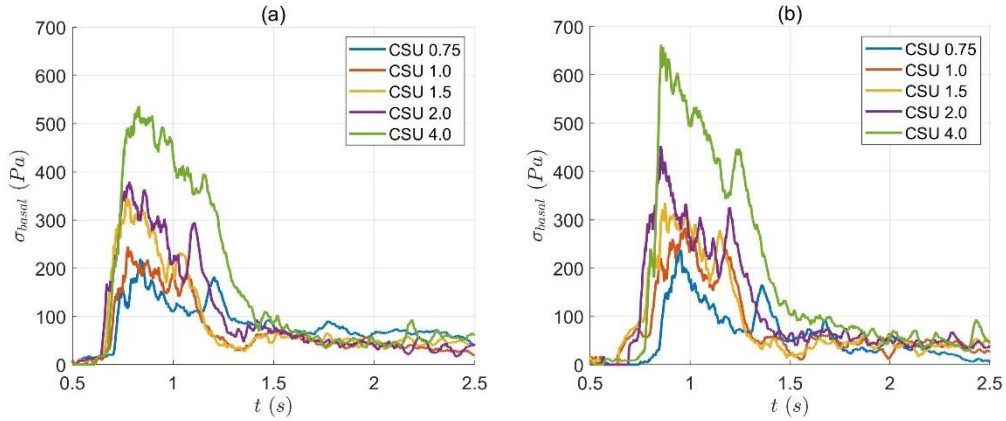

Figure 5-18: Contrasts of basal normal stresses (σ_{basal}) for CSU flows at (a) the upslope position and (b) the downslope position.

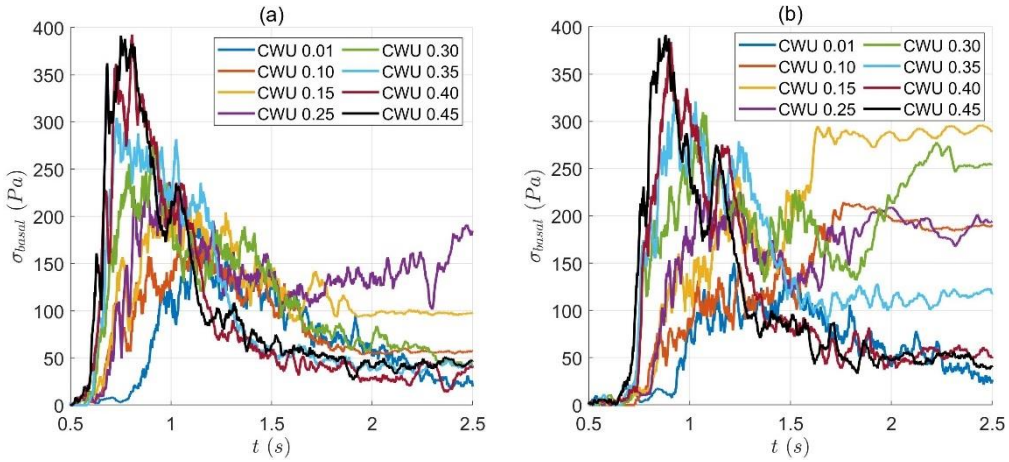

Figure 5-19: Contrasts of basal normal stresses (σ_{basal}) for CWU flows at (a) the upslope position and (b) the downslope position.

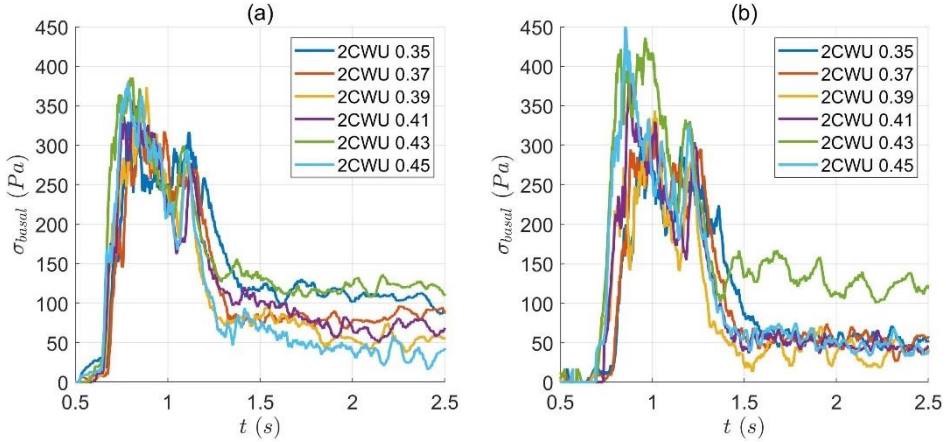

Figure 5-20: Contrasts of basal normal stresses (σ_{basal}) for 2CWU flows at (a) the upslope position and (b) the downslope position.

Time histories of basal pore pressure (p_{basal}) development for all the fluid-mixed granular flows are given below: Figure 5-21 (a) and (b) contrast the p_{basal} measured at the downslope position in

CSU and 2CWU tests (as the upslope pore pressure transducer signals are unavailable for those tests); Figure 5-22 presents more detailed data of CWU wet tests, distributing the upslope p_{basal} for unsaturated flows (w = 0.01 – 0.25) to subplot (a), the downslope p_{basal} for unsaturated flows to (b), the upslope p_{basal} for saturated flows (w = 0.3 – 0.45) to (c), and the downslope p_{basal} for saturated flows to (d); noting that the terms "unsaturated" and "saturated" here are relative to the saturation water content w = 0.256 for ceramic-bead samples at rest. As the shape of the p_{basal} profile does not necessarily follow the evolution of flow height (as shown in Figure 5-17), the "main surge" of each flow is represented by solid lines to highlight the part of flow analysis of interest, while the precursory grains and flow tail are plotted by dashed lines. In Figure 5-21, p_{basal} increases with source volume and water content; with a small volume (V_{bulk} = 0.75 – 1L) or low water content (w = 0.35 – 0.39), the negative p_{basal} persists on the time axis longer than the short period when flow enters the PIV-detected zone, where it is expected to be unsaturated, and the positive p_{basal} only appears at the flow rear close to the tail; when the flow is of larger initial volume or higher water content, a positive p_{basal} tends to occur over the entire main surge (except for the leading edge which is always comprised of dry / unsaturated grains).

Detailed p_{basal} evolution with water content in Figure 5-22 introduces an insight into the pore fluid effects. At both the upslope and downslope positions, the p_{basal} gradually drops to a stable negative value when the flow is dry; this p_{basal} history is probably due to the fact that water that initially fills in the transducer hole (see Sec. 3.1.4) is removed by the passage of dry grains. Then from w = 0.01 to 0.1, the negative p_{basal} grows stronger than that in "CWU 0.00", indicating a suction is applied to the pore pressure transducer; this suction weakens as the water content increases from 0.1 to 0.25 but, within this range, the flow is still dominated by the negative p_{basal}. When water content increases to 0.3, the peak of p_{basal} values within the main surge can rise above zero, even though this positive p_{basal} does not persist long and the majority of the main surge still experiences negative pore pressure. After w > 0.3, the positive p_{basal} increasing with the water content dominates the flow, but cannot exceed the theoretical steady-flow pressure (Figure 5-17 (b)). Additionally, the p_{basal} values at the upslope position appear always to be higher than those at the downslope position, implying that the positive pore pressure is weakened as the flow moves downslope.

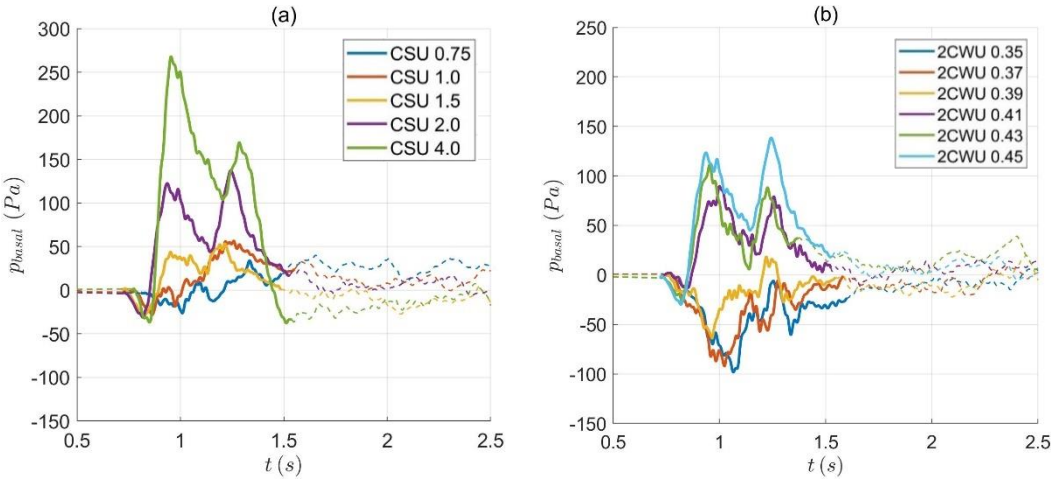

Figure 5-21: Contrasts of downslope basal pore pressures (p_{basal}) for (a) CSU flows and (b) 2CWU flows. Solid lines denote the "main surge" and dashed lines the other parts.

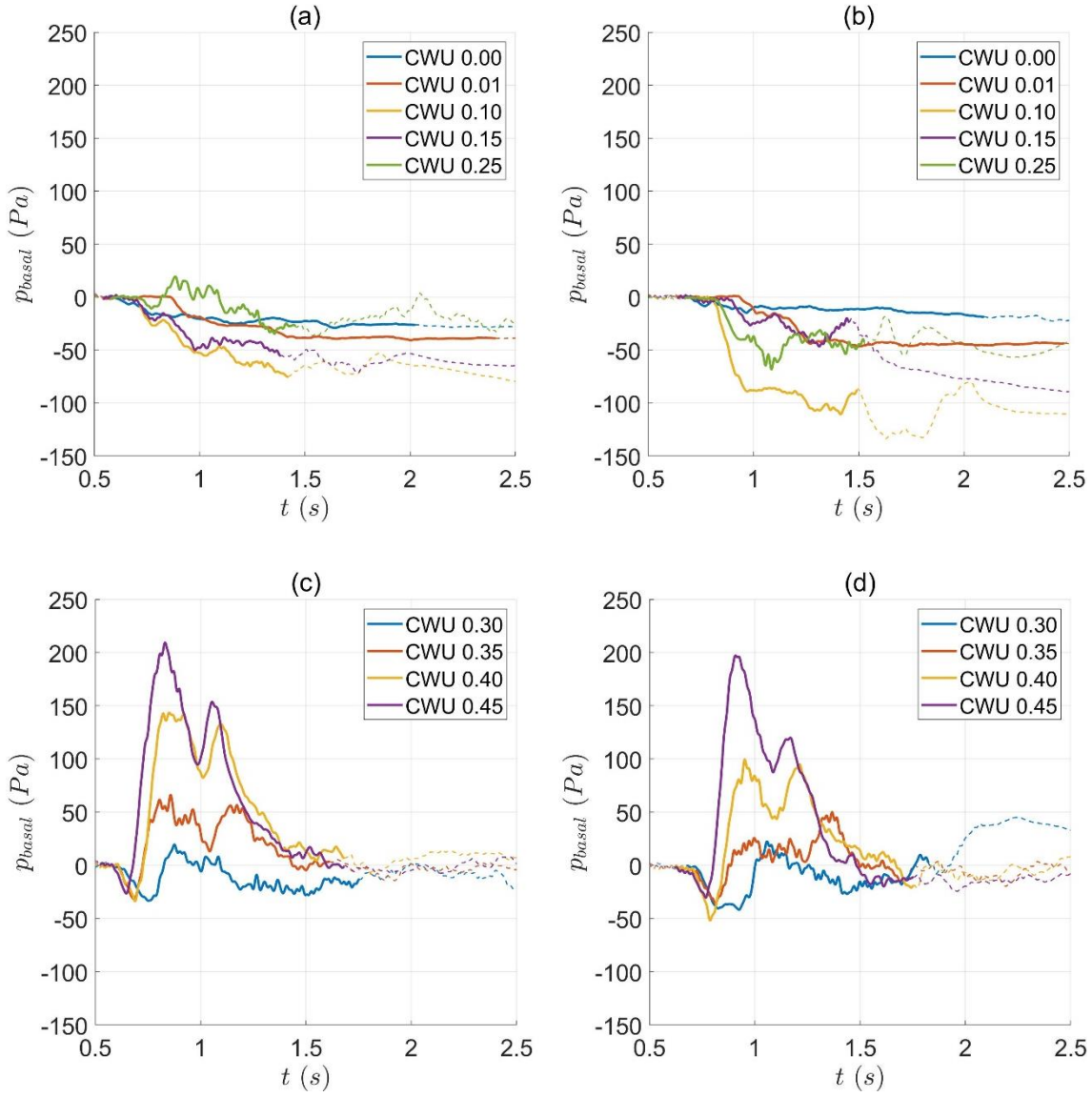

Figure 5-22: Basal pore pressures (p_{basal}) for CWU flows against time, including unsaturated flows at (a) the upslope position and (b) downslope position, and saturated flows at (c) the upslope position and (d) downslope position.

5.5. Flow Velocity

Velocity profiles for CSU, CWU and 2CWU flows are separately given in Figure 5-23, Figure 5-24 and Figure 5-25, where velocity curves for each flow are plotted with the time interval of t* = 5%, i.e. 5% of the "main surge" duration starting from the leading edge, and red dashed lines represent the position of the basal patch centre (as shown in Figure 3-6); the velocity curves in yellow are closer to the flow front while those in blue are closer to the tail. All the subplots (a) present the actual velocity data while subplots (b) give the velocity data fitted by power functions (see Sec. 3.2.3); power-fitted velocities generally match well with the actual data curves, giving confidence in applying them to further analyses. As depicted in the following figures, the velocity magnitudes decrease from the flow front (yellow curves) to the flow tail (blue curves) within each main surge of a flow and increase with both source volume (Figure 5-23) and water content (Figure 5-24 and Figure 5-25).

To straightforwardly observe the change in the shape of velocity profiles with test variables, the velocity curve at the maximum flow height is chosen to represent each flow in CSU (Figure 5-26) and CWU (Figure 5-28) groups, as the flow head (where the peak flow height appears) containing the highest percentage of the flow mass should contribute most to the impact force of fluid-mixed granular flows. As a supplement, to reduce the stochasticity of using only one curve to represent the flow head, Figure 5-27 and Figure 5-29 add five velocity curves both before and after the time index of peak flow height (i.e. eleven curves altogether), where every two curves are spaced with twice the PIV time interval, which is twice the reciprocal of framerate (see Sec. 3.2.2). For all the velocity profile figures, the actual velocity (u) data against flow height (h) are given in subplots (a) whereas the velocities normalised by the depth-averaged velocity (u/u_{ave}) against the normalised flow height (z/h) are in subplots (b).

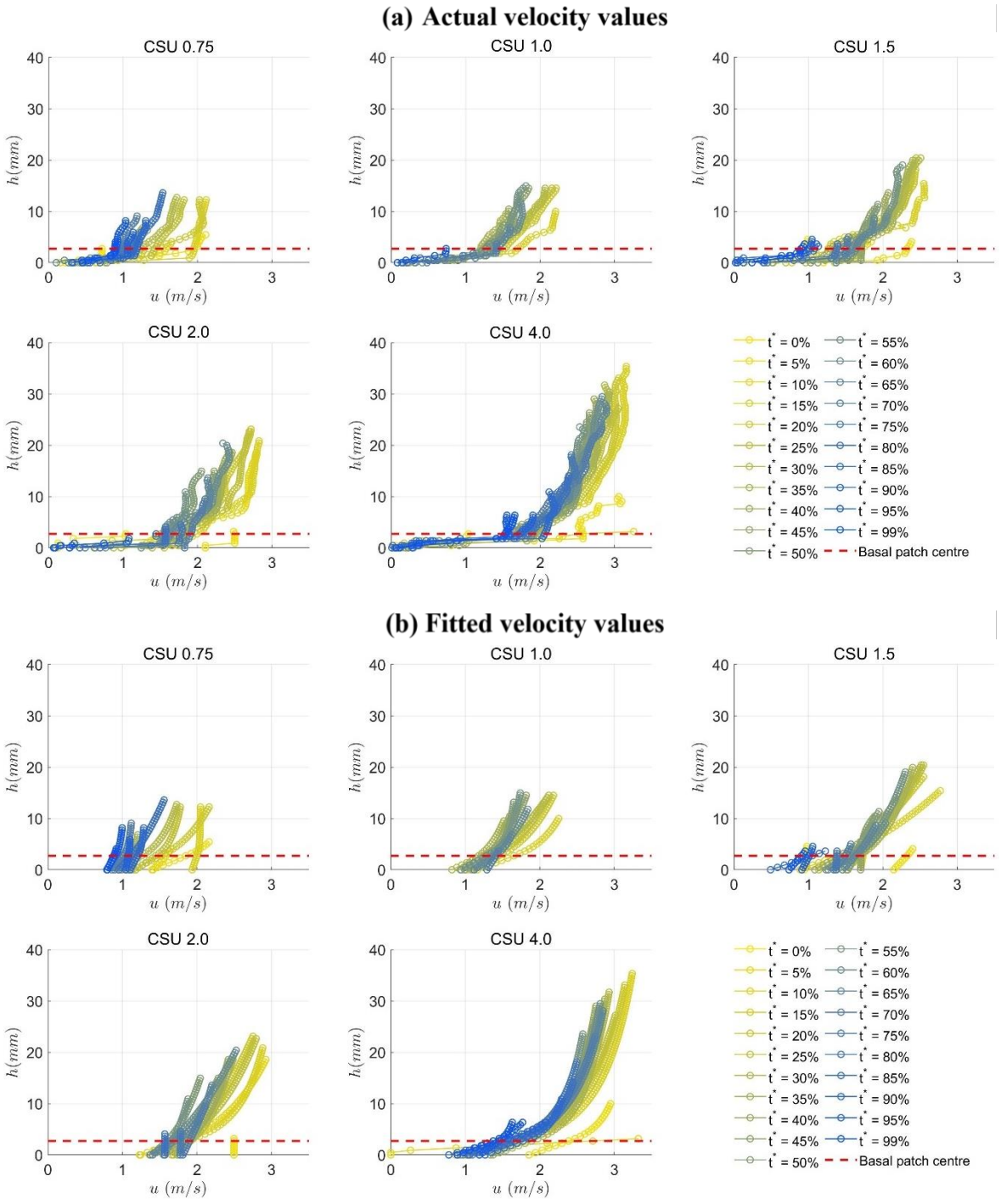

Figure 5-23: Velocity profiles of CSU flow distributed in subplots with (a) actual velocity data and (b) power-fitted velocity data. Velocity curves are plotted every 5% time for the "main surge" duration. Yellow curves are closer to the flow front and blue to the flow rear; red dash lines denote the position of the basal patch centre.

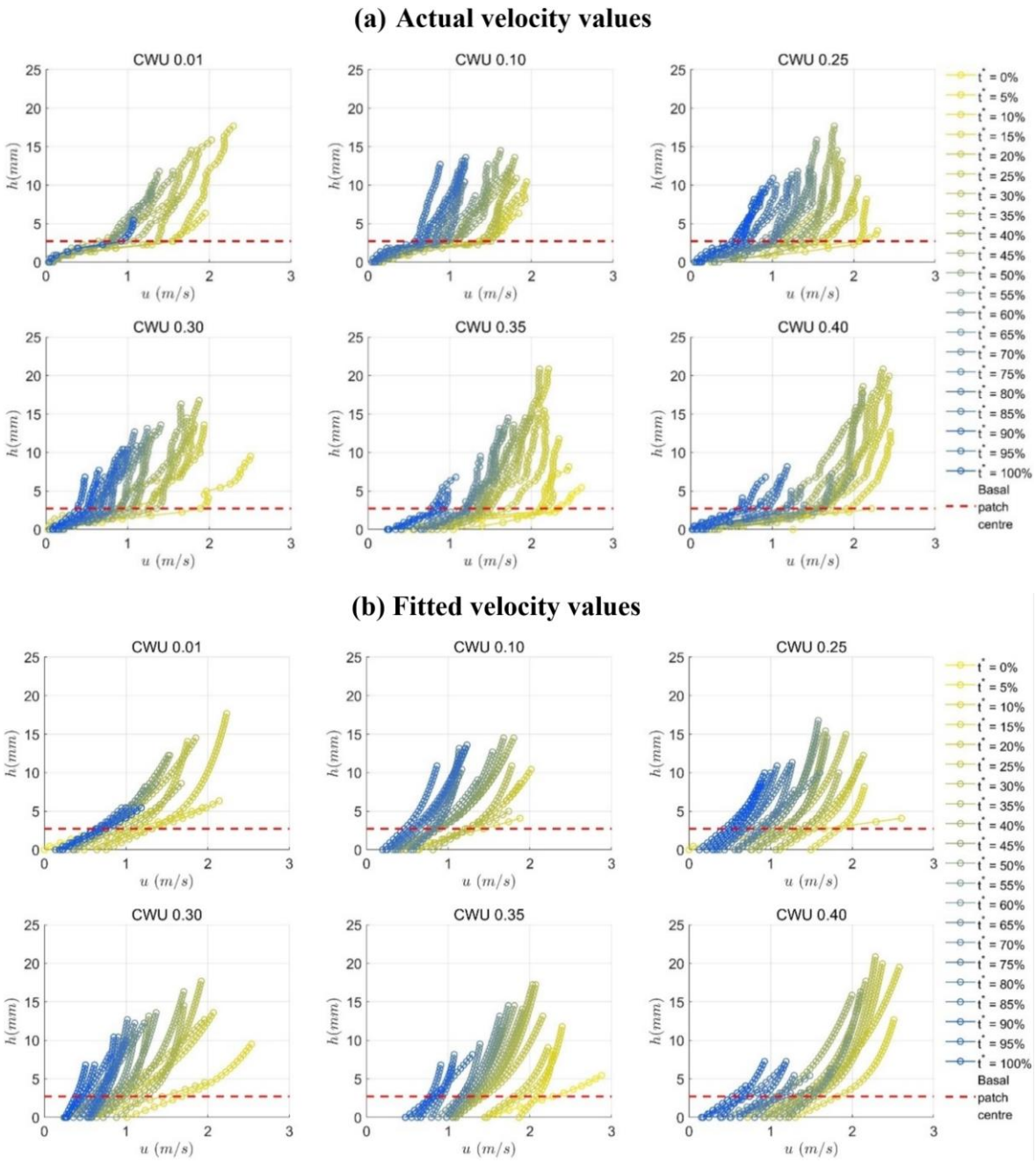

Figure 5-24: Velocity profiles of CWU flow distributed in subplots with (a) actual velocity data and (b) power-fitted velocity data. Velocity curves are plotted every 5% time for the "main surge" duration. Yellow curves are closer to the flow front and blue to the flow rear; red dash lines denote the position of the basal patch centre.

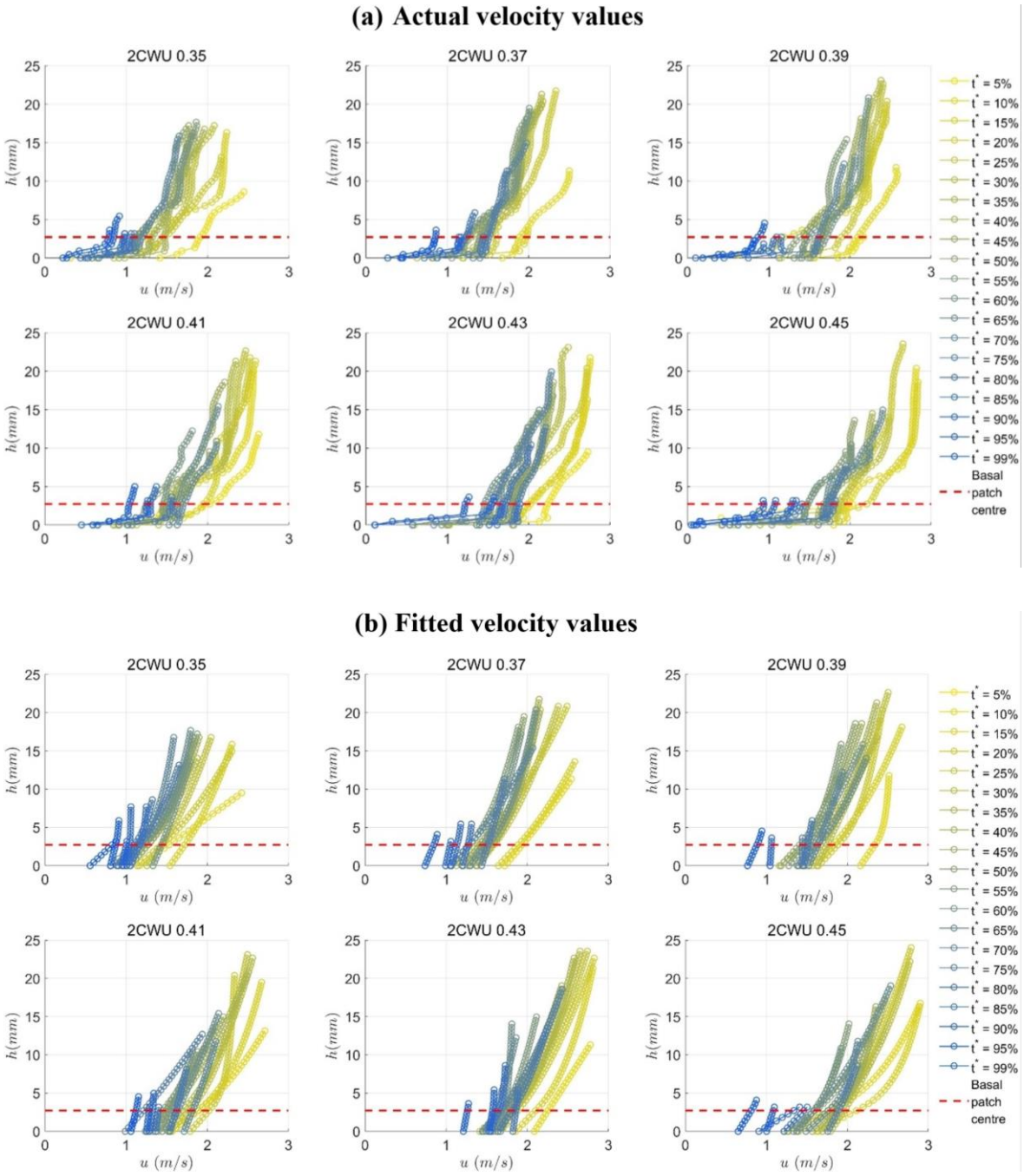

Figure 5-25: Velocity profiles of 2CWU flow distributed in subplots with (a) actual velocity data and (b) power-fitted velocity data. Velocity curves are plotted every 5% time for the "main surge" duration. Yellow curves are closer to the flow front and blue to the flow rear; red dash lines denote the position of the basal patch centre.

Velocity profiles of CSU flows in Figure 5-26 (a) suggest that, with an increased source volume, velocity is notably increased for most of the flow height except for the basal layer, and the shape of the velocity profile becomes more curved, giving a larger difference between the surface velocity and slip velocity; this change in shape is more obviously shown in Figure 5-26 (b), where the u/u_{ave} values at the basal boundary clearly show a decreasing trend with source volume while those in the rest part of the normalised flow height remain similar. Meanwhile, when water

content increases, the velocity curve throughout the flow height of a CWU flow tends to consistently grow larger (Figure 5-28 (a)) and its shape becomes closer to that of a "plug flow" with a higher normalised slip velocity and a lower normalised surface velocity (Figure 5-28 (b)). These velocity evolution tendencies are consistent and are supported by the averaged velocity profiles presented in Figure 5-27 and Figure 5-29 for CSU and CWU tests; the averaged range is 0.01s, which is close to 1% the main surge duration, both before and after the peak flow height. Overall, the difference between velocities in the upper portion of the flow and the slip velocity at the basal boundary is magnified by a larger source volume but is reduced by higher water content.

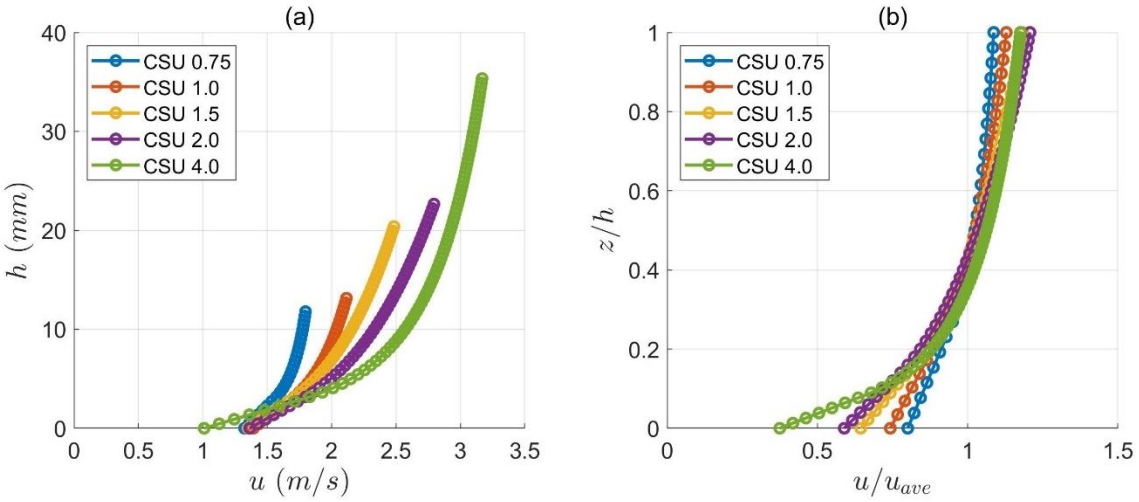

Figure 5-26: Velocity profiles at the peak flow height for all CSU flows. (a) Actual velocity against flow height, and (b) normalised velocity (by depth-averaged velocity) against normalised flow height.

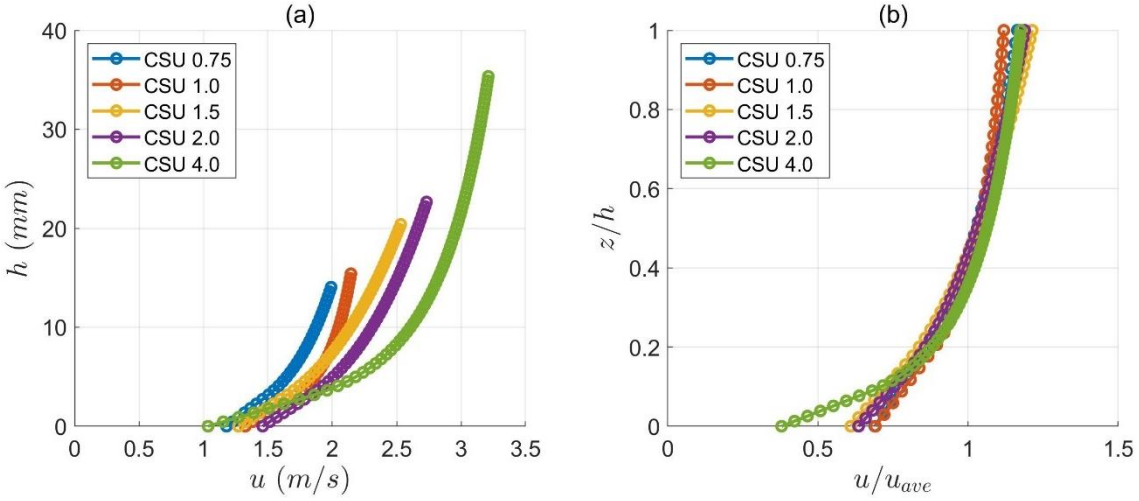

Figure 5-27: Velocity profiles averaged over 0.02s around the peak flow height for all CSU flows. (a) Actual velocity against flow height, and (b) normalised velocity (by depth-averaged velocity) against normalised flow height.

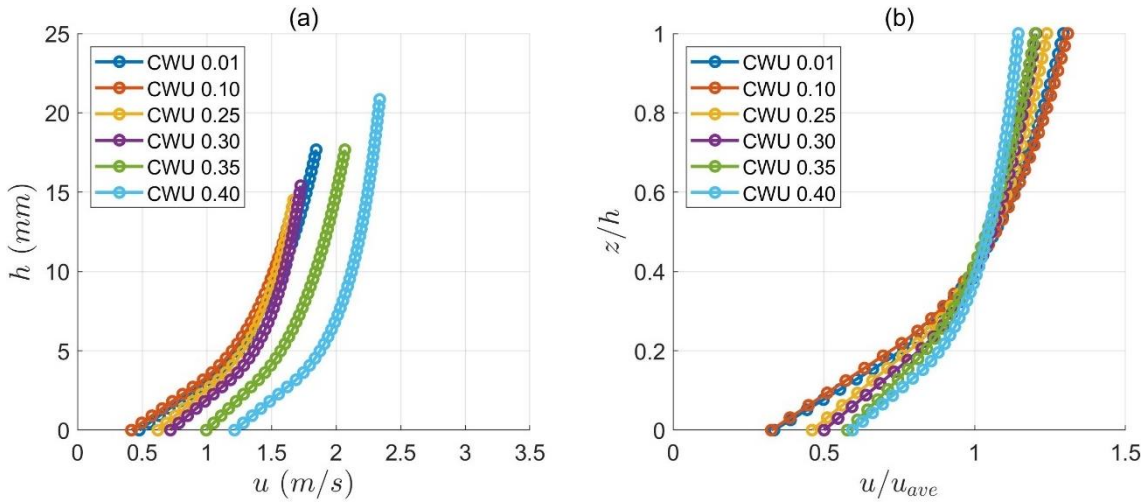

Figure 5-28: Velocity profiles at the peak flow height for all CWU flows. (a) Actual velocity against flow height, and (b) normalised velocity (by depth-averaged velocity) against normalised flow height.

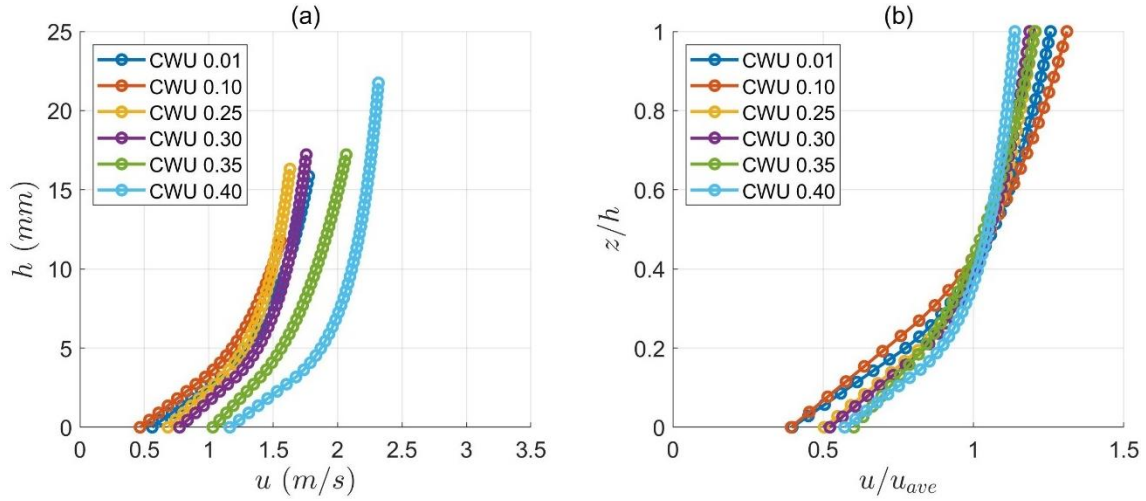

Figure 5-29: Velocity profiles averaged over 0.02s around the peak flow height for all CWU flows. (a) Actual velocity against flow height, and (b) normalised velocity (by depth-averaged velocity) against normalised flow height.

Depth-averaged velocity histories of CSU flows and CWU flows are given in Figure 5-30 (a) and (b), where u_{ave} data within the main surge part of each flow are plotted in star marks. The depth-averaged velocities overall decrease from the flow head to the flow tail but exhibit two-wave shapes similar to flow height profiles in Figure 5-14 and Figure 5-15, reaching the maximum velocity shortly after entering the PIV-detected zone and then gradually dropping before showing a second rise-and-fall with a smaller peak velocity; this trend is less apparent with low water content (Figure 5-30 (b)), especially when the flow material is slightly wetted (w = 0.01). The u_{ave} of fluid-mixed flows increases remarkably with source volume and also increases slightly with water content except for the "CWU 0.01" test, where larger u_{ave} values than those of the w = 0.1 flow are produced; this shows that high water content generally enhances the flow

head velocity but at low value it can reduce the head velocity, similar to its influence on the bulk flow mobility (Figure 5-7) and basal pore pressure (Figure 5-22).

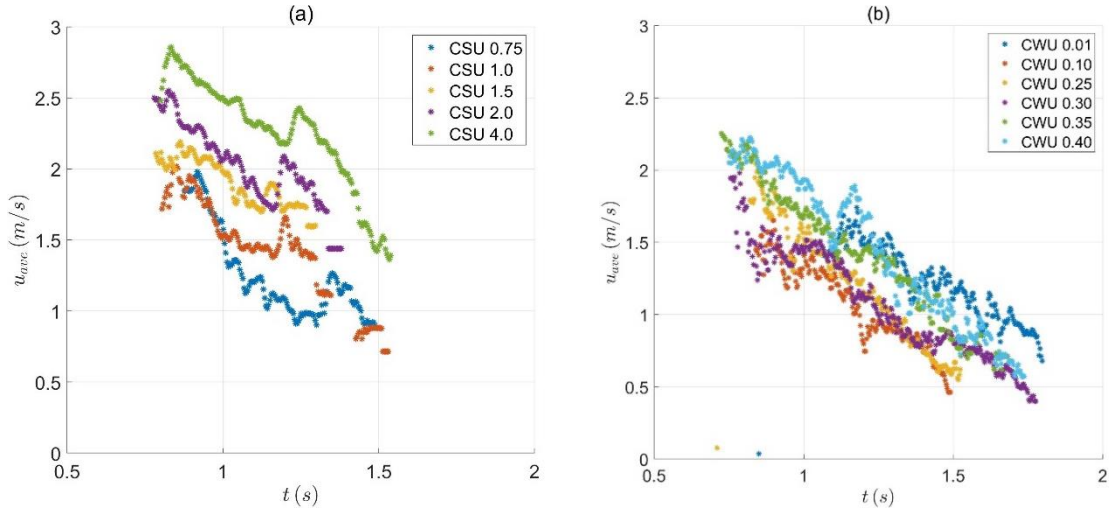

Figure 5-30: Time histories of depth-averaged velocities of (a) CSU and (b) CWU flows.

5.6. Dimensional Analysis

Dimensional analysis results identifying the flow regime and dominant momentum transfer mechanism are given below. The local values of dimensionless numbers (which are determined according to Sec. 3.5) of CSU flows calculated based on the fitted velocities and distributed across the normalised flow height (z/h) are plotted in Figure 5-31 and those of CWU flows are in Figure 5-32; the Savage number (N_{Sav}), Bagnold number (N_{Bag}) and friction number (N_{fric}) are allocated in subplots (a), (b) and (c) respectively. For each tested flow, a data curve taken at the peak flow height is depicted in the corresponding subplot, similar to the cases of Figure 5-26 and Figure 5-28; the black dashed line appearing in each subplot represents the threshold value of the demonstrated dimensionless number, which yields 0.1 for N_{Sav}, 200 for N_{Bag} and 100 for N_{fric} (see Sec. 2.3).

Local values of all three numbers seem not to notably vary with a source volume lower than 2L: N_{Sav} is higher at the basal boundary and lower in the upper portion of the flow with a minor increase at the top surface, N_{Bag} continuously grows from the top to the bottom with an increasing rate, and N_{fric} is smaller at both boundaries and larger in the middle of the flow height. When the source volume increases from 2L to 4L, however, the N_{Sav} values in the upper portion of the flow significantly drop (even to the level below the threshold value at z/h = 0.6 – 0.8) and

the N_{fric} values accordingly increase, whereas N_{Bag} values in the same part of the flow height only decrease slightly. Hence, on the whole, a larger source volume should reduce the N_{Sav} and N_{Bag} while increasing the N_{fric}, indicating reduced importance of solid inertia, an enhanced level of solid friction and a relatively stable influence of fluid viscous shear. For CWU flows, the structures of all three numbers in Figure 5-32 are similar to those in Figure 5-31 but exhibit more gradual evolution with water content. N_{Sav} distributed along the upper portion of the flow height stays the same when the water content increases from 0.01 to 0.1 and then consistently decreases with the water content greater than 0.1; meanwhile, N_{Sav} at the basal layer does not show notable difference with water content. N_{Bag} across the depth continues to reduce with water content, partly because of the growing equivalent viscosity of pore fluid as calculated by Eq. (3-3) until the flow material achieves saturation. The entire curve of N_{fric} shifts to the left-hand side as the water content increases and the biggest reduction of the N_{fric} value occurs when w grows from 0.01 to 0.1.

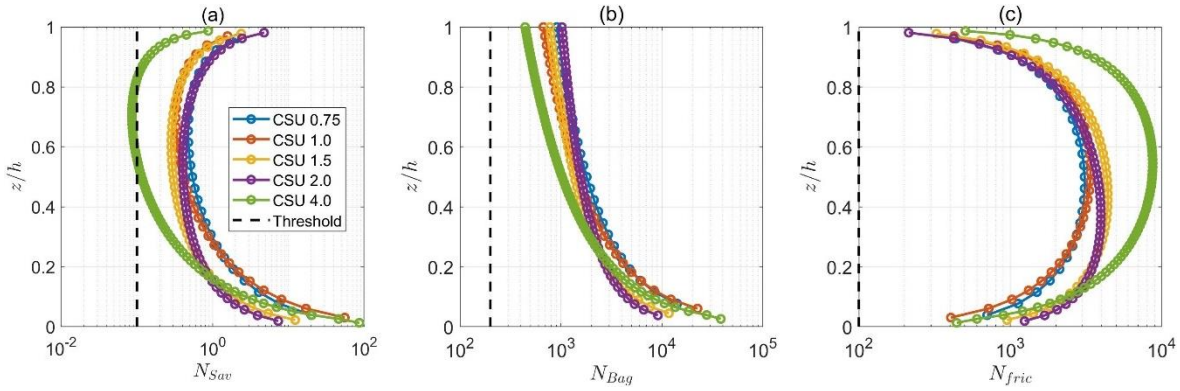

Figure 5-31: Local values of (a) Savage number, (b) Bagnold number and (c) friction number across the normalised height at the peak flow height for all CSU flows.

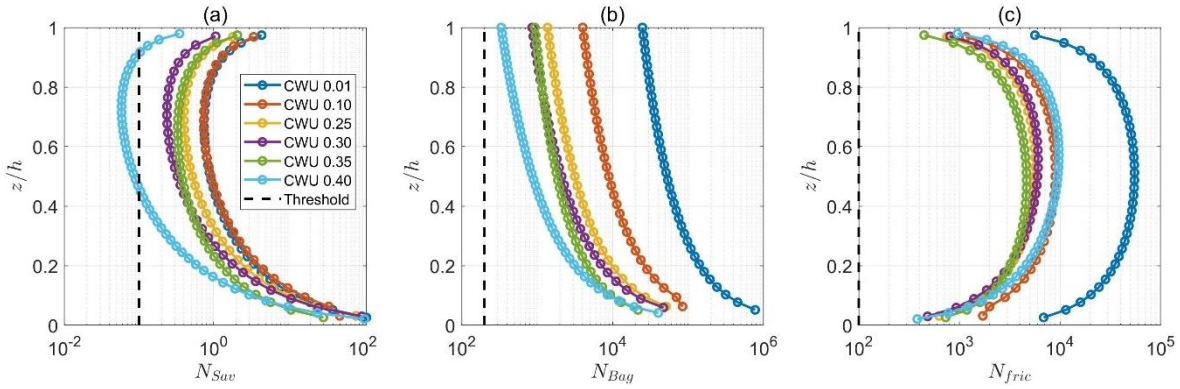

Figure 5-32: Local values of (a) Savage number, (b) Bagnold number and (c) friction number across the normalised height at the peak flow height for all CWU flows.

To demonstrate the flow regime within the entire main surge of fluid-mixed granular flows, the mean values of all three dimensionless numbers ($\overline{N}_{Sav}$, $\overline{N}_{Bag}$ and $\overline{N}_{fric}$) across the depth are plotted in Figure 5-33 for CSU flows and Figure 5-34 for CWU flows, in which data points are plotted against the normalised flow height (h/δ) and are divided into two marker types: hollow circles represent the data before the peak flow height and asterisks the data after. CSU flows in Figure 5-33 give some chaotic data after the peak flow height when $h/\delta \leq 2$ which corresponds to the part close to the flow tail; this issue results from the velocity profiles for the shallow part of the flow near the flow tail (the blue curves in Figure 5-23 (b) and Figure 5-24 (b)), where the velocity gradients (and hence the shear rates) can be different when the flow heights are very close, leading to the larger difference in the values of dimensionless numbers within a small h/δ range. When $h/\delta > 3$ in Figure 5-33, $\overline{N}_{Sav}$ and $\overline{N}_{Bag}$ decrease whereas $\overline{N}_{fric}$ increases with the normalised flow height; the increase in source volume vaguely enhances $\overline{N}_{Sav}$ and $\overline{N}_{Bag}$ but seems not to notably affect $\overline{N}_{fric}$ values. In general, source volume does not pose a very strong impact on the flow regime of the CSU saturated granular flows.

The influence of water content on $\overline{N}_{Sav}$, $\overline{N}_{Bag}$ and $\overline{N}_{fric}$ is more prominent. Data points for each test in Figure 5-34 are distributed within a confined range which looks rather consistent in shape between different tests, showing straightforward evolution with both normalised height and water content. In the thicker part of a flow (where h/δ is larger), $\overline{N}_{Sav}$ becomes smaller, $\overline{N}_{Bag}$ tends to be slightly smaller, and $\overline{N}_{fric}$ rises markedly; this suggests slightly reduced solid inertial stress (as $\overline{N}_{Bag}$ does not decrease much and viscosity does not change with flow height), notably stronger solid frictional stress and relatively stable fluid viscous shear stress. With a higher water content, $\overline{N}_{Sav}$ shows a reduction from w = 0.01 to 0.3 and then rises back slightly from w = 0.3 to 0.4; this is conceptually understandable as the solid grains are initially more firmly in contact with each other as water fills the pores but then tend to loosen up and be suspended in the fluid when fully immersed. Similarly, $\overline{N}_{Bag}$ greatly reduces as the flow material becomes saturated (w = 0.01 – 0.3) and then remains stable when the water content further increases; this means that fluid viscous shear grows stronger during the saturation of the sample. $\overline{N}_{fric}$ values overall decrease with water content, indicating an increased level of viscous shear relative to Coulomb friction, although the data from w = 0.25 to 0.35 overlap with each other. In addition, all three dimensionless numbers are above their respective threshold values for the most part of CSU and CWU flows; this means that, referencing the definitions of those numbers in Sec. 2.3, solid inertia dominates the momentum exchange within the fluid-mixed flow, followed by solid friction, and fluid viscous shear is the least important interaction.

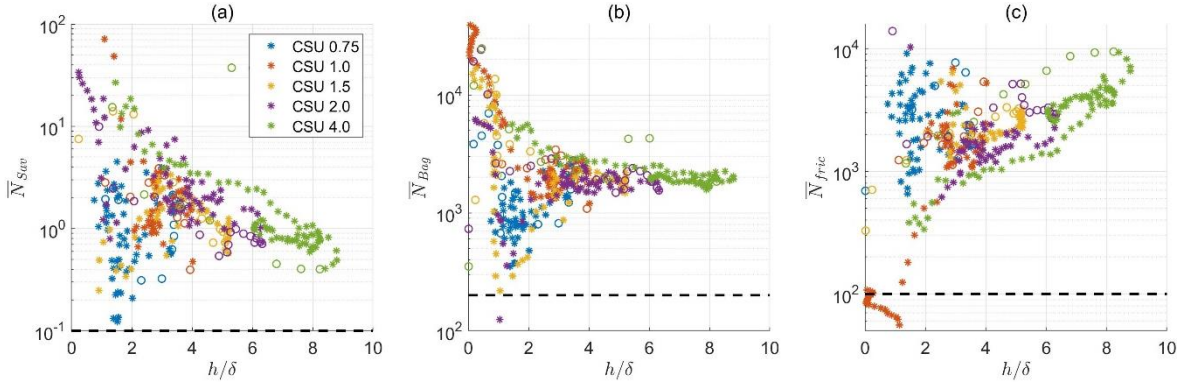

Figure 5-33: Mean values across the depth of (a) Savage number, (b) Bagnold number and (c) friction number against the normalised flow height by averaged grain size for all CSU flows, in which hollow circles denote the flow part before the maximum flow height while asterisks the part after.

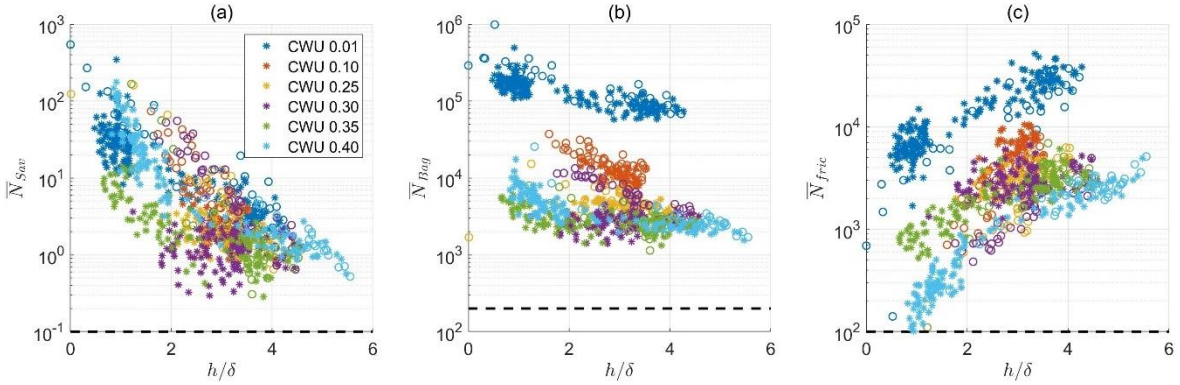

Figure 5-34: Mean values across the depth of (a) Savage number, (b) Bagnold number and (c) friction number against the normalised flow height by averaged grain size for all CWU flows, in which hollow circles denote the flow part before the maximum flow height while asterisks the part after.

6. Well-graded Flow Results

Preface

Well-graded granular flows include two types of test groups: the MSG (Maple Mud, Saturated, Well-Graded) group with varying source volume and the MWG (Maple Mud, Wet, Well-Graded) group with evolving water content; both groups use water-mixed polydisperse solid material with a fixed designed grain size distribution. Details about the experimental setup, source material and test procedure of small-scale flume tests can be found in Chapter 3.

This chapter exhibits the results of MSG and MWG tests and is structured as follows: Sec. 6.1 introduces the test conditions and measurements; Sec. 6.2 gives the macroscopic morphology of flow deposits, as well as the analysed results of bulk flow mobility and grain size distribution; Sec. 6.3 demonstrates the longitudinal flow profiles and the comparisons of flow heights; Sec. 6.4 provides basal normal stress and basal pore pressure data collected from all the tests; Sec. 6.5 provides velocity information of well-graded flows, including velocity profiles and time history of depth-averaged velocities; finally, Sec. 6.6 shows the Savage number, Bagnold number and friction number estimation, including their local values and mean values across the flow height, to determine the evolution of momentum exchange within well-graded granular flows.

6.1. Test Information

The test variable for the MSG group is source volume (or bulk volume of dry solids) whereas for the MWG group, it is gravimetric water content; correspondingly, the water content in MSG flows (0.22) and source volume in MWG tests (2 litres) are constant. Values of the variable are

shown in the test labels, e.g. "MSG 2.0" means the tested flow is the saturated flow with 2L source volume and "MWG 0.30" represents a wet flow with 0.3 water content; "MSG 2.0" and "MWG 0.22" represent the same experiment where the saturated well-graded flow is produced by a source material of 2L Maple Mud with 0.22 water content. The designed water content of 0.22 for MSG tests is slightly more than the saturating water content (0.21, see Sec. 3.1.4) of the Maple Mud sample at rest and is determined based on a series of preliminary tests to ensure the runout can be kept within the horizontal runout channel.

Test information for the MSG and MWG groups are recorded respectively in Table 6-1 and Table 6-2, where the data sources, including source material, final deposit and morphological analysis (see Sec. 3.4), are listed. Most parameters in the following tables are also presented and are explained in Sec. 4.1 and Sec. 5.1, which give test information of dry and wet uniform flow tests; however, some parameters for the Maple Mud sample need further explanation due to the special meaning or different measurement approach: (i) dry density is the averaged density of closely-packed Maple Mud samples, which are shaken in the measuring jar to the minimum bulk volume achievable; (ii) the bulk dry volume of the Maple Mud sample also corresponds with the close packing to guarantee a relatively stable value; as the samples were prepared according to a specific recipe, bulk volume measurement for every sample is difficult and time-consuming, especially for solids in larger volumes (e.g. 3L and 4L); hence the bulk dry volume is directly calculated by the measured mass of the sample divided by the obtained dry density; (iii) void ratio and porosity is estimated from the saturating water content due to the difficulty of applying the measurement approach (as described in Sec. 3.1.4) to every tested sample, which must be stirred while being poured into the hopper to prevent the clustering and consolidation as much as possible.

Test		MSG 0.75	MSG 1.0	MSG 1.5	MSG 2.0	MSG 3.0	MSG 4.0
Source measurements	Bulk dry volume (L)	0.75	1	1.5	2	3	4
	Dry density (g/cm^3)	1.85					
	Solid mass (g)	1387.48	1850.01	2775.01	3700.01	5550.02	7399.98
	Fluid mass (g)	305.66	407.45	611.23	814.53	1221.2	1628.26
	Water content	0.22					
	Void ratio	0.39					
	Porosity	0.28					
	Volume in the hopper (cm^3)	1042.24	1389.68	2084.51	2779.35	4169.02	5558.66
	Bulk density (g/cm^3)	1.611					

Deposit measurements	**Runout (mm)**	520	630	950	1291	2090	2550
	Inclined length (mm)	100	140	200	170	150	240
Morphological analysis	**Travel angle (°)**	26.8	25.8	23.8	22.5	19.1	20.4

Table 6-1: Test information of MSG tests with varying source volumes.

Test		**MWG 0.20**	**MWG 0.22**	**MWG 0.24**	**MWG 0.26**	**MWG 0.28**	**MWG 0.30**
Source measurements	**Bulk dry volume (L)**	2					
	Dry density (g/cm^3)	1.85					
	Solid mass (g)	3700.01					
	Fluid mass (g)	740.44	814.53	888.23	962.45	1036.65	1110.63
	Water content	0.2	0.22	0.24	0.26	0.28	0.3
	Void ratio	0.39					
	Porosity	0.28					
	Volume in the hopper (cm^3)	2779.35					
	Bulk density (g/cm^3)	1.598	1.611	1.611	1.611	1.611	1.611
Deposit measurements	**Runout (mm)**	920	1291	1587	2034	2153	2490
	Inclined length (mm)	160	170	220	130	20	110
Morphological analysis	**Travel angle (°)**	24.5	22.5	21.6	19.5	17.6	17.2

Table 6-2: Test information of MWG tests with varying water content.

6.2. Deposit Analysis

Well-graded granular flows can produce different deposition forms as shown in Figure 6-1, in which the deposits of three preliminary tests with different source volumes (V_{bulk}) and water content (w) are displayed. When V_{bulk} = 1L and w = 0.2, the majority of well-graded sediments are inadequately mobilised to move towards the outlet of the horizontal runout channel but tend to pile up near the flume end (Figure 6-1 (a)); the 1L well-graded flow with a higher water content of 0.3 can form a typical forward heap where sediments pile up at the distal end of the deposit (Figure 6-1 (b)); the deposit of the flow with V_{bulk} = 2L and w = 0.35 is very thin and evenly distributed in the runout channel like a sheet of sediment, suggesting that the deposits of well-graded flows at high water content can be stretched and elongated to a considerably large extent (Figure 6-1 (c)). The deposition process of the "MSG 2.0" (also labelled as "MWG 0.22") flow (Figure 6-2) details the runout behaviours of well-graded flows. The flow head starts to decelerate after rushing into the horizontal runout channel (Figure 6-2 (a)) while the following

flow body keeps its high speed; when being impeded by the decelerated leading edge, particles within the flow body simultaneously climb up and push forward those at the flow front, forming a granular heap that looks slightly squeezed or concentrated (Figure 6-2 (b)); this heap moves forward mainly as an entirety for a short period (Figure 6-2 (c)) before the longitudinal stretching of the heap takes the dominance in the increase in travel distance, making the heap distribute more evenly in the runout channel and the heap surface possesses a lower curvature (Figure 6-2 (d)). This highlights a relatively low basal friction of the well-graded sediments: the entire granular heap can move forward during and after its formation, and the stretching tendency of the heap can push the sediments at the front to slide for a certain distance; this can be related to the grain size segregation occurring in well-graded flows (see Sec. 2.1.3), where fine particles tend to concentrate at the bottom of the granular body (as can be observed in Figure 6-1 (b) and (c)) and thus reduce the basal friction.

Deposit morphologies of MSG and MWG flows are plotted in Figure 6-3, in which the horizontal scales are five times the vertical scales and each deposit's Centre of Gravity (COG) is denoted by a filled circle sharing the same colour as that of the deposit outline. The side-view geometry of each deposit is depicted in solid lines except for "MSG 4.0", which is drawn in dashed lines to show that it was produced by a failed test. Well-graded solids can settle, agglomerate and be consolidated very quickly inside the hopper and, if not stirred continuously by hand (which is the most reliable approach to ensure a thorough mixing all over the hopper base) while being poured into water, the consolidated grains can be stuck on the sidewalls and at

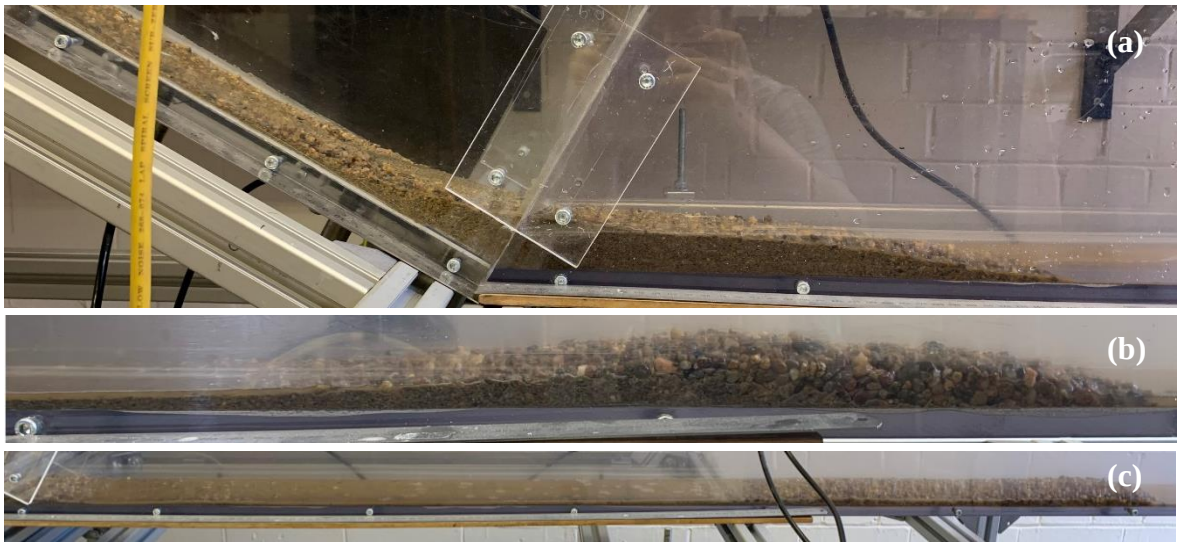

Figure 6-1: Deposits of well-graded pre-tests with (a) V_{bulk} = 1L, w = 0.2, (b) V_{bulk} = 1L, w = 0.3, and (c) V_{bulk} = 2L, w = 0.35.

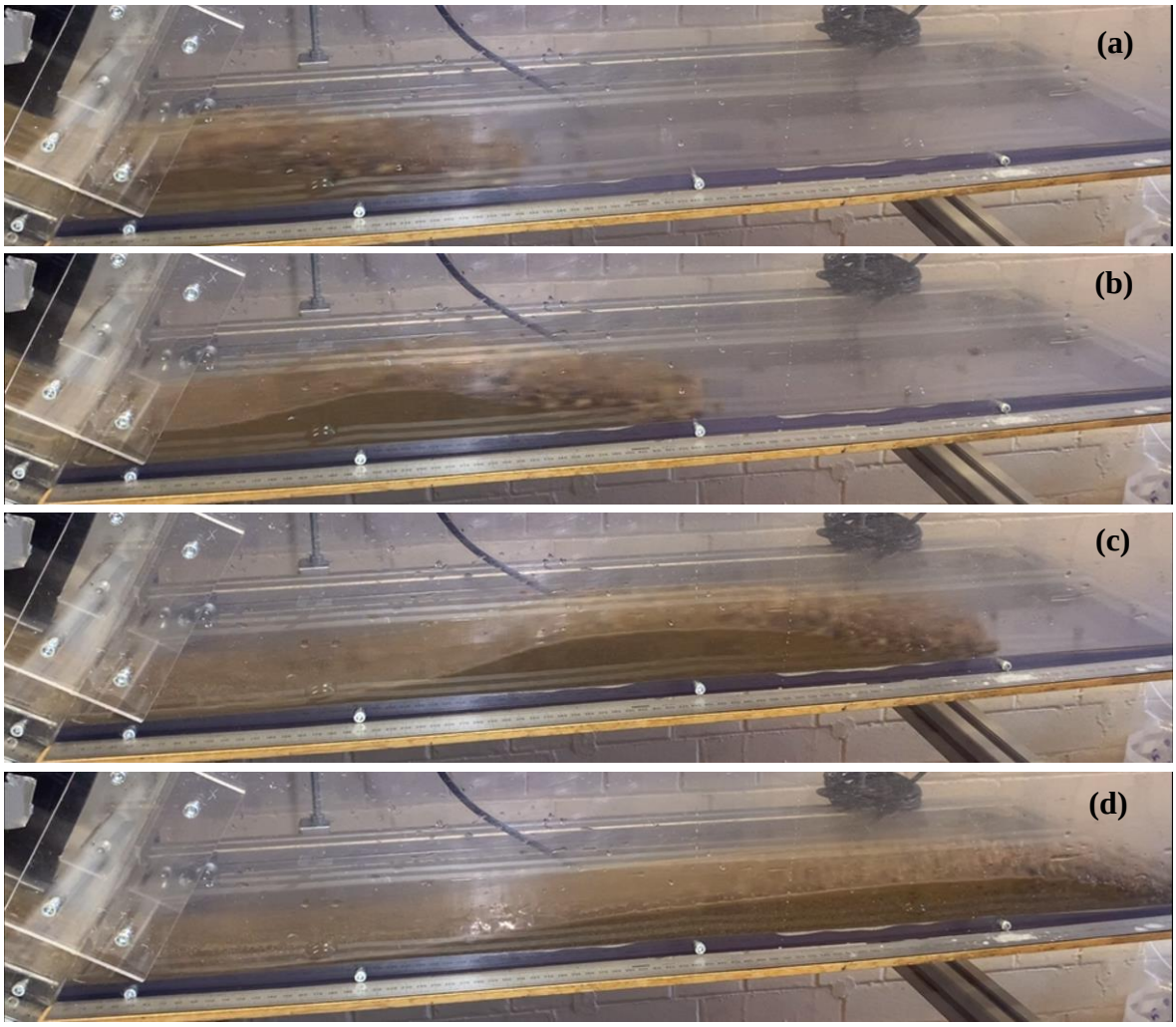

Figure 6-2: Deposition process of MSG 2.0 (also known as MWG 0.22) flow. (a) The flow head enters the runout channel; (b) the following flow body climbs up the decelerated front and pushes the combined heap forward; (c) the entire heap moves forward while its concentrated shape remains relatively stable; (d) the heap stretches forward into a shape with a slightly-inclined top surface, extending the runout distance further.

the corners of the hopper, as demonstrated in Figure 6-4. Source material of a lower volume can be properly agitated with very little solids remaining inside the hopper after the material release; however, once the source volume reaches four litres, the solids become too heavy to stir manually, leaving a large number of grains immobilised exactly as shown in Figure 6-4 and making the material that drops out slowly (and sometimes even intermittently) from the hopper appear more like clusters of sediment instead of an adequately-fluidised mixture. Three trials had been carried out with the "MSG 4.0" test condition and none of them can produce a satisfactory granular flow; nevertheless, the deposit information of one trial has been recorded to give a rough impression of the final result that a 4L well-graded flow may lead to.

Deposit geometries of well-graded granular flows as well as their COG positions evolve with both source volume and water content. A larger source volume gives longer travel distance and

pushes the COG farther while keeping a relatively stable deposit geometry, which is shaped as a forward heap thicker near the front with its maximum thickness not varying much between MSG tests (Figure 6-3 (a)); the only exception is the deposit of the failed test "MSG 4.0" which, compared with the "MSG 3.0" deposit, gives a shorter COG distance and a larger heap length that is composed of a thin layer of sediments at the front margin. Both the travel distance and COG position of the MWG flows increase with a higher water content from w = 0.2 to 0.3, but the deposit becomes thinner and elongated, indicating a stronger stretching trend of the granular body (Figure 6-3 (b)); this suggests that more pore fluid can facilitate the dilation of well-graded material, i.e. grains lose contact more easily, and that the deposit is likely in a compressed condition before this stretching occurs, e.g. the concentrated heap as shown in Figure 6-2 (c) or the shortest and thickest "MWG 2.0" deposit in Figure 6-3 (b) that probably stops deforming before the dilation development. Additionally, contrasting the deposits of "MWG 0.20" and "MWG 0.30", which are the 2L well-graded flows with 0.2 and 0.3 water content, with those presented in Figure 6-1 (a) and (b) with 1L material and the identical water content shows that, at the same water content, a larger source volume of Maple Mud is more influenced by pore fluid, resulting in a deposit that propagates farther, both due to a larger number of mobilised sediments (w = 0.2) and a larger amount of dilation (w = 0.3).

Bulk flow mobility of MSG and MWG flows analysed by travel distance (L) and travel angle (α_T) are displayed in Figure 6-5 and Figure 6-6, respectively. With both a larger source volume and a higher water content, the travel distance of the well-graded flows continuously increases and the travel angle consistently decreases (leaving out the outlier "MSG 4.0" which is denoted by a hollow circle and is connected with other MSG data points by a dashed line in Figure 6-5); in each subplot, data points can approximately form a straight line, suggesting that the bulk flow mobility of Maple Mud flows almost linearly grows with both source volume and water content. Considering that the poorly-mobilised deposit as shown in Figure 6-1 (a) does not appear in the MSG and MWG test groups, these linear relationships may fail when the test condition involves a smaller source volume and/or lower water content.

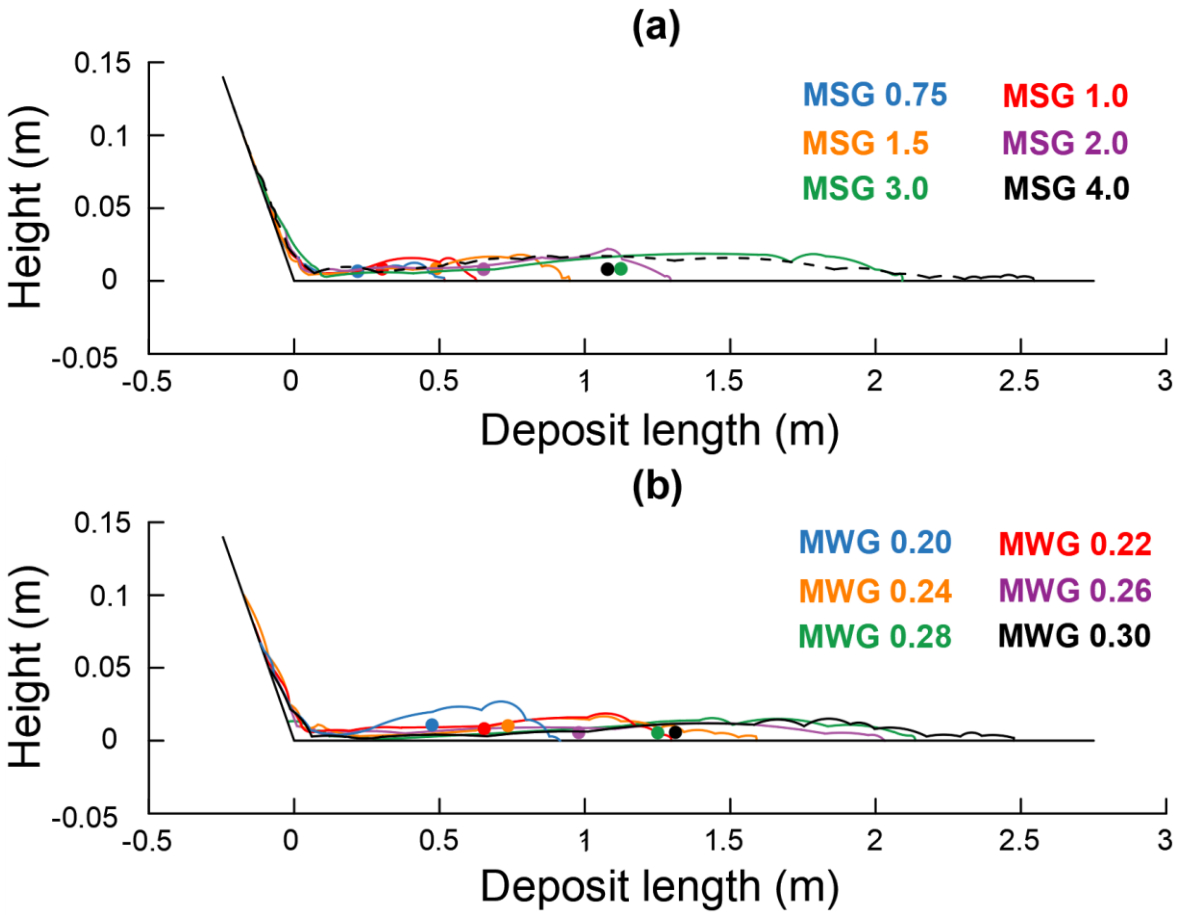

Figure 6-3: Deposit side-view outlines of (a) MSG flows and (b) MWG flows. The horizontal scale is 5 times the vertical scale. Filled dots represent the locations of the centre of gravity (COG).

Figure 6-4: Maple Mud consolidated and stuck inside the hopper when the source material is not adequately stirred before release.

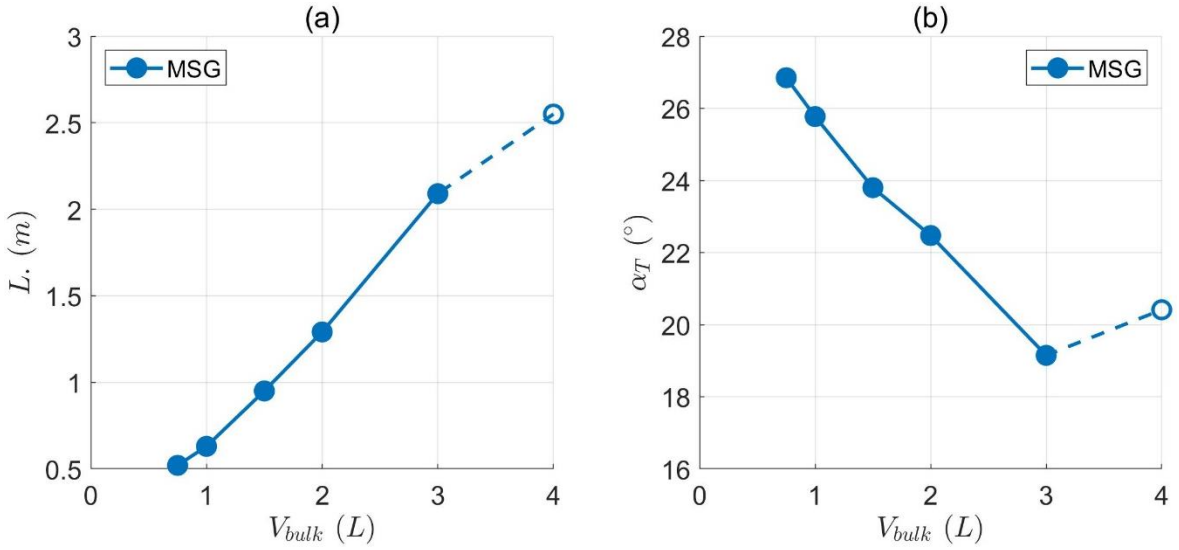

Figure 6-5: Evolution of (a) travel distance (L) and (b) travel angle (α_T) of MSG flows with source volume (V_{bulk}). Dashed lines and hollow circles imply that the V_{bulk} = 4L data point is an outlier.

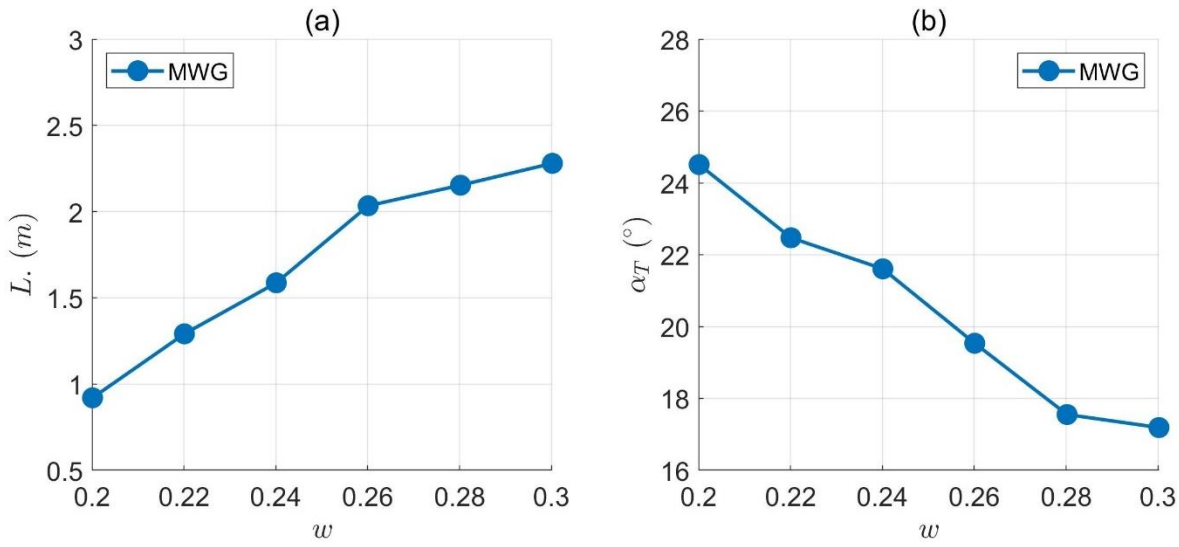

Figure 6-6: Evolution of (a) travel distance (L) and (b) travel angle (α_T) of MWG flows with water content (w).

Grain size segregation along the longitudinal direction very evidently occurs in the deposits of well-graded flows as shown in Figure 6-7, where the flow with 1L solids and 0.3 water content is taken as the example. Coarser sediments mostly concentrate at the front of the deposit and fine solids immersed in water tend to stay at the rear; grain size seems to decrease continuously from the distal end of the deposit to the proximal end. To more clearly illustrate the grain size distribution (GSD) of the well-graded deposits, the sieve analysis results of the MSG and MWG deposits are provided in Figure 6-8 (a) and (b), where four different source volumes and two water content values are included. For each deposit, sediments were sectionally collected and sieved, either every 200 mm or 400 mm, depending on the deposit length; in Figure 6-8, this

sectionalised length is expressed by the distance to the front margin normalised by the deposit length, denoted as L*, and the resultant GSD curve of each deposit section is depicted in different colours, where yellow indicates the section close to the distal end of deposit and blue the section near the proximal end; noting that L* = 0 represents the distal end of the deposit, opposite to the customary rule which defines the beginning of the deposit as the original point. For easy contrast, the designed GSD of the original sample (also presented in Figure 3-4) is also drawn in all the subplots in black curves. All the deposits in Figure 6-8 show similar evolution of GSD with the position: GSD curves of sediments in the deposit front (around L* < 40%) are everywhere larger than the GSD of source material, while those of sediments in the latter half (about L* > 50%) are all smaller than the source GSD; moreover, GSD range of different deposits seems not to vary noticeably between different tests, indicating that size segregation may be independent of source volume and water content.

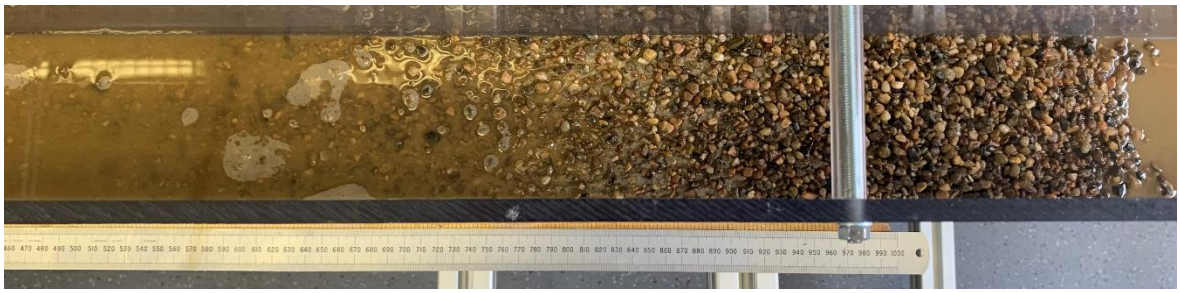

Figure 6-7: An example of the segregated deposit produced by a well-graded granular flow with 1L grains and 0.3 water content.

The mean size D_{50} of the deposit needs to be analysed as it can be utilised to represent the D_{50} of the moving flow surge (see Sec. 3.5). Figure 6-9 (a) plots the approximated D_{50} distribution curves of all the analysed deposits from the distal end (L* = 0) to the proximal end (L* = 100%), with a black dashed line denoting D_{50} of the source material. Each D_{50} curve is determined from the sectionally-analysed deposit GSD data, as shown in Figure 6-9 (b) which uses the "MSG 2.0" deposit as an example to show the approximation process: D_{50} at the midpoint of each deposit section (L* = 7.5% for the section L* = 0 – 15%) takes the value of the D_{50} of this section (which is the apparent intersection between a GSD curve and the horizontal line of 50% passing), and the data between each pair of midpoints are estimated by the linear interpolation method; particularly, data between L* = 0 and the first midpoint are determined by extending the neighbouring interpolation line, and data between L* = 100 and the last midpoint are assigned in the same way. The approximated D_{50} curves for different tests in Figure 6-9 (a) show good agreement ("MSG 4.0" aside), echoing the observation that different Maple Mud tests produce

similar deposit GSD; therefore, the longitudinal D_{50} distribution across the deposit can be assumed to be identical throughout all the tests and collapse onto one curve (except for those of

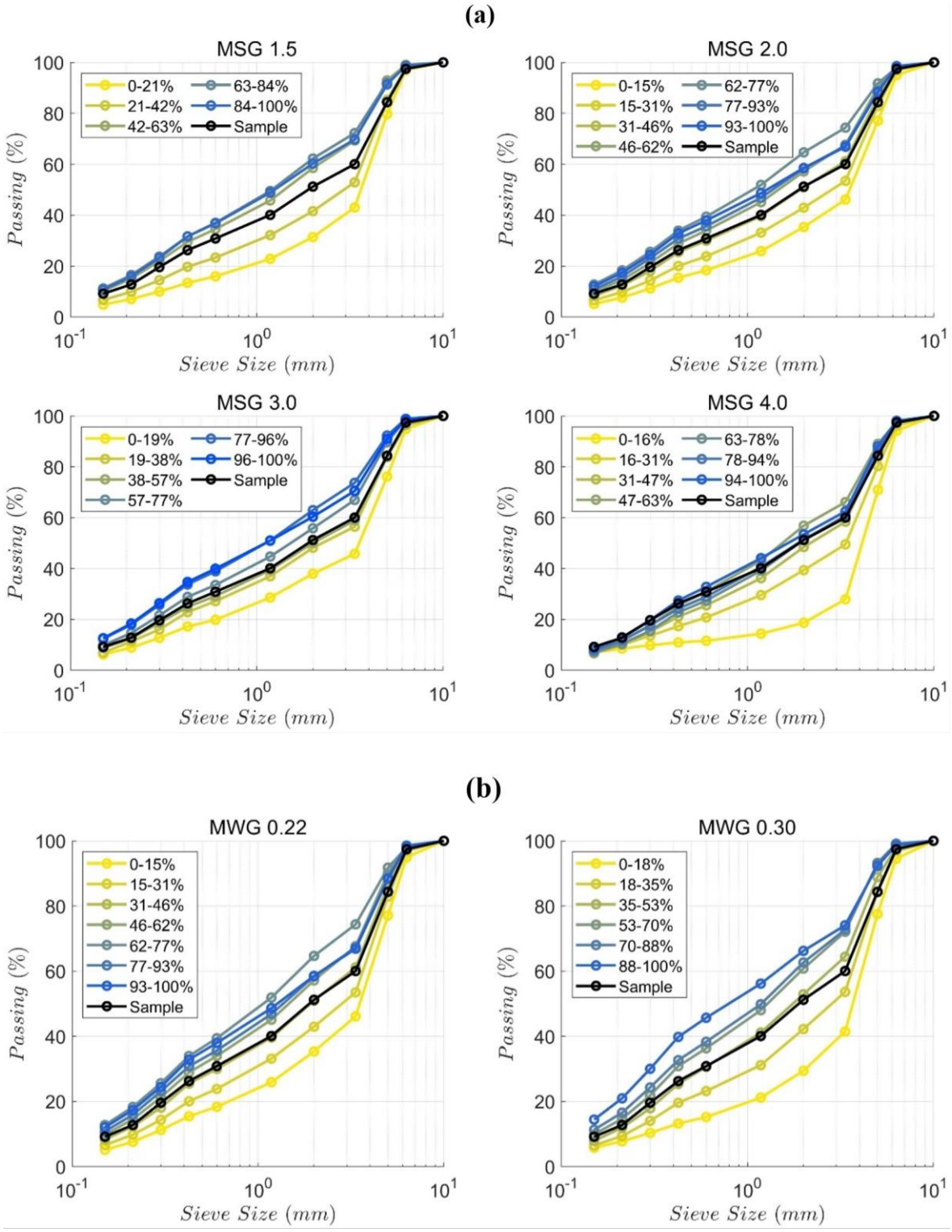

Figure 6-8: Grain size distribution of the (a) MSG and (b) MWG deposits. Yellow curves denote the deposit section closer to the distal end of the runout channel while blue curves denote the proximal end touching the flume; the black curves are the designed grain size distribution of the source material.

"MSG 4.0") in Figure 6-9 (a). For simplicity, a bilinear fitting is applied to all the approximated D_{50} data points, as shown in Figure 6-9 (c), where D_{50} from L* = 0% to 50% are fitted into one solid line and those from L* = 50% to 100% into another dashed line. As a "main surge" part is defined for each tested well-graded flow that is typically excessively long (see Sec. 3.3), D_{50} of the "main surge" can be simplified to only match the line of L* = 0 – 50%, which can be expressed by a function as:

$$D_{50}(L^*) = -4.85 \cdot L^* + 4.064, \qquad L^* = 0 - 0.5 \tag{6-1}$$

while the line of L* = 50 – 100% is assumed to fit the long flow tail part, which contributes less to the runout behaviours and is not the focus of further analysis.

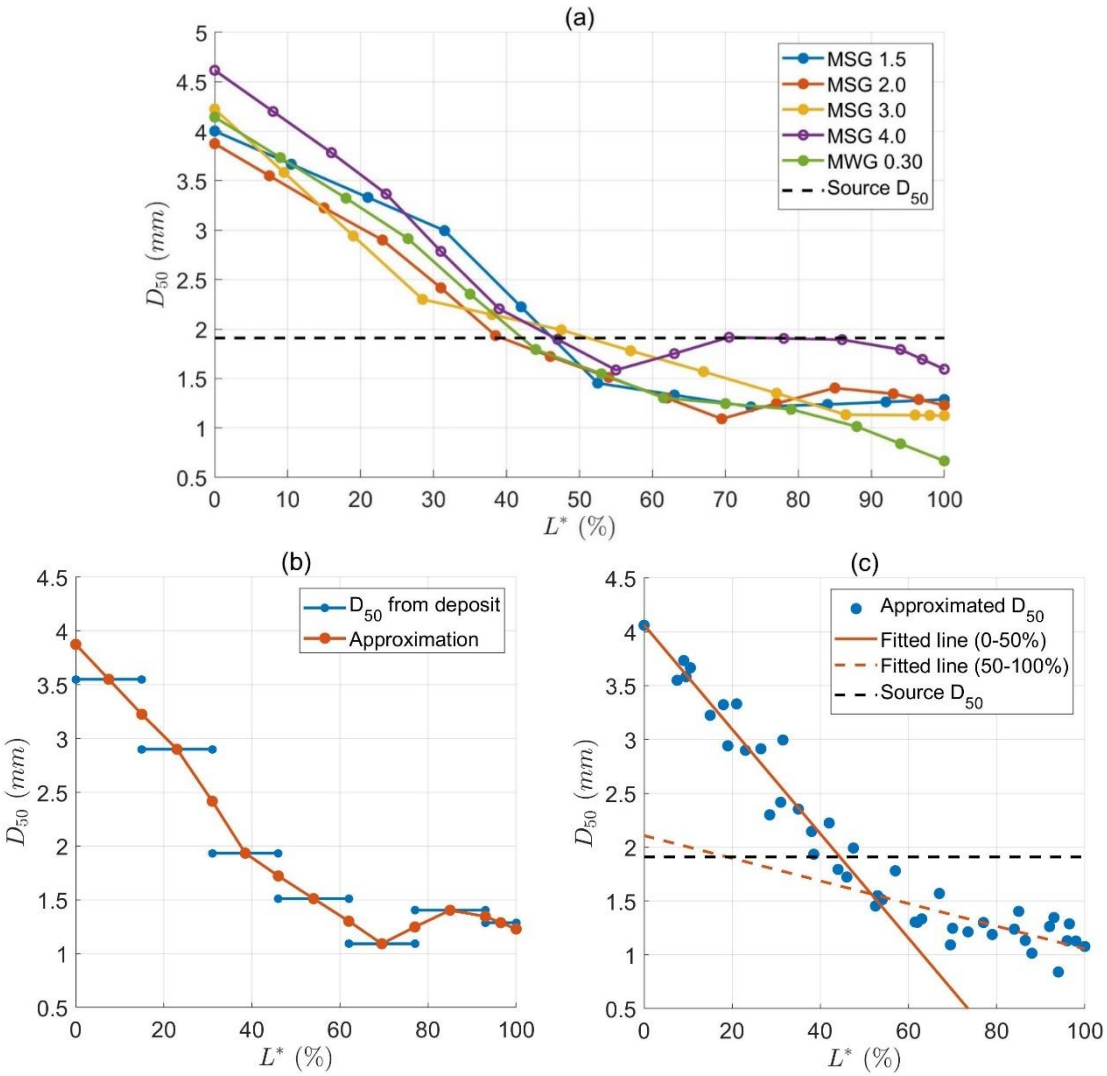

Figure 6-9: (a) The approximated D_{50} distribution of the well-graded flow deposits. (b) The determination of the approximated D_{50} distribution (red curve) based on the actual D_{50} data (blue horizontal lines) of sectionalised deposit (taking MSG 2.0 deposit as an example). (c) Bilinear fittings of the approximated D_{50} data points of all the tests.

6.3. Flow Profile

The side-view profiles of MSG and MWG flows captured by the high-speed camera at the downslope sensor-mounted zone are provided in Figure 6-10 and Figure 6-11, in which each row gives a tested flow with a different test variable while the three columns represent the leading edge, the main flow body and the flow tail from the right-hand side to the left-hand side (as the flow is moving from left to right in the camera view). The criteria of image selection for well-graded flows are the same as those for uniform flows (see Sec. 5.3); that is, the photograph of the leading edge is taken where a group of grains that are closely apart from each other touches the right-hand margin of the image, that of the main body is chosen where the maximum flow depth reaches the right-hand edge, and that of flow tail is represented by the frame where the main surge just passes the camera view, i.e. where the change in flow height becomes unnoticeable after a sharp drop. The leading edge is typically full of coarse sediments and the thin flow tail is mainly composed of fine solids, with a few coarse grains rolling downslope. In the main body, an "oblique" boundary line separating the darker coarser grains and the lighter finer grains can be observed; a probable physical interpretation is that this boundary line is the margin of extruded fine particles, before which those darker coarser grains do not fill up the channel width, while after which the flow material starts to crowd the channel and to pressurise the sidewalls, pushing a layer of fines to the sidewall. For MSG flows, the main flow body grows thicker with an increasing source volume, whereas the leading edge and flow tail remain similar; the exception of the test with 4L source volume gives a very thick leading edge where grains are bonded together as a cluster, showing that the flow material is poorly-fluidised. For MWG tests with increasing water content, the leading edge seems to become thinner with more dispersed grains, the flow tail seems slightly wavier, and the thickness of the main body stays similar or slightly reduces; however, the aforementioned boundary line between coarser and finer grains becomes closer to the leading edge and farther away from the captured image of the main body taken near the maximum flow height. In addition, an extension tendency that makes flow thickness reduce during the motion from upslope to downslope position (i.e. from one side of the camera view to the other) can be observed in most of the well-graded flows.

Another important finding is that the flow motion seems to highly depend on the agitation condition of the source material. Three trials with "MWG 0.30" test conditions were conducted and they generated different flow profiles as shown in Figure 6-12, in which each row represents an individual trial and two columns give the images of the first and second surges (i.e. the part

where the rise of flow height is observable). The first trial gave steeper surge fronts, a larger flow height difference between the two surges and some splashing material; the second trial, compared with the first one, led to a longer and thinner flow body that looks highly stretched, with a relatively smoother or flatter top flow surface; the third trial appears in an intermediate state between the other two trials. Referencing the profiles of the "MSG 4.0" flow, the flow in the first trial is likely the least agitated as the concentrated solids seem to need more time to allow more fine grains to suspend in the fluid phase; the flow in the second trial is probably the most agitated due to its high level of material extension which should occur under the circumstance where the grains are sufficiently dispersed rather than firmly interlocked with each other; the third trial seems to give a moderate agitation condition and hence is selected to represent the "MWG 0.30" flow. This issue is essentially the limitation of the small-scale experiment: the hopper shape with a wide top and a narrow bottom facilitates the consolidation of the source material and hampers the use of an electric mixer or agitator; the compromised manual agitation can thoroughly stir the source material to guarantee the successful test initiation but is difficult to control and maintain the agitation condition. Even with the help of an electric mixing tool, whether a stable agitation condition can be held at a small scale is still doubtful, given the short settlement time scale of the well-graded material. In summary, the initial condition of small-scale well-graded granular flows is difficult to keep consistent, resulting in relatively poor repeatability of well-graded flow experiments.

Flow height measurements using the ultrasonic sensor and PIV analysis generally agree with each other for well-graded granular flows. The contrast between these two flow height measurements for MSG and MWG test groups is given in Figure 6-13 (a) and (b), where data from the ultrasonic sensor are denoted by blue asterisks and from the PIV by red curves. The ultrasonic sensor responses seem highly credible as Maple Mud flows produce no saltated grains that can interfere with sensor signals on the flow surface (see Sec. 4.3). PIV detection, on the other hand, usually gives flow height estimation slightly lower than (but still similar to) sensor signals around the surge peaks, especially in the case of "MWG 0.26" where PIV analysis fails to capture the first surge peak; this may result from the ultrasonic sensor detecting the height at the centre of the flow, which is thicker than that at the sidewall where the PIV analysis is applied. Also, the part close to the flow tail is commonly very thin, hence PIV analysis may not generate accurate results. Therefore, for Maple Mud flows, ultrasonic sensor responses are used to describe flow height.

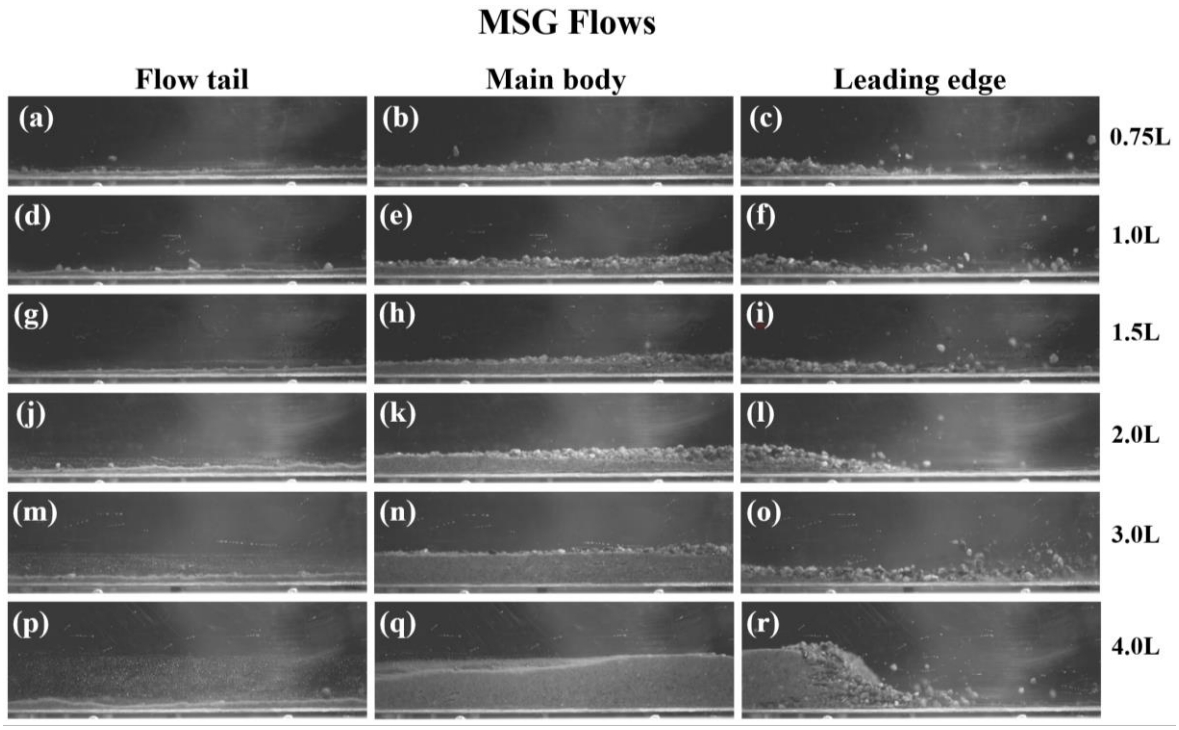

Figure 6-10: Recorded profiles of MSG flows where the camera view is tilted at 30° to make its bottom side parallel with the inclined flume bed. Three columns are the flow tail, main body and leading edge of each tested flow, while five rows are five tested flows with evolving source volumes that are exhibited in the test labels at the right-hand side margin.

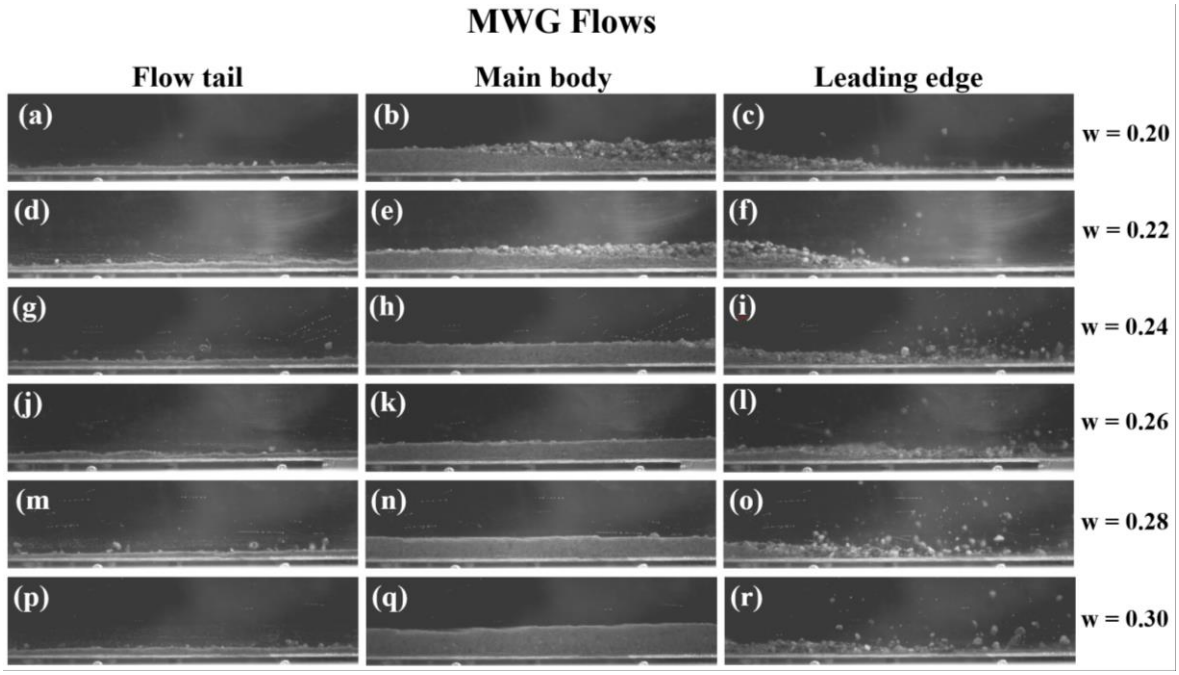

Figure 6-11: Recorded profiles of MWG flows where the camera view is tilted at 30° to make its bottom side parallel with the inclined flume bed. Three columns are the flow tail, main body and leading edge of each tested flow, while five rows are five tested flows with an evolving water content that are exhibited in the test labels at the right-hand side margin.

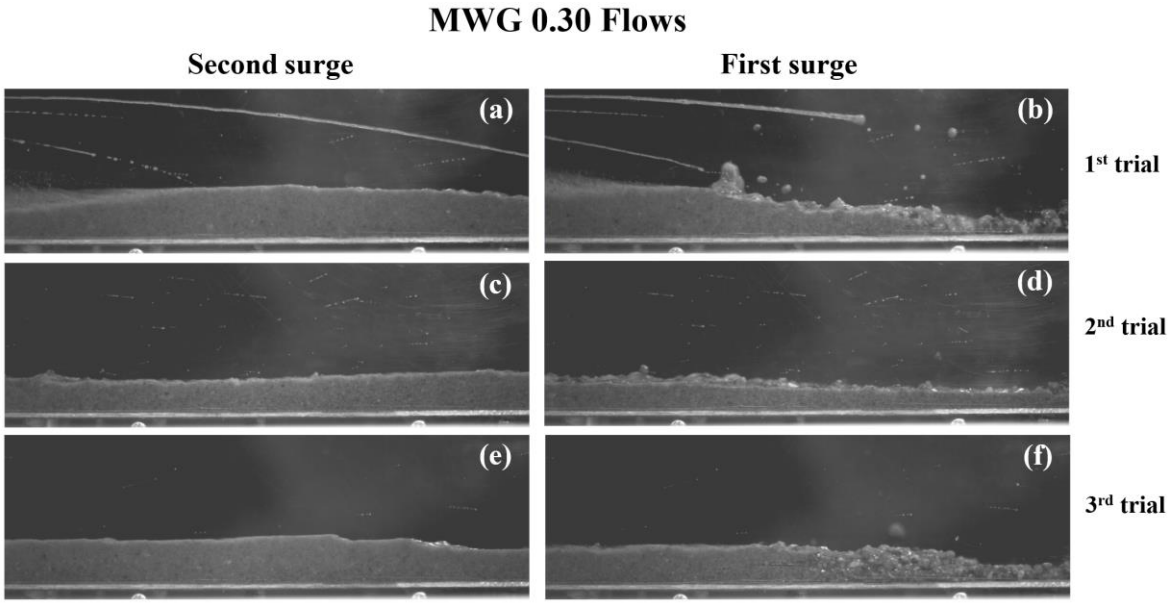

Figure 6-12: Recorded profiles of three trials of the MWG 0.30 flow. Two columns are the first and second surges of each flow, while three rows are three separate trials with different initial agitation conditions.

Flow height evolution of MSG and MWG flows with time are respectively exhibited in Figure 6-14 and Figure 6-15, where the "main surge" part of each flow (see Sec. 3.3) is plotted by solid lines and other parts are presented by dashed lines; the absolute flow heights (h) are included in subplots (a) and the flow heights normalised by the averaged grain size (h/δ) are in subplots (b). the averaged grain size, δ, for well-graded Maple Mud is expressed by the location-depended mean grain size (see Sec. 6.2) denoted by $D_{50}(x^*)$, where x* is the flow length relative to the "main surge" duration, ranging from 0% at the start of the main surge to 100% at the end of the main surge. This relative flow length can be derived from the absolute flow length, x, which, at a certain time, t, can be estimated by:

$$x(t) = \sum_{0}^{t} u_{ave}(\mathrm{t})\Delta t \tag{6-2}$$

in which t is time, $u_{ave}(t)$ is depth-averaged velocity varying with time, and Δt is the time interval of the PIV analysis which is equivalent to the reciprocal of framerate, yielding 1/3000 second (see Sec. 3.2.2); the relative flow length x* at t can then be calculated by:

$$x^*(t) = \frac{x(t) - x(t^* = 0)}{x(t^* = 1) - x(t^* = 0)} \tag{6-3}$$

where t* is the time normalised by the "main surge" duration, hence t* = 0 means the start of the main surge and t* = 1 denotes the end. Combined with Eq. (6-1) which gives a linear

simplification of D_{50} distribution across the front half of the deposit, D_{50} (also the averaged grain size δ) values within the "main surge" part as a function of x* are described by:

$$\delta = D_{50}(x^*) = -2.425 \cdot x^* + 4.064, \qquad x^* = 0 - 1 \tag{6-4}$$

noting that the equation is altered in response to the range of the independent variable changing from L* = 0 – 0.5 (in Eq. (6-1)) to x* = 0 – 1.

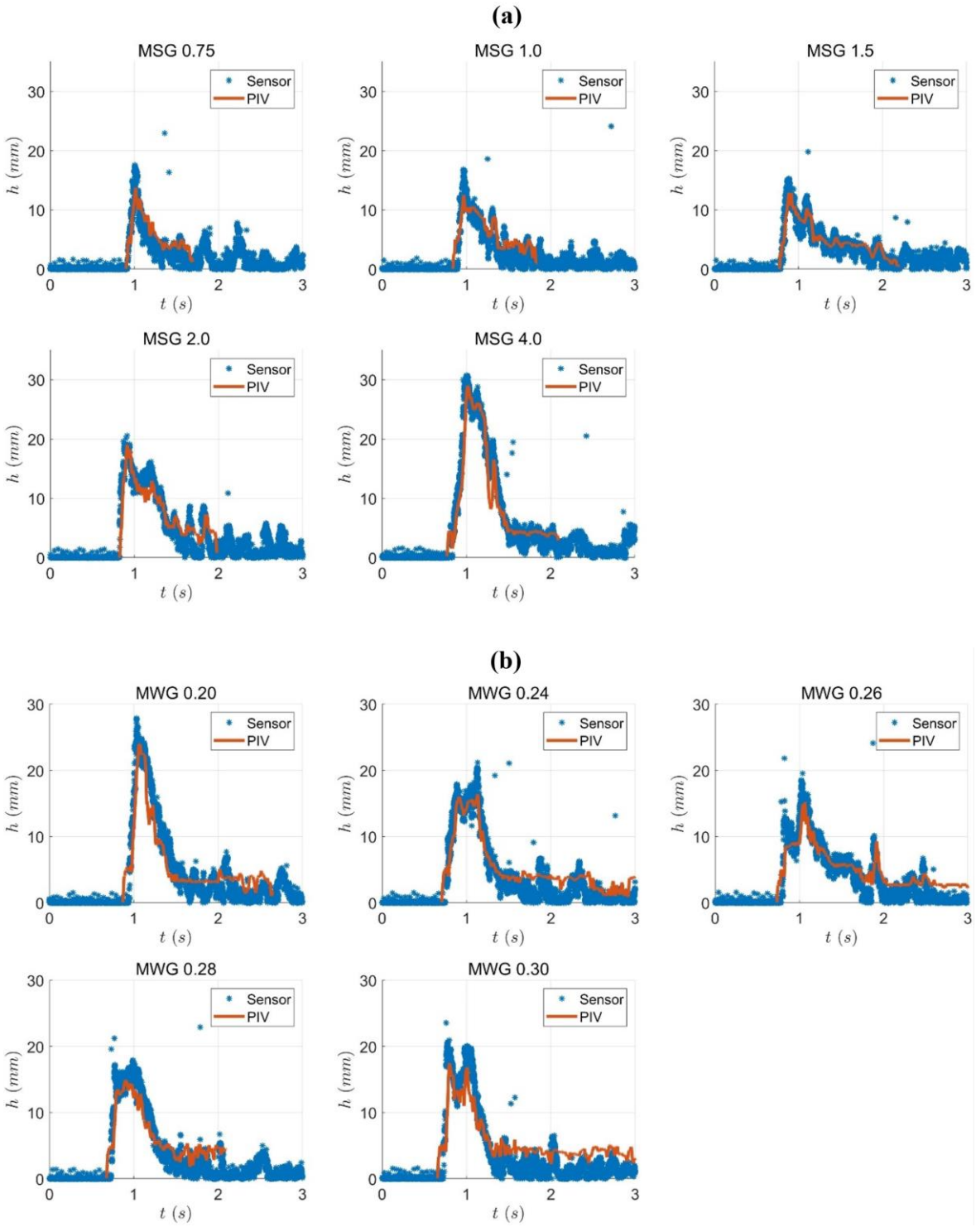

Figure 6-13: Contrasts between flow height of (a) MSG flows and (b) MWG flows measured by the ultrasonic sensor (in blue asterisks) and PIV analysis (in red lines).

The contrast among the MSG flow heights (Figure 6-14) shows that well-graded flow generally grows thicker with an increased source volume, but the maximum height of the 0.75L flow looks larger than those of the 1L and 1.5L flows. All the MWG flows (Figure 6-15) give similar flow height profiles except for the "MWG 0.20" flow which produces the thickest flow. These non-systematically evolving flow heights can be attributable to the aforementioned unstable agitation condition of the source material. Furthermore, although the averaged grain size (δ) varies with the spatial location (x*, which is controlled by the time value), discrepancies in the distribution on the time axis are narrow between the absolute flow height (h) and the normalised flow height (h/δ); this indicates that the microscopic length scale (i.e. grain size δ) and the macroscopic length scale (i.e. flow size h) are roughly correlated for well-graded material.

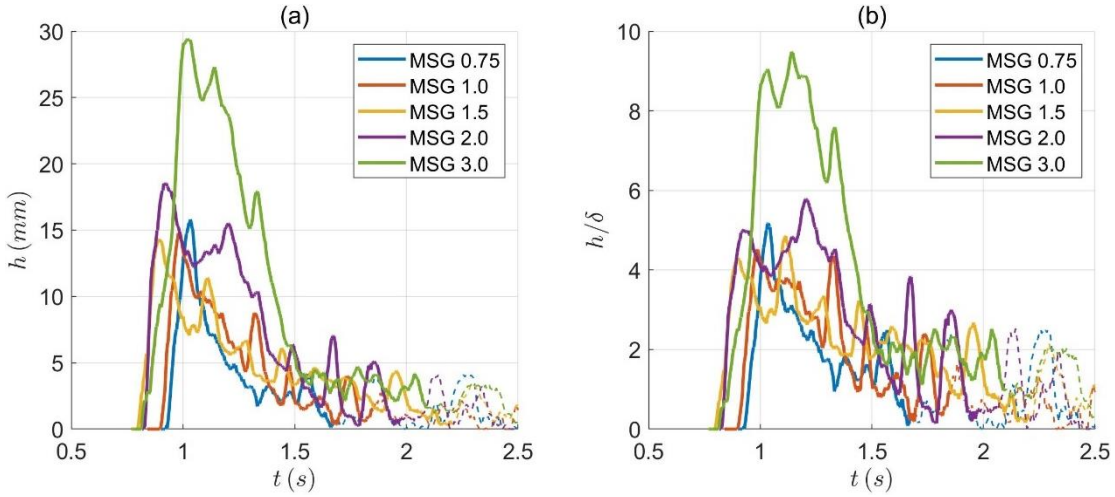

Figure 6-14: Time histories of (a) absolute MSG flow height and (b) MSG flow height normalised by average grain size, in which the "main surge" of the flow is highlighted by the solid line and other parts are in dashed lines.

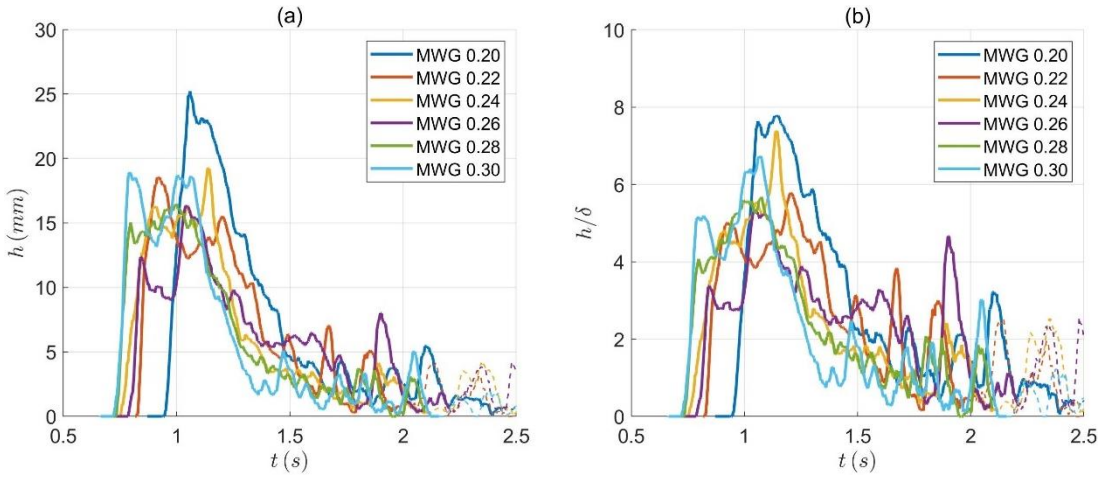

Figure 6-15: Time histories of (a) absolute MWG flow height and (b) MWG flow height normalised by averaged grain size, in which the "main surge" of the flow is highlighted by the solid line and other parts are in dashed lines.

6.4. Basal Normal Stress and Pore Pressure

Basal normal stress (σ_{basal}) and basal pore pressure (p_{basal}) were acquired from well-graded flow experiments. For all the MSG and MWG flows, the σ_{basal} and p_{basal} measured at the downslope sensor-installed position are contrasted with the theoretical steady-flow normal stress (σ_{st} as defined in Eq. (4-1)) and pore pressure (p_{st} as given in Eq. (5-1)) generated at the flume bed in Figure 4-8 (a) and (b), where data within the "main surge" part of the flow are presented by solid lines and those collected from other parts are in dashed lines; note that p_{st} due to the fluid weight is estimated by the flow height (Eq. (5-1)), hence the water surface is presumed equivalent to the top surface of the flow. The curve shapes of σ_{basal} and σ_{st} for all the well-graded tests are overall similar but the measured σ_{basal} is consistently larger than the theoretical value σ_{st}, suggesting that the actual basal normal stress always exceeds the pressure provided by the weight of the moving flow material; this is probably due to the phenomenon that stress signal can respond to the load not applied to the grains directly above the load cell, instead of miscalibration of load cells (see Appendix A). The basal pore fluid pressure (p_{basal}) mainly shows negative values with a small source volume and/or low water content when the theoretical steady-flow pressure (p_{st}) is consistently positive; when well-graded flow possesses a larger source volume or higher water content, p_{basal} gradually becomes dominated by positive values that are closer to or even greater than p_{st} values, especially for the MWG flows with w = 0.28 – 0.3 where significant excess pore pressure appears.

Basal normal stresses (σ_{basal}) for MSG and MWG flows are given in Figure 6-17 and Figure 6-18, respectively, where all the subplots (a) depict σ_{basal} at the upslope position while subplots (b) present those at the downslope position. Most well-graded flows show a common tendency that the upslope σ_{basal} values are larger than the downslope ones, agreeing with the extension of flow material observable in the high-speed images (see Sec. 4.3), except the "MSG 3.0" flow where σ_{basal} at both positions give similar responses and the "MWG 0.20" flow where the downslope σ_{basal} has a larger maximum value than the upslope σ_{basal}; this may imply that extension trend is more difficult to develop in a large-volume or unsaturated well-graded flow, perhaps because the source material is less fluidisable under the same agitation condition due to the larger mass (in the large-volume sample) or internal suction effects (in the unsaturated sample, see Sec. 2.4.1). Overall, basal normal stress increases with the source volume (Figure 6-17): σ_{basal} curves are quite close when the source volume is between 0.75L and 1.5L, but show notable increments responding to the source volume from 1.5L to 4L. With higher water content, however, no systematic evolution can be found in MWG flows (Figure 6-18): when the water content increases from 0.22 to 0.3, the downslope p_{basal} remain quite similar while the upslope p_{basal} curves present larger differences but without showing a regular pattern; this may indicate that water content poses less impact on the basal normal stress than the initial agitation condition which can affect the extension extent of the flow material and hence the flow height distribution.

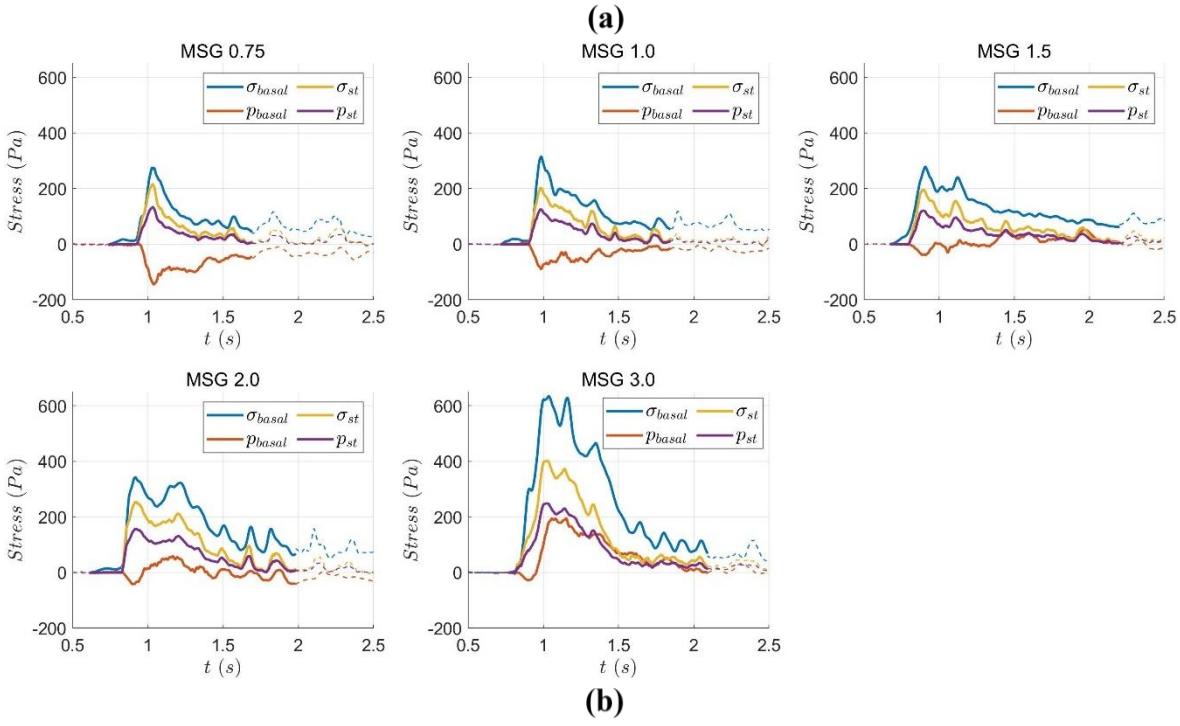

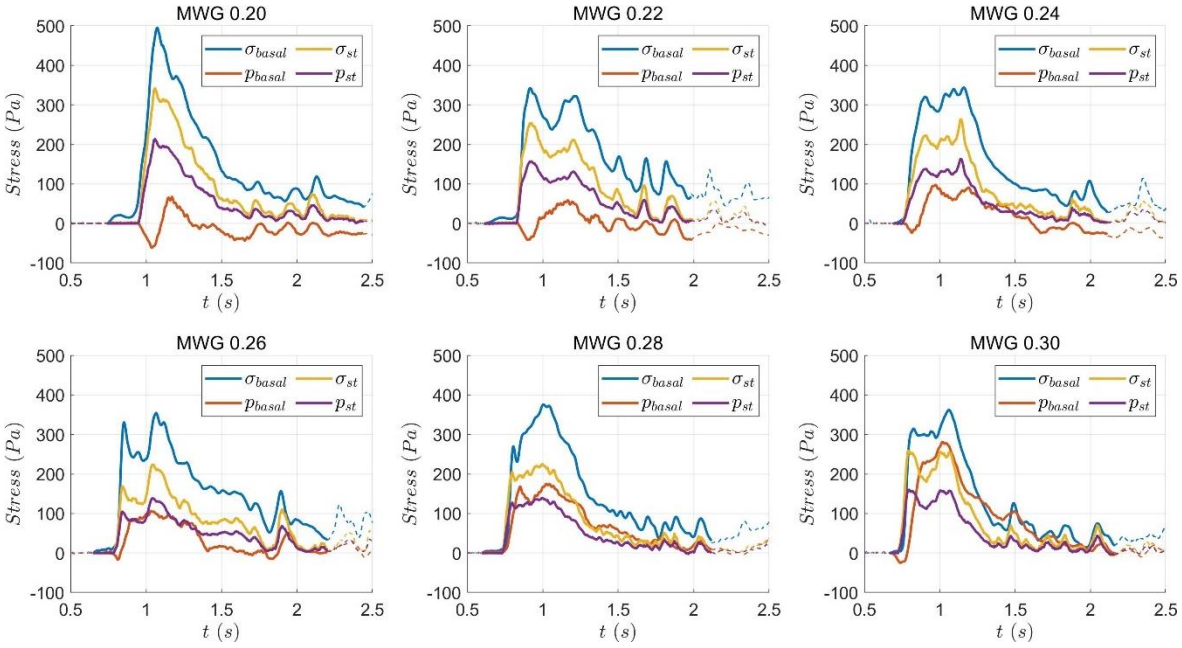

Figure 6-16: Contrasts between basal normal stress (σ_{basal}), basal pore pressure (p_{basal}), theoretical steady-flow basal normal stress (σ_{st}) and theoretical steady-flow basal pore pressure (p_{st}) at the downslope position. Data from (a) MSG flows and (b) MWG flows are shown; solid lines denote the "main surge" part of the flow while dashed lines denote other parts.

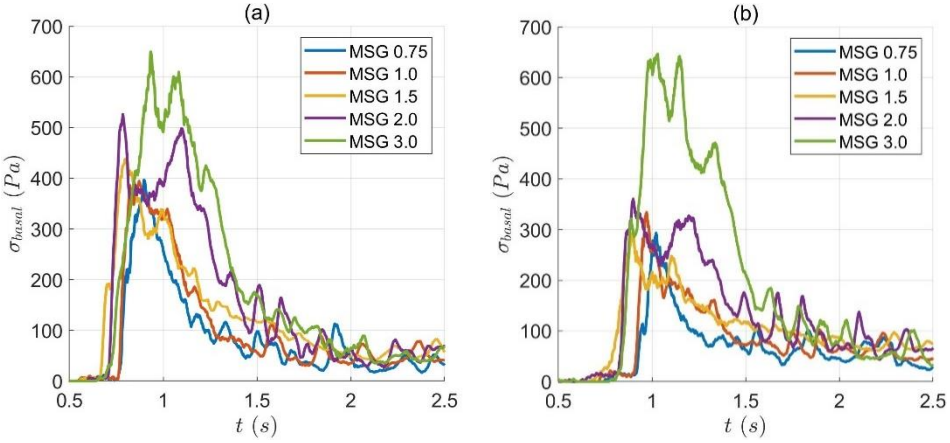

Figure 6-17: Contrasts of basal normal stresses (σ_{basal}) for MSG flows at (a) the upslope position and (b) the downslope position.

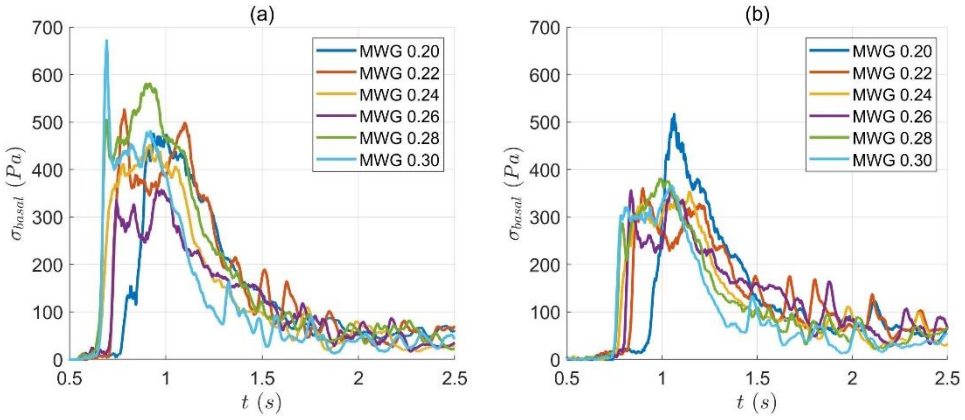

Figure 6-18: Contrasts of basal normal stresses (σ_{basal}) for MWG flows at (a) the upslope position and (b) the downslope position.

Basal pore pressures (p_{basal}) for MSG and MWG flows against time are contrasted in Figure 6-19 and Figure 6-20, where solid lines denote the "main surge" part of the flow whereas dashed lines denote the others; similar to the normal stress figures, p_{basal} data collected from the upslope and the downslope positions are assigned to subplots (a) and (b). On the whole, smaller source volumes and lower water content give lower p_{basal} (which can be negative), while larger volumes and higher water content give higher p_{basal}; however, individual tests may be out of tune with this overall pattern when compared with other tests having relatively close values of the test variable; for example, the upslope p_{basal} for "MSG 0.75" looks higher than that for "MSG 1.0", and p_{basal} curves for MWG flows in Figure 6-20 (a) seem to be distributed in random order when w = 0.22 – 0.3. Considering the difficulty of pore pressure measurement and the possibility of transducer error, the downslope p_{basal} data giving higher consistency should be the main object of analysis. The downslope p_{basal} values in Figure 6-19 (b) are mostly negative when the source volume is smaller than 1.5L, with their distribution on the time axis reducing with source volume but still sufficient to cover the entire surge; the positive p_{basal} starts to appear and occupies the latter half of the "main surge" duration when source volume increases to 1.5L; above 1.5L, the positive values then grow with source volume and dominate the p_{basal} distribution on the time axis, whereas the negative values are confined at the leading edge of the flow which is expected to be dry or unsaturated. With an increased water content for MWG flows (Figure 6-20 (b)), the negative part of the p_{basal} persists for a shorter time and its peak value at the flow front decreases (i.e. less negative and closer to zero), while the positive part of p_{basal} lasts longer and its peak value is higher. Noting that even for the "MWG 0.20" flow where the source material is initially unsaturated, the time history of p_{basal} still gives a notable part dominated by positive pore pressure within the main surge, instead of a main surge that is entirely controlled by negative pore pressure as in "MSG 0.75"; thus, the source volume of well-graded flows appears to have a crucial influence on the development and decline of suction effects.

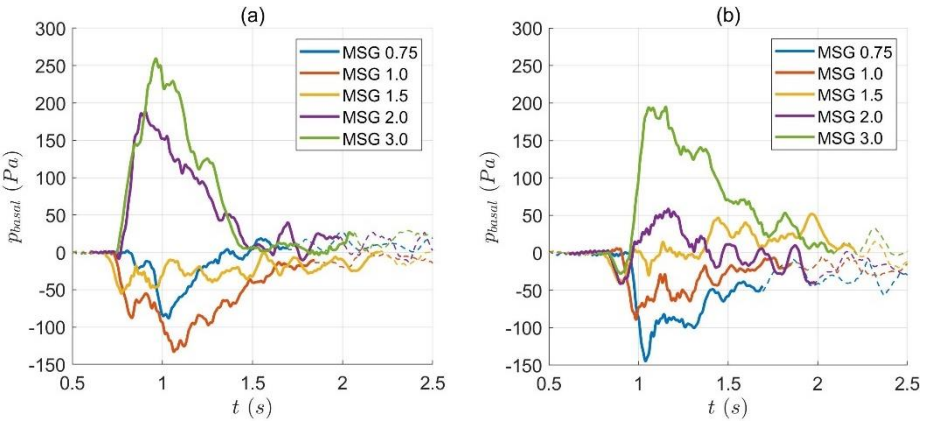

Figure 6-19: Basal pore pressures (p_{basal}) for MSG flows against time, including unsaturated flows at (a) the upslope position and (b) the downslope position, and saturated flows at (c) the upslope position and (d) downslope position. The "main surge" part of the flow is in solid lines and other parts are in dashed lines.

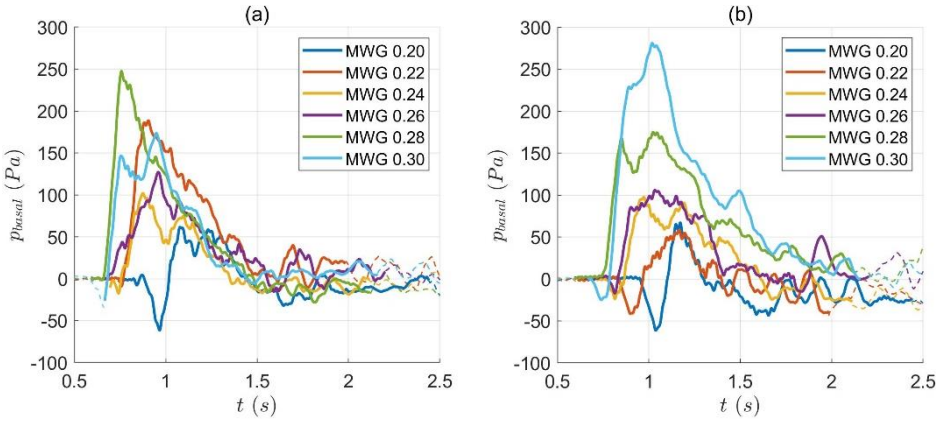

Figure 6-20: Basal pore pressures (p_{basal}) for MWG flows against time, including unsaturated flows at (a) the upslope position and (b) the downslope position, and saturated flows at (c) the upslope position and (d) downslope position. The "main surge" part of the flow is in solid lines and other parts are in dashed lines.

6.5. Flow Velocity

Velocity profiles for MSG and MWG flows are illustrated in Figure 6-21 and Figure 6-22, where velocity curves for each flow are plotted with the time interval of t* = 5%, i.e. 5% of the "main surge" duration (see Sec. 6.3), and the red dashed lines mark the position of the basal patch centre (as shown in Figure 3-6); the velocity curves in yellow are closer to the flow front while those in blue are closer to the tail. All the subplots (a) present the actual velocity data while subplots (b) display the velocity data fitted by power functions (see Sec. 3.2.3). Several features can be observed from the actual velocity profiles of well-graded granular flows. (i) Flow velocity gradually decreases from the flow front (yellow curves) to the flow tail (blue curves). (ii) Slip velocities are extremely low at the basal boundary; as no-slip boundary condition is a typical assumption in fluid dynamics (Day, 1990), this suggests that the well-graded flow material in motion can be effectively regarded as a viscous fluid. (iii) Large difference in value exists between surface velocity and slip velocity in the flow head (yellowish parts), indicating a strong bulk shear of the flow material. (iv) The local velocity structures around the maximum flow height can present a portion of lower values below the surface flow layer, resulting in the velocity curves shaped more like zigzags; this can be caused by two possible factors as highlighted in Figure 6-23: the first is that surface grains may not touch the sidewall and hence may move at a slightly higher velocity than the portion below does (this should not have a major effect as the surface velocity would be too high, assuming the lower velocities are believable); whereas the second is that darker grains visible in the camera view (which give more image

texture and are likely to experience more sidewall friction than the fine particles do) are coarser, heavier and have greater inertial movement than the fines, hence may result in a reduction in the local velocity estimation that is averaged over a patch in the PIV analysis; the second effect due to the inertial grain movement is weakened near the basal layer of the flow as the distance normal to the bed is reduced, hence lower velocities mainly appear in the upper portion of the flow height. Given that lower velocity data in the zigzag curves are probably real but not necessarily important, the power-fitted velocity profiles in Figure 6-21 (b) and Figure 6-22 (b) can be deemed adequately reliable to represent the flow kinematics.

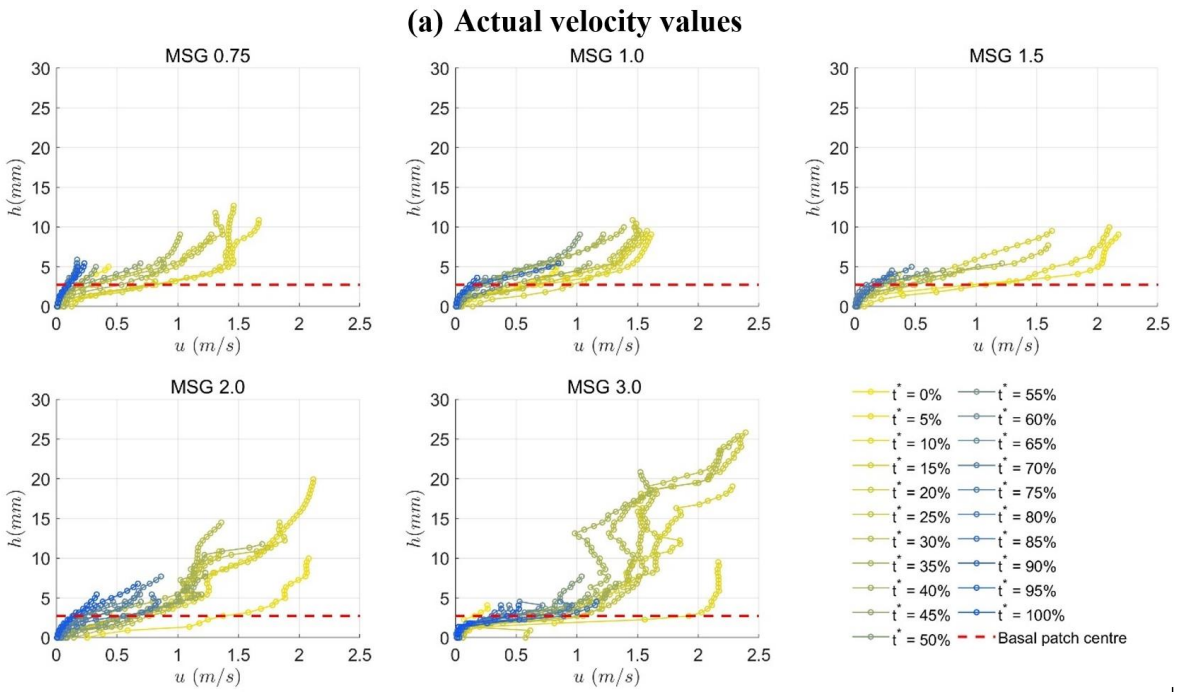

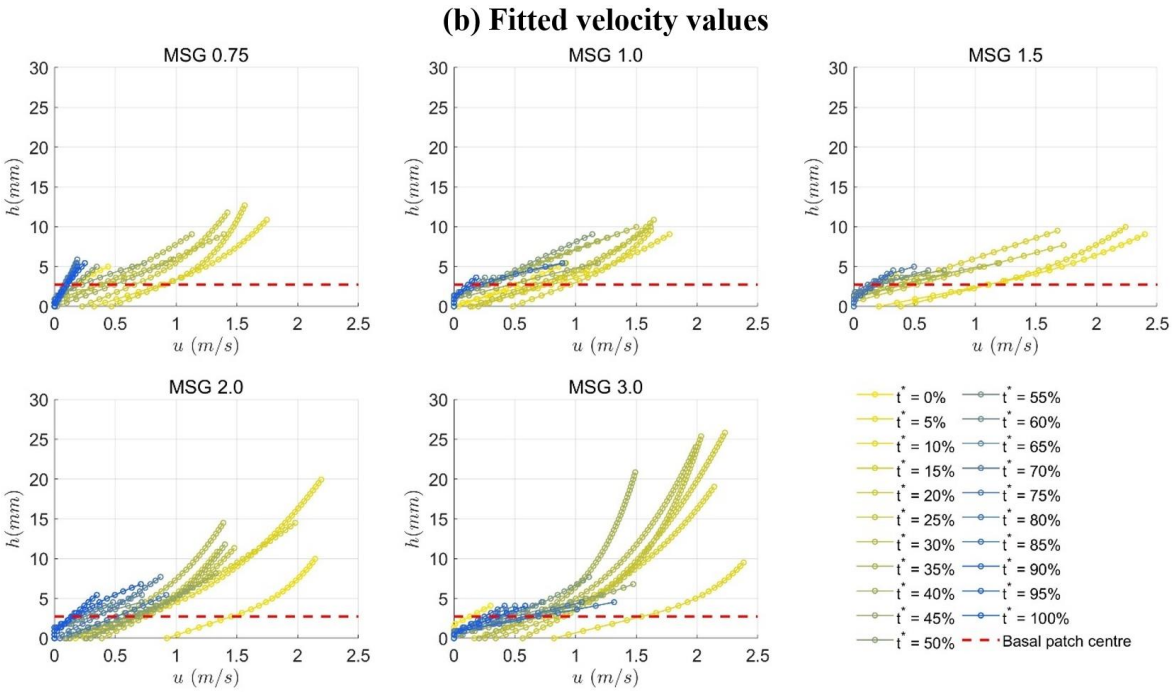

Figure 6-21: Velocity profiles of MSG flow distributed in subplots with (a) actual velocity data and (b) power-fitted velocity data. Velocity curves are plotted every 5% time for the "main surge" duration. Yellow curves are closer to the flow front and blue to the flow rear; red dash lines denote the position of the basal patch centre.

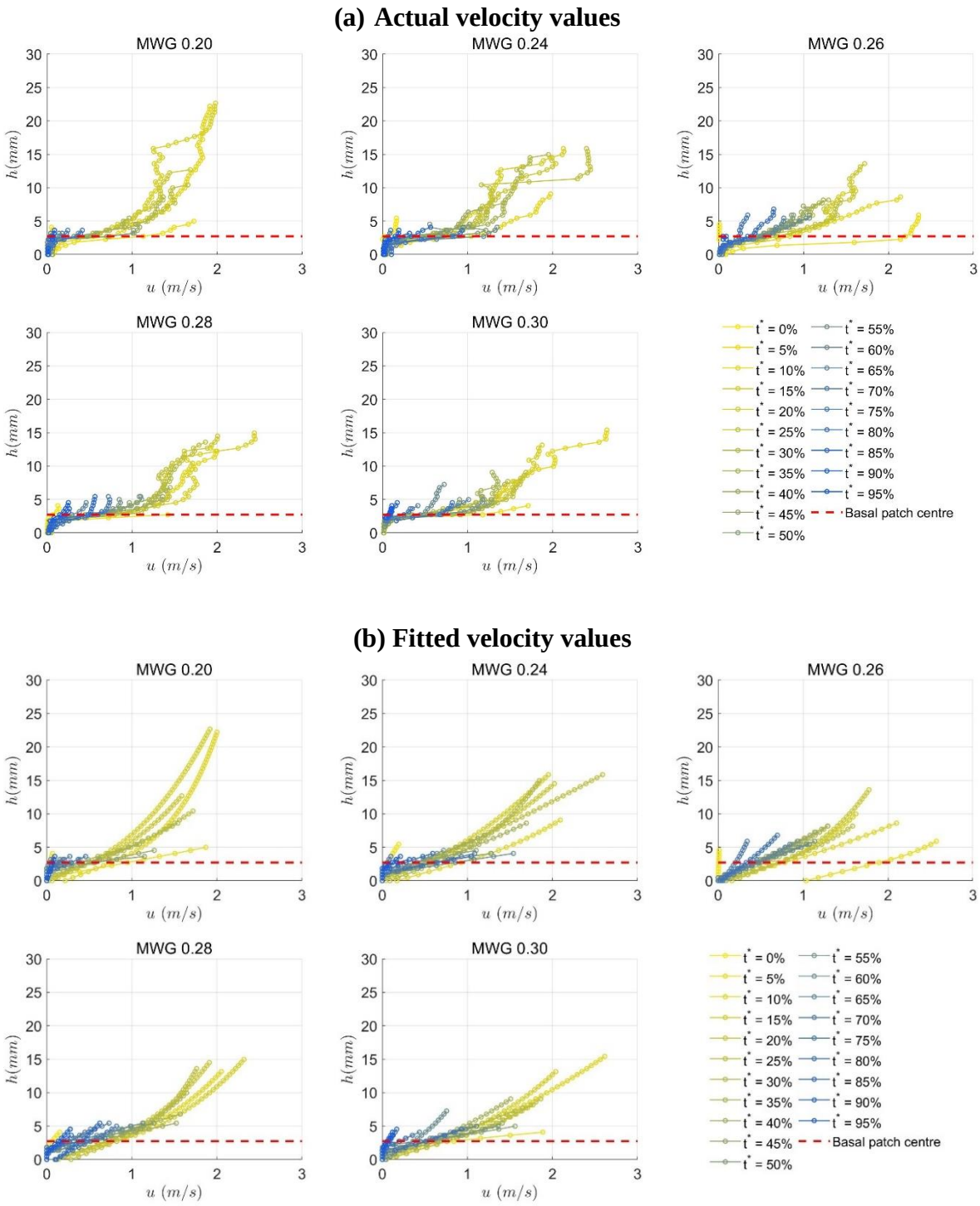

Figure 6-22: Velocity profiles of MWG flow distributed in subplots with (a) actual velocity data and (b) power-fitted velocity data. Velocity curves are plotted every 5% time for the "main surge" duration. Yellow curves are closer to the flow front and blue to the flow rear; red dash lines denote the position of the basal patch centre.

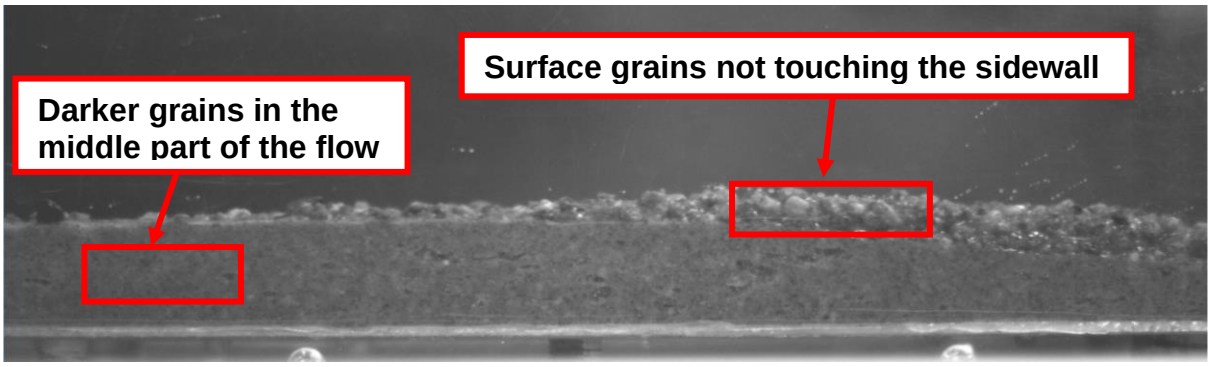

Figure 6-23: Possible causes of the unsmooth actual velocity profiles in well-graded flows.

To straightforwardly show the change in the shape of well-graded velocity profiles with different test variables, the velocity curves at their respective maximum flow height are taken from all the Maple Mud flows and are then combined with Figure 6-24 (for the MSG group) and Figure 6-26 (for the MWG group), similar to the presentation of ceramic bead flow results (see Sec. 5.5); the supplements Figure 6-25 and Figure 6-27 aim to reduce the stochasticity of using only one instantaneous curve to represent the flow head by using velocity profiles averaged over 0.02 second around the time index of peak flow height (0.01s both before and after). For all the velocity profile figures, the actual velocity (u) data against flow height (h) is given in subplots (a) whereas the velocity normalised by the depth-averaged velocity (u/u_{ave}) against the normalised flow height (z/h) is in subplots (b).

With an increased source volume (Figure 6-24Figure 4-11 and Figure 6-25), the actual velocity curve around the peak flow height does not show a consistent evolution: velocity magnitude grows with V_{bulk} increasing from 0.75L to 1.5L, but decreases with V_{bulk} from 1.5L to 4L; the fitted slip velocity seems to slightly reduce with the source volume but, given that the actual slip velocities of MSG flows are all close to zero (Figure 6-21 (a)), those values of about 0.5m/s may be overestimated. Meanwhile, the u/u_{ave} profiles of MSG flows show a clear trend that the difference between surface velocity and slip velocity increases with source volume, with the velocity gradient becoming larger and more uniform across the normalised flow height. For MWG flows shown in Figure 6-26 and Figure 6-27, however, all the velocity curves are pretty close in shape and magnitude with no observable evolution pattern with water content, whether described by the actual or normalised values; therefore, the increase in water content does not lead to significant differences in the velocity profile of well-graded flows.

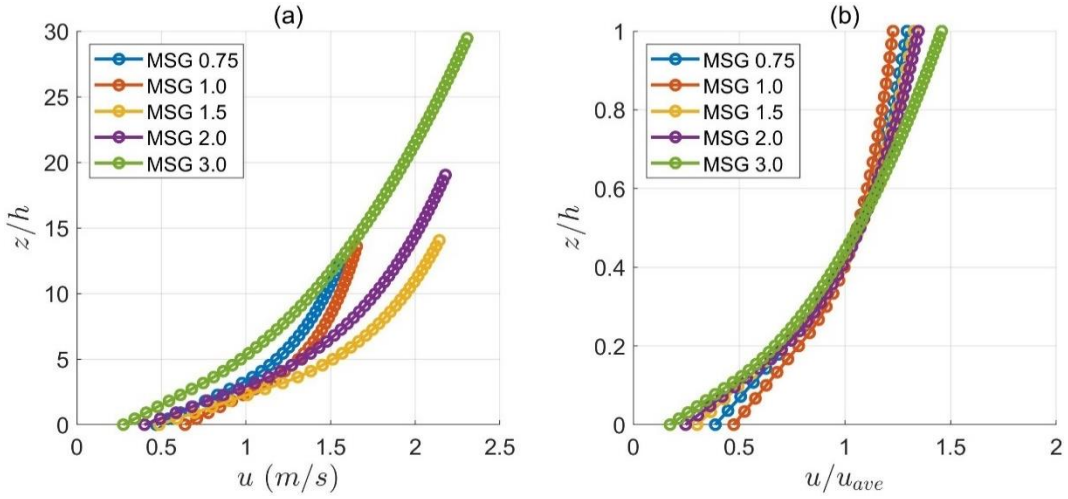

Figure 6-24: Velocity profiles at the peak flow height for all MSG flows. (a) Actual velocity against flow height, and (b) normalised velocity (by depth-averaged velocity) against normalised flow height.

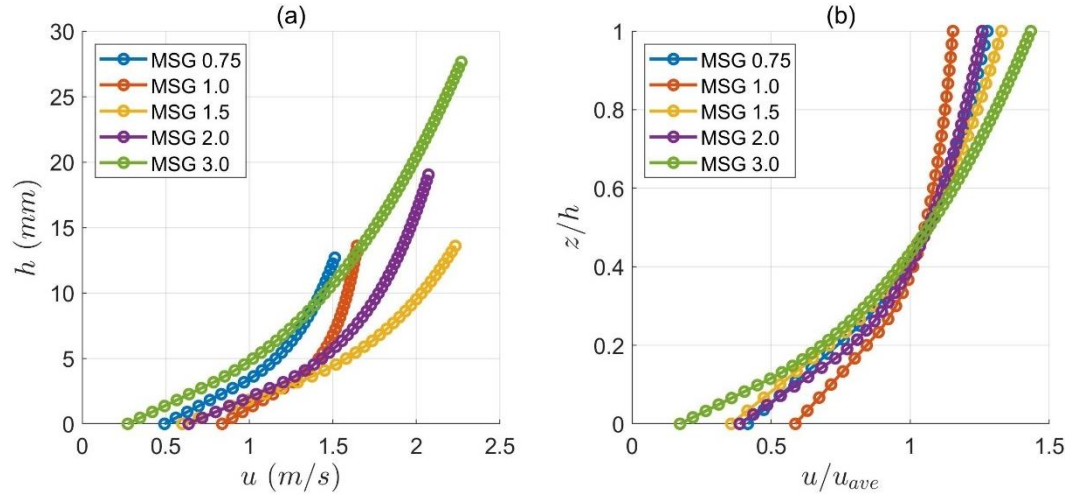

Figure 6-25: Velocity profiles averaged over 0.02s around the peak flow height for all MSG flows. (a) Actual velocity against flow height, and (b) normalised velocity (by depth-averaged velocity) against normalised flow height.

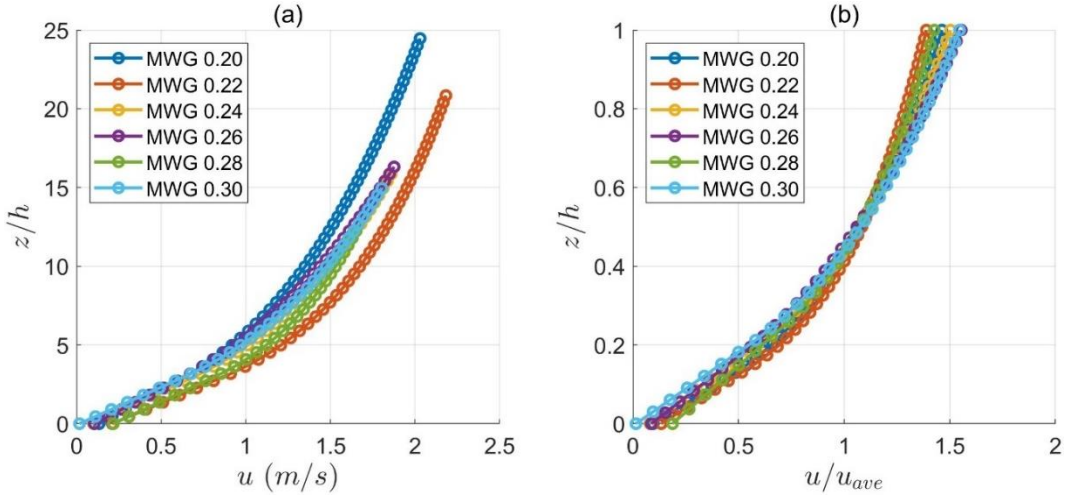

Figure 6-26: Velocity profiles at the peak flow height for all MWG flows. (a) Actual velocity against flow height, and (b) normalised velocity (by depth-averaged velocity) against normalised flow height.

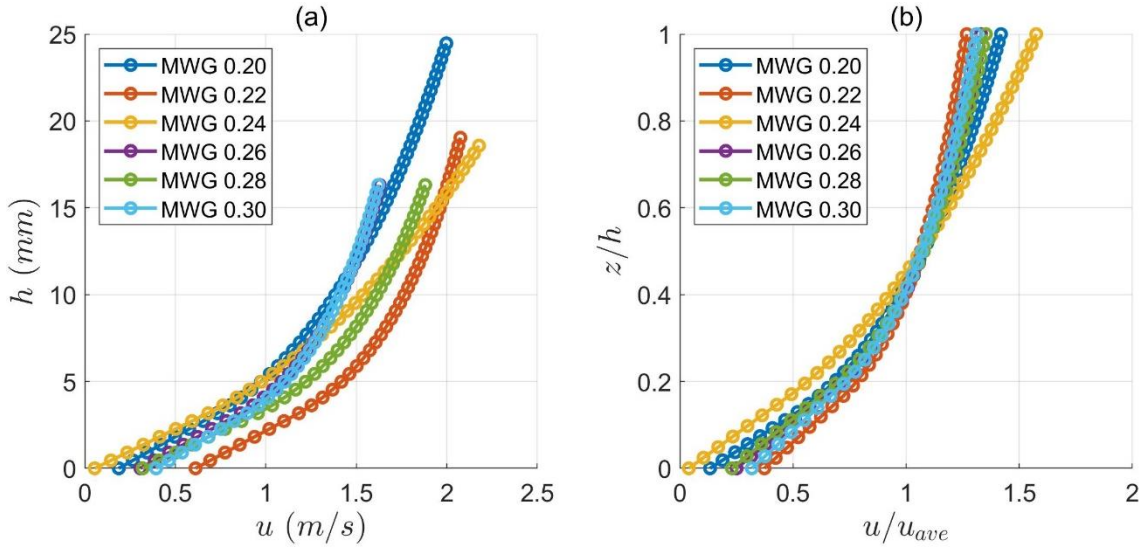

Figure 6-27: Velocity profiles averaged over 0.02s around the peak flow height for all MWG flows. (a) Actual velocity against flow height, and (b) normalised velocity (by depth-averaged velocity) against normalised flow height.

Depth-averaged velocity histories of MSG flows and MWG flows are separately given in Figure 6-28 (a) and (b), where u_{ave} data within the "main surge" part of each flow are plotted by asterisks. The u_{ave} of each well-graded flow firstly rises to its maximum value when the main surge enters the PIV-analysed zone and then overall continuously drops (with several small ups-and-downs in between) to an extremely low value slightly more than zero when approaching the flow tail. Furthermore, the u_{ave} generally increases with source volume (Figure 6-28 (a)) but the velocity profiles collected from the maximum flow height do not show a similar relationship (Figure 6-24), implying that the location of the peak flow height on the time axis relative to the beginning of the "main surge" is inconsistent for well-graded flows of the different source volume. On the other hand, u_{ave} curves with different water content remain very close to each other throughout the "main surge" duration (Figure 6-28 (b)); this again highlights that well-graded flow velocity is influenced by the change in source volume but seems barely dependent on water content.

6.6. Dimensional Analysis

Estimation of three dimensionless numbers, i.e. the Savage number (N_{Sav}), Bagnold number (N_{Bag}) and friction number (N_{fric}), which identify the flow regime and dominant momentum transfer mechanism and are determined based on the D_{50} grain size that varies with the location within the "main surge" (Eq. (6-4)), are presented below. The local dimensionless numbers (see

Sec. 3.5 for the computation) of MSG flows based on the fitted velocities and distributed across the normalised flow height (z/h) are given in Figure 6-29 and those of MWG flows are in Figure 6-30, in which N_{Sav}, N_{Bag} and N_{fric} are separately exhibited in subplots (a), (b) and (c). For each well-graded flow, a data curve of the interested dimensionless number is taken at the peak flow height is depicted in the corresponding subplot to show the structure of local values; the black dashed line appearing in each subplot represents the threshold value of the demonstrated dimensionless number, namely 0.1 for N_{Sav}, 200 for N_{Bag} and 100 for N_{fric} (see Sec. 2.3).

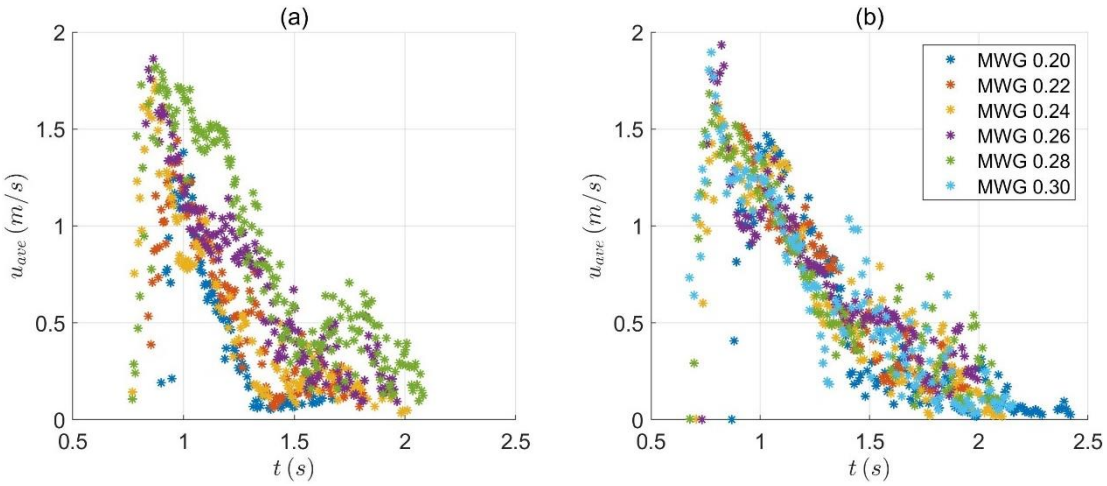

Figure 6-28: Time histories of depth-averaged velocities of (a) MSG and (b) MWG flows.

Each dimensionless number gives similar structures of local values across the normalised flow height (z/h) for all the well-graded flows, whether varying in source volume or water content: N_{Sav} is larger near both boundaries (although values at the top surface tend to be lower than those close to the bed) and smaller in the middle portion of the flow height, N_{Bag} continuously grows from the top to the bottom with a gradually increased rate, and the N_{fric} curves are shaped roughly similar to the mirrored profiles of N_{Sav}, smaller at the boundaries and larger in the middle. The profiles of three dimensionless numbers do not vary systematically with different source volumes, as shown in Figure 6-29. In contrast, with increased water content, the local values of N_{Sav} tend to become higher, those of N_{Bag} remain relatively stable and those of N_{fric} tend to decrease; this indicates that more pore fluid in well-graded flows can reduce the importance of solid friction in the momentum exchange while not notably interfering with the effects of solid inertia and fluid viscous shear.

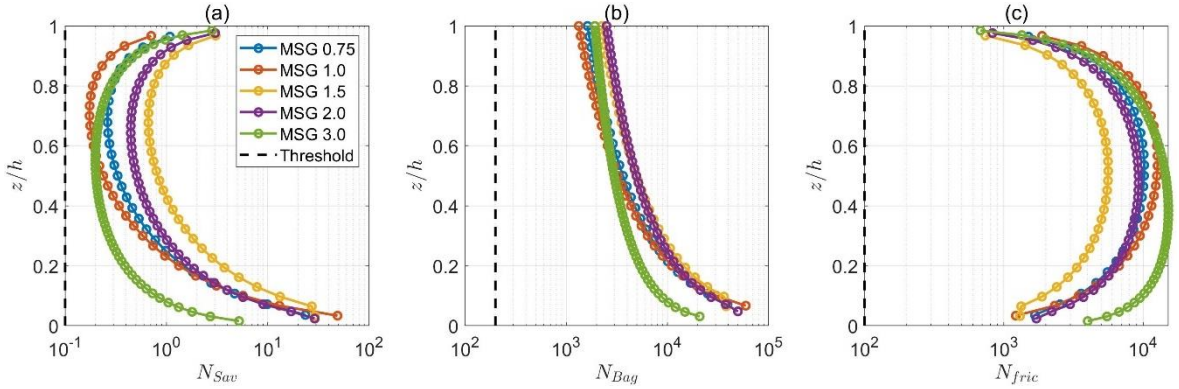

Figure 6-29: Local values of (a) Savage number, (b) Bagnold number and (c) friction number across the normalised height at the peak flow height for all MSG flows.

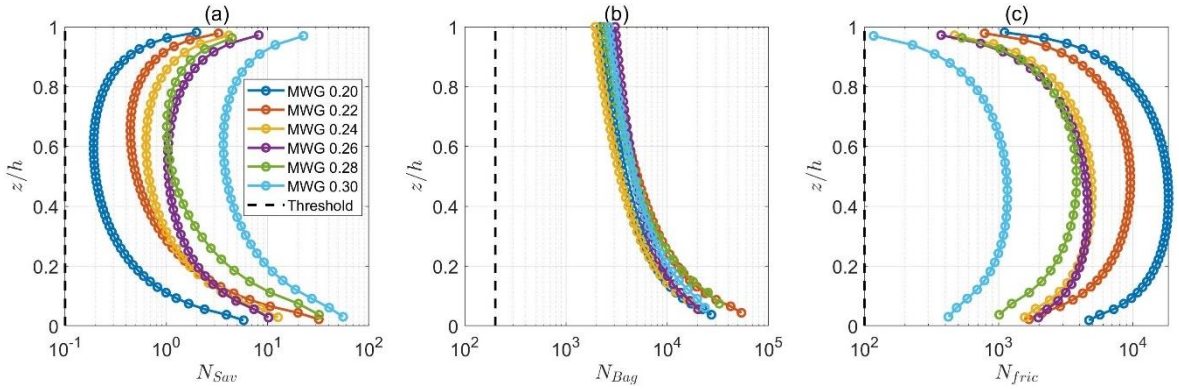

Figure 6-30: Local values of (a) Savage number, (b) Bagnold number and (c) friction number across the normalised height at the peak flow height for all MWG flows.

Mean values of all three dimensionless numbers ($\overline{N}_{Sav}$, $\overline{N}_{Bag}$ and $\overline{N}_{fric}$) across the flow depth are given in Figure 6-31 for MSG flows and Figure 6-32 for MWG flows, where data points are presented against the normalised flow height (h/δ); in each subplot corresponding with each dimensionless number, data appearing before the peak flow height are denoted by hollow circles whereas those after the peak flow height are represented by asterisks. The relationships of each dimensionless number with h/δ for well-graded flows are similar to those for fluid-mixed uniform flows as described in Sec. 5.6, hence are not reiterated here; various values of $\overline{N}_{Sav}$ and $\overline{N}_{Bag}$ (similar to Figure 5-33) around h/δ = 2 are most likely due to the different shapes of velocity profiles (i.e. from almost vertical to highly tilted). A larger source volume does not seem to notably change the well-graded flow regime as data points of all the MSG flows are highly overlapping (Figure 6-31). With higher water content, on the other hand, $\overline{N}_{Sav}$ shows a small increase, $\overline{N}_{Bag}$ remains relatively similar and $\overline{N}_{fric}$ displays a clear decrease (Figure 6-32); this implies that the solid frictional stress is probably reduced by a larger amount of pore fluid, causing the flow regime to become more inertial and more viscous. Moreover, all three

dimensionless numbers are above their respective threshold values in most well-graded flows, indicating that solid inertia is the dominant momentum transfer mechanism while viscous shear is the least important dynamical interaction; the exceptions are MWG flows with high water content ($w \geq 0.26$) where a considerable number of $\overline{N}_{fric}$ data points are below the threshold when $h/\delta < 3$, indicating that viscous shear stress starts to dominate over the solid frictional stress in the shallow part of the flow. Furthermore, Figure 6-33 and Figure 6-34 give plots of mean values of three dimensionless numbers calculated from a fixed sample D_{50} value, as this is the usual practice. Contrasted with Figure 6-31 and Figure 6-32 which utilise the time-dependent average grain size, mean values of dimensionless numbers using sample D_{50} do not show remarkable differences; this may be related to the small experimental scale where flow size is not sufficiently thick and long to present clearer difference.

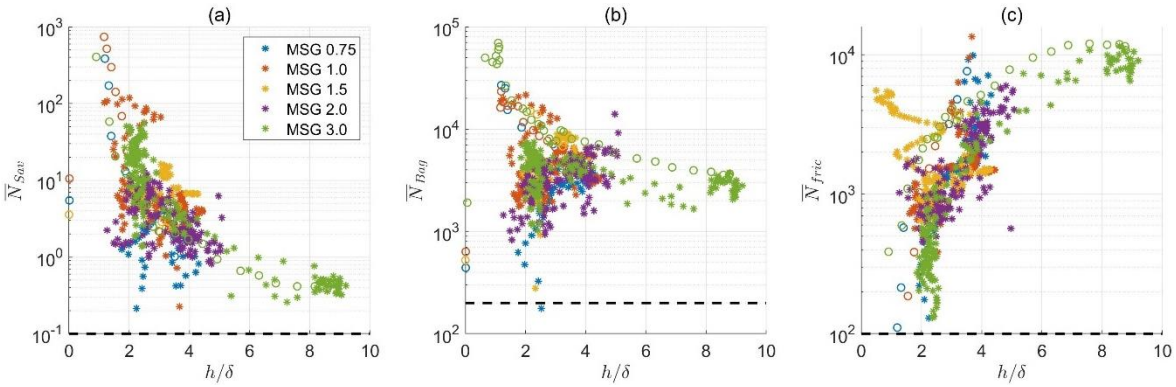

Figure 6-31: Mean values across the depth of (a) Savage number, (b) Bagnold number and (c) friction number against the normalised flow height by averaged grain size for all MSG flows, in which hollow circles denote the flow part before the maximum flow height while asterisks denote the part after.

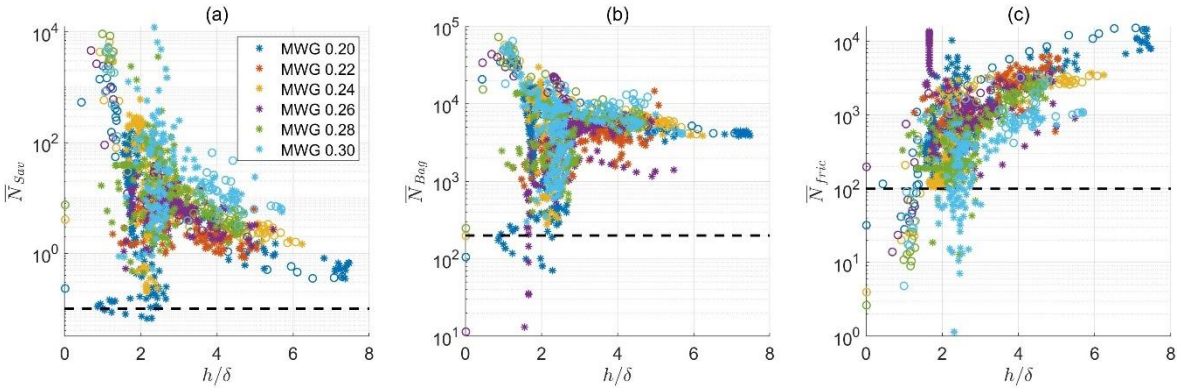

Figure 6-32: Mean values across the depth of (a) Savage number, (b) Bagnold number and (c) friction number against the normalised flow height by averaged grain size for all MWG flows, in which hollow circles denote the flow part before the maximum flow height while asterisks denote the part after.

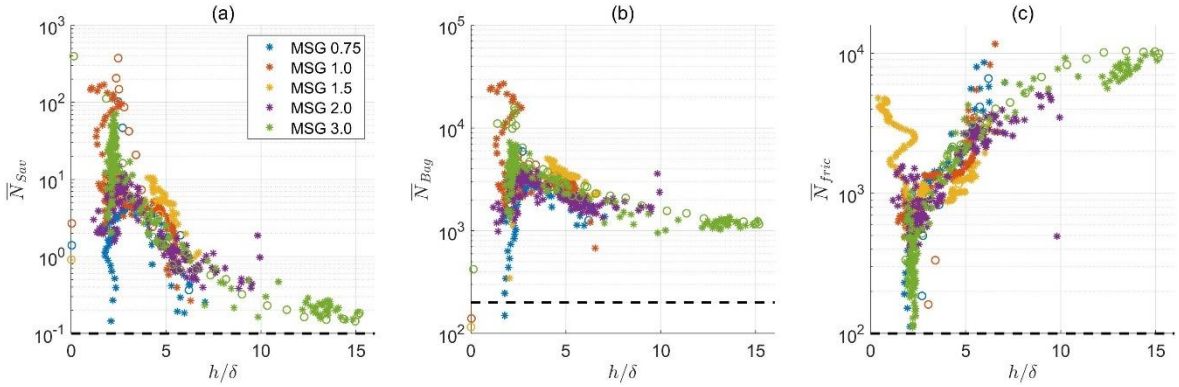

Figure 6-33: Mean values across the depth of (a) Savage number, (b) Bagnold number and (c) friction number against the normalised flow height by the sample D_{50} for all MSG flows, in which hollow circles denote the flow part before the maximum flow height while asterisks denote the part after.

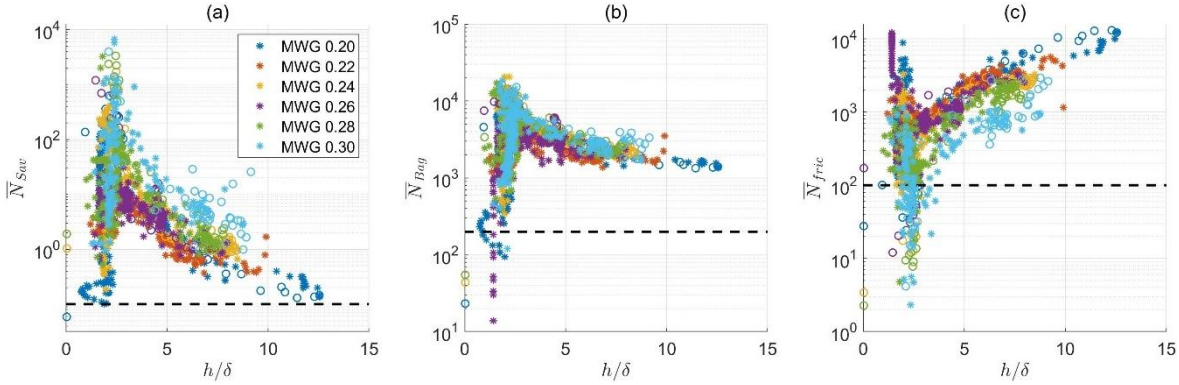

Figure 6-34: Mean values across the depth of (a) Savage number, (b) Bagnold number and (c) friction number against the normalised flow height by the sample D_{50} for all MWG flows, in which hollow circles denote the flow part before the maximum flow height while asterisks denote the part after.

7. Discussion

Preface

So far, the experimental results of dry uniform flows (CDU), fluid-mixed uniform flows (CSU and CWU) and fluid-mixed well-graded flows (MSG and MWG) have been given in the previous Chapter 4, 5 and 6. This chapter aims to put the data resulting from different flow constituents together for comparisons and contrasts to deduce the fundamental roles of pore fluid and polydispersity in granular-flow mechanisms.

This chapter falls into a few separate sections discussing the following topics: Sec. 7.1 contrasts the runout behaviours of flows with different material compositions and attempts to find the decisive physical process to the bulk flow mobility according to the deposition mechanism; Sec. 7.2 analyses the influence of different flow constituents on the flow velocity and shear mechanism; Sec. 7.3 pays attention to the behaviour of the fluid phase within a granular flow surge, trying to interpret the unusual responses of basal pore-pressure transducers, which present smooth evolutions from suction to buoyancy with both source volume and water content; lastly, Sec. 7.4 contrasts the data acquired in this study with those from other works to roughly show the impacts of particle size and scale effect.

7.1. Runout Behaviours

7.1.1. Contrast of Bulk Flow Mobility

In Sec. 4.2, 5.2 and 6.2, the longitudinal deposit shapes of dry uniform flows, fluid-mixed uniform flows and wet well-graded flows are given separately. To highlight the similarity and differences in runout behaviours caused by different source materials, deposit outlines of ceramic

bead flows (both dry and wet) and Maple Mud flows are contrasted in Figure 7-1 and Figure 7-2 based on source volume and water content, respectively. As described in the previous chapters, dry uniform beads (CDU), fluid-mixed uniform beads (CSU and CWU) and well-graded Maple Mud (MSG and MWG) produce different morphologies related to their different deposition processes, which are straightforwardly shown in the following figures.

With a small source volume of 0.75L (Figure 7-1), all three flow constituents result in similarly short travel distances and positions of Centre of Gravity (COG), despite the different deposit shapes of a backward heap given by the "CDU 0.75" flow, a thick plump forward heap by the "CSU 0.75" flow and a thin flat heap by the "MSG 0.75" flow; when the source volume increases to 2L, the deposit shapes remain nearly identical (suggesting that their respective deposition mechanisms are unchanged) but their bulk mobility show clear differences: the COG of CDU flow stays more or less at the same place, that of CSU flow moves significantly farther, while that of MSG flow is located not as far as the COG of CSU flow when their travel distances are similar. Note that the water content for MSG tests was 0.22, lower than half of the value of 0.45 used in CSU tests; this means that well-graded material can give similar bulk flow mobility at a much lower water content, i.e. with a lot less pore fluid within the flow body.

If holding the same source volume and water content, the well-graded Maple Mud exhibits remarkably higher mobility than that of the uniform ceramic beads, as shown in Figure 7-2, where the deposits resulting from two litres of different source materials are contrasted; note that the contrasted water content values of 0.25 for ceramic beads ("CWU 0.25") and 0.24 for Maple Mud ("MWG 0.24") are very close but unidentical, whereas the 0.3 water content is the same for both materials ("CWU 0.30" compared with "MWG 0.30"). From the water content w = 0.25 to 0.3, the deposit of wet ceramic bead flow shows increased mobility but still less than that of a dry flow at the same source volume; on the other hand, Maple Mud flow with water content increasing from 0.24 to 0.3 presents a larger boost in the bulk mobility, which exceeds that of "CDU 2.0" deposit even when w = 0.24; although no dry well-graded tests were conducted as the fine sands and silt contained in Maple Mud would very likely be scattered, a dry Maple Mud flow would probably form a heap thicker near the proximal end towards inclined flume or in the middle (similar to the dry chute-flow deposit of polydisperse sediments reported by other researchers, e.g. Cagnoli and Romano (2012) and Yang et al. (2015)), hence its final COG position would probably be slightly farther than that of the "CDU 2.0" deposit but not likely past that of "MWG 0.24" since the forward heap indicates that most solids are pushed toward its distal end.

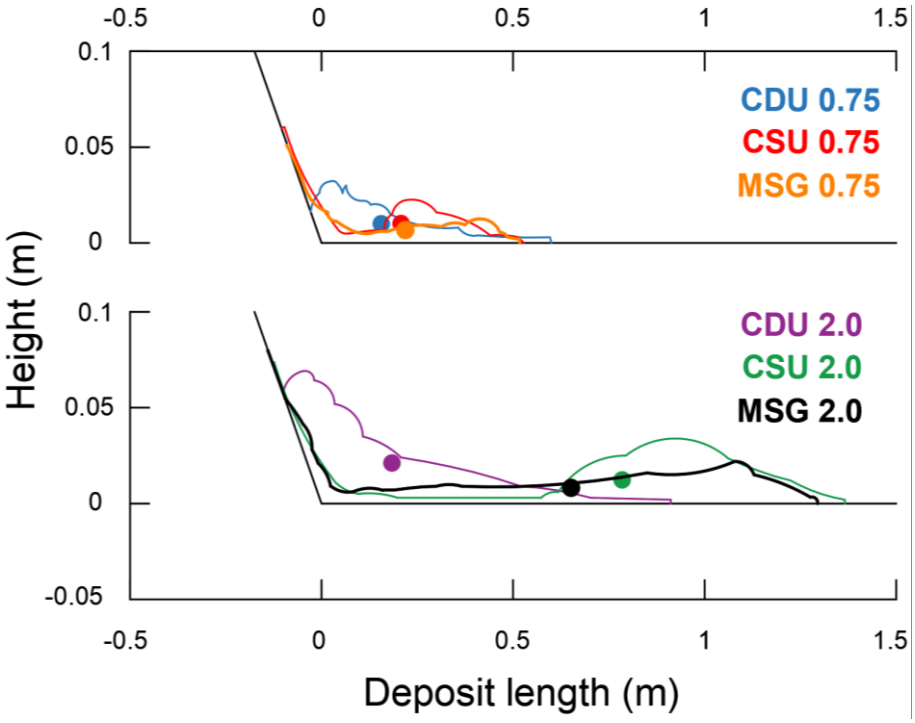

Figure 7-1: Contrast between the deposits of 0.75L and 2L flows composed of dry uniform beads (CDU), saturated uniform beads (CSU) with 0.45 water content and saturated well-graded soils (MSG) with 0.22 water content.

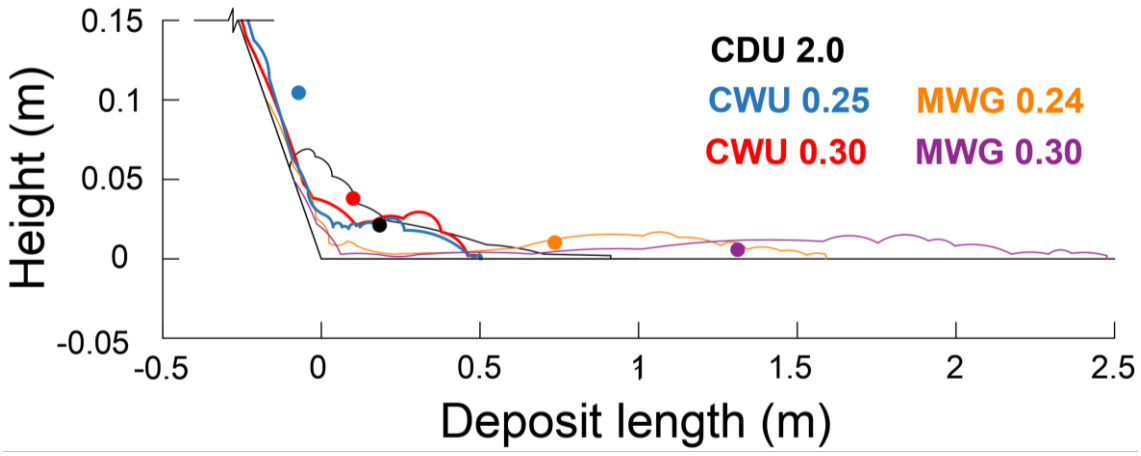

Figure 7-2: Contrast between the deposits of 2L flows composed of wet uniform beads (CWU) and well-graded soils (MWG) at similar water content; the deposit of 2L dry uniform flow (CDU) is plotted as a benchmark to surmise the deposit of 2L dry well-graded flow.

Bulk mobility of ceramic bead flows and Maple Mud flows against water content is contrasted in Figure 7-3 (variable source volume) and Figure 7-4 (variable water content), where subplots (a) and (b) respectively give the travel distance (L) and travel angle (α_T) profiles; similar to Figure 6-5, the 4L Maple Mud flow is represented by a hollow circle connected with other data points by a dashed line, due to the defective experiment. As shown in Figure 7-3, the well-graded flows present similar travel distance and travel angle results to the uniform flows but at a far lower water content: the water content for MSG flows is 0.22 while that for CSU flows is 0.45. Travel

distance and travel angle profiles given in Figure 7-4, also agree with that polydispersity enhances bulk flow mobility: the well-graded MWG flows exhibit significantly higher travel distance and lower travel angle than the uniform CWU flows do; note that the CWU test group covers a wider range of water content (w = 0.01 – 0.4) than the MWG group does because practically the Maple Mud becomes more difficult to agitate with a smaller amount of moisture and thus the source material may be inadequately fluidised.

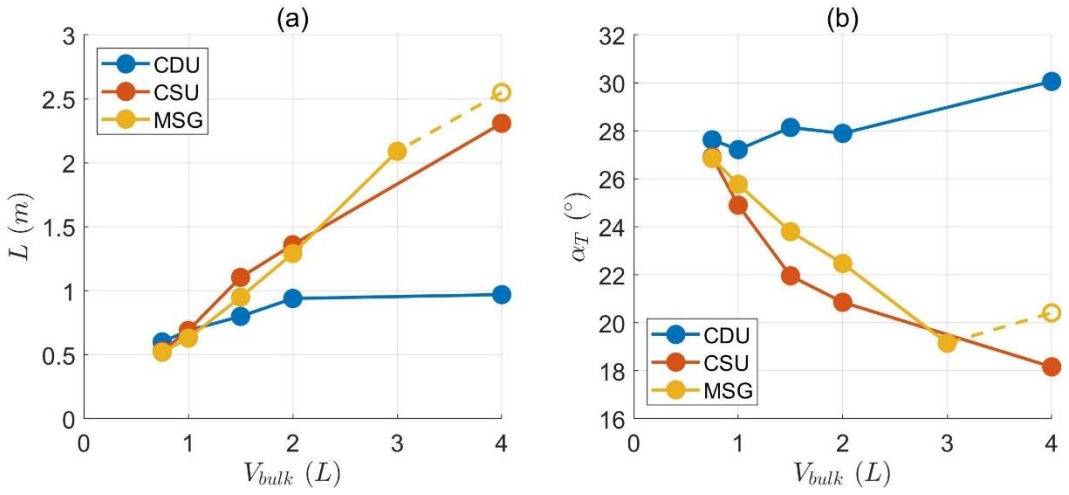

Figure 7-3: Contrast between the granular flows composed of uniform beads and well-graded soils with different source volume against (a) travel distance and (b) travel angle.

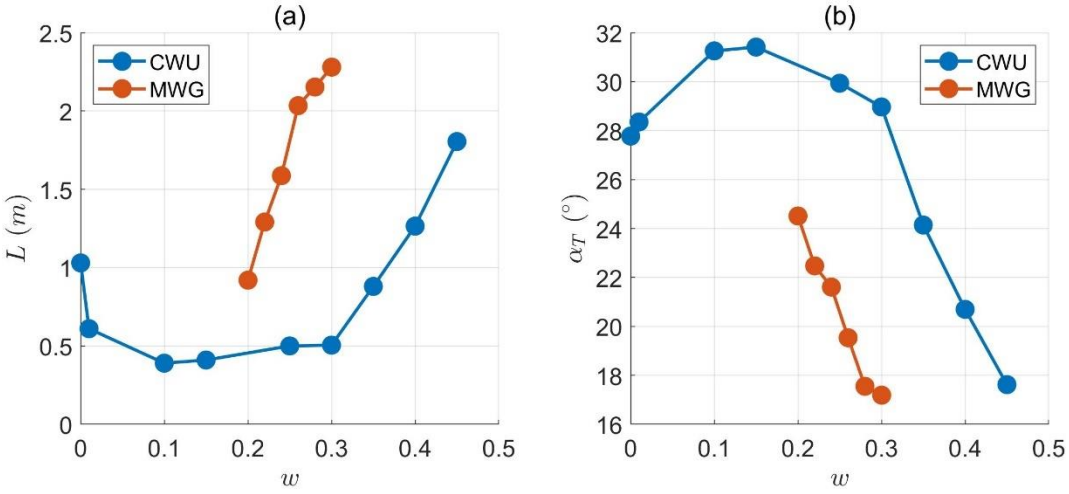

Figure 7-4: Contrast between the granular flows composed of uniform beads and well-graded soils with different water content against (a) travel distance and (b) travel angle.

Another interesting finding is that the close-to-linear relationship of bulk mobility with the water content can be found in Figure 7-4 for both the uniform and well-graded flow material; for consistency, here travel angle is used to characterise bulk flow mobility and to show its relationship with water content, as it is physically more reliable than the macroscopic travel

distance. The approximate linearity of the α_T profile of CWU tests roughly starts somewhere between w = 0.25 and 0.3, which may be associated with the boundary condition that the deposit COG moves across the start of the horizontal runout channel; thus, an assumption can be made that the travel angle begins to increase close to linearly with water content when the deposit COG leaves the inclined flume end along the horizontal direction. The start point of this approximate linearity is determined by an "imaginary COG" which is the intersection point between a vertical line drawn from one end of the horizontal channel and a line crossing the COGs of "CWU 0.25" and "CWU 0.30" deposits, as illustrated in Figure 7-5. The travel angle corresponding with this "imaginary COG" yields 29.2° for unsaturated ceramic beads and 30.4° for unsaturated Maple Mud; for simplicity, a boundary travel angle of 30° is used; this value, equivalent to the slope angle, may suggest a dependency of the close-to-linear growth in bulk flow mobility on the channel condition. The contrast between the evolution of travel angle with water content for CWU and MWG flows is then presented in Figure 7-6, in which two lines crossing the dashed line of α_T = 30° are fitted from the data within the close-to-linear range. The most conspicuous point to note is that the fitted lines of uniform flows and well-graded flows appear to have identical slopes; this extends the finding that uniform flows with different source volumes exhibit similar linear relationships between travel distance and water content, as shown in Figure 5-8, and implies that the linearity of bulk mobility against water content seems independent of flow material. The well-graded Maple Mud flows produce lower α_T (hence higher bulk mobility) than the uniform ceramic beads at the same water content. The fitted line of MWG flows intersects with the boundary travel angle at about w = 0.125, below which a concave curve with a maximum α_T (corresponding with the minimum bulk mobility) is expected, similar to the CWU data. Based on the influence of source volume, as given in Figure 5-8, and the observation of 1L Maple Mud deposits (Figure 6-1), the well-graded flow with a larger volume should lead to higher bulk mobility at a certain water content and a fitted line shifting towards w = 0, i.e. the deposit COG can move into the horizontal channel at a lower water content.

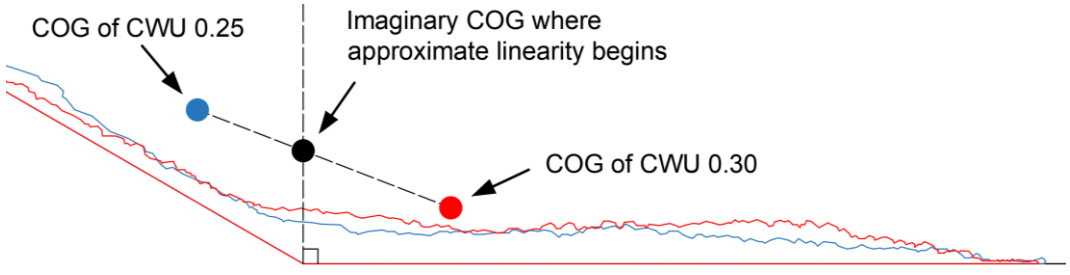

Figure 7-5: A schematic diagram of the determination of the imaginary COG related to the start point of the approximately linear relationship between travel angle and water content.

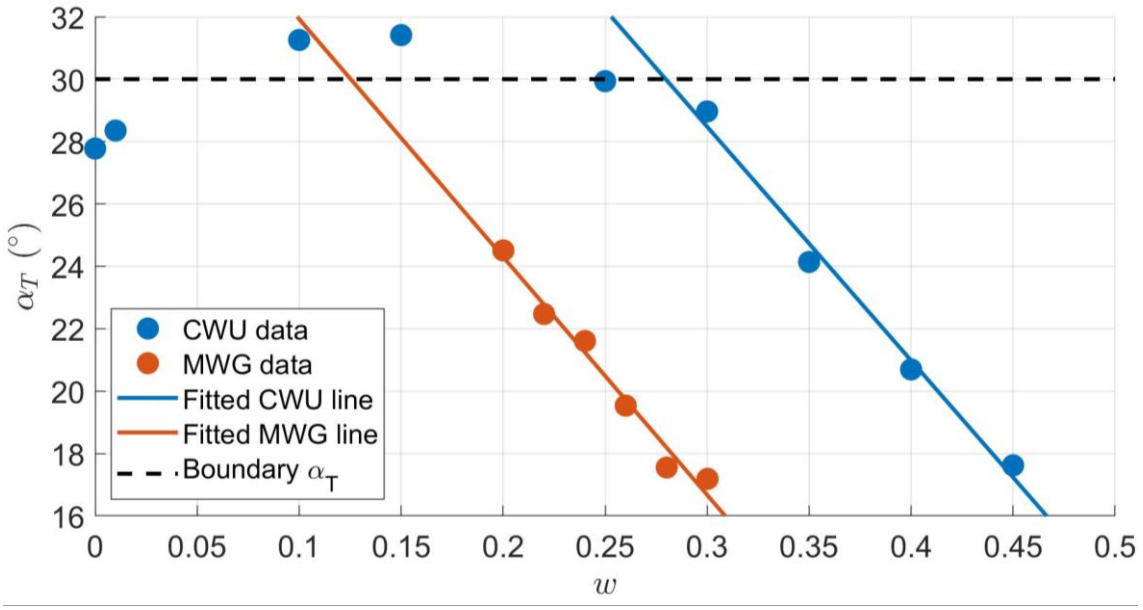

Figure 7-6: Contrast between the fitted lines of CWU flows (when $w \geq 0.3$) and MWG flows, where a black dashed line denotes the boundary travel angle representing the start of linearity.

7.1.2. Deposition Mechanism

Different source material composition gives a different deposition process, as illustrated in Figure 4-1, Figure 5-2 and Figure 6-2. The runout behaviours after granular flows rush into the horizontal channel can be phenomenologically divided into two types: (i) a sliding movement of the entire granular mass and (ii) a partial grain movement relative to the stopped deposit (e.g. the "climbing" of wet uniform beads and the "stretching" of well-graded Maple Mud), which mainly contribute to the further extension of COG position; the former may mainly depend on the flow velocity when entering the horizontal channel and the frictional resistance provided by the channel (mainly at the basal boundary), while the latter is likely controlled by intergranular contacts which represents the internal energy dissipation, given that the shear is borne dominantly by solids rather than fluid as the friction number very rarely goes below its threshold value for any kind of tested flow (see Sec. 4.6, 5.6 and 6.6). In particular, when most of the wet flow material cannot move into the horizontal channel (e.g. the CWU data points above the black dashed line in Figure 7-6), the shear strength of the granular mass is likely enhanced by the matric suction and hence the flow is effectively retarded (Vanapalli et al., 1996; Zhou et al., 2016).

Physically, bulk flow mobility expresses energy efficiency by considering all the energy loss as being due to "apparent friction" along the flow path. Although an accurate quantitative energy computation is difficult to achieve, a relative comparison based on the energy perspective is possible between the flows within the same test group, where their deposition mechanisms are more likely to be dominated by the same physical process. When the deposit propagation is mainly controlled by intergranular contacts, in which case the velocity difference may be ignored between tests or the granular mass can hardly shear and move to the flume end, the bulk flow mobility mainly results from the work done by Coulomb friction which is the function of effective normal stress. For simplicity, shear stress (τ) rather than shear force is used in the calculation, which then derives the frictional work of the entire "main surge" per unit basal area (or, considering that the 2D flow path, per unit flow length) along the entire downslope process:

$$\overline{W_F} = \sum \Delta\tau \cdot \mathrm{X} = \sum_{t^*=0}^{t^*=1} \sigma'_{basal}(t) \cdot tan\phi' \cdot X \qquad (7\text{-}1)$$

in which Δτ is the shear stress on a unit volume of the flow (i.e. the shear stress generated during a PIV frame interval Δt), σ'_{basal} is the downslope effective basal normal stress, Φ' is the internal friction angle, and X is the distance along the slope from the point under the centre of the hopper gate to the downslope load cell which takes a fixed value of 1.379m. The internal friction angle Φ' for ceramic beads is 33.7° while for Maple Mud is assumed to be 42.5°, which is a median value of 40° for well-graded gravels (Koloski et al., 1989) and 45° for well-graded angular sands (Obrzud, 2010). Note that $\overline{W_F}$ is not physically well-defined and should be regarded only as a quantitative approach to compare the work done by the internal friction because (i) the intergranular friction proportionate to the σ'_{basal} presumes a triangular stress distribution along the flow depth (see Sec. 3.5), (ii) the intergranular friction forces do not necessarily act along the direction colinear with basal friction and thus with the flow direction, and (iii) basal normal stress (and hence the intergranular friction) per unit flow length is simplified to maintain a fixed value throughout the entire downslope motion and this is clearly not true. Shear strength of the flow material may be more appropriate for characterising the internal energy loss than shear stress estimated from the basal normal stress, but its calculation is an unsolved issue; nevertheless, $\overline{W_F}$ values should be adequate for contrasting the performance of Coulomb friction inside the flows with similar conditions.

When the most important runout behaviour is the sliding movement, in which case the internal energy dissipation is relatively small or is similar across different tests, the bulk flow mobility

may be mainly determined by the kinetic energy or the basal friction (i.e. the external energy dissipation). Given that the channel beds for both the inclined (roughened aluminium) and horizontal parts (acrylic) are relatively smooth, the dominant physical factor should be the kinetic energy within the entire main surge which is calculated by:

$$\overline{E_k} = \sum \frac{1}{2}\frac{\Delta m}{\Delta A} \cdot {u_{ave}}^2 = \sum_{t^*=0}^{t^*=1} \frac{1}{2}\rho h(t) \cdot {u_{ave}}^2(t) \qquad (7\text{-}2)$$

where ρ is the bulk density of flow material, h is the flow height, u_{ave} is the depth-averaged velocity, Δm is the mass of a unit flow volume, and ΔA is the basal area of a unit flow volume; $\overline{E_k}$ then physically means the kinematic energy of the entire "main surge" of the flow per unit basal area (or per unit flow length); this definition includes the basal area so that it can be roughly comparable with $\overline{W_F}$. Noting that the variations in flow height and depth-averaged velocity are only considered along the longitudinal direction within the main surge, while the flow density is assumed uniform.

Depending on the test conditions, either $\overline{W_F}$ or $\overline{E_k}$ estimated from the flow dynamics should reflect the dominant physical process in the deposition mechanism and hence its relationship with the test variable should be similar to how bulk flow mobility is related to the test variable; considering that simple parameters may be preferred to predict the flow mobility, the effective normal stress σ'_{basal} and the depth-averaged velocity u_{ave} at the time where flow height reaches its maximum (as a representative of the flow head) for each tested flow are also chosen to show their evolution patterns. For CDU flows (where most grains are left on the slope instead of running into the horizontal channel) and MWG flows (where the difference in deposit morphology mainly comes from the extent of stretching, i.e. the partial grain movement), the frictional work $\overline{W_F}$ and effective stress σ'_{basal} may be used to predict the bulk flow mobility as shown in Figure 7-7 and Figure 7-8, respectively. Overall, the profiles of α_T, σ'_{basal} and $\overline{W_F}$ display similar evolution patterns with small discrepancies at a few points. Meanwhile, for CSU flows (where the deposit shapes are similar and the climbing movement of grains cannot further extend the travel distance) and MSG flows (where the similar deposit shapes suggest a close extent of material stretching), the kinetic energy $\overline{E_k}$ and the depth-averaged velocity u_{ave} can be chosen to present their relationship with the source volume, as exhibited in Figure 7-9 and Figure 7-10. Note that higher $\overline{E_k}$ and u_{ave} indicate higher bulk flow mobility which is equivalent to a lower travel angle α_T; for the convenience of observation and comparison, the y-axes in the subplots (a) of Figure 7-9 and Figure 7-10 are reversed. Despite the consistently growing $\overline{E_k}$, an

interesting finding is that the u_{ave} data (taken at the maximum flow height) of MSG flows completely fails to form a curve in a similar shape to the α_T curve, but those of CSU flows can provide a curve shape close to the α_T profile which is even closer than the $\overline{E_k}$ curve; this indicates that well-graded Maple Mud cannot produce a head velocity that varies systematically with source volume (as also can be seen in Figure 6-24 and Figure 6-25), while the bulk mobility of saturated uniform flows is mostly connected with the head velocity. Nevertheless, these results show that, although $\overline{W_F}$ and $\overline{E_k}$ are but cursory energy estimations and σ'_{basal} and u_{ave} are not directly relevant to energy, bulk mobility of granular flows may be predicted by dynamical parameters if the dominant grain movement in the deposition mechanism can be identified.

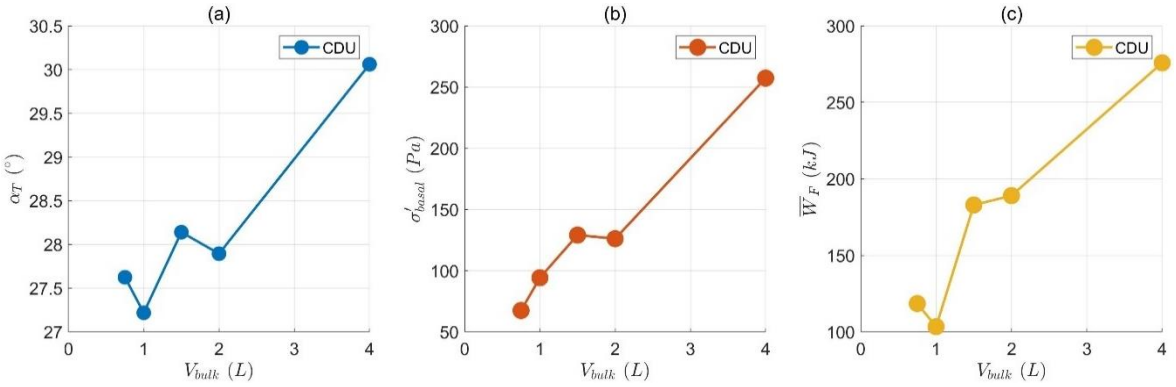

Figure 7-7: Similar evolution patterns of (a) travel angle (α_T), (b) effective basal normal stress (σ'_{basal}) at the peak flow height and (c) estimated work done by the internal friction throughout the main surge ($\overline{W_F}$); each data point is from one ceramic-bead dry uniform (CDU) test with different source volume (V_{bulk}).

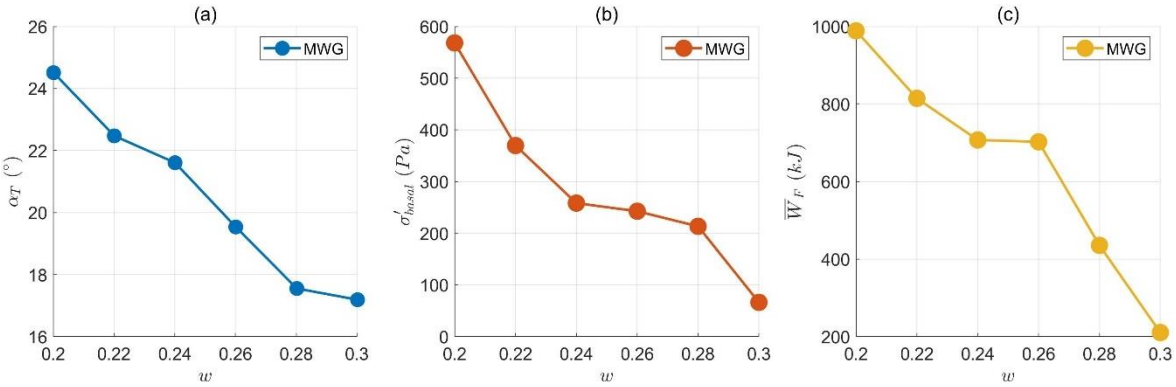

Figure 7-8: Similar evolution patterns of (a) travel angle (α_T), (b) effective basal normal stress (σ'_{basal}) at the peak flow height and (c) estimated work done by the internal friction throughout the main surge ($\overline{W_F}$); each data point is from one Maple-mud wet well-graded (MWG) test with fixed 2L source volume and different water content (w).

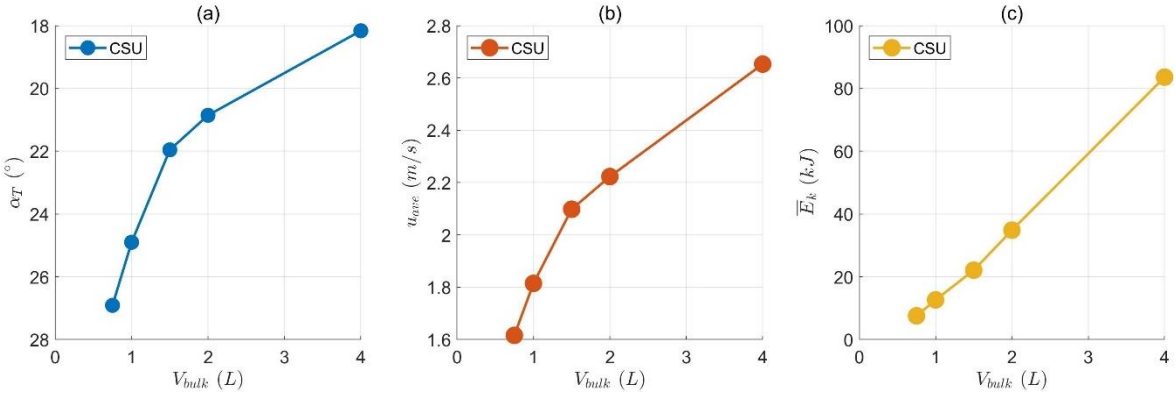

Figure 7-9: Similar evolution patterns of (a) travel angle (α_T) with reverse axis, (b) depth-averaged velocity (u_{ave}) at the peak flow height and (c) kinematic energy in the main surge ($\overline{E_k}$); each data point is from one ceramic-bead saturated uniform (CSU) test with fixed 0.45 water content and different source volume (V_{bulk}).

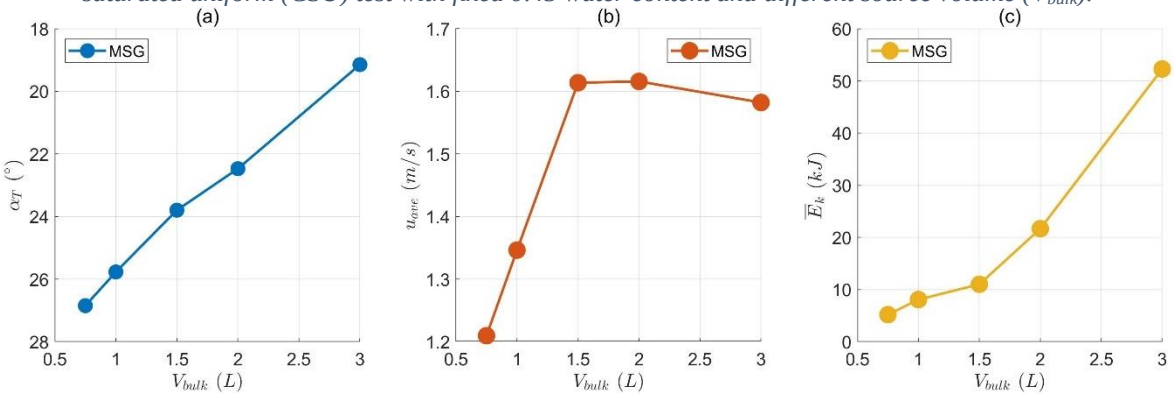

Figure 7-10: Similar evolution patterns of (a) travel angle (α_T) with reverse axis, (b) depth-averaged velocity (u_{ave}) at the peak flow height and (c) kinematic energy in the main surge ($\overline{E_k}$); each data point is from one Maple-mud saturated well-graded (MSG) test with fixed 0.22 water content and different source volume (V_{bulk}).

The deposition mechanisms of CWU flows are more complex as the involved water content ranges widely from 0.01 to 0.4: at low water content, the shear strength is enhanced by suction and hence the deposition should be determined by internal friction; when the flow is saturated at high water content (e.g. w ≥ 0.3 as shown in Figure 7-6), most of the flow material can move into the horizontal channel and thus the flow velocity which controls the sliding of the granular heap should take dominance. Also, $\overline{W_F}$ is calculated as the sum of all the unit flow volume in the "main surge", hence its value can sharply drop when the flow is prematurely terminated (i.e. the "main surge" duration becomes shorter) due to the grains in unsaturated flows piling up on the slope (e.g. "CWU 0.10" and "CWU 0.15" as described in Sec. 5.3); this is contrary to the understanding that this piling-up phenomenon should be the consequence of a larger shear resistance to the flow motion because of a stronger effect of internal friction; this reveals an essential drawback of the $\overline{W_F}$ definition. Referencing Sec. 5.4 in which the basal pore pressure values varying with water content are found to be roughly in line with the evolution of bulk flow mobility, here the p_{basal} is selected to describe the increased internal friction in unsaturated

uniform flows from the perspective of the suction effect; from each CWU test, the p_{basal} value at its absolute maximum is taken from the "main surge" part. As for the saturated part of CWU flows, the depth-averaged velocity at the peak flow height should match the travel angle profile better than the kinetic energy, similar to the CSU flows (Figure 7-9). Figure 7-11 depicts the similarity between the curves of α_T, u_{ave} and p_{basal} against water content for 2L wet uniform (CWU) flows and marks the value of the 2L dry uniform (CDU) flow in each subplot by a black dashed line, below which the bulk mobility can be deemed retarded whereas above which the mobility is enhanced. When $w \geq 0.3$, all three parameters present approximately linear growth, while when $w \leq 0.3$ they commonly show convex curves below the dashed line. This suggests that, for wet flows composed of uniform ceramic beads, the decrease in flow head velocity and the retardment of deposit propagation are firmly related to the suction effect. On the other hand, for the well-graded MWG flows (variable water content), where the deposition should be controlled by internal friction, no notable suction effect is evident (Figure 6-20), while MSG flows (variable volume) in which negative p_{basal} values can be found (Figure 6-19) have their deposition processes dominated by sliding movement; hence p_{basal} and α_T for well-graded flows may not be expected to show high relevance. However, as presented in Figure 7-12 and Figure 7-13, although not perfectly similar, p_{basal} curves for MSG and MWG flows with their respective variables successfully capture the overall shapes of α_T curves surprisingly well; this highlights the contribution of pore fluid pressure to the runout behaviours of well-graded flows, despite the lack of a clear physical description.

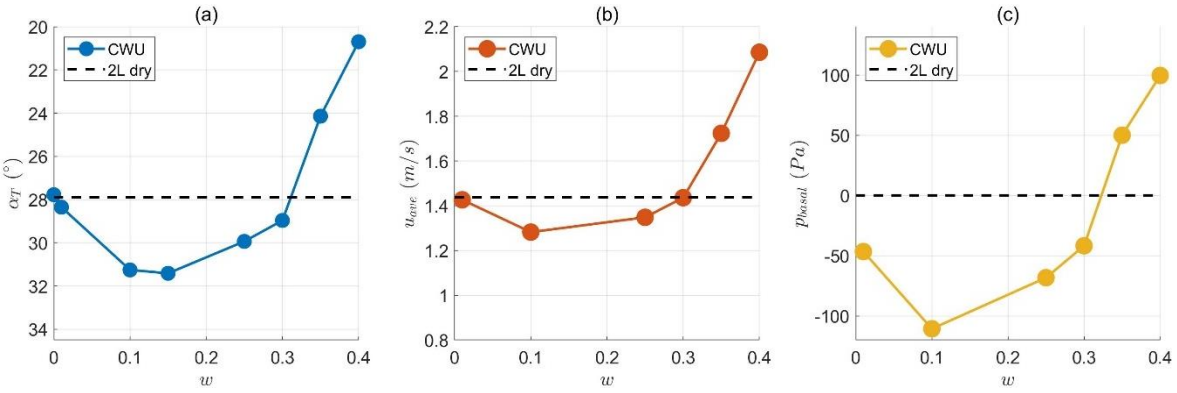

Figure 7-11: Similar evolution patterns of (a) travel angle (with reverse axis), (b) depth-averaged velocity at flow head and (c) basal pore fluid pressure at the absolute maximum; data are from CWU flows varying with water content.

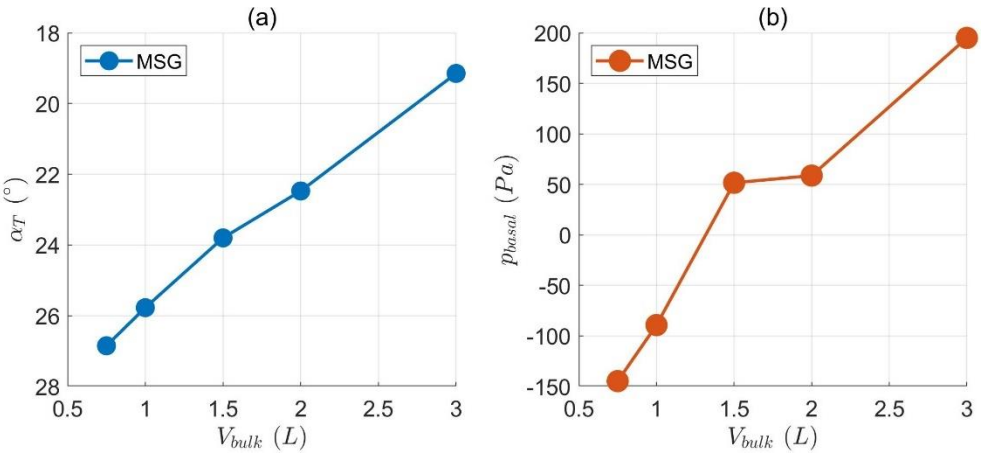

Figure 7-12: Evolution patterns of (a) travel angle (with reverse axis), (b) basal pore fluid pressure at the absolute maximum; data are from MSG flows varying with water content.

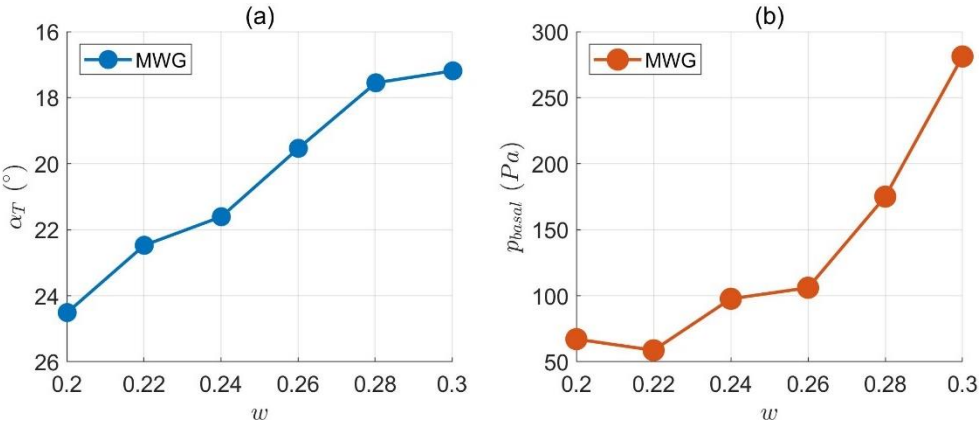

Figure 7-13: Evolution patterns of (a) travel angle (with reverse axis) and (b) basal pore fluid pressure at the absolute maximum; data are from MWG flows varying with water content.

7.2. Velocity and Shear Mechanism

7.2.1. Depth-averaged Velocity

Depth-averaged velocities of ceramic bead flows and Maple Mud flows are contrasted in Figure 7-14, where the flows depicted in subplots (a) and (b) are in correspondence with the deposits in Figure 7-1 and Figure 7-2. When source volumes increase from 0.75L to 2L (Figure 7-14 (a)), the average velocity u_{ave} values for dry uniform flows remain the same, those of saturated uniform flows (w = 0.45) dramatically rise from below that of dry flow velocities to above, and those of well-graded flows (w = 0.22) slightly increase but remain low. For flows with close (0.24 against 0.25) or identical (0.3), water content (Figure 7-14 (b)), uniform ceramic beads and

well-graded Maple Mud both present similar u_{ave} curves, although the u_{ave} values of CWU flows are considerably higher than those of MWG flows; also, with the water content range included in the subplot, velocities produced by 2L of both source materials are lower than that of the 2L dry uniform flow. The u_{ave} of uniform ceramic beads can exceed that of a dry flow given a higher water content (Figure 7-11), but that of well-graded Maple Mud does not noticeably vary with water content (Figure 6-28) and stays much lower than the u_{ave} of dry uniform flow; this means that polydispersity of the flow material can significantly hamper the growth of flow velocity during the downslope motion.

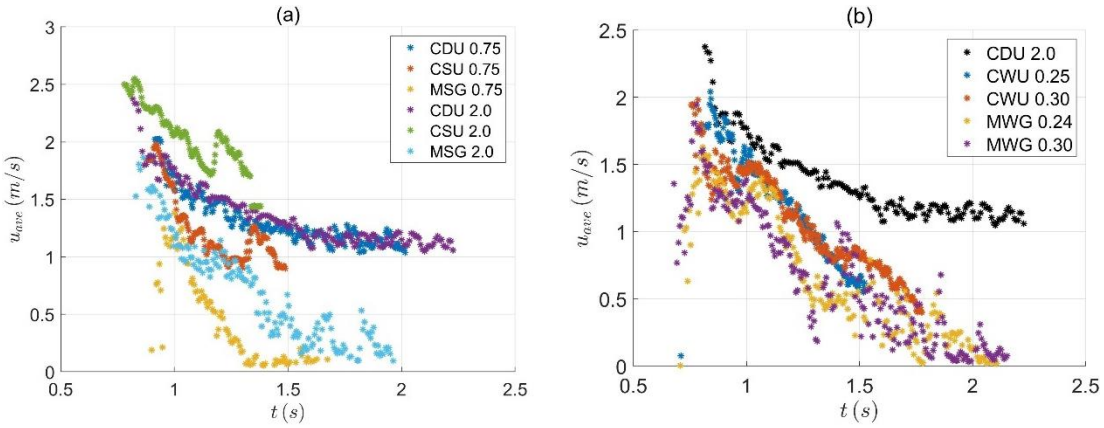

Figure 7-14: Contrast between depth-averaged velocities between uniform and well-graded flows. (a) Flows with 0.75L and 2L source volumes and different water content (w = 0.45 for ceramic beads and w = 0.22 for Maple Mud), and (b) 2L flows with 0.25 (or 0.24) and 0.3 water content, benchmarked with the 2L dry uniform flow.

From the comparison between the depth-averaged velocities (Figure 7-14) and the deposit longitudinal morphologies (Figure 7-2) of CWU and MWG flows, the Maple Mud flows with the lowest velocities can produce the highest bulk flow mobility; in other words, the high mobility of well-graded granular flows can be produced without a large flow velocity; in contrast, the bulk mobility of ceramic bead flows seems highly relevant to the magnitude of the flow head velocity (Figure 7-9 and Figure 7-11). Scrutiny of velocity profiles is required to analyse the generation of depth-averaged velocities.

7.2.2. Shape of Velocity Profile

Velocity profiles of granular flows with different constituents (i.e. dry uniform, wet uniform and wet well-graded) have been demonstrated previously in Sec. 4.5, 5.5 and 6.5. Inspired by Li et al. (2021), a simple method to quantitatively describe the velocity curve shapes across different tests is established based on two parameters: (i) the ratio of slip velocity to depth-averaged velocity, u_{slip}/u_{ave}, a larger value (from 0 to 1) of which means a steeper secant line of the velocity curve,

and (ii) the ratio of two velocity differences, (u_{ave} - u_{slip})/(u_{surf} - u_{slip}), which suggests if the slip velocity (u_{slip}) is closer to the depth-averaged velocity (u_{ave}) or surface velocity (u_{surf}); the value of (u_{ave} - u_{slip})/(u_{surf} - u_{slip}) approaching 0 means the velocity curve is nearly vertical in the lower portion and horizontal at the surface boundary, the value close to 1 means the velocity curve is roughly vertical in the upper portion and horizontal at the basal boundary, and the value equals 0.5 when the velocity curve shapes in a straight line. Figure 7-15 gives the coordinate plane of these two parameters, in which different positions correspond with different velocity curve shapes that are also depicted.

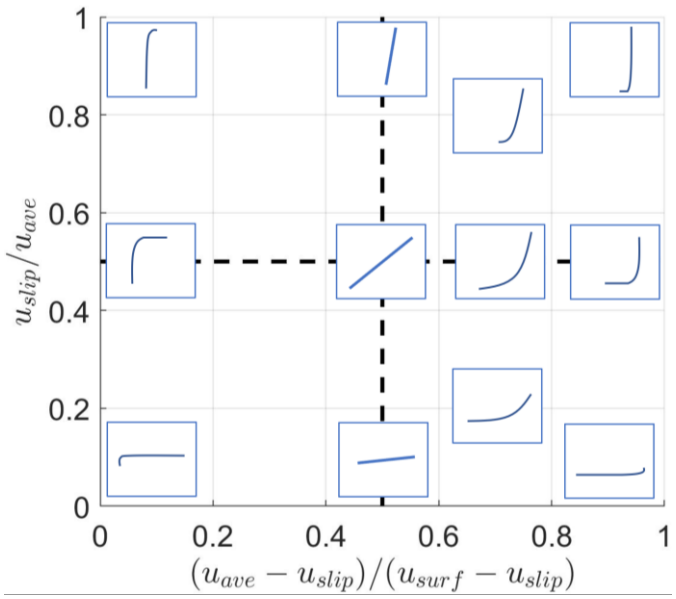

Figure 7-15: Schematic diagram of all the velocity shapes determined and represented by two parameters.

Velocity profile shapes of all the tested flows can be quantified by the aforementioned two parameters and then be plotted on the coordinate plane in Figure 7-15 as separate data points. For ceramic bead flows, data points representing the velocity curve shape taken every 10% of the "main surge" duration (i.e. t* = 10%, see Sec. 6.3) are given in Figure 7-16; while data points for Maple Mud tests are distributed in Figure 7-17. The results more straightforwardly summarise the development patterns observed in velocity profiles (Sec. 4.5, 5.5 and 6.5). Dry uniform flows tend to give more linear velocity profiles, in which the curvature in the lower portion of the flow slightly increases with the source volume; when pore fluid exists, the velocity profiles of saturated uniform flows become overall more curved and, compared with the dry flow, the upper portion of the flow grows more vertical with a larger source volume (Figure 7-16 (a)). With increasing water content, however, the distribution of CWU data points increases in the ordinate (Figure 7-16 (b)), indicating that the slip velocity continuously increases relative to the velocity

of the upper portion of the flow height. On the other hand, the velocity curves of well-graded flows give similar distribution ranges whether evolving with source volume or water content: the slip velocities (u_{slip}) are commonly at 0 and a constantly large difference is shown between the surface and slip velocities.

The shear mechanism of granular flows with different flow constituents can be reflected in the velocity profile shapes. Dry uniform ceramic beads tend to shear globally and uniformly at a relatively low extent across the flow depth; the increase in source volume tends to lessen the local shear rates in the upper portion of the flow and enlarge the local shear rates near the flume bed. A larger source volume tends to confine the shear movement of the uniform ceramic beads to the neighbourhood of the basal layer of the flow, i.e. to localise the shear movement; this localisation trend has previously been reported by Li et al. (2021). Since shallower dry uniform flows give larger $\overline{N}_{Sav}$ (i.e. the mean value of Savage number across the flow depth, see Figure 4-15) and hence a more collisional flow regime, the globally-uniform shear can be interpreted as the inertial movement reducing the contact stress between uniform beads, leading to lower local velocity gradients from the surface to the bottom. When the flow grows thicker due to a larger source volume, greater normal stress is generated with the flow depth and intergranular enduring contacts are therefore increasingly stronger towards the flume bed (thicker flow gives lower $\overline{N}_{Sav}$ and increasing solid friction in Figure 4-15); these frictional contacts increasing with the depth cause the grains closer to the flume bed to dissipate more energy and lose more velocity, leading to velocity profiles with smoothly-increasing gradients from the surface to the bottom.

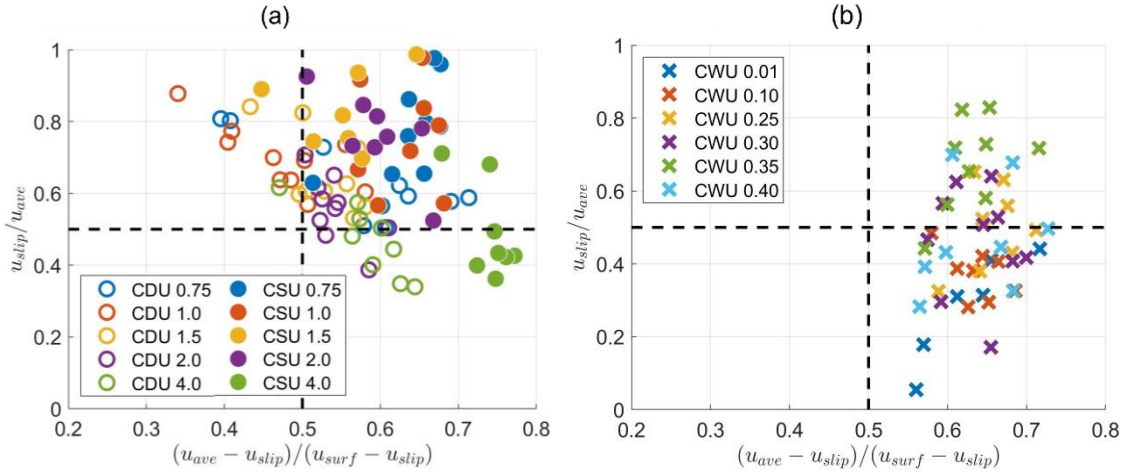

Figure 7-16: The distribution range of the velocity profile shapes of ceramic bead flows. (a) The contrast between dry (hollow circles) and saturated uniform flows (solid circles) with different source volumes, and (b) the contrast between wet uniform flows (crosses) at different water content.

(a) (b)

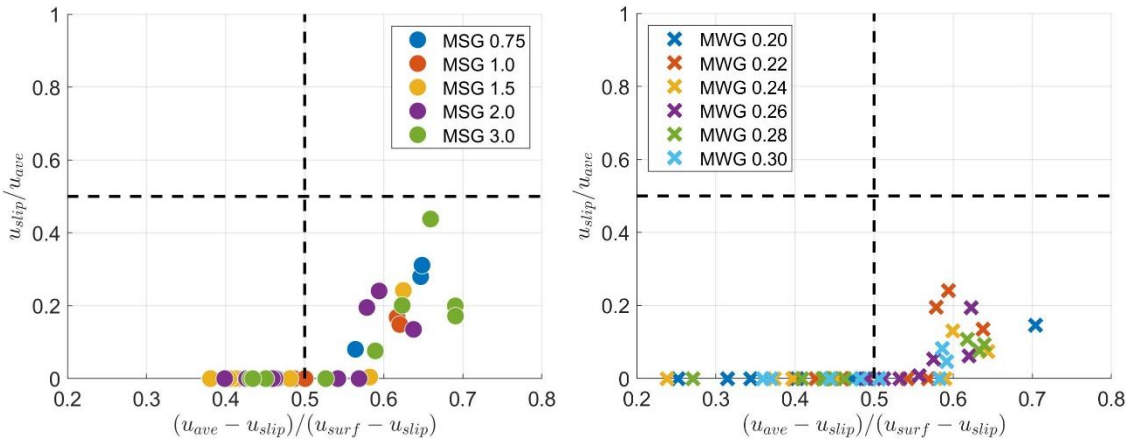

Figure 7-17: The distribution range of the velocity profile shapes of Maple Mud flows. (a) The contrast between saturated well-graded flows (solid circles) with different source volumes, and (b) the contrast between wet well-graded flows (crosses) at different water content.

When the uniform ceramic beads are saturated with water, the local shear rates in the upper portion of the flow height are lessened whereas in the lower portion are enlarged; the influence of source volume seems similar to dry uniform flows but is strengthened by the existence of pore fluid. Additionally, a more slippery basal boundary is found with higher water content. These results indicate that for uniform flows composed of large, heavy, rough pseudo-spheres, the fundamental role of pore fluid seems to be to reduce the solid frictional stress due to enduring contacts. In the upper portion of the flow, the alleviation of interparticle friction allows the grain movement to be less dragged by the shear resistance, thereby producing smaller velocity differences; at the flow-bed boundary, the basal grain layer experiences lower friction with the grains above (the local shear rate at their interface hence increases) than with the flume bed when the flow thickens, while the friction with the bed can also be reduced by more pore fluid being involved in the flow body. Additionally, the depth-averaged velocity of uniform flows cannot increase with the source volume without the presence of pore fluid (Figure 7-14 (a)); therefore, solid frictional interactions seem to control the velocity increase of dry uniform flows, echoing the finding that bulk flow mobility can be roughly represented by the frictional work (Figure 7-7).

For well-graded flows constituted of realistic angular soils, grains barely move at the basal layer but are highly sheared at the free surface, showing dramatic bulk shear rates, which can be defined by the ratio of the difference between surface and slip velocities to the flow height as:

$$\Gamma = \frac{u_{surf} - u_{slip}}{h} \tag{7-3}$$

The bulk shear rates of well-graded flows are notably higher than those of uniform flows at close water content (Figure 7-18). The low depth-averaged velocities of wet Maple Mud flows are likely to be directly attributed to the low (commonly zero) slip velocities, which shows a high flow resistance at the flume bed and implies that the theory of dry fine grains spreading at the flume-bed interface and lubricating the basal friction (Yang et al., 2015) is not applicable to wet polydisperse flows. Pore fluid still reduces the solid friction (as suggested by $\overline{N}_{fric}$ of MWG flows in Figure 6-32) but seems unable to produce the plug-flow profile as in uniform flows; instead, the shear is globally stronger and relatively more uniform than that of uniform flows. This is probably because the mono-sized spherical grains are more explicitly stratified and shear movement tends to develop between the grain layers, hence the extent of shear can be straightforwardly expressed by the local shear rate; for the well-graded angular soils, however, the shear movement seems to be performed by "plastic" deformation of the flow material which makes the flow thinner during the downslope motion, giving high plastic strains across the flow height to overcome the strong interactions between dense, interlocked well-graded solids. The fundamental difference between the monodisperse and polydisperse wet granular flows seems in the deformation pattern of the flow material: uniform spheres tend to have interlayer translational movements like in a plane-shear configuration, while well-graded soils tend to propagate along the flow direction through extension or plastic deformation.

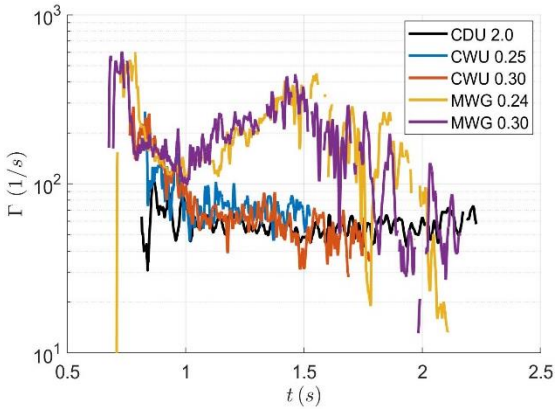

Figure 7-18: Contrast between bulk shear rates of ceramic bead flows and well-graded flows.

The plastic deformation can also partly explain the high mobility of well-graded flows. In the deposition process of well-graded flows (Figure 6-2), the flow surge can be compressed and then dilated, during which the deposit propagates farther; hence the ability to perform the compression and dilation is the key to high bulk flow mobility. The higher water content and the resultant decreased solid friction reduce the "yield strength" of the granular mass, allowing the

deformation to more easily develop, whether during the downslope motion or deposition; also, the lower void ratio of the well-graded material helps to maintain the pore fluid inside the granular body. Therefore, even with the low flow velocity, well-graded flows can produce high mobility when a high level of plastic deformation (characterised by bulk shear rate) is presented.

7.3. Fluid Phase in Flow Surge

7.3.1. Saturated Surge

The relationship between pore fluid pressure, head velocity and bulk mobility of uniform flows is provided in Figure 7-11. When $w \leq 0.3$, negative pore pressures that occupy most of the "main surge" duration (Figure 5-22) are connected with the retardment of bulk flow mobility; as negative pore pressure should not be detected in a saturated surge, it can be deduced that the granular body moving downslope is effectively unsaturated within this range of water content. Note that the saturation water content (w_{sat}) for ceramic beads at rest is 0.256 (see Sec. 3.1.4), lower than the water content of 0.3 which still gives an unsaturated surge; therefore, the pore space must expand during the flow motion and the porosity of a flowing granular mass must be higher than that of its static source material. Another supporting information is that, as shown in Figure 5-12 where coloured water can be observed by eyes, pore fluid can be seen to spill from the pores of uniform ceramic beads at a high water content of $w = 0.45$ but is held within the granular body of the wet flow with $w = 0.35$, which also exceeds $w_{sat} = 0.256$. Considering that the leading edge of a granular flow surge is known to be unsaturated (Figure 2-3), pore fluid can always fill only part of the granular flow surge. A schematic diagram showing the typical position of the fluid phase in a granular flow surge is depicted in Figure 7-19 (a) and is modified from Meng et al. (2022); the fluid phase tends to be lower than the top surface of the granular body and to be gradually left behind the flow front during the downslope motion.

To estimate the saturation degree of a moving flow surge, the position of the intersection between the water surface and the top surface of the granular body is identified as marked in Figure 7-19 (a). The saturation degree of a granular flow surge is higher (i.e. a larger proportion of the surge is filled with a continuous fluid phase) when this intersection point (after which the water surface should be visible and above the top of grains) is closer to the leading edge, indicating that the boundary of the fluid phase (i.e. the dark blue curve covering the blue shading

in Figure 7-19 (a)) moves upward and/or towards the flow front. This intersection point is then searched for in the captured high-speed images for each fluid-mixed uniform test. Figure 7-19 (b) presents a frame as an example in which the start of the visible water surface enters the PIV mesh; the time index of this frame is recorded for each test when a visible water surface (more precisely, the ripple observable at the sidewall) can be found and is then converted into the time normalised by the "main surge" duration, t* (see Sec. 6.3). The results of t* values corresponding to the start of visible water surface are given in Figure 7-19 (c) for CSU flows with varying source volume and (d) for CWU flows with evolving water content. When the source volume of the uniform flow with w = 0.45 increases from 0.75L to 4L (Figure 7-19 (c)), the visible water surface appears from the rear of the main surge (t* is almost 0.7) to very close to the leading edge (t* is lower than 0.2), indicating that the saturation degree of the surge is remarkably increased; this may be because the flow regime becomes more frictional and the intergranular enduring contacts are strengthened in a thicker flow (see the $\overline{N}_{Sav}$ plot in Figure 5-33), hence the volume of pore space shrinks and the same percentage of moisture can fill up more pores within the surge. For 2L uniform flows with different water content (Figure 7-19 (d)), the water surface is only visible when $w \geq 0.35$ and its appearance position also approaches increasingly closer to the flow front with higher water content. The most important finding is that, when the water content is below a certain value (0.35 in the case of 2L ceramic beads), the surface of a continuous fluid phase cannot be found in a wet granular flow; this means that pore fluid may be insufficient to fill up the interstitial spaces of even a portion of the surge and may only be adequate to form liquid bridges (as illustrated in Figure 2-6) between the grains in that portion; hence the flow surge in this scenario may be effectively "unsaturated ".

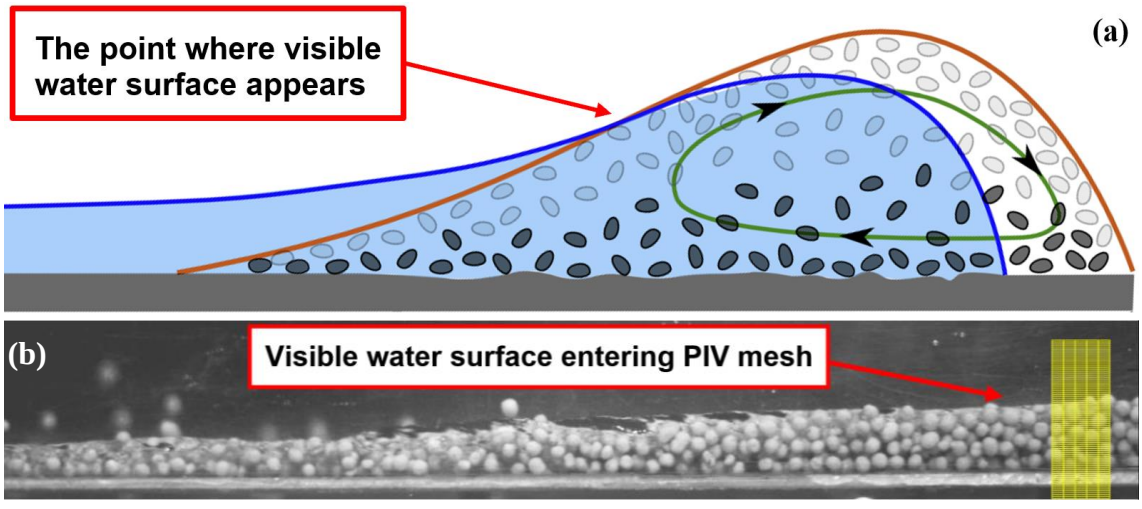

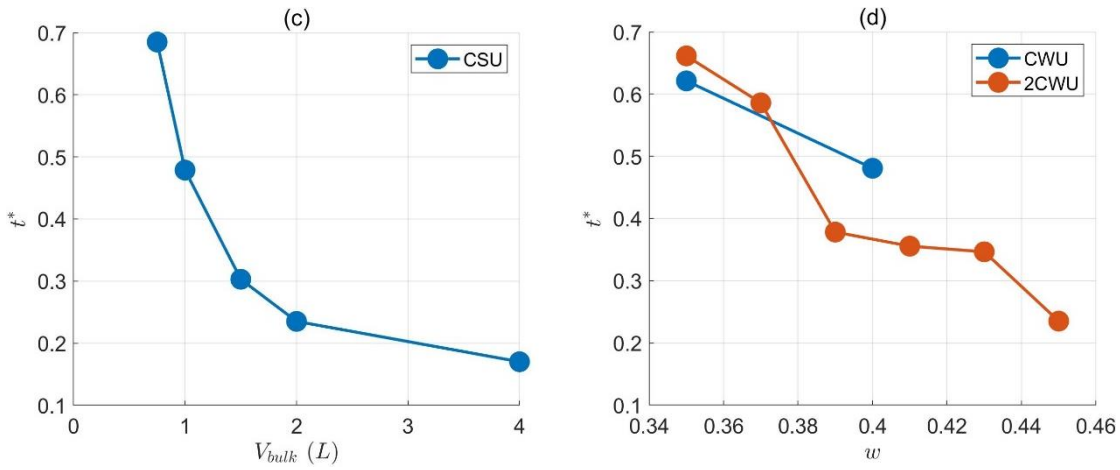

Figure 7-19: Visible water surface in granular flows. (a) Schematic diagram of granular flow (after Meng et al. (2022)), where the intersection between the surface of the water phase (dark blue curve surrounding the blue shading) and that of the granular body (brown curve) is pointed out; (b) the frame when the start of visible water surface enters the PIV mesh; (c) the normalised time t where visible water surface appears in saturated uniform flows (w = 0.45) and (d) the normalised time t* where visible water surface appears in 2L wet uniform flows with different water content.*

7.3.2. Unsaturated Surge

Conceptually, the desaturation of the flow surge at low water content is easy to understand as the small amount of moisture can only adhere to the grain surfaces and cannot pressurise the flume bed by its weight; the oddity is that the negative basal pore pressures detected by the pore-pressure transducer (PPT) do not neatly dovetail with the theoretical suction values. As shown in Figure 2-7 (a), matric suction, which is prevailingly defined as the pressure difference between the air and water applied to the meniscus (Zhang et al., 2019), should decrease with the saturation degree (hence the water content) of the granular medium; the strongest suction should be found in the least wetted granular medium. However, the lowest p_{basal} values occur in the CWU flows at about w = 0.1 rather than at w = 0.01 (Figure 5-22 and Figure 7-11), suggesting that the PPT responses are not solely (or mainly) caused by matric suction. To set up a reference, the total suction pressure (ψ) across the air-water interface based on the capillary tube model (Lu and Likos, 2004) can be calculated by:

$$\psi = \frac{2T_s \cdot \cos\theta_c}{r_p} \tag{7-4}$$

Where T_s is the surface tension of water which equals 71.79 mN/m at 25°C, θ_c is the contact angle of the grain-water interface and r_p is the radius of the pore space, which is equivalent to the radius of the curved meniscus in a capillary tube. For the uniform ceramic beads used in CWU flows, θ_c is assumed to be 35° as the contact angle of SiO_2 (i.e. the major chemical component of

Denstone 2000 ceramic beads) is normally between 10° and 60° (Watanabe, 2009); r_p can be determined from the geometrical relationship given in Figure 7-20 (a) and can be expressed by a function of the filling angle, θ_f, and grain size, δ, as:

$$r_p = \frac{\delta\,(\tan\theta_f)^2}{4\,(1-\tan\theta_f)} \tag{7-5}$$

in which the averaged grain size δ = 3.85 mm for ceramic beads. Filling angle (θ_f), instead of water content (w) which is usually used in SWCC, is adopted here to characterise matric suction (ψ) for ceramic beads, giving a relationship as plotted in Figure 7-20 (b). The matric suction seems incredibly high (more than 10kPa) with a small filling angle (because of a small amount of water). However, the PPT at the flume bed does not necessarily sense all of this strong suction as it is physically a tenacity to hold the water within the liquid bridge, instead of a sustained attraction to actively suck the surrounding fluids; for instance, when a slightly-wetted sphere is attached to the top filter of PPT, the PPT is not expected to detect an extreme suction but rather a small drop of pressure due to a tiny bit of water escaping from the transducer hole and adhering to the grain surface.

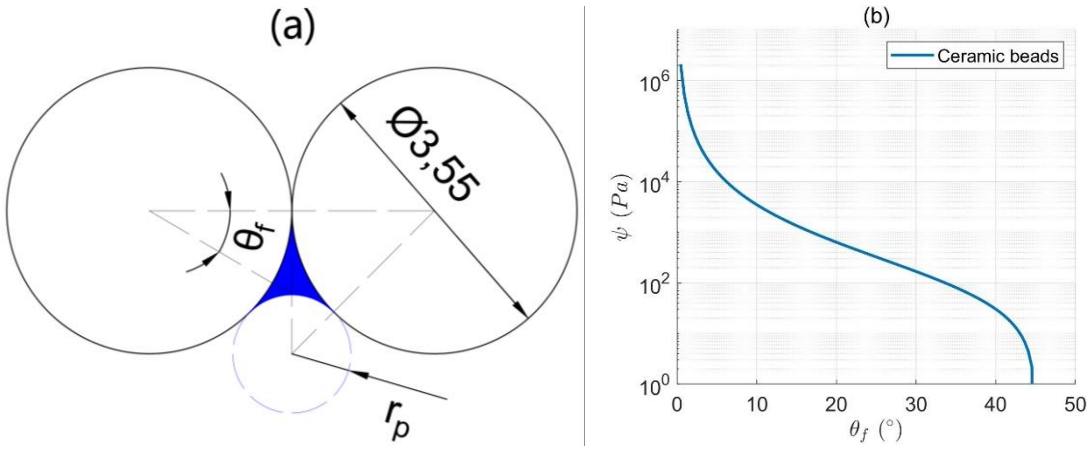

Figure 7-20: (a) The geometry of a meniscus between two mono-sized ceramic beads (unit: mm). (b) The relationship between matric suction (ψ) and the filling angle (θ_f) for the uniform ceramic beads.

Furthermore, the filling angle θ_f can be inversely computed from the relationship given by Lu and Likos (2004) as:

$$w = \lambda\frac{\rho_s}{\rho_w}\left(\frac{1}{\cos\theta_f}-1\right)^2\left[1-\left(\frac{\pi}{2}-\theta_f\right)\cdot\tan\theta_f\right] \tag{7-6}$$

where w is the gravimetric water content and λ is a coefficient associated with the arrangement of spherical particles according to Dallavalle (1943); λ = 9 when the void ratio e = 0.34 and λ =

9/2 = 4.5 when e = 0.91; the averaged void ratio of the uniform ceramic beads is 0.582, close to the median of the two given void ratio values, hence λ can take the value of 9/1.5 = 6. This equation predicts that θ_f reaches 45° at w = 0.1; in other words, suction should not occur or extremely low when the water content exceeds 0.1, clearly contradicting the acquired p_{basal} data. In summary, the basal pore pressure obtained by external measurements cannot be described by matric suction based on capillarity.

A satisfactory explanation of the mechanism of the suction detected at the basal boundary of the moving unsaturated granular flow surge does not yet seem to be available. However, some reasonable conjectures can be made according to the observed phenomena. (i) The negative p_{basal} is likely associated with the flow motion and the relevant parameters like flow velocity or the expanded pore size; the high flow velocity (specifically, the velocity of a series of menisci where air pressure is applied) may lead to a negative pressure due to Bernoulli's Principle, and the expansion of pore space may result in a sustained suction. (ii) The shear strength of the unsaturated granular flow seems able to explain the appearance of the minimum bulk flow mobility (Zhou et al., 2016), which also shows relevance to the p_{basal} of wet uniform flows (Figure 7-11); hence the coupled effect influencing the shear strength (see Eq. (2-12)), namely the development of matric suction and the increase in water content wetting more grains, may also play roles in the generation of suction at the basal boundary. (iii) Considering that the dilation of the solid phase and the backward motion of the fluid phase relative to the flow front both exist during the flow motion, suction may always occur in the desaturated part of the flow surge, the range of which depends on the relative volumes of pore space and pore fluid (e.g. near the dry leading edge when pore space is relatively small, or across the entire surge when moisture is relatively low); the basal pore fluid pressure can then be interpreted as the result of the competition between the suction and the fluid weight.

7.4. Particle Size and Scale Effect

In this study, only one product of mono-sized pseudo-spherical particles was used for uniform flows and GSD (grain size distribution) was designed to be constant for well-graded flows, hence the influence of varying grain size is not achievable from the test results; however, comparable data can be found in the literature. Li et al. (2021) conducted similar small-scale flume experiments, where the flume inclined at 45° is 2.5 m long and 0.2 m wide and forms a 2D flow

path with the horizontal channel, using dry angular quartz sands with averaged sizes of 0.175, 0.375, 0.75, 1.5 and 3.5 mm (labelled as "GS1" to "GS5" in sequence). Normalised velocity profiles (u/u_{ave}) against the normalised flow height (z/h) in Li's tests are given in Figure 7-21, where velocity data of flows with an 8 dm^3 source volume and different grain sizes are depicted in subplot (a) whereas those of flows with the "GS1" grain size and different source volumes are in subplot (b); solid curves denote the fitted velocity profiles; the source volume values of "V1", "V2" and "V3" are 2, 5 and 8 dm^3. The lowest source volume produces a linear velocity curve and the highest volume gives the most curved profile where velocity gradients are increased near the bed and are decreased in the upper portion of the flow; this is very similar to the CDU (Figure 7-21 (c)) and CSU (Figure 7-21 (d)) velocities (with varying source volumes). Velocity profiles become more linear with larger grain sizes, implying a more globally-uniform shear mechanism and a more collisional flow regime. Bulk flow mobility systematically increases with grain size, agreeing with the finding in Figure 7-7 that bulk mobility of dry granular flows decreases with the extent of solid frictional stress. Additionally, unlike CDU flows, Li's tested flows can produce depth-averaged velocity increasing with source volume; this may be related to the application of angular solid material, the larger slope angle or the larger scale.

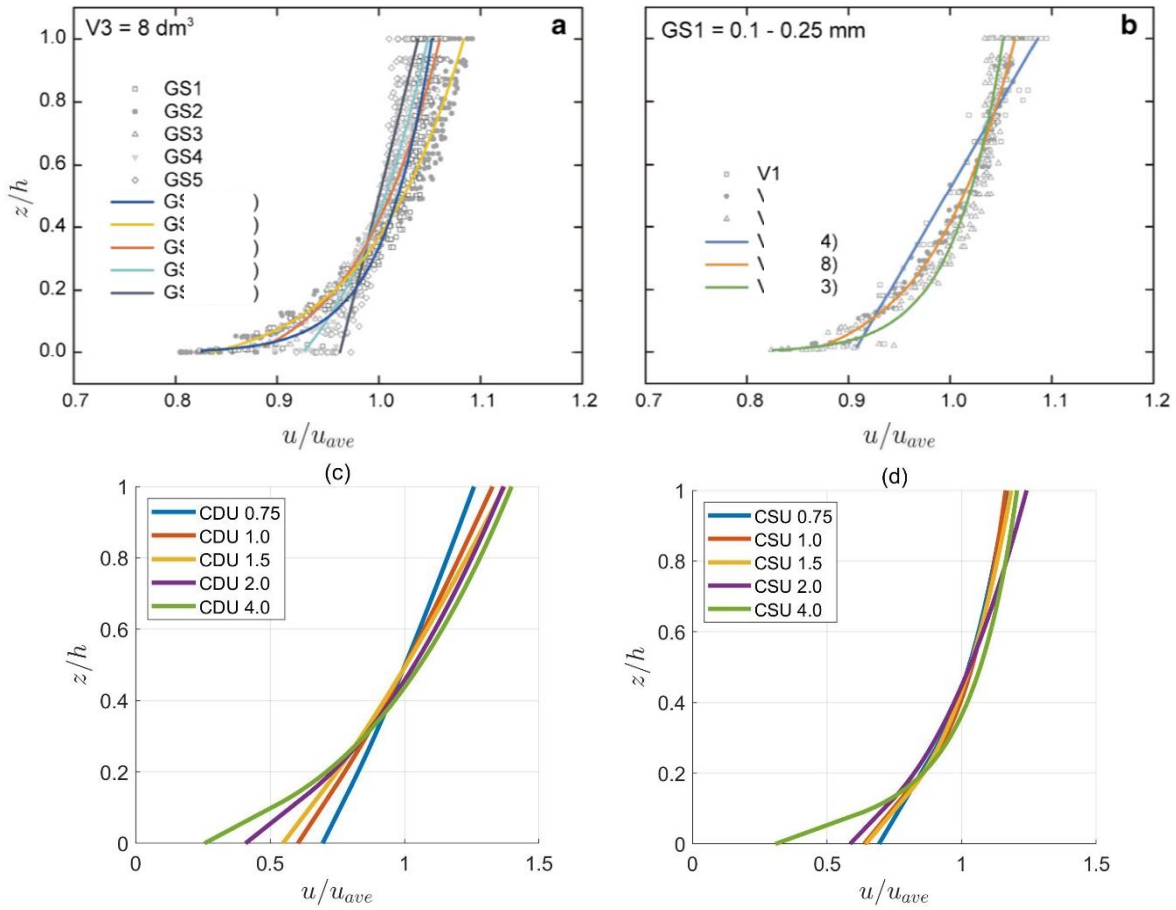

Figure 7-21: Velocity profiles normalised by the depth-averaged velocity of granular flows with (a) the same source volume and different grain sizes (from GS1 to GS5), and (b) the same grain size and different source volumes (from V1 to V3); plots are modified from Li et al. (2021). Comparator velocity profiles of (c) CDU dry flows and (d) CSU saturated flows with increasing source volumes.

Coombs (2018) and Taylor-Noonan et al. (2022) conducted large-scale flume experiments with the identical Denstone 2000 product to the one used in uniform flow tests in this study (note that the studies were made in collaboration with this one at the University of Sheffield). The large-scale flume employed in both of these studies was The Queen's University landslide flume, which possesses a slope length of 8.23 m (about 5.8 times that of the small-scale flume), a width of 2.03 m (about 20 times that of the small-scale flume) and a slope angle of 30° (the University of Sheffield flume slope was set to be the same as Queen's slope which is not adjustable). Coombs' tests covered different grain sizes (including 3, 6, 13 and 25 mm in nominal sizes) and different source volumes (from 0.2 m^3 to 1.4 m^3). With a larger grain size, the dry uniform flow at a fixed source volume of 0.4 m^3 becomes more dispersed and dilute (indicating a more collisional flow regime), gives higher flow velocity and produces a larger flow height but with a decreased normalised flow height (h/δ). Meanwhile, averaged velocities of Coombs' tested flows are reduced with source volume increasing from 0.2 m^3 to 1.0 m^3 and nominal grain size being fixed at 25 mm; this seems to both disagree with CDU flows in this study, where the velocity barely varies with source volume, and the results of Li et al. (2021), where the velocity increases with the source volume; because of the same material, the depth-averaged velocities of larger-volume CDU flows (e.g. over 0.2 m^3) are more likely to decrease with the source volume, like in Coombs' tests. The travel angle profile of Coombs' flows presents a small increase with source volume, ranging roughly from 25° to 28°, as displayed in Figure 7-22 (a); while CDU flows in this study lead to travel angles increasing from about 27° to 30° with source volumes from 7.5×10^{-4} m^3 to 4×10^{-3} m^3 (Figure 4-3 (b)); considering the large difference in the flow scale, the 2° discrepancy in travel angle seems quite small and thus bulk flow mobility of dry uniform flows composed of the identical ceramic beads seems relatively similar across different scales.

Taylor-Noonan et al. (2022) (hereafter referred to as "TN" for convenience) has provided results of both dry and saturated granular flows using exactly the same ceramic beads with a 3 mm nominal size as those in the uniform tests of this study. For TN's saturated flows, water was poured into the source material until just over the top surface of grains, hence the utilised water content should be about 0.256 or simply 0.26 (see Sec. 3.1.4). The bulk mobility of TN's flows is as shown in Figure 7-22 (a), in which the travel angle of dry uniform flows slightly increases

from 27° to 28° when source volume grows from 0.2 m^3 to 0.8 m^3 (with a small drop at the largest volume) and that of saturated uniform flows consistently decreases from 26° to 20° in response to the increase in source volume from 0.2 m^3 to 1.0 m^3. Travel angles of TN's dry flows with different volumes are very close to each other and are similar to those of Coombs' dry flows caused by 25 mm grains; while travel angles of small-scale CDU dry flows are overall larger, but only by up to 2° more than those of large-scale flows. Travel angles of CSU saturated flows exhibited in Figure 5-6 (b) give a large decrease from 27° to 18° with the increased source volume from 7.5×10^{-4} m^3 to 4×10^{-3} m^3; this is again quite close to the 26° to 20° travel angle difference resulting from TN's saturated flows; however, it should be noted that water content in CSU flows is 0.45, much bigger than the value of 0.26 in TN's saturated flows. In general, bulk flow mobility of ceramic bead flows with varying source volumes is relatively similar across different scales, whether dry or saturated.

TN's large-scale saturated uniform flows also produced pore fluid effects similar to those occurring in the small-scale CSU flows. Velocity profiles of TN's flows (both dry and saturated) with different source volumes at their respective peak flow heights are depicted in Figure 7-23; for contrast, velocity profiles at the peak flow heights of CDU and CSU flows are collected in Figure 7-24. Large-scale flows overall generate thicker flow bodies (40 – 60 mm) and higher velocities throughout the flow depth (1 – 3 m/s for dry flows and 1 – 5 m/s at most for saturated flows); in contrast, the small-scale CDU flows only give approximately 0.5 – 2 m/s from the bed to the surface, while CSU flows give about 1 – 3.2 m/s. However, the velocity profile shapes of saturated flows relative to those of dry ones present remarkable similarities between

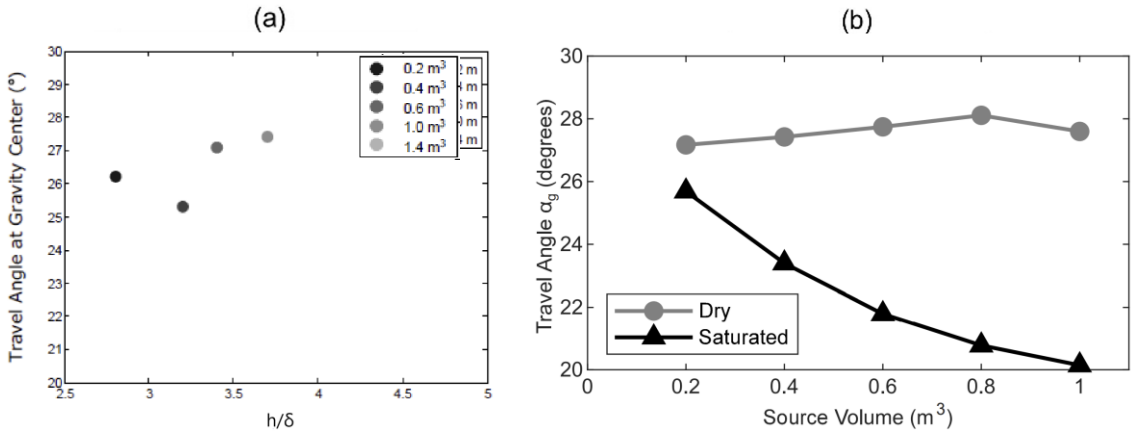

Figure 7-22: Travel angles of large-scale ceramic bead flows varying with source volumes. Data are from (a) dry uniform flows in Coombs (2018) (with modifications) and (b) dry and saturated granular flows in Taylor-Noonan et al. (2022).

different scales: aside from the commonly large increase in flow velocity when mixed with pore fluid, the velocity gradients of dry flows are more consistent across the depth, while those of saturated flows are lower in the upper portion and higher near the bed; this shows that the shear localisation mentioned in Sec. 7.2.2 due to the increase in source volume (and hence flow height) is valid in large-scale flows as well. TN's saturated flows further suggested that the thickness of this highly-sheared basal grain layer seems not to vary with the increased flow height; this is understandable as the intergranular solid friction is reduced by pore fluid (which is also pointed out as one of the conclusions of TN's work), a larger flow thickness can increase both the normal stress and the fluid buoyancy near the flume bed, hence a high level of local shearing can still develop at the basal grain layer. Last but not least, with the use of highly permeable monodisperse spheres, excess pore pressure has never been observed in saturated uniform flows at both small (in this study) and large scales (in TN's flows); this means that even without generation of internal suction, pore fluid in uniform granular flows may only provide buoyancy but it is sufficient to cause the increase in flow velocity and bulk flow mobility.

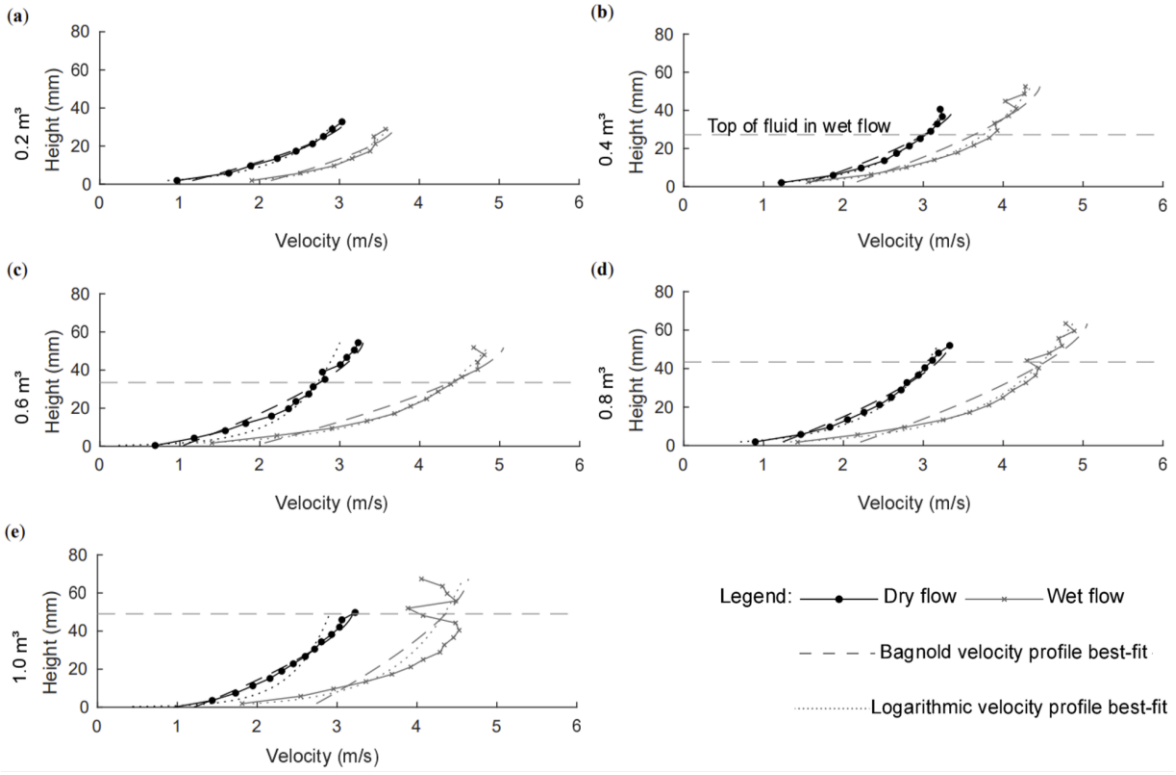

Figure 7-23: The velocity profiles of large-scale dry and saturated granular flows with different source volumes; each curve is taken at the maximum flow height of each test (after Taylor-Noonan et al. (2022)).

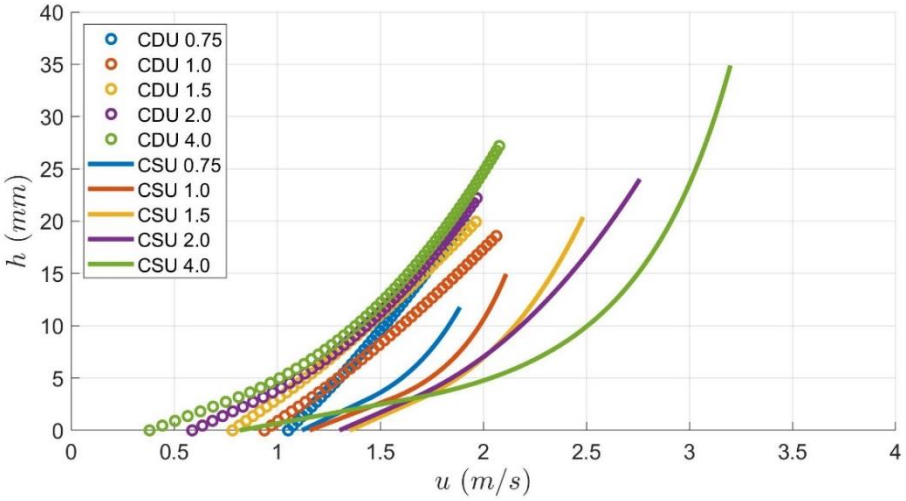

Figure 7-24: The velocity profiles of CDU and CSU granular flows with different source volumes; each curve is taken at the maximum flow height of each test.

8. Conclusion

The present thesis has focused on the experimental investigation of small-scale granular flows down an inclined flume with different material compositions from dry to saturated and from uniform to well-graded. This study was motivated by the poor understanding of the evolutionary process of granular-flow behaviours in response to the complexification of material composition from idealised to realistic and successfully captured a few essential differences in flow behaviours at both macroscopic and microscopic levels among the dry uniform, wet uniform and wet well-graded granular flows. The performed work includes the experimental conduct and data analysis of granular flows with those aforementioned three different flow conditions. The major findings of this thesis are briefly summarised below:

(i) Bulk flow mobility at the centre of gravity (COG) of dry granular flows slightly decreases with the source volume, while that of wet granular flows increases with both the source volume and water content except when the flow is highly unsaturated. Runout behaviours

of granular flows vary with different material compositions and accordingly the bulk flow mobility at COG shows high relevance to parameters representing the different deposition mechanisms. With increasing source volumes, the deposition process of dry uniform flows seems to be dominantly determined by solid friction, while that of saturated uniform flows and saturated well-graded flows by head velocity; their travel angle profiles can also be roughly predicted by those parameters. The wet uniform flows with evolving water content appear to be mainly controlled by suction (i.e. negative pore pressure) when the flow surge is practically unsaturated at low water content and by head velocity when saturated at high water content; hence both parameters exhibit correlations with the travel angle profile. The well-graded flows seem to be matched better by the internal energy estimation than by bulk parameters: the bulk flow mobility depends more on kinetic energy for flows with increasing source volume, while on the solid friction work for flows with evolving water content; in addition, the development of basal pore pressure also shows a certain degree of relevance to the travel angle.

(ii) Low water content retards bulk flow mobility while high water content enhances mobility. The relationship of travel angles of wet uniform flows with water content ranging from 0.01 to 0.45 is shaped like a "checkmark", in which the maximum travel angle (i.e. the minimum bulk mobility) is found at about $w = 0.1$. The travel angle of 2L wet granular flows is larger than that of the 2L dry flow within the range of $w \leq 0.3$, beyond which the travel angle is lower than that of dry flow; the transition from lower mobility to higher mobility is quite smooth. This is directly associated with the measured basal pore pressure data, where strong suction is shown within the flow surge when mobility is retarded and buoyancy (via positive pore pressure) is produced when mobility is enhanced. Similar runout properties can also be found in well-graded flows.

(iii) When there is no evident suction effect (i.e. when the water content is relatively high), a linear relationship between water content and bulk mobility of wet granular flows within a 2D flow path can be fitted; its intercept increases (here increasing denotes higher mobility) with source volume and the non-uniformity of grain size, while its slope seems independent of these two factors. This indicates that, at the same water content, the bulk mobility of larger granular flows is higher than that of smaller flows, while that of well-graded flows is higher than that of uniform flows; also, the exhibition of a suction effect occurs at a lower water content for a larger source volume and for well-graded solid material.

(iv) No excess pore pressure has been found in fluid-mixed uniform flows composed of large, highly-permeable pseudo-spheres, indicating that the pore fluid contribution to high bulk flow mobility of wet uniform flows is only through buoyancy.

(v) Depth-averaged velocities of wet uniform flows systematically increase with both source volume and water content, but those of dry uniform flows and well-graded flows do not show considerable change with either; hence this suggests that pore fluid can reduce internal energy loss in a uniform material, to allow an efficient velocity increase. Also, well-graded flows produce the lowest velocities but the highest bulk mobility, indicating that polydispersity enables high bulk mobility to be produced without the assistance of high flow velocity.

(vi) The fundamental role of pore fluid is to adjust the intergranular contact stress. Suction in unsaturated flows due to a small amount of pore fluid binds the grains more tightly and increases the shear strength of the flow material. Buoyancy in saturated flows at higher water content alleviates the enduring contacts between solids; in uniform flows, this effect helps to generate smaller velocity loss and lessened local shear rates across the flow depth, thereby producing velocity profiles shaped like a "plug flow"; in well-graded flows, this allows plastic deformation of the flow material more easily to develop, giving the flow material a higher potential to propagate farther.

(vii) The fundamental role of polydispersity is to change the deformation pattern of the flow material. The uniform pseudo-spherical grains under enduring contacts tend to have interlayer translational movement, hence the deformation of flow material is similar to that in the plane-shear configuration. The flow surge of well-graded soils, however, can barely develop such interlayer motion due to the stronger contact stresses between interlocked grains of various sizes, which should also be responsible for the no-slip basal boundary and hence the low depth-averaged velocity; instead, it has an extension tendency to become thinner but longer during the flow motion, similar to the "yielding" or "failure" of soils; this deformation pattern causes a dramatically high bulk shear rate. Furthermore, the high bulk flow mobility of well-graded flows may also be attributed to the material deformation: the flow surge is compressed and then dilated throughout the deposition process; given that the lower permeability of well-graded soils helps to generate large pore pressures and enable them to persist, a larger extent of deformation may imply a higher potential to develop a similarly large extent of re-deformation, thereby producing higher bulk mobility.

8.1. Limitations

This experimental study is limited by a few issues resulting from the designed small-scale flume system. (i) The hopper with a narrow opening caused inconvenience in mixing and agitating the source material, especially for the well-graded Maple Mud which can easily consolidate inside the hopper (see Sec. 6.2). (ii) The aluminium flume bed is rather smooth and its surface roughness can decrease after conducting multiple flow tests, causing inconsistent flume conditions across different test groups; the flume bed was slightly smoother when doing well-graded flow tests than that when doing uniform flow tests (note that its smoothness was designed to match that of the Queen's flume). (iii) The limited length of the horizontal runout channel due to space restrictions hindered the application of larger source volumes and higher water content. (iv) Non-transparent source materials only allowed observations of the flow event and non-intrusive velocity measurements at the sidewall, where the flow velocity is known to be lower than that in the centre of the flow (e.g. Jop et al. (2005); Bryant et al. (2014)); this means that data acquired from PIV analysis cannot precisely represent the kinematic properties of the tested flow. (v) The 2D flow path enabled easy comparisons, both across different tests and with the large-scale flume tests carried out at Queen's University, Canada, but also prevented the flow deposit from lateral spreading and forming an alluvial fan, which is one of the most typical runout behaviours of realistic debris flows.

8.2. Future Work

Future work after this study may consider covering the following issues. (i) Analysing techniques like Particle Tracking Velocimetry (PTV) may be utilised to more accurately capture the volume fraction or concentration of the solid grains in motion; this will allow a more accurate estimation of the variation in pore space and may deepen the insight into the suction generation in unsaturated granular flows. (ii) Wider ranges of source volume and water content may be designed for well-graded materials to complete the spectrum of flow behaviours; this will need a larger space to conduct flume experiments. (iii) Flume inclination can be altered to show the influence of slope angle. (iv) A flume bed with higher surface roughness (such as the bed attached with coarse sands) may be employed to investigate if slip velocity still increases with water content.

Appendices

A Data Acquisition Equipment

A-1 Product Information

Data acquisition equipment includes a high-speed camera, an ultrasonic sensor, two load cells (LCs) and two pore-pressure transducers (PPTs). The high-speed camera chosen for this study is Phantom Miro 310 which can capture images at up to 3260 fps and at a full resolution of 1280 × 800 pixels. The Phantom Camera Control software compatible with the camera serves as the user interface to customise the camera settings (e.g. framerate, recording duration, resolution, edge trigger) and to store, edit and convert the captured cine file. This camera is easy to set up, can give adequate image quality and framerates for performing PIV analysis, and has been utilised in previous studies such as Sanvitale and Bowman (2012) and Gollin et al. (2017b). Some tradeoffs must be considered to achieve ideal image quality in the shooting process. The increase in framerate can result in smaller displacement between two frames, allowing better PIV estimation, but it also increases the shutter speed and hence reduces the image brightness, which can be enhanced by adjusting the lens aperture and adding an external light source (a floodlight in this study). The framerate also reduces the recording duration as the total number of frames that can be stored temporarily in the camera drive has an upper limit; for the camera setting in this study, the maximum number of frames available for one footage is around 8300.

The S18UUAQ series barrel ultrasonic sensor made by Banner Engineering is utilised to measure the granular flow thickness. This sensor is mounted on an aluminium angle fixed on the flume sidewall, with its head 30 mm from the sidewall top and 226 mm from the flume bed, ensuring to cover the granular flow within the operating range of 30 - 300 mm.

The selected LCs are LUX-B-ID Compact Tension/Compression Load Cell provided by Kyowa Electronic Instruments, a highly-sensitive, water-proof, stainless-steel canister force transducer. This LC type is suitable for measuring both tension and compression with a rated capacity of ±50 N, which is normally far greater than the load applied during the small-scale flume experiments; this capacity is preferable mainly for avoiding accidental overload or damage to LCs when storing, carrying, installing and uninstalling them. The load receiver on the LC is a screw-shaped element and a cylindrical loading plate with a 26 mm diameter is screwed on the load receiver to measure the basal normal stress over the area of the loading plate. The LC is fixed on an L-shaped bracket and is installed beneath the flume bottom (Figure A), with the loading plate reaching out the drilled hole (ending up as in Figure 3-2 (b)); the top surface of the loading plate is positioned slightly lower than the flume bed surface to avoid the lateral impact caused by grains hitting the plate rim.

Pore-pressure transducers are PDCR 810 General Purpose Pressure Transducer from Druck Ltd. Selected sensors can accurately measure both positive and negative pressure ranging up to ±350 mbar or ±35 kPa, and is also sensitive to small rises in pressure. PPT is installed on the flume bottom through a ¼ British Standard Pipe (BSP) threaded hole (Figure A). To guarantee effective PPT performance, the threaded hole must be saturated with water without any leakage or entrained air bubbles. A zero-pressure point is defined by the condition where the threaded hole with no covering is filled with water using a syringe; after that, the saturating step must be done to achieve a zero PPT reading every time before running a new test.

Figure A-1: Load cell and pore pressure transducer mounted beneath the flume bottom.

A-2 PPT Filters

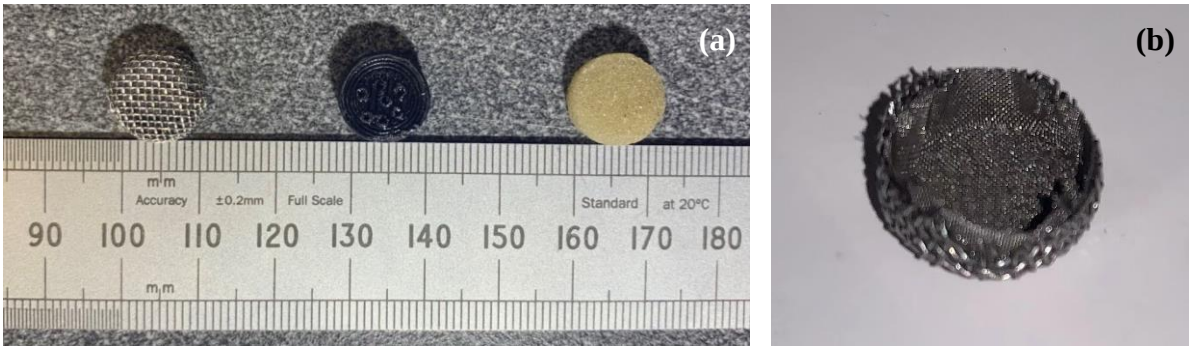

Figure A-2: Alternative PPT filters. (a) metal mesh with 0.5 mm apertures (left), 3D-printed cap (middle) and porous stone (right); (b) two-layer mesh where the inner layer is a 0.1 mm finer mesh while the outer layer is the 0.5 mm mesh.

As described in Sec. 3.1.1, filters are needed to cover the PPT threaded holes, preventing the grains from falling into the threaded holes. For uniform granular flows in this study, the 3.85 mm Denstone 2000 ceramic beads can be easily blocked by metal mesh with a 0.5 mm aperture size, as shown in the left-hand side of Figure A-2 (a); the metal mesh has been proved in uniform tests to pose very little or no impact on the fluid in the PPT hole, hence not affecting the PPT signals. For well-graded flows, fine sands and silt content in Maple Mud can drop into the mesh apertures and interfere with PPT responses. Thus plugs that can filter out finer particles are required for well-graded granular flows.

Two more options other than mesh were available for finer PPT filters. The black plug presented in the middle of Figure A-2 (a) has also been employed in large-scale experiments at Queen's University and is prepared by 3D printing as a cap with a few small circular holes on the top surface; this cap allows convenient PPT saturation, which can be simply done by putting the syringe needle through one of the cap holes and injecting water into the PPT threaded hole. Porous stones (the one on the right-hand side of Figure A-2 (a)) are commonly utilised as filters in experiments; this type of stone is hard, rigid, and has the advantage of adjustable permeability: they are waterproof in dry conditions while are completely permeable when fully de-aired by water.

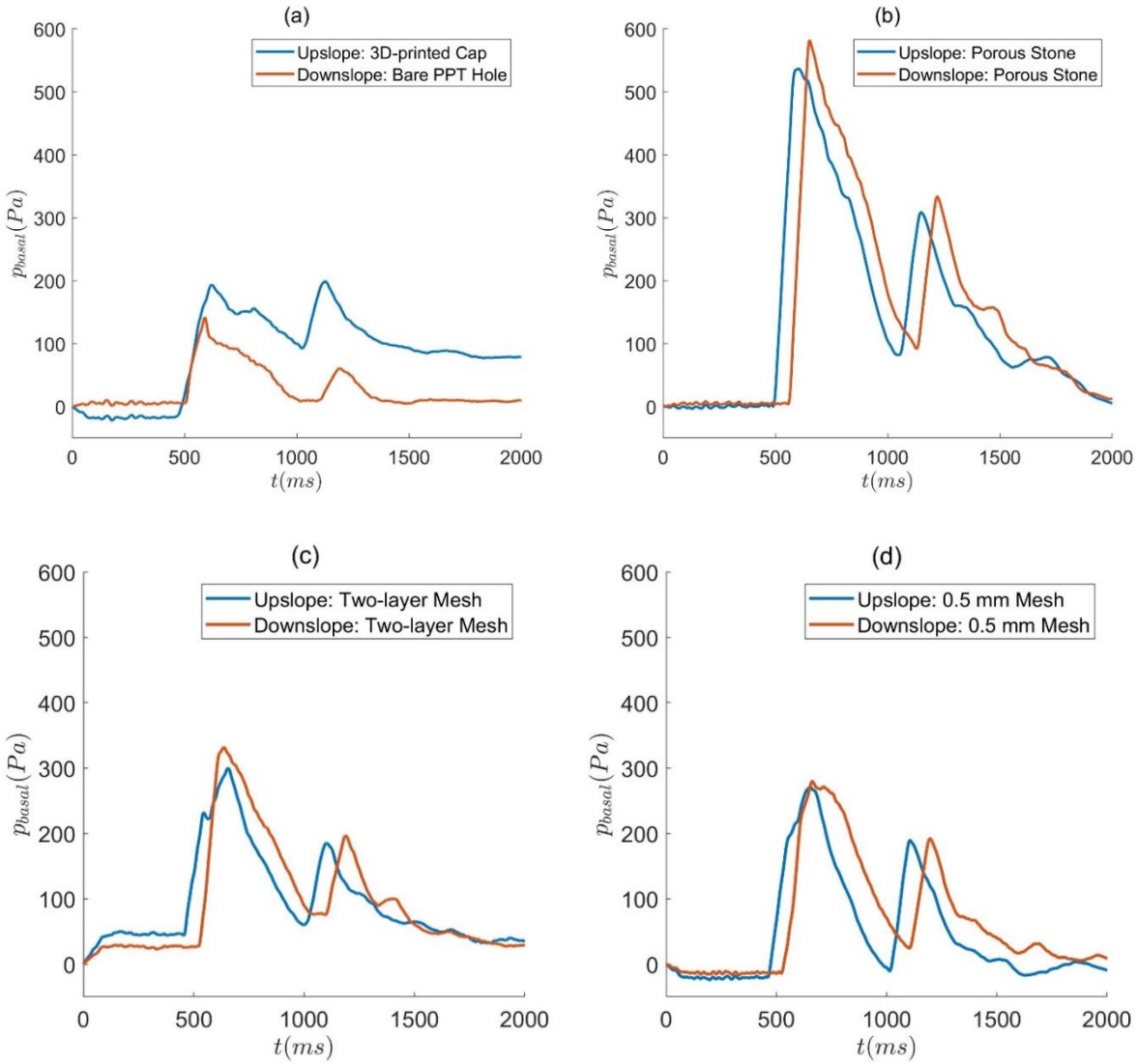

Figure A-3: Water trials using different PPT filters. (a) 3D-printed cap; (b) porous stone; (c) two-layer mesh; (d) outer mesh only.

However, trials using water flow suggested that these two alternative filters can result in abnormally high values of PPT signals. Figure A-3 (a) shows pore pressure responses to a water flow (about 1.5 – 2 litres in volume) passing by the upslope PPT capped by the 3D-printed cap and the downslope one without any covering. Since no grains were involved, the downslope PPT signal can be regarded as a benchmark, proving that the upslope PPT values are excessively high and remain high after the flow surge passes. In contrast, the trial represented in Figure A-3 (b) with porous stones poured about 2L of water into the flume but obtained over 500 Pa peak basal fluid pressure, approximately 5 times the peak value in the bare-hole case; this cannot be real even if considering more water was used. Although Figure A-3 only gives an example trial for each PPT filter, the phenomenon represented in each subplot can commonly be found when applying corresponding filters. Those high pressures prove that the 3D-printed cap and porous

stone can interact with the water inside the PPT hole; specially, the persistent high pressures indicate that water is difficult to flow out from the 3D-printed cap. The solid phase of saturated porous stone can perhaps transfer its exerted load to the coupling fluid phase within the stone, and hence to the fluid inside the PPT hole; an example of evidence is that the PPT signal notably increases when the porous stone is tapped, whereas similar increase occurs only when pressing the 0.5 mm metal mesh and covering most apertures. A possible explanation for the persistent pressure is that 3D-printed material allows a layer of water film to be formed due to surface tension; this water film adheres to the inner top surface of the cap, jamming the small apertures and holding the water inside. This phenomenon can also lead to a "false high value" of PPT signals, which occurs in the PPT saturation process: when water is injected into the threaded hole, the water film can result in a PPT reading higher than zero; consequently, a portion of water needs to be pushed out from the hole to reach zero pressure; however, suction applied on water film when water escapes from the threaded hole can pose extra force onto the PPT, in which case zero reading can be achieved when the threaded hole is not fully saturated; this extra force disappears immediately when the water film breaks after some time (a few tens of seconds to several minutes), resulting in a sharp drop of PPT signal. Magnitudes of pressure difference caused by these issues may not be significant in larger-scale experiments as higher fluid pressure can be produced; in this study, however, the basal pore pressures from small-scale granular flows are commonly less than 1 kPa, hence even small errors in pressure readings are better to be prevented. In summary, both porous stone and 3D-printing material are not ideal for PPT filters.

Metal mesh still appeared to be the appropriate choice of the PPT filter as it can avoid interacting with PPT responses. To block finer particles, another mesh with a 0.1 mm aperture size was put inside the original 0.5 mm mesh, forming a two-layer mesh as shown in Figure A-2 (b). The outer mesh can support coarser and heavier clasts so that the mesh does not bend or deform due to the load exerted by granular flow, while the inner mesh ensures finer particles can be filtered out. Figure A-3 (c) and (d) compare the 2L water flow trials using respectively the two-layer mesh and the 0.5 mm outer layer mesh only. As the 0.5 mm mesh does not influence the PPT signals, the pore pressure curve in Figure A-3 (d) can be deemed accurate, thereby Figure A-3 (c) which presents a close curve suggests that the two-layer mesh is capable of giving correct PPT responses. Therefore, the two-layer mesh was selected for capping the PPT threaded holes in the well-graded flow tests.

A-3 Sensor Calibration

All the sensors have been carefully calibrated to determine the slope and intersect of a linear input-output relationship. For load cells, three calibration ranges were tested: 1 N, 10 N and 40 N (which is close to their rated capacity of 50 N), as demonstrated in Figure A-4. Raw normal stress data from a few trials give a fluctuation maximum of about 6 kPa, which can be converted into a 3.1856 N normal force on a 530.93 mm^2 area of the loading plate. The 40 N calibration range sacrifices resolution, hence the reading is not adequately accurate under a very small applied load; considering the small load from granular flows, a higher sensitivity for a low loading range is preferred. However, as can be seen in Figure A-4 (a), a slightly ladder-shaped input-output profile was found from the lowest 1 N calibration limit, indicating that LCs are not highly sensitive to tiny variations of loading; this calibration range may underestimate the normal stress reading**.** In the end, the LC calibration range was determined to be 10 N as shown in Figure A-4 (b), balancing both linearity and resolution.

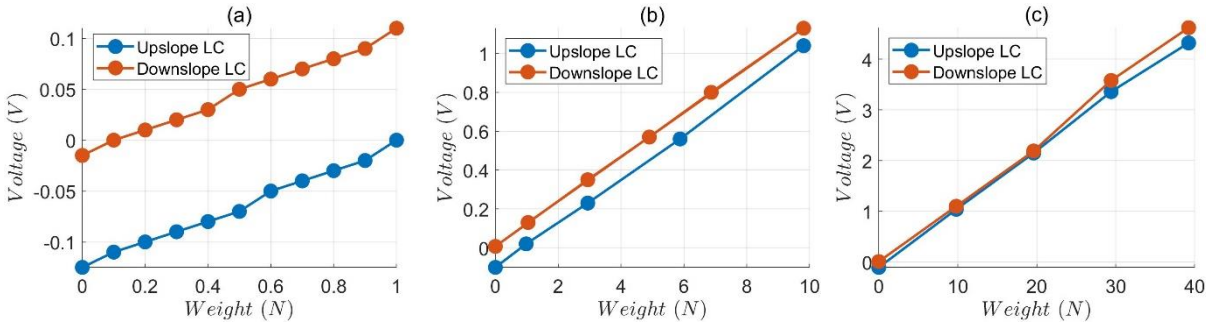

Figure A-4: Load cell calibrations within the input range of (a) 1 N, (b) 10 N and (c) 40 N.

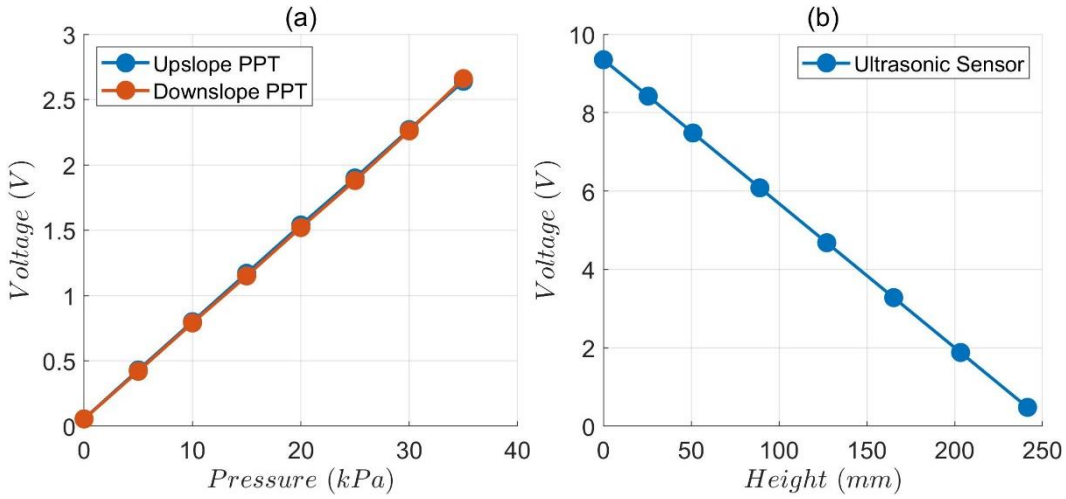

Figure A-5: Calibrations for (a) PPTs and (b) ultrasonic sensor.

The pore pressure transducers were calibrated by an electronic pressure calibrator, which allows convenient control of pumping pressure increments. The calibration range was from 0 to the rated capacity of 35 kPa, with calibration points determined every 5 kPa. As depicted in Figure A-5 (a), calibration points of different PPTs are highly close, exhibiting a good product consistency. The reliability of PPT is also validated by trials with water at static state and water flow in motion. Figure A-6 (a) shows the configuration of static water trials where water is blocked inside the inclined flume and pressurises the PPT on the flume bed; trials were conducted both with and without the metal mesh to ensure the mesh, as the chosen filter above PPT, does not interfere with the obtained signals, which are given in Figure A-6 (b). Note that load cells were fully sealed by tapes to retard leaking and the ultrasonic sensor cannot receive the signal reflected from the 30° water surface (see A-4), thus normal stress and flow height data are not available. The height of water column above the PPT was manually measured to be 38.97 mm with the mesh and 36.02 mm without the mesh, leading to the theoretical steady-flow pressures (Eq. (5-1)) of 331 Pa and 306 Pa, very close to the PPT-measured data in Figure A-6 (b). PPT responses and load cell signals due to water flow also agree with each other, as presented in the example given in Figure A-7, showing that both sensors can provide believable data.

The ultrasonic sensor was calibrated after being installed in position. Since the ultrasonic sensor measures the distance from the object within its operating range, a higher flow is equivalent to a closer distance to the sensor. Therefore, the distance between the sensor head and flume bed surface was set to zero, and increasingly higher output values were set in response to the higher surface of overlying concrete blocks with approximately the same thickness of 40 mm. As a result, a negative slope (i.e. a lower output voltage responding to a closer sensed object and a larger block height) was obtained to the calibration curve, and direct reading of the flow height value was then achieved.

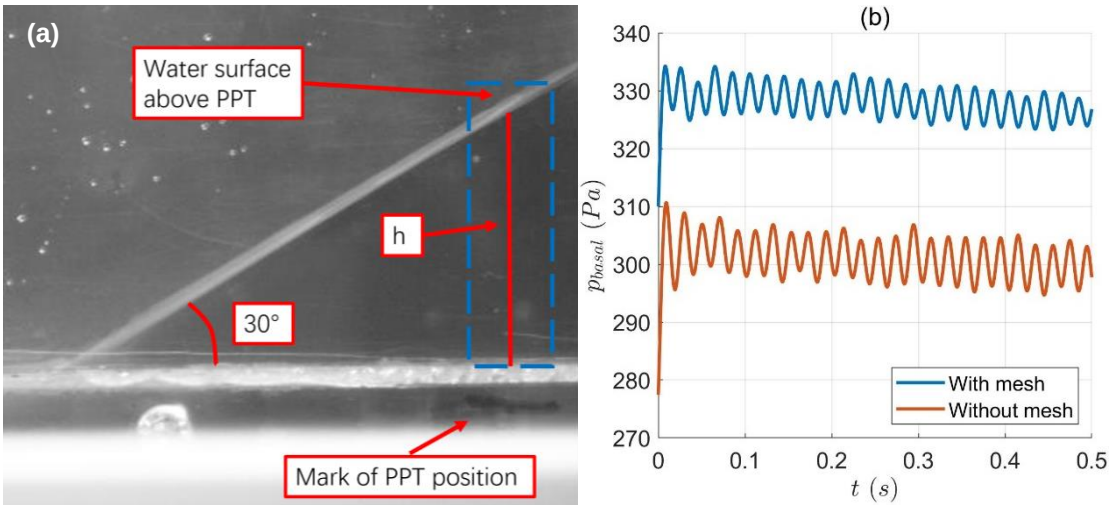

Figure A-6: (a) The configuration of static water trials; (b) signals of PPT (with and without the metal mesh) in response to hydrostatic pressure.

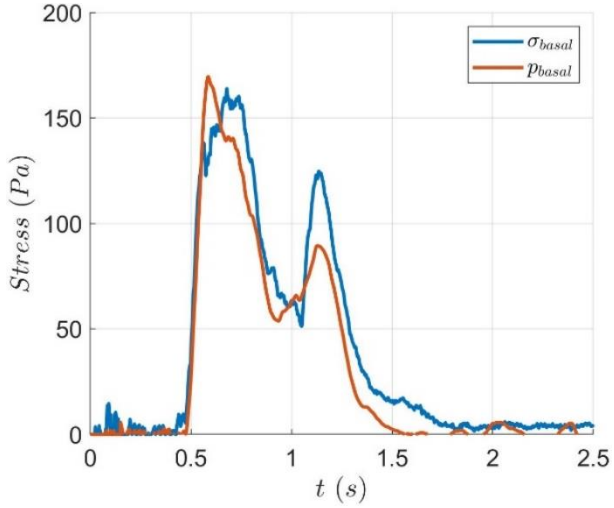

Figure A-7: Signals of load cell and PPT at the downslope position.

A-4 Source of Error

Sensor errors are inevitable in practice. Error generation of LC is connected with the mounting configuration. The loading plate attached to LC should ideally experience no lateral confinement to accurately measure the normal force, hence a small gap is kept between the loading plate rim and the drilled hole on the flume bed; to deal with the concomitant technical problems, such as grains falling into the gap and the loading plate tilted under temporary torque, the gap is sealed with silicon grease. However, silicon grease cannot completely seal the gap and small particles (e.g. fine sands, silts, ceramic fragments) can still be trapped inside the gap, interfering with the normal stress measurement. This kind of error is difficult to quantify as it is affected by the number and position of the trapped fines: if the particles are stuck at one side of the gap, a torque

can be applied to the loading plate; this possible unbalanced condition makes it difficult to predict whether the normal stress measurement may be overestimated or underestimated. In the experimentation, the influence of this error was reduced by cleaning the gap around LC after a group of tests is done, ensuring a relative consistent LC condition throughout the test group; additionally, LCs were re-zeroed before conducting the first test in every lab work day to cancel other minor effects on the loading plate.

PPT errors are mainly caused by the interaction between the filter upon the transducer hole and the fluid within the hole (Appendix A-2); this error was minimised by employing metal meshes that pose no significant impact on PPT signals. Another minor issue is that the PDCR 810 PPT seems very sensitive to the change in temperature; thus re-zeroing the PPT is reasonable when two tests are a few days apart.

The biggest issue with the ultrasonic sensor is that the measurement is most accurate when the detected surface is normal to the sensor (i.e. parallel to the flume bed); with an increased angle between the flume bed and flow surface, a larger portion of the reflected ultrasonic energy is deflected and cannot travel back to the sensor, reducing the measurement accuracy; the sensor eventually gives no response when the detected surface makes an angle larger than about 15° - 20° with the flume bed. This effect is weaker when the measured flow surface passes very fast and is obvious when the material moves slow or has no motion. Similarly, the measurement can be inaccurate when the particles saltate at the surface of a highly collisional dry granular flow. Therefore, the detection of flow surface is mainly determined by PIV analysis and the ultrasonic sensor response is used for reference.

B Sensor Signal Processing

B-1 Noise Removal

To differentiate noises from meaningful data, some trials were conducted with flowing-down grains fully blocked before hitting the load cells (Figure B-1). Theoretically the response of the load cell, on which no load was applied, should be a flat line at zero in this case. The actual load cell response is as shown in Figure B-2 with the title ”input signal”; this waveform displays some noises in the initial stage of the test, probably due to the flume bed vibration when grains dropped in from the hopper. By now, the flume has been fixed to the supporting frames both above and beneath the flume; this stabilization measure greatly reduces the flume vibration.

Figure B-1: Noise test with grains obstructed before touching the upslope load cell.

Noises were removed from the data by the Fast Fourier Transform (FFT) filter. This filter allows a direct manipulation of selected bands in the frequency domain, i.e. it can control signals with certain frequencies. Figure B-2 shows the FFT filtering process utilized in the data processing part of this study. (i) An “input spectrum” was obtained by applying FFT to the “input signal” in time domain. (ii) Two major ranges of spikes were identified in the input spectrum, with frequencies from $10^{2.5}$ = 316.228 Hz to about 3000 Hz, and 33 kHz to 35.684 kHz at the other

side of the symmetrical position. (iii) Individual spikes between the main noisy ranges, i.e. from 3 kHz to 33 kHz, were also found. (iv) A "cleared spectrum" was then achieved after setting the detected spike amplitudes to zero. (v) finally a "cleared signal" was derived from the inverse FFT of the cleared spectrum. The input and cleared spectrums in the logarithm of frequency domain are also plotted in Figure B-2 in order to get a more detailed view of the spectrum in low frequencies. The load cell signal becomes stable and reasonable after the FFT filtering.

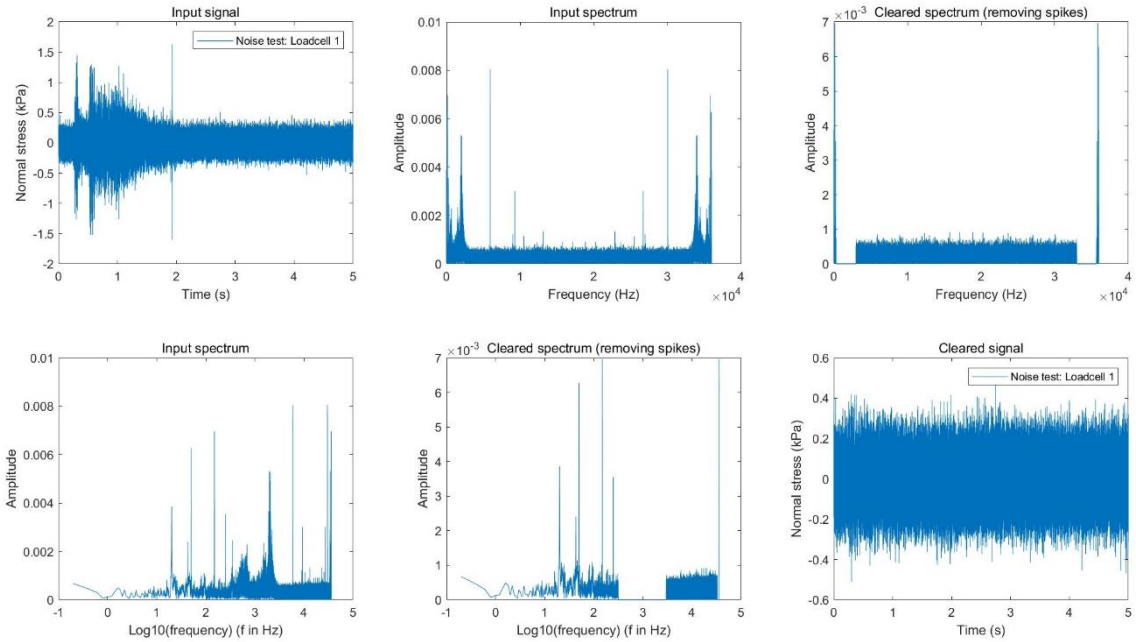

Figure B-2: FFT filtering process of the load cell signal from a noise test.

Then the FFT filter was applied to real experimental data collected from CDU30 tests. The load cell signal from CDU30 (5), which is the test with the largest 4 litres volume of the grains, are used to exhibit the FFT filtering process in Figure B-3. Note that the effect of major spike ranges (316,228 - 3000 Hz and 33 – 35.684 kHz) is distinctly higher than but only other individual spikes, but also the same spikes in Figure B-2, proving that volume (and hence mass) of grains does amplify the manifestation of noises in those frequencies, and thus proving that flume vibration resulted from grain entering is responsible for noises in these frequencies. The load cell signal after FFT filtering ("cleared signal") shows a reliable noise removal outcome, as the signal fluctuation amplitude is reduced and the saltation in the early stage of the test is disappeared. The FFT results of data in CDU30 tests acquired from two load cells and the ultrasonic sensor are as shown in Figure B-4.

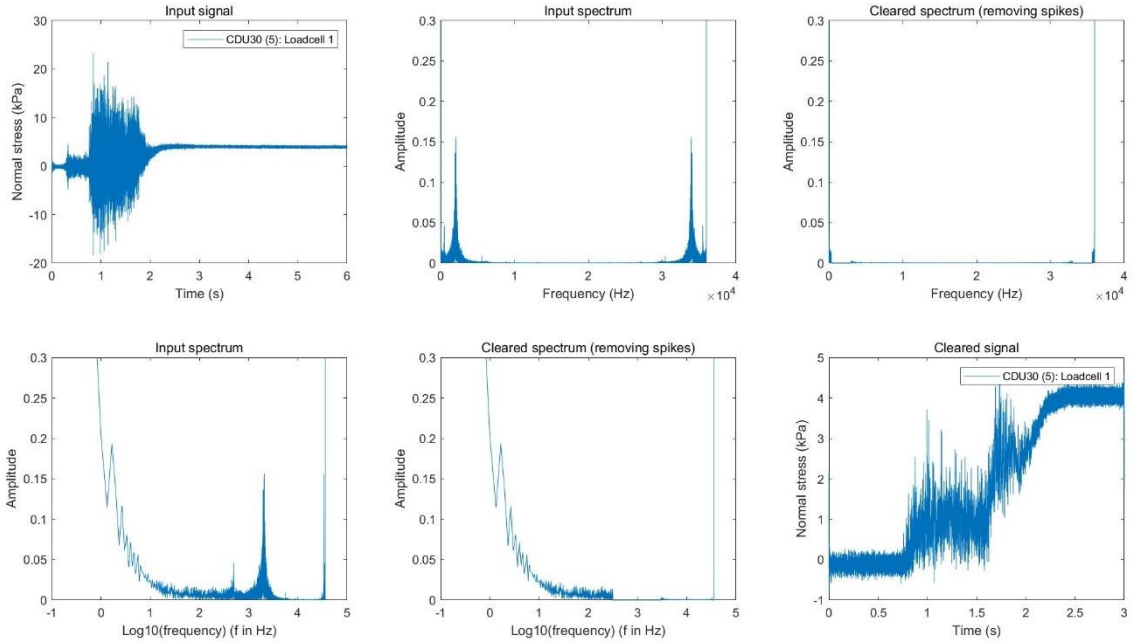

Figure B-3: FFT filtering process of the load cell signal from CDU30 (5).

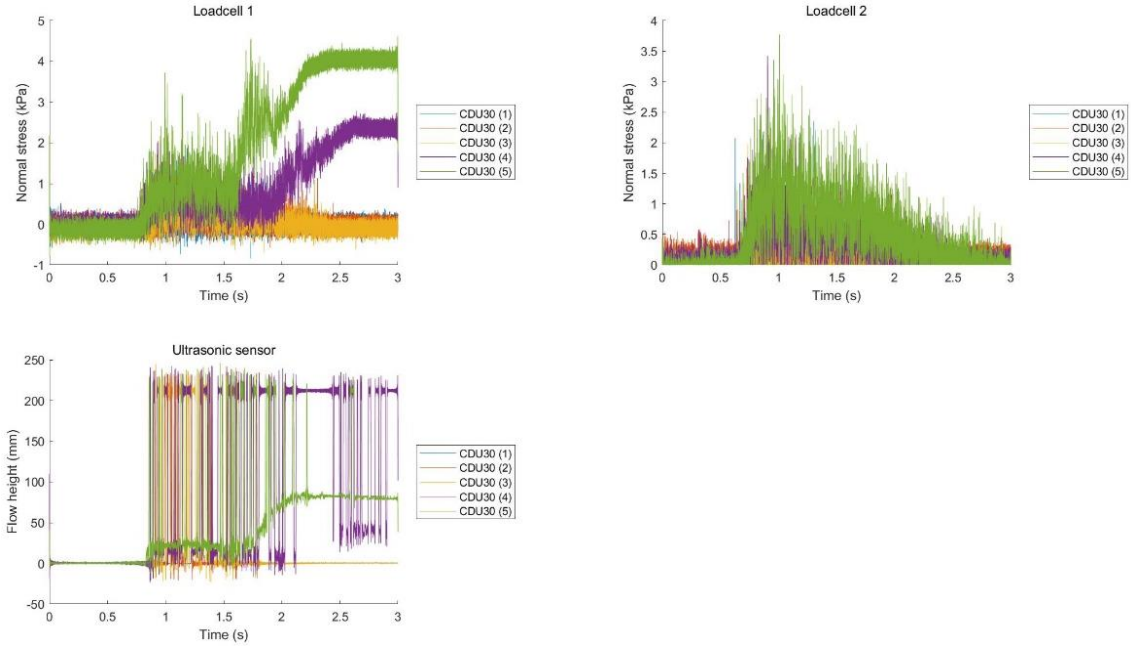

Figure B-4: FFT filtering results of the data from CDU30 (5).

B-2 Outliers Replacement

Outliers can be detected and replaced automatically using MATLAB. To find local outliers differing from the surrounding data within a certain range, a moving window method was

applied. This approach uses three parameters, i.e. “fillmethod”, “movmethod” and “window”, to determine and manipulate local outliers.

(i) “Fillmethod” specifies the value to replace an outlier. In this study, the outliers are refilled with the previous non-outlier value. This is mainly for countering the “dead zone” outputs in ultrasonic sensor responses: a “dead zone” signal can maintain for a short period of time; thus when the window is moving forward along the time axis, the previous value is more reliable.

(ii) “Movmethod” defines the local outlier identification method over the moving window length. For more accurate detection, outliers are determined as data more than three local scaled median absolute deviation from the local median.

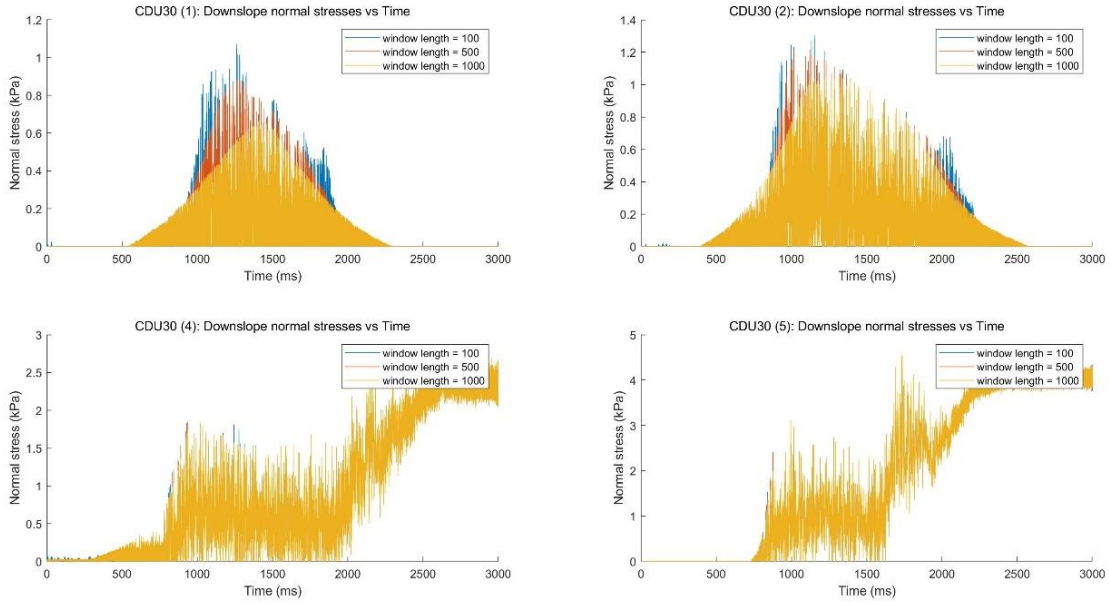

Figure B-5: Moving-window outlier replacement results with different window lengths: 100, 500 and 1000 data points.

(iii) “Window” represents the size of the moving window in which data are processed. As data evolution over time, i.e. x-axis, requires no processing and only variation in y-direction needs to be controlled, the window size in this study was defined as a duration vector, represented by the number of data points within this duration. For determining an appropriate window size, different window length (100, 500 and 1000 data points) were tested and the results are as shown in Figure B-5. This figure, which uses data from downslope load cell signals for example, shows that window length makes less difference for the test with larger volume of grains. However, for low material volumes, data curves

start to lose their original shapes with 1000 points window length. Therefore, the window length was decided to be 500 data points.

B-3 Data Smoothing

Two smoothing schemes were employed in sequence: averaging data points, and applying 1-D digital filter to data curves. Data were averaged by replacing a certain range of points with the mean value of this range. Figure B-6 shows the comparison of the load cell 1 data curves for the tests with the smallest and largest material volumes with the averaged curves. Obviously, from 100 to 1000, a larger averaging range gives a smoother output; yet, as this approach reduces data size (e.g. averaging every 100 data means substituting one point for every 100 points), higher possibility of information loss and data distortion comes with larger averaging range. Thus the averaging range should be selected with caution.

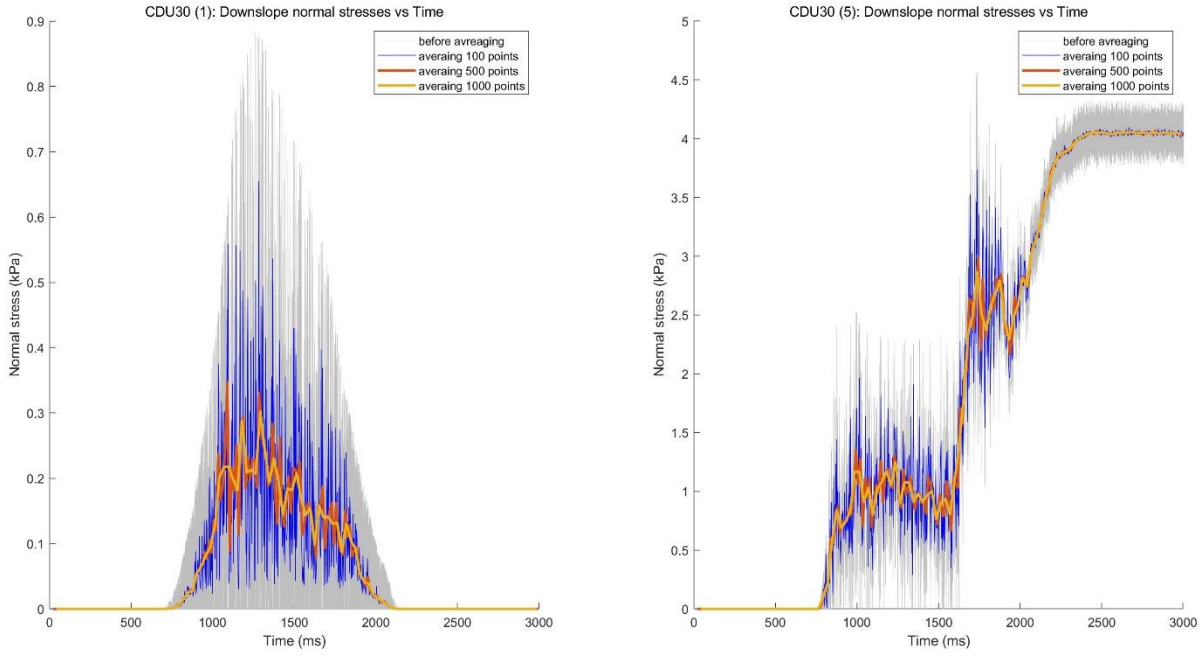

Figure B-6: Downslope load cell data smoothed by averaging every 100, 500, and 1000 data points.

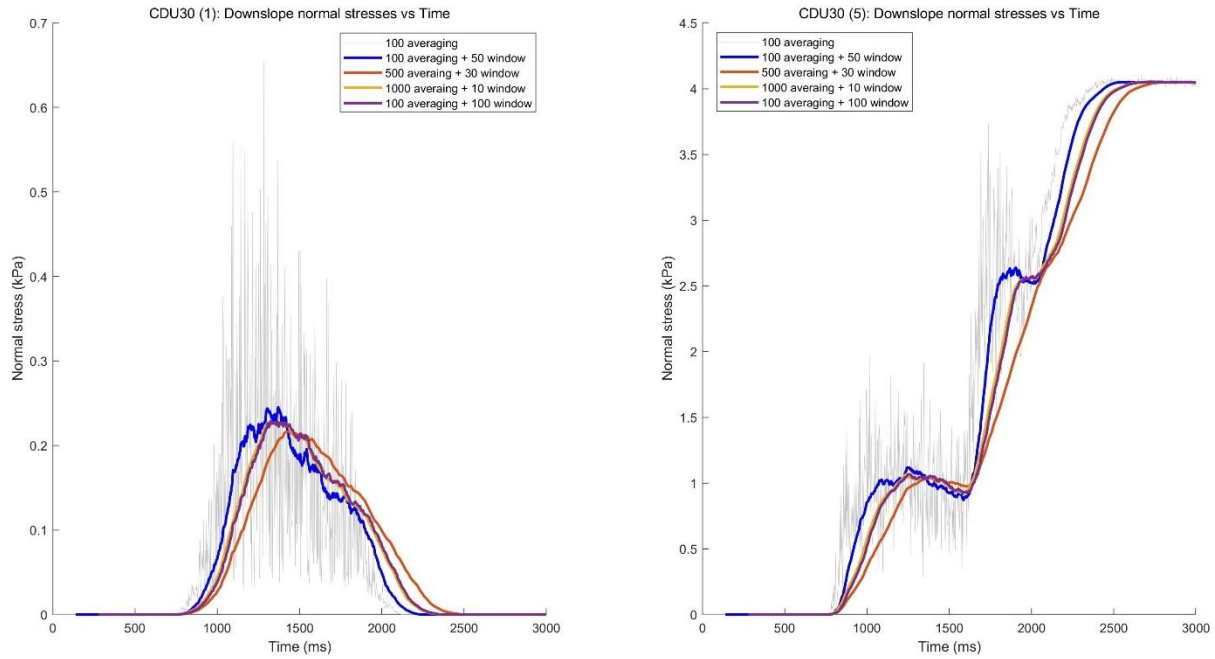

Figure B-7: Downslope load cell data smoothed by 1-D filter after averaging.

As all series of data can be regarded as vectors varying with time, a moving-average filter is chosen for smoothing the data collected. Similar to the moving window outlier-removing approach as mentioned in Appendix B-2, this 1-D filter computes the mean value of data contained in the moving window with a user-defined window length. The main difference of this method with the direct data averaging is that data size stays the same before and after filtering. To compare the filtering outcomes and to prevent over-filtering, four different combinations of averaging range and filtering window length were examined: 100 points averaging range combines with 50 points window length, 500 averaging range with 30 window length, 1000 averaging range with 10 window length, and 100 averaging range with 100 window length (Figure B-7); data smoothed only by averaging every 100 points (grey curves) were set as references to display the deviation after filtering. Note that 1000 averaging and 10 window length treatment gives the same output as 100 averaging and 100 window length filtering do, confirming that these two smoothing effects are equivalent for the final superposition. To achieve the balance between the accuracy and smoothness, the scheme of 100 points averaging range and 50 points window length is preferred for the lowest distortion and an acceptable smoothness.

The control of data size by averaging is necessary even though 1-D filter can give the same smoothing result. The data acquisition rate of all the transducers is 36 kHz, while the image sampling rate for PIV analysis is 2000 pictures per second, which equals to 2 kHz. A match of

time scale, i.e. the same data size for each vector, is required when combining sensor signals with kinematical information to derive complex parameters such as the Savage number. As a result, a common divisor of 36000 and 2000 close to 100, which is 90, was decided to be the averaging range.

C Velocity Processing

C-1 PIV Error Reduction

The generation of error is inevitable even under the optimal PIV performance, yet the error can be minimized with proper detection and prevention. Some systematic errors clearly depend on the patch size selection (Hart, 2000). When patch length is too small relative to the displacement, the number of grains in one image might vastly differs from that in the next image, yielding an error called "loss-of-pair" which increases the background noise; when patch size gets larger, measurement resolution reduces consequently. For experimental granular flows, the patch size strongly links with the grain size and test conditions such as lighting and image texture, which can be enhanced by using textured solid grains (roughened, irregular-shaped or coloured) or by increasing the image density (the mean particle numbers per patch). An image density ranging from 5 to 10 particles per patch has been recommended by Adrian et al. (2011); an optimal spherical grain image size of 2 to 4 pixel units has been empirically estimated by Prasad et al. (1992). A proper patch size choice should not be less than twice the displacement (i.e. the overlapping degree of the image pair), otherwise a correct cross-correlation peak detection cannot be guaranteed according to Nyquist-Shannon sampling theorem (Raffel et al., 2018); a preferable patch size has been suggested to be more than quadruple the maximal displacement magnitude (Keane and Adrian, 1992).

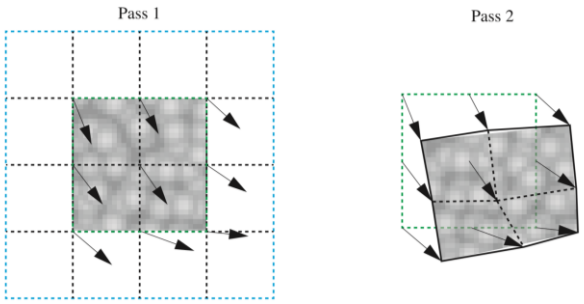

Figure C-1: Schematic illustration of window deformation algorithm (Gollin, 2017).

Another error known as "gradient bias" is caused by the large flow velocity gradient near the bottom boundary (Keane and Adrian, 1992). This can be produced from the combine action of

higher flow shear rate and greater basal frictional drag (e.g. non-slip boundary). As a result, when applying a standard static spatial domain correlation (i.e. when the interrogation window has a defined and fixed shape), grains with discrepant velocities can coexist in an individual patch, confusing the velocity estimate of the patch; within a given time span, slower particles can remain in the subimage from which faster particles have left, thereby biasing the displacement estimates with a broader intensity peak of the cross-correlation matrix. This type of error can be alleviated when adopting multi-pass iterative algorithms with window deformation approach (Scarano and Riethmuller, 2000; Scarano, 2001).

The window deformation algorithm enables a single patch to generate variant displacement vectors at 9 nodes (5 definition nodes and 4 interpolated nodes on the sides), as shown in Figure C-1. Therefore, displacements of nodes as well as deformed subimages, rather than rigid displacements of windows and static subimages, can be predicted from an initial standard correlation pass between an image pair. In the next pass, the initial undeformed patches in the first image needs to cross-correlate with the "presumed" deformed patches in the next contiguous image, searching for the best matches for all the subimages; the following passes repeat this cross-correlation, comparing the original patches with the deformed estimations in multiple (the number is user-defined) subsequent images; in each pass, remaining displacements of an patch are determined and are then added to the previous displacement results. Afterwards, the whole process repeats centring on the following images sequentially, until all the images are covered (Thielicke, 2014). The multi-pass iteration method refines the displacement computation while avoiding excessive mesh division, thus enhancing spatial resolution without triggering loss-of-pair under larger displacements, particularly appropriate for analysing highly-sheared granular flows.

C-2 Errors in Measured Velocities

The GeoPIV software used in this study generates a static mesh with uniform-sized rectangular patches. Measures have been taken to reduce the potential errors, for instance: the mesh consisting of four columns of patches allows each velocity profile to be averaged from a wider partially-overlapped domain (see Figure 3-6), the largest displacement between an image pair is smaller than the patch size and the length of the search zone so that the best match of the subimage within each patch can definitely be found, etc. As the patch shape and the uniform

patch arrangement cannot be modified in the software, the PIV measurement accuracy mainly depends on the selection of patch size. In the early stage of this study, 48×48 pixels patch was used to produce smoother velocity profiles as each velocity curve is averaged over a larger area. However, the large patch makes PIV measurement less sensitive to local displacement, potentially losing some small variations in local velocities; additionally, the use of smaller patches in which fewer solid grains are contained is possible due to the relatively close distance between the camera and flume sidewall and the image texture of solid materials. Thus, 24×24 pixels (approximately 1.4 ceramic-bead diameter) patch was determined for the PIV performance to capture more details in local velocity structures (see Sec. 3.2.2).

In this study, most analyses were based on instantaneous velocity profiles, in which the noticeable unreal data and outliers have been removed in postprocessing, while the velocity profiles averaged over 0.02s (i.e. 0.01s, which is roughly 1% of the main surge duration, both before and after the moment of interest) are mainly to support the evolution pattern derived from instantaneous velocities. Good agreements between the instantaneous and averaged velocity profiles can suggest fewer error generation in PIV analyses. Figure C-2 shows the averaged velocity profiles taken at 25%, 50% and 75% of the main surge duration of CSU 4.0 flow as an example, compared with instantaneous velocity data taken from the 0.02s averaging range around the selected time; the confidence interval, presented as dashed lines surrounding the red averaged velocity curve, is set to two standard deviations, referring to the selection of Sanvitale and Bowman (2017). Almost all the instantaneous velocities fall within the range of confidence intervals around the averaged velocity profiles, indicating a reasonable accuracy of PIV measurements.

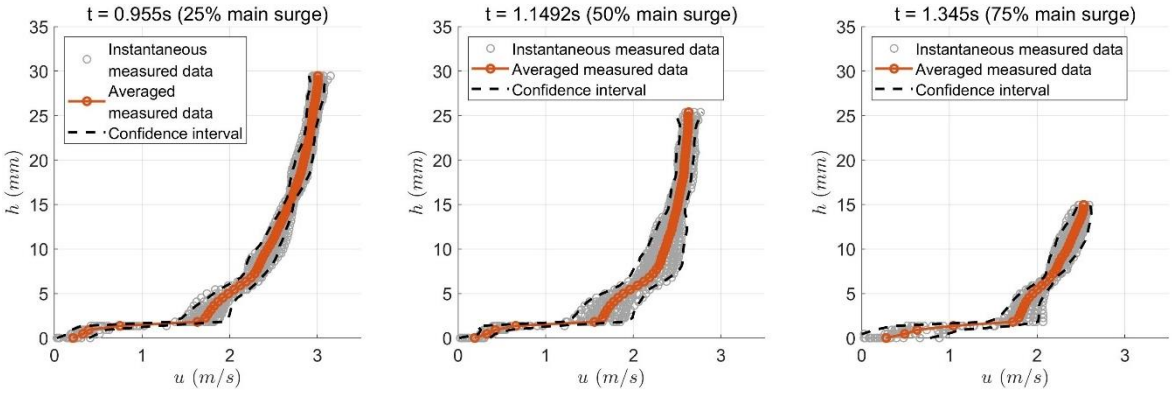

Figure C-3: Instantaneous velocity profiles, averaged velocity profiles over 0.02s and the range of confidence interval of two standard deviations. Velocity data are taken at the flow head, main body and flow tail (25%, 50% and 75% of the main surge duration).

C-3 Power-function Fitting

For all the tested flows, the best power-function fitting is applied to each velocity curve. The general form of the fitted power function can be written as:

$$u(z) = A \cdot z^B + C \tag{C-1}$$

where z is elevation normal to the flume bed while A, B and C are fit parameters; the values of A, B and C in some uniform (labelled with "U") and well-graded flows (labelled with "W") are shown in Figure C-4 as examples and the corresponding velocity curve shapes are characterised in Figure 7-16 and Figure 7-17. Note that identifying the best power fits in this study is not to fit velocity profiles with fixed selected frameworks but to indicate different deformation patterns occurring in different granular flows.

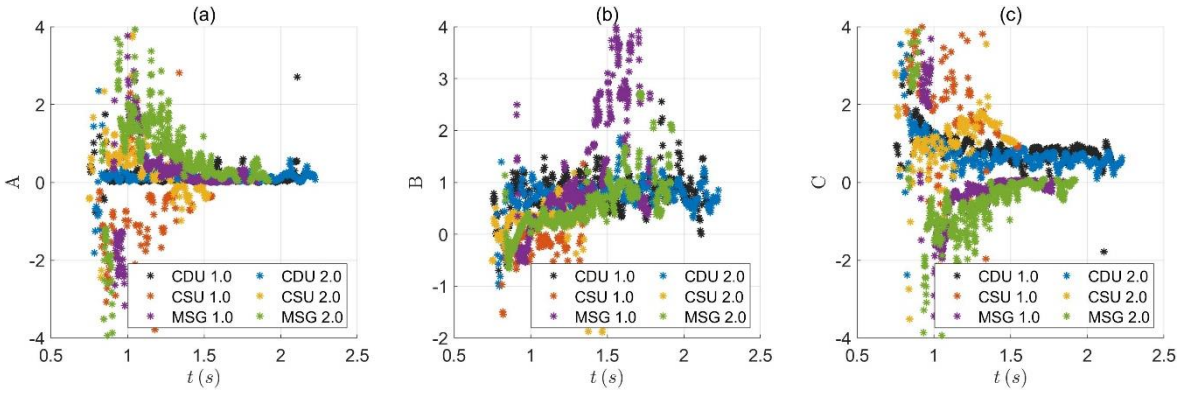

Figure C-4: Fit parameters A, B and C in the fitted power function $u(z) = A \cdot z^B + C$ for some examples of tested flows with 1L and 2L source volumes, including ceramic-bead dry uniform (CDU) flows, ceramic-bead saturated uniform (CSU) flows and Maple-mud saturated well-graded (MSG) flows.

References

ADRIAN, L., ADRIAN, R. J. & WESTERWEEL, J. 2011. *Particle image velocimetry*, Cambridge University Press.

AGUIRRE, M. A., GRANDE, J. G., CALVO, A., PUGNALONI, L. A. & GéMINARD, J.-C. J. P. R. L. 2010. Pressure independence of granular flow through an aperture. 104**,** 238002.

ALEXANDER, A., MUZZIO, F. & SHINBROT, T. 2004. Effects of scale and inertia on granular banding segregation. *Granular Matter,* 5**,** 171-175.

ALONSO, E. E., GENS, A. & JOSA, A. 1990. A constitutive model for partially saturated soils. *Géotechnique,* 40**,** 405-430.

ANDREOTTI, B., FORTERRE, Y. & POULIQUEN, O. 2013. *Granular media: between fluid and solid*, Cambridge University Press.

ARATTANO, M., MARCHI, L. J. P., CHEMISTRY OF THE EARTH, P. B. H., OCEANS & ATMOSPHERE 2000. Video-derived velocity distribution along a debris flow surge. 25**,** 781-784.

ARATTANO, M. & MARCHI, L. J. S. 2008. Systems and sensors for debris-flow monitoring and warning. 8**,** 2436-2452.

BAGNOLD, R. A. 1954. Experiments on a gravity-free dispersion of large solid spheres in a Newtonian fluid under shear. *Proceedings of the Royal Society of London. Series A. Mathematical and Physical Sciences,* 225**,** 49-63.

BARKER, T., SCHAEFFER, D. G., BOHóRQUEZ, P. & GRAY, J. 2015. Well-posed and ill-posed behaviour of the-rheology for granular flow. *Journal of Fluid Mechanics,* 779**,** 794-818.

BELKHATIR, M., SCHANZ, T., ARAB, A., DELLA, N. & KADRI, A. 2014. *Insight into the effects of gradation on the pore pressure generation of sand-silt mixtures,* ASTM International.

BISHOP, A. W. 1959. The principle of effective stress. *Teknisk ukeblad,* 39**,** 859-863.

BOWMAN, E., KAITNA, R., MCARDELL, B., MCELWAINE, J., SANVITALE, N., TAKE, W., TAYLOR-NOONAN, A. & ZHAO, Y. The Rosetta Stone project–integrating experimental results on debris flow mechanics across the scales: first results. XIII International Symposium on Landslides, 2021. : International Society for Soil Mechanics and Geotechnical Engineering.

BREARD, E. C., DUFEK, J., FULLARD, L. & CARRARA, A. 2020. The Basal Friction Coefficient of Granular Flows With and Without Excess Pore Pressure: Implications for Pyroclastic Density Currents, Water - Rich Debris Flows, and Rock and Submarine Avalanches. *Journal of Geophysical Research: Solid Earth,* 125**,** e2020JB020203.

BRENNEN, C. E. 2005. *Fundamentals of multiphase flow*, Cambridge university press.

BRYANT, S. K., TAKE, W. A. & BOWMAN, E. T. 2014. Observations of grain-scale interactions and simulation of dry granular flows in a large-scale flume. *Canadian Geotechnical Journal,* 52**,** 638-655.

CAGNOLI, B. & ROMANO, G. 2010a. Effect of grain size on mobility of dry granular flows of angular rock fragments: An experimental determination. *Journal of Volcanology and Geothermal Research,* 193**,** 18-24.

CAGNOLI, B. & ROMANO, G. 2010b. Pressures at the base of dry flows of angular rock fragments as a function of grain size and flow volume: Experimental results. *Journal of volcanology and geothermal research,* 196**,** 236-244.

CAGNOLI, B. & ROMANO, G. P. 2012. Effects of flow volume and grain size on mobility of dry granular flows of angular rock fragments: A functional relationship of scaling parameters. *Journal of Geophysical Research: Solid Earth,* 117.

CAMPBELL, C. S. 1990. Rapid granular flows. *Annual Review of Fluid Mechanics,* 22**,** 57-90.

CARMAN, P. C. J. T. I. C. E. 1937. Fluid flow through granular beds. 15**,** 150-166.

CARMAN, P. C. J. T. J. O. A. S. 1939. Permeability of saturated sands, soils and clays. 29**,** 262-273.

CARTER, R. 1975. A discussion and classification of subaqueous mass-transport with particular application to grain-flow, slurry-flow, and fluxoturbidites. *Earth-Science Reviews,* 11**,** 145-177.

CHENG, Y. M., FUNG, W. H. I., LI, L., LI, N. J. N. H. & SCIENCES, E. S. 2019. Laboratory and field tests and distinct element analysis of dry granular flows and segregation processes. 19**,** 181-199.

CHIALVO, S. & SUNDARESAN, S. 2013. A modified kinetic theory for frictional granular flows in dense and dilute regimes. *Physics of Fluids,* 25**,** 070603.

CONWAY, S. L., LIU, X. & GLASSER, B. J. 2006. Instability-induced clustering and segregation in high-shear Couette flows of model granular materials. *Chemical engineering science,* 61**,** 6404-6423.

COOMBS, S. 2018. *A Physical Investigation of the Flow Structure and Mobility Behaviour of Collisional Granular Landslides.*

COUSSOT, P. & MEUNIER, M. 1996. Recognition, classification and mechanical description of debris flows. *Earth-Science Reviews,* 40**,** 209-227.

DA CRUZ, F., EMAM, S., PROCHNOW, M., ROUX, J.-N. & CHEVOIR, F. 2005. Rheophysics of dense granular materials: Discrete simulation of plane shear flows. *Physical Review E,* 72**,** 021309.

DALLAVALLE, J. M. 1943. *Micromeritics*, LWW.

DAVIES, T. R. H. 1988. Debris flow surges: a laboratory investigation. *Mitteilungen der Versuchsanstalt fur Wasserbau, Hydrologie und Glaziologie an der Eidgenossischen Technischen Hochschule Zurich,* 96.

DAY, M. A. J. E. 1990. The no-slip condition of fluid dynamics. 33**,** 285-296.

DELANNAY, R., VALANCE, A., MANGENEY, A., ROCHE, O. & RICHARD, P. 2017. Granular and particle-laden flows: from laboratory experiments to field observations. *Journal of Physics D: Applied Physics,* 50**,** 053001.

DENLINGER, R. P. & IVERSON, R. M. 2001. Flow of variably fluidized granular masses across three - dimensional terrain: 2. Numerical predictions and experimental tests. *Journal of Geophysical Research: Solid Earth,* 106**,** 553-566.

DUNATUNGA, S. & KAMRIN, K. 2015. Continuum modelling and simulation of granular flows through their many phases. *Journal of Fluid Mechanics,* 779**,** 483-513.

FISHER, R. 1926. On the capillary forces in an ideal soil; correction of formulae given by WB Haines. *The Journal of Agricultural Science,* 16**,** 492-505.

FREDLUND, D., MORGENSTERN, N. R. & WIDGER, R. 1978. The shear strength of unsaturated soils. *Canadian geotechnical journal,* 15**,** 313-321.

GARZó, V. & DUFTY, J. 1999. Dense fluid transport for inelastic hard spheres. *Physical Review E,* 59**,** 5895.

GDR MIDI 2004. On dense granular flows. *The European Physical Journal E,* 14**,** 341-365.

GOLLIN, D. 2017. *An investigation on the collisional behaviour of granular flows.* University of Sheffield.

GOLLIN, D., BERZI, D. & BOWMAN, E. T. 2017a. Extended kinetic theory applied to inclined granular flows: role of boundaries. *Granular Matter,* 19**,** 1-16.

GOLLIN, D., BREVIS, W., BOWMAN, E. T. & SHEPLEY, P. 2017b. Performance of PIV and PTV for granular flow measurements. *Granular Matter,* 19**,** 1-16.

GOREN, L., AHARONOV, E., SPARKS, D. & TOUSSAINT, R. 2010. Pore pressure evolution in deforming granular material: A general formulation and the infinitely stiff approximation. *Journal of Geophysical Research: Solid Earth,* 115.

GOUJON, C., DALLOZ-DUBRUJEAUD, B. & THOMAS, N. 2007. Bidisperse granular avalanches on inclined planes: A rich variety of behaviors. *The European Physical Journal E,* 23**,** 199-215.

GRAY, J., WIELAND, M. & HUTTER, K. 1999. Gravity-driven free surface flow of granular avalanches over complex basal topography. *Proceedings of the Royal Society of London. Series A: Mathematical, Physical and Engineering Sciences,* 455**,** 1841-1874.

GRAY, J. M. N. T. 2018. Particle segregation in dense granular flows. *Annual review of fluid mechanics,* 50**,** 407-433.

GRAY, J. M. N. T., GAJJAR, P. & KOKELAAR, P. 2015. Particle-size segregation in dense granular avalanches. *Comptes Rendus Physique,* 16**,** 73-85.

GUYON, E., HULIN, J.-P., PETIT, L. & MITESCU, C. D. 2015. *Physical hydrodynamics*, Oxford university press.

HAINES, W. B. 1925. Studies in the physical properties of soils: II. A note on the cohesion developed by capillary forces in an ideal soil1. *The Journal of Agricultural Science,* 15**,** 529-535.

HAMPTON, M. A. 1979. Buoyancy in debris flows. *Journal of Sedimentary Research,* 49**,** 753-758.

HART, D. P. 2000. PIV error correction. *Experiments in fluids,* 29**,** 13-22.

HAZEN, A. 1892. *Some Physical Properties of Sands and Gravels: With Special Reference to Their Use in Filtration*.

HAZEN, A. 1911. Discussion: Dams on sand foundations. *Transactions, American Society of Civil Engineers,* 73.

HEIM, A. 1932. *Bergsturz und Menschenleben*, Fretz & Wasmuth.

HILL, K. M., CAPRIHAN, A. & KAKALIOS, J. 1997. Axial segregation of granular media rotated in a drum mixer: Pattern evolution. *Physical review. E, Statistical physics, plasmas, fluids, and related interdisciplinary topics,* 55**,** 4386-4389.

HOLTZ, R. & KOVACS, W. 1981. An Introduction to Geotechnical Engineering. *Peck, RB, Hanson, WE and Foundation Engineering*.

HOLYOAKE, A. J. & MCELWAINE, J. N. 2012. High-speed granular chute flows. *Journal of Fluid Mechanics,* 710**,** 35-71.

HORNBAKER, D., ALBERT, R., ALBERT, I., BARABáSI, A.-L. & SCHIFFER, P. 1997. What keeps sandcastles standing? *Nature,* 387**,** 765-765.

HOTTA, N. & OHTA, T. 2000. Pore-water pressure of debris flows. *Physics and Chemistry of the Earth, Part B: Hydrology, Oceans and Atmosphere,* 25**,** 381-385.

HOTTA, N. J. N. H. & SCIENCES, E. S. 2012. Basal interstitial water pressure in laboratory debris flows over a rigid bed in an open channel. 12**,** 2499-2505.

HUANG, B., GUO, C., TANG, Y., GUO, J. & CAO, L. 2019. Experimental Study on the Permeability Characteristic of Fused Quartz Sand and Mixed Oil as a Transparent Soil. *Water,* 11**,** 2514.

HUNGR, O. 1995. A model for the runout analysis of rapid flow slides, debris flows, and avalanches. *Canadian Geotechnical Journal,* 32**,** 610-623.

HUNGR, O., COROMINAS, J. & EBERHARDT, E. 2005. Estimating landslide motion mechanism, travel distance and velocity. *Landslide risk management.* : CRC Press.

HUNGR, O., EVANS, S. & HUTCHINSON, I. 2001. A Review of the Classification of Landslides of the Flow Type. *Environmental & Engineering Geoscience,* 7**,** 221-238.

HüRLIMANN, M., MCARDELL, B. W. & RICKLI, C. 2015. Field and laboratory analysis of the runout characteristics of hillslope debris flows in Switzerland. *Geomorphology,* 232**,** 20-32.

HüRLIMANN, M., RICKENMANN, D. & GRAF, C. J. C. G. J. 2003. Field and monitoring data of debris-flow events in the Swiss Alps. 40**,** 161-175.

HUTCHINSON, J. General report, morphological and geotechnical parameters of landslides in relation to geology and hydrogeology. Landslides, Proceedings of the Fifth International Symposium on Landslides, 1988, 1988. : .

HUTTER, K., SVENDSEN, B. & RICKENMANN, D. 1994. Debris flow modeling: A review. *Continuum mechanics and thermodynamics,* 8**,** 1-35.

IVERSON, R. M. 1993. Differential equations governing slip-induced pore-pressure fluctuations in a water-saturated granular medium. *Mathematical geology,* 25**,** 1027-1048.

IVERSON, R. M. 1997. The physics of debris flows. 35**,** 245-296.

IVERSON, R. M. 2015. Scaling and design of landslide and debris-flow experiments. *Geomorphology,* 244**,** 9-20.

IVERSON, R. M. & DENLINGER, R. P. 2001. Flow of variably fluidized granular masses across three-dimensional terrain: 1. Coulomb mixture theory. *Journal of Geophysical Research: Solid Earth,* 106**,** 537-552.

IVERSON, R. M. & LAHUSEN, R. G. 1989. Dynamic pore-pressure fluctuations in rapidly shearing granular materials. *Science,* 246**,** 796-799.

IVERSON, R. M. & LAHUSEN, R. G. 1993. Friction in debris flows: Inferences from large-scale flume experiments. *Hydraulic engineering,* 93**,** 1604-1609.

IVERSON, R. M., LOGAN, M., LAHUSEN, R. G. & BERTI, M. 2010. The perfect debris flow? Aggregated results from 28 large-scale experiments. *Journal of Geophysical Research: Earth Surface,* 115.

JANSSEN, H. 1895. Versuche über Getreidedruck in Silozellen/Zeitschr. d. Vereines deutscher Ingenieure. Vol. 39.№. 35. P. 1045-1049.

JOHNSON, A. M. 1965. *A model for debris flow,* The Pennsylvania State University.

JOHNSON, A. M. 1970. *Physical processes in geology: A method for interpretation of natural phenomena; intrusions in igneous rocks, fractures, and folds, flow of debris and ice*, Freeman, Cooper.

JOHNSON, A. M. 1984. Debris flow. *Slope instability*.

JOP, P., FORTERRE, Y. & POULIQUEN, O. 2005. Crucial role of sidewalls in granular surface flows: consequences for the rheology. *Journal of Fluid Mechanics,* 541**,** 167-192.

JOP, P., FORTERRE, Y. & POULIQUEN, O. 2006. A constitutive law for dense granular flows. *Nature,* 441**,** 727-730.

KAITNA, R., DIETRICH, W. & HSU, L. 2014. Surface slopes, velocity profiles and fluid pressure in coarse-grained debris flows saturated with water and mud. *Journal of Fluid Mechanics,* 741**,** 377-403.

KAITNA, R., PALUCIS, M. C., YOHANNES, B., HILL, K. M. & DIETRICH, W. E. 2016. Effects of coarse grain size distribution and fine particle content on pore fluid pressure and shear behavior in experimental debris flows. *Journal of Geophysical Research: Earth Surface,* 121**,** 415-441.

KEANE, R. D. & ADRIAN, R. J. 1992. Theory of cross-correlation analysis of PIV images. *Applied scientific research,* 49**,** 191-215.

KOLOSKI, J. W., SCHWARZ, S. D. & TUBBS, D. W. J. E. G. I. W. 1989. Geotechnical properties of geologic materials. 1**,** 19-24.

KOZENY, J. J. R. A. O. S., VIENNA, PROC. CLASS I 1927. Uber kapillare leitung der wasser in boden. 136**,** 271-306.

KUMARAN, V. 2006. The constitutive relation for the granular flow of rough particles, and its application to the flow down an inclined plane. *Journal of Fluid Mechanics,* 561**,** 1-42.

LEONARDI, A., CABRERA, M., WITTEL, F. K., KAITNA, R., MENDOZA, M., WU, W. & HERRMANN, H. J. 2015. Granular-front formation in free-surface flow of concentrated suspensions. *Physical Review E,* 92**,** 052204.

LI, K., WANG, Y.-F., LIN, Q.-W., CHENG, Q.-G. & WU, Y. 2021. Experiments on granular flow behavior and deposit characteristics: implications for rock avalanche kinematics. *Landslides,* 18**,** 1779-1799.

LOIS, G., LEMAîTRE, A. & CARLSON, J. M. 2005. Numerical tests of constitutive laws for dense granular flows. *Physical Review E,* 72**,** 051303.

LOUGE, M. Y. 2003. Model for dense granular flows down bumpy inclines. *Physical Review E,* 67**,** 061303.

LU, N. & LIKOS, W. J. 2004. *Unsaturated Soil Mechanics*, Wiley.

MAJOR, J. J. 1996. *Experimental studies of deposition by debris flows: Process, characteristics of deposits, and effects of pore-fluid pressure.* University of Washington.

MANZELLA, I. & LABIOUSE, V. 2013. Empirical and analytical analyses of laboratory granular flows to investigate rock avalanche propagation. *Landslides,* 10**,** 23-36.

MARCHI, L., ARATTANO, M. & DEGANUTTI, A. M. J. G. 2002. Ten years of debris-flow monitoring in the Moscardo Torrent (Italian Alps). 46**,** 1-17.

MCARDELL, B. W., BARTELT, P. & KOWALSKI, J. 2007. Field observations of basal forces and fluid pore pressure in a debris flow. *Geophysical Research Letters,* 34.

MCCARTHY, J. 2009. Turning the corner in segregation. *Powder Technology,* 192**,** 137-142.

MCCOY, S. W., KEAN, J. W., COE, J. A., STALEY, D. M., WASKLEWICZ, T. A. & TUCKER, G. E. 2010. Evolution of a natural debris flow: In situ measurements of flow dynamics, video imagery, and terrestrial laser scanning. *Geology,* 38**,** 735-738.

MCDOUGALL, S. & HUNGR, O. 2004. A model for the analysis of rapid landslide motion across three-dimensional terrain. *Canadian Geotechnical Journal,* 41**,** 1084-1097.

MENG, X., JOHNSON, C. & GRAY, J. J. J. O. F. M. 2022. Formation of dry granular fronts and watery tails in debris flows. 943.

MIDDLETON, G. V. Experimental studies related to problems of flysch sedimentation. 1970. : .

MITARAI, N. & NAKANISHI, H. 2005. Bagnold scaling, density plateau, and kinetic theory analysis of dense granular flow. *Physical review letters,* 94**,** 128001.

MORO, F., FAUG, T., BELLOT, H. & OUSSET, F. 2010. Large mobility of dry snow avalanches: Insights from small-scale laboratory tests on granular avalanches of bidisperse materials. *Cold Regions Science and Technology,* 62**,** 55-66.

OBRZUD, R. 2010. *The hardening soil model: A practical guidebook,* Zace Services.

OGAWA, S. Multitemperature theory of granular materials. Proc. of the US-Japan Seminar on Continuum Mechanical and Statistical Approaches in the Mechanics of Granular Materials, 1978, 1978. : Gakajutsu Bunken Fukyu-Kai, 208-217.

OKADA, Y. J. J. O. F. R. 2014. Functions of Chisan dams in large-scale granular mass-flow experiments on Sakurajima volcano pumiceous clasts. 19**,** 493-500.

PAREZ, S., AHARONOV, E. & TOUSSAINT, R. 2016. Unsteady granular flows down an inclined plane. *Physical review E*, 93**,** 042902.

PARSONS, J. D., WHIPPLE, K. X. & SIMONI, A. 2001. Experimental study of the grain-flow, fluid-mud transition in debris flows. *The Journal of Geology*, 109**,** 427-447.

PHILLIPS, J. C., HOGG, A. J., KERSWELL, R. R. & THOMAS, N. H. 2006. Enhanced mobility of granular mixtures of fine and coarse particles. *Earth and Planetary Science Letters,* 246**,** 466-480.

PIERRAT, P. & CARAM, H. S. 1997. Tensile strength of wet granula materials. *Powder Technology,* 91**,** 83-93.

PIERSON, T. C. 1981. Dominant particle support mechanisms in debris flows at Mt Thomas, New Zealand, and implications for flow mobility. *Sedimentology,* 28**,** 49-60.

PIERSON, T. C. 1986. Flow behavior of channelized debris flows Mount St. Helens Washington. *Hillslope Processes***,** 269-296.

PIRES-STURM, A. P. & DEJONG, J. T. 2022. Influence of Particle Size and Gradation on Liquefaction Potential and Dynamic Response. *Journal of Geotechnical and Geoenvironmental Engineering,* 148**,** 04022045.

POULIQUEN, O. 1999. Scaling laws in granular flows down rough inclined planes. *Physics of fluids,* 11**,** 542-548.

POULIQUEN, O. & FORTERRE, Y. 2002. Friction law for dense granular flows: application to the motion of a mass down a rough inclined plane. *Journal of fluid mechanics,* 453**,** 133-151.

PRASAD, A., ADRIAN, R., LANDRETH, C. & OFFUTT, P. 1992. Effect of resolution on the speed and accuracy of particle image velocimetry interrogation. *Experiments in Fluids,* 13**,** 105-116.

PUDASAINI, S. P. & HUTTER, K. 2003. Rapid shear flows of dry granular masses down curved and twisted channels. *Journal of Fluid Mechanics,* 495**,** 193-208.

RAFFEL, M., WILLERT, C. E., SCARANO, F., KäHLER, C. J., WERELEY, S. T. & KOMPENHANS, J. 2018. *Particle image velocimetry: a practical guide*, Springer.

RAYMOND, G. P. 2002. Reinforced ballast behaviour subjected to repeated load. *Geotextiles and Geomembranes,* 20**,** 39-61.

RUMPF, H. The strength of granules and agglomerates. Agglomeration-Proceedings of the First International Symposium on Agglomeration, Philadelphia, 1962, 1962. : , 379-418.

SANVITALE, N. 2010. An experimental study on saturated granular flows and its application to the physical modelling of debris flows.

SANVITALE, N. & BOWMAN, E. T. 2012. Internal imaging of saturated granular free-surface flows. *International Journal of Physical Modelling in Geotechnics,* 4**,** 129-142.

SANVITALE, N. & BOWMAN, E. T. 2017. Visualization of dominant stress-transfer mechanisms in experimental debris flows of different particle-size distribution. *Canadian Geotechnical Journal,* 54**,** 258-269.

SARNO, L., CARRAVETTA, A., TAI, Y.-C., MARTINO, R., PAPA, M. & KUO, C.-Y. 2018. Measuring the velocity fields of granular flows–Employment of a multi-pass two-dimensional particle image velocimetry (2D-PIV) approach. *Advanced Powder Technology,* 29**,** 3107-3123.

SAVAGE, S. & LUN, C. 1988. Particle size segregation in inclined chute flow of dry cohesionless granular solids. *Journal of fluid mechanics,* 189**,** 311-335.

SAVAGE, S. & SAYED, M. 1984. Stresses developed by dry cohesionless granular materials sheared in an annular shear cell. *Journal of Fluid Mechanics,* 142**,** 391-430.

SAVAGE, S. B. 1984. The mechanics of rapid granular flows. *Advances in applied mechanics.* : Elsevier.

SAVAGE, S. B. & HUTTER, K. 1989. The motion of a finite mass of granular material down a rough incline. *Journal of fluid mechanics,* 199**,** 177-215.

SCARANO, F. 2001. Iterative image deformation methods in PIV. *Measurement science and technology,* 13**,** R1.

SCARANO, F. & RIETHMULLER, M. L. 2000. Advances in iterative multigrid PIV image processing. *Experiments in Fluids,* 29**,** S051-S060.

SCHATZMANN, M. 2005. *Rheometry for large particle fluids and debris flows.* ETH Zurich.

SCHOLTèS, L., HICHER, P. Y., NICOT, F., CHAREYRE, B. & DARVE, F. 2009. On the capillary stress tensor in wet granular materials. *International journal for numerical and analytical methods in geomechanics,* 33**,** 1289-1313.

SILBERT, L. E., ERTAŞ, D., GREST, G. S., HALSEY, T. C., LEVINE, D. & PLIMPTON, S. J. 2001. Granular flow down an inclined plane: Bagnold scaling and rheology. *Physical Review E,* 64**,** 051302.

SLICHTER, C. S. 1902. The motions of underground waters. : Govt. Print. Off.

SMITH, G., DAVIES, T., MCSAVENEY, M. & BELL, D. J. L. 2006. The Acheron rock avalanche, Canterbury, New Zealand—morphology and dynamics. 3**,** 62-72.

STANCANELLI, L., LANZONI, S. & FOTI, E. J. W. R. R. 2015. Propagation and deposition of stony debris flows at channel confluences. 51**,** 5100-5116.

STRAUB, S. 1996. Self-organization in the rapid flow of granular material: evidence for a major flow mechanism. *Geologische Rundschau,* 85**,** 85-91.

TAKAHASHI, T. 1978. Mechanical characteristics of debris flow. *Journal of the Hydraulics Division,* 104**,** 1153-1169.

TAKAHASHI, T. 1981. Debris flow. *Annual review of fluid mechanics,* 13**,** 57-77.

TAKAHASHI, T. 1991. *Debris Flow*, Taylor & Francis.

TAKAHASHI, T. 2001. Mechanics and simulation of snow avalanches, pyroclastic flows and debris flows. *Particulate gravity currents***,** 9-43.

TAYLOR-NOONAN, A. M., BOWMAN, E., MCARDELL, B., KAITNA, R., MCELWAINE, J. & TAKE, A. 2022. Influence of pore fluid on grain-scale interactions and mobility of granular flows of differing volume.

TE CHOW, V. 1959. *Open-channel Hydraulics*, McGraw-Hill.

TERZAGHI, K. & PECK, R. B. 1948. Soil Mechanics. *Engineering Practice. John Wiley and Sons, Inc., New York.*

THAN, V. D., KHAMSEH, S., TANG, A. M., PEREIRA, J.-M., CHEVOIR, F. & ROUX, J.-N. 2017. Basic mechanical properties of wet granular materials: a DEM study. *Journal of Engineering Mechanics,* 143**,** C4016001.

THIELICKE, W. 2014. *The flapping flight of birds: Analysis and application*, University of Groningen.

URSO, M. E. D., LAWRENCE, C. J. & ADAMS, M. J. 1999. Pendular, funicular, and capillary bridges: results for two dimensions. *Journal of colloid and interface science,* 220**,** 42-56.

URUMOVIĆ, K., URUMOVIĆ SR, K. J. H. & SCIENCES, E. S. 2016. The referential grain size and effective porosity in the Kozeny–Carman model. 20**,** 1669-1680.

VANAPALLI, S., FREDLUND, D., PUFAHL, D. & CLIFTON, A. 1996. Model for the prediction of shear strength with respect to soil suction. *Canadian geotechnical journal,* 33**,** 379-392.

VARNES, D. J. 1978. Slope movement types and processes. *Special report,* 176**,** 11-33.

VOELLMY, A. 1955. Über die Zerstörungskraft von Lawinen. *Schweizerische Bauzeitung,* 73**,** 246.

WATANABE, T. J. J. O. T. C. S. O. J. 2009. Wettability of ceramic surfaces-A wide range control of surface wettability from super hydrophilicity to super hydrophobicity, from static wettability to dynamic wettability. 117**,** 1285-1292.

WHEELER, S. & SIVAKUMAR, V. 1995. An elasto-plastic critical state framework for unsaturated soil. *Géotechnique,* 45**,** 35-53.

WHIPPLE, K. X. 1997. Open-channel flow of Bingham fluids: applications in debris-flow research. *The Journal of Geology,* 105**,** 243-262.

WHITE, D., TAKE, W. & BOLTON, M. 2003. Soil deformation measurement using particle image velocimetry (PIV) and photogrammetry. *Geotechnique,* 53**,** 619-631.

WILLIAMS, J. C. 1976. The segregation of particulate materials. A review. *Powder Technology,* 15**,** 245-251.

YANG, K., XU, Z.-M., TIAN, L., WANG, K., REN, Z., TANG, Y.-J., LUO, J.-Y. & GAO, H.-Y. 2020. Significance of coarse clasts in viscous debris flows. *Engineering geology,* 272**,** 105665.

YANG, Q., SU, Z., CAI, F. & UGAI, K. 2015. Enhanced mobility of polydisperse granular flows in a small flume. *Geoenvironmental Disasters,* 2**,** 1-9.

YANO, K. & DAIDO, A. 1965. Fundamental study on mud-flow. *Bulletin of the Disaster Prevention Research Institute,* 14**,** 69-83.

YIN, M., RUI, Y. & XUE, Y. 2019. Centrifuge study on the runout distance of submarine debris flows. *Marine Georesources & Geotechnology,* 37**,** 301-311.

ZHANG, C., LU, N. J. J. O. G. & ENGINEERING, G. 2019. Unitary definition of matric suction. 145**,** 02818004.

ZHANG, S., LI, X. & DU, Y. 2022. A numerical model of discrete element–Liquid bridge–Liquid thin film system for wet deforming granular medium at low saturation. *Powder Technology,* 399**,** 117217.

ZHOU, G., WRIGHT, N. G., SUN, Q. & CAI, Q. 2016. Experimental Study on the Mobility of Channelized Granular Mass Flow. *Acta Geologica Sinica - English Edition,* 90**,** 988-998.

ZHOU, G. G. & NG, C. W. 2010. Dimensional analysis of natural debris flows. *Canadian Geotechnical Journal,* 47**,** 719-729.

ZHOU, Z.-H., REN, Z., WANG, K., YANG, K., TANG, Y.-J., TIAN, L. & XU, Z.-M. 2018. Effect of excess pore pressure on the long runout of debris flows over low gradient channels: a case study of the Dongyuege debris flow in Nu River, China. *Geomorphology*, 308**,** 40-53.